PROPERTIES OF DAO WHITE DWARFS

Thesis submitted for the degree of

Doctor of Philosophy

at the University of Leicester

by

Simon A. Good

X-ray and Observational Astronomy Group

Department of Physics and Astronomy

University of Leicester

October, 2003

Declaration

I hearby declare that no part of this thesis has been previously submitted to this or any other University as part of the requirement for a higher degree. The work described herein was conducted by the undersigned except for contributions from colleagues as acknowledged in the text.

SA Good

Simon A. Good
September 8, 2004

UV AND OPTICAL STUDIES OF THE PHYSICAL PROPERTIES OF DAO WHITE DWARFS

Simon A. Good

ABSTRACT

An investigation into the physical properties and evolutionary status of DAO white dwarfs has been conducted, using optical and far-UV observations. Out of the 22 objects for which optical data were obtained, the spectrum of only one is best fitted by a stratified H+He composition model; this may be an object transferring between the He- and H-rich cooling sequences. Homogeneous models are preferred for the remainder, but with 90% confidence in less than half the objects. The DAOs fall into two groups: The low $T_{\rm eff}$, high log g objects have temperatures and gravities that are similar to the majority of the DAs and mostly consist of DAO+dM binaries. The high $T_{\rm eff}$, low log g objects, which make up approximately two thirds of the sample, have relatively high luminosities for white dwarfs, and the most likely mechanism that is countering the gravitational settling for these objects is mass loss. When this ceases these objects will become low-mass DAs.

A search for evidence of binarity in the far-UV FUSE observations of 22 objects yielded positive results for only 5, suggesting that the majority of DAOs are descended from isolated stars. As seen in the DAs, the $T_{\rm eff}$ derived from Balmer and Lyman lines for objects hotter than $\sim$50,000 K were found to be different, with the latter yielding the higher temperature. For 7 objects, the Lyman lines are so shallow that a model with $T_{\rm eff} >$ 120,000 K is required to reproduce them. An investigation of the strength of photospheric absorption lines showed that the low log g objects have high heavy element abundances compared to DAs, whereas the DAO+dM binaries have slightly elevated lighter element abundances, with the heavier elements abundances similar to those seen in the DAs. This is qualitatively consistent with mass loss and accretion from a companions wind respectively, as the explanation for the helium that is observed in the spectra of the stars.

PUBLICATIONS

Barstow, M.A., Good, S.A., Bannister, N.P., Burleigh, M.R., Holberg, J.B., Bruhweiler, F.C., Napiwotzki, R., Cruddace, R.G. and Kowalski, M.P. **2003** 'High resolution EUV and FUV spectroscopy of DA white dwarfs' in NATO Advanced Research 13th European Workshop on White Dwarfs. 2003. Capodimonte, Italy. Kluwer Academic Publishers. 105. 121-124.

Barstow, M.A., Good, S.A., Burleigh, M.R., Hubeny, I., Holberg, J.B. and Levan, A.J., **2003**. 'A comparison of DA white dwarf temperatures and gravities from FUSE Lyman line and ground-based Balmer line observations'. MNRAS. In press.

Barstow, M.A., Good, S.A., Holberg, J.B., Burleigh, M.R., Bannister, N.P., Hubeny, I. and Napiwotzki, R., **2002**. 'FUSE observations of PG1342+444: new insights into the nature of the hottest DA white dwarfs'. MNRAS. **330**, 425-434.

Barstow, M.A., Good, S.A., Holberg, J.B., Hubeny, I., Bannister, N.P., Bruhweiler, F.C., Burleigh, M.R. and Napiwotzki, R., **2003**. 'Heavy-element abundance patterns in hot DA white dwarfs'. MNRAS. **341**, 870-890.

Barstow, M.A., Holberg, J.B., Hubeny, I., Good, S.A., Levan, A.J. and Meru, F., **2001**. 'A comparison of DA white dwarf temperatures and gravities from Lyman and Balmer line studies'. MNRAS. **328**, 211-222.

Burleigh, M., Barstow, M., Good, S., Bond, H.E. and Holberg, J. **2003** 'Far-UV observations of Sirius-like binaries'. in NATO Advanced Research 13th European Workshop on White Dwarfs. 2003. Capodimonte, Italy. Kluwer Academic Publishers. 105. 341-344.

Burleigh, M.R., Barstow, M.A., Schenker, K.J., Sills, A.I., Wynn, G.A., Dobbie, P.D. and Good, S.A., **2001**. 'The low-mass white dwarf companion to Beta Crateris'. MNRAS. **327**,1158-1164.

Burleigh, M.R., Levan, A.J., Good, S.A., Barstow, M.A. and Holberg, J.B., **2003**. 'FUSE observations of Sirius-like binaries'. MNRAS. In press.

Good, S.A., Barstow, M.A., Burleigh, M.R., Holberg, J.B., Sing, D., Napiwotzki, R. and Bruhweiler, F.C. **2003** 'Spectroscopic determination of mass for a sample of DAO white dwarfs'. in NATO Advanced Research 13th European Workshop on White Dwarfs. 2003. Capodimonte, Italy. Kluwer Academic Publishers. 105. 143-146.

Holberg, J.B., Sing, D., Barstow, M.A. and Good, S. **2001** 'HS 1136+6646: A new short period DAP + dMe system' in Annual Scientific Meeting of the Astronomische Gesellschaft at the JENAM 2001. Munich. 18, 106.

Schuh, S.L., Heber, U., Dreizler, S., O'Toole, S., Jeffery, C.S., Falter, S., et al., **2003**. 'PG 1605+072 in WET XCov22: Support for the multi site spectroscopic telescope'. Baltic Astronomy. 12, 55-70.

Schuh, S.L., Nagel, T., Deetjen, J.L., Dreizler, S., Handler, G., O'Brien, M.S. et al., **2002** 'Preliminary results of the WET Xcov 22 campaign at Calar Alto Observatory' in NATO Advanced Research 13th European Workshop on White Dwarfs. 2002. Capodimonte, Italy: Kluwer Academic Publishers. 105, 263.

Sing, D.K., Holberg, J.B., Barstow, M.A., Burleigh, M., Good, S., Oswalt, T., Howell, S. and Brinkworth, C. **2003** 'HS1136+6646: A Hot DAO.5K6V Young Post-CE Pre-CV Binary.' in NATO Advanced Research 13th European Workshop on White Dwarfs. 2003. Capodimonte, Italy. Kluwer Academic Publishers. 105. 349-350.

Sing, D.K., Holberg, J.B., Burleigh, M.R., Good, S.A., Barstow, M.A., Oswalt, T.D., Howell, S.B. and Brinkworth, C.S., **2003**. 'Spectroscopic and photometric analysis of HS1136+6646: a hot young DAO+K7V post-common envelope pre-cataclysmic variable binary'. Ap.J., In press.

ACKNOWLEDGEMENTS

There are many people I should thank in these acknowledgements, half of who I would probably forget if I attempted to list them all, so I shall stick to the people who have contributed most to my work and life during my PhD. First of all I'd like to thank Martin for his all that he has taught me, and the advice and guidance that he has provided throughout my PhD. Thanks also to Matt Burleigh and Jay Holberg for introducing me to observing and for the help they have given. Also to Paul Dobbie for some useful discussions.

Thanks also to all the postgrads and postdocs who have made life in the XROA group fun and interesting, but who are far too numerous to mention by name. However, particular mention must go to Alex and Kim for sharing an office with me for 3 years, Tim for helping to keep coffee going, and the XBLAST players: Alex, Darach, Darren, James and Nick – Alex and I were really not ganging up on you!

Finally a big thanks to my parents and sister – I will finally stop being a student now! And of course to Lizzie, who I probably would not have met if I hadn't done this PhD.

OVERVIEW

The work presented in this thesis is aimed at understanding the physical properties and evolutionary history of an unusual type of white dwarf, the DAOs, by investigating the properties of a large sample of these objects. The DAOs are unusual since their spectra contain both hydrogen and helium lines, which is difficult to explain as the high gravity that exists within the white dwarf atmosphere should cause the helium to sink to below the line forming region of the star. To introduce the subject, I use Chapter 1 to describe the formation and general properties of white dwarfs. Chapter 2 then describes the possible explanations for the presence of helium, and includes a list of DAO white dwarfs. The data analysed in this thesis cover two wavelength regions – optical and far-UV. Chapter 3 deals with the analysis and results from the optical data. By comparing atmospheric and evolutionary models with the real spectra, the fundamental parameters of the star are determined. The relatively large sample size allows the population of DAOs to be studied. The remaining data chapters then cover the reduction, analysis and results from the far-UV data, which were taken by the FUSE satellite. Unfortunately, many of the FUSE spectra are contaminated by molecular hydrogen in the line of sight to the target. I describe FUSE in Chapter 4, and the method I have used to account for the molecular hydrogen in order to allow the white dwarf spectrum to be analysed in Chapter 5. In Chapter 6 I use FUSE observations to search for radial velocity shifts in photospheric heavy element lines, which would indicate binarity. This has important implications since the composition of a white dwarf that is formed within a binary system can be altered if it evolves within a binary system. The fundamental parameters of the white dwarfs are then determined from the FUSE data in Chapter 7. Unfortunately, as related in Chapter 8, the results from optical and FUSE data are are not always consistent. A study of the composition of DAO white dwarfs is described in Chapter 9. Finally, I summarise my conclusions in Chapter 10.

Contents

List of Figures

List of Tables

Chapter 1

Introduction to white dwarf stars

1.1 Introduction

White dwarfs are the endpoint of stellar evolution for 98% (Wood, 1992) of stars, including the Sun, so knowledge of their formation, composition and structure is vital to our understanding of stellar astrophysics. Since the mass of a white dwarf is typically half that of the Sun, but contained within a volume only the size of the Earth, they are very dense, compact objects, which are supported by electron degeneracy pressure. The hot, high gravity conditions provide an opportunity to study physics under conditions that are unreproducible in a laboratory and as white dwarfs have no internal energy source, they cool slowly over millions of years, with the oldest white dwarfs used to place limits on the age of the galaxy. The identification of white dwarfs as the progenitors of type 1a supernovae has also fuelled much interest in their evolution. This chapter describes the formation and general properties of white dwarfs stars.

1.2 Evolution from the main sequence

All stars with mass $<8\,M_{\odot}$ will eventually become white dwarfs (Iben-Jr, 1991). Stars more massive than this will die in a supernova explosion and become neutron stars or black holes. The exact evolutionary path that a star follows on its way to becoming a white dwarf differs according to its mass, with higher mass stars evolving faster; the possible routes that a star takes before becoming a white dwarf are summarised below.

1.2.1 Isolated stars

Stars form as a result of gravitational collapse in molecular clouds. As collapse progresses, the potential energy of the matter that will make up the star changes from a value that is close to zero to being negative. Since the total energy of the system must be constant, this energy must be radiated away or converted into other forms, such as thermal energy, which heats the star. Calculation of the mechanical energy that was given to the Sun by this collapse (which, since the virial theorem states that this energy (E) is related to the potential (U) by $E = \frac{1}{2}U$, is half the change in gravitational potential), suggests that if this were its only energy source, at its current luminosity it could only emit energy for 10^7 yr. This is known as the Kelvin-Helmholtz time scale. However, this is orders of magnitude less than 4×10^9 yr that is estimated as the age of the Moon (Carroll & Ostlie, 1996). An alternative energy source for stars is nuclear fusion of hydrogen to form helium, which can occur if the core of the star gets hot enough. Assuming that 10% of the Sun's mass can be used to fuse hydrogen into helium, then its 'nuclear time scale' is 10^{10} yr, which is consistent with the age of the Moon (Carroll & Ostlie, 1996). This occurs through the proton-proton cycle for stars less massive than $\sim$1.2 M$_\odot$ (de Loore & Doom, 1992). For more massive, hotter, stars the CNO cycle can take place. However below a mass of approximately 0.08 M$_\odot$, the temperature of the core never becomes hot enough to begin nuclear reactions, while stars more massive than 90 M$_\odot$ never become stable because of thermal oscillations in their centres (Carroll & Ostlie, 1996). Stars for which stable core hydrogen burning is occurring lie on the Hertzsprung-Russell (HR) diagram on the 'main sequence' (see Figure 1.1). The time it takes to begin stable hydrogen burning and join the main sequence depends on the mass of the star, with a 0.5 M$_\odot$ star taking $>1 \times 10^8$ years, a star like the Sun taking 5×10^7 yr and for a 15 M$_\odot$ star 60,000 yr (Iben, 1965). Once on the main sequence, a star stays there for most of its lifetime, for example the Sun will be on the main sequence for about 80% of its life (Zeilik et al., 1973). A star's luminosity is related to its mass by the relationship (Zeilik et al., 1973):

$$\frac{L}{L_\odot} = \left(\frac{M}{M_\odot}\right)^{3.3}$$

Hence, a star's lifetime is related to the Sun's by (Zeilik et al., 1973):

$$\frac{t}{t_\odot} = \frac{\frac{M}{M_\odot}}{\frac{L}{L_\odot}} = \left(\frac{M}{M_\odot}\right)^{-2.3}$$

Therefore, if the Sun stays on the main sequence for 10^{10} years, a 0.5 M$_\odot$ star will remain there for $\sim 5 \times 10^{10}$ yr, but a 15 M$_\odot$ will leave the main sequence after only $\sim 2 \times 10^7$

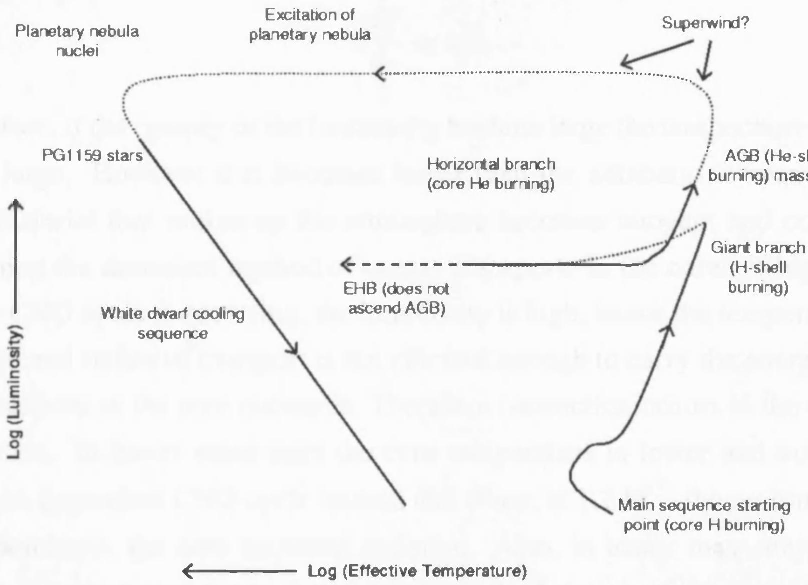

FIGURE 1.1. Hertzsprung-Russell diagram of the evolution of stars from the main sequence to a white dwarf. Reproduced from Burleigh (1997), originally from Marsh (1995).

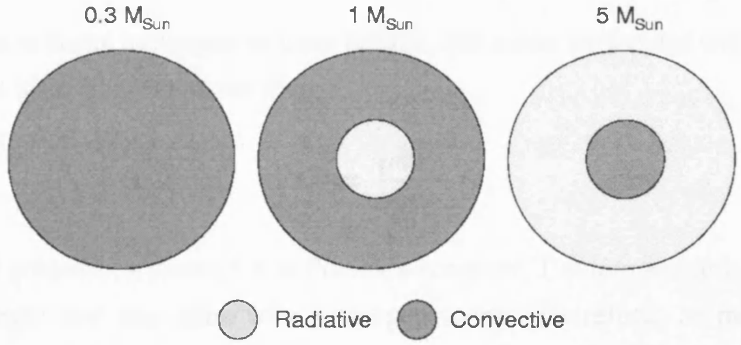

FIGURE 1.2. Diagram (not to scale) of the location of radiative and convective zones within stars of mass 0.3, 1 and 5 $M_\odot$.

yr. As a result of the slow evolution of lower mass stars, the most massive stars observed in globular clusters that are still in the main sequence phase of their lives are 0.8 $M_\odot$ (Iben-Jr, 1991).

The internal structure of a star also depends on its mass (Figure 1.2). The temperature gradient for radiative transport is related to opacity ($\bar{\kappa}$) and local radiative luminosity (L_r) by (Carroll & Ostlie, 1996):

$$\frac{dT}{dr} \propto \bar{\kappa} L_r$$

Therefore, if the opacity or the luminosity become large the temperature gradient also becomes large. However if it becomes larger than the adiabatic temperature gradient then the material that makes up the atmosphere becomes buoyant and convection sets in, becoming the dominant method of energy transport. In the cores of high mass stars, where the CNO cycle is occurring, the luminosity is high, hence the temperature gradient is also high and radiative transport is not efficient enough to carry the energy released by nuclear reactions in the core outwards. Therefore convection occurs in the cores of these massive stars. In lower mass stars the core temperature is lower and output from the temperature dependent CNO cycle lessens and when, at 1.2 $M_\odot$, the proton-proton chain starts to dominate, the core becomes radiative. Also, in lower mass stars, the opacity of the star increases near the surface because of the location of the hydrogen ionisation zone. This has the effect of increasing the temperature gradient in the outer layers of the star and so stars with mass $<\sim$1.3 $M_\odot$ have convection zones near their surfaces (Carroll & Ostlie, 1996). In lower mass stars, the bottom of the convection zone gets closer to the centre, and for stars less than 0.3 $M_\odot$ the entire star is convective Carroll & Ostlie (1996).

In a star, as it burns hydrogen to form helium, the mean molecular weight of the core increases. The ideal gas law states that:

$$P = \frac{\rho k T}{\mu m_H}$$

where P is the pressure, ρ density, k is Planck's constant, T is temperature, μ is the mean molecular weight and m_H mass of a hydrogen atom. Therefore, as mean molecular weight increases, pressure decreases and the core must contract as a consequence of the condition of hydrostatic equilibrium, which states that a pressure gradient must exist to counteract the force of gravity:

$$\frac{dP}{dr} = -G\frac{M_r \rho}{r^2}$$

where P is pressure, r the distance from the centre of the star, G the gravitational constant, M_r the mass within a sphere of radius r and ρ is the density. According to the virial thereom, half the released gravitational energy will be converted into heat, increasing the temperature of the core. This increases the rate of nuclear reaction, and the luminosity and effective temperature of the star increases. It moves upwards and to the left along the main sequence on the HR diagram.

Eventually, all the hydrogen in the core is exhausted. This happens first in the centre of the core for the lower mass stars and then gradually extends outwards. However, for the more massive stars, as the core is well mixed by convection, the hydrogen is exhausted suddenly. This leaves behind a core that is essentially composed of helium, and since its luminosity is zero, it is isothermal. The star contracts due to the loss of energy brought about by the end of the core hydrogen burning phase. Hydrogen shell burning then occurs, which creates helium and slowly increases the size of the core. In addition, some of the energy is used in making the outer layers of the star expand and it becomes a giant.

As the mass of the isothermal core increases, it must become more compressed in order to support itself in hydrostatic equilibrium. The maximum size of an isothermal core that is able to support itself from collapse using gas pressure is 8% of the total mass of the star (this is known as the Schönberg-Chandrasekhar limit). If this limit is to be exceeded, the core must become partially degenerate so that the ideal gas pressure can be supplemented by electron degeneracy pressure. This occurs in stars less massive than 2 $M_{\odot}$ (Carroll & Ostlie, 1996). Once the temperature in the core becomes high enough, helium burning can occur through the triple alpha process. In the stars with degenerate cores, pressure is not related to temperature, only density ($P \propto \rho^{\frac{5}{3}}$ for non-relativistic electrons), and so as helium burning begins the temperature increases, but the pressure is unaffected and the core does not expand. The triple alpha process is highly temperature dependent, so the rate of reaction increases causing a thermal runaway called the helium flash. This only lasts for a few seconds, but releases 10^{11} $L_{\odot}$, which is comparable to the luminosity of the entire galaxy (Carroll & Ostlie, 1996). Most of the energy that is generated is absorbed by the atmosphere of the star, and some is used to lift the degeneracy and expand the core, decreasing the density and temperature, reducing the rate of reaction.

When the helium is exhausted, degeneracy sets in within the carbon-oxygen core. Outside this is a layer of helium. Helium shell burning can begin and the star goes through another red giant phase. Hydrogen can also be reignited in an outer shell and the helium shell burning starts to turn on and off periodically. This occurs because the hydrogen shell burning is creating helium and adding to the mass of the helium layer, and it becomes slightly degenerate. Once the temperature of the helium shell is high enough a helium flash occurs, driving the hydrogen shell outward, cooling it and turning it off. Once the helium burning rate has decreased again sufficiently, the hydrogen shell reignites, repeating the process. The period between these thermal pulses range from thousands of years for stars of the order 5 $M_{\odot}$, to hundreds of thousands or years for 0.6 $M_{\odot}$ stars (Carroll & Ostlie, 1996), with the pulses themselves lasting only few tens

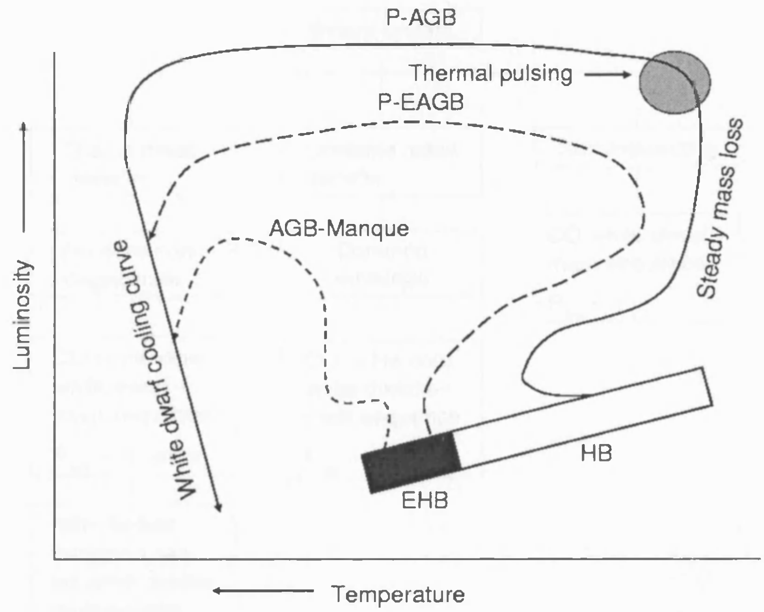

FIGURE 1.3. Evolution to white dwarfs from the horizontal branch. Reproduced from Dorman et al. (1993).

of years (de Loore & Doom, 1992). Luminosity increases with each pulse, and the star moves vertically on a path on the HR diagram known as the asymptotic giant branch (AGB). However, if the star is less than 1 $M_{\odot}$, it cannot begin helium shell burning (de Loore & Doom, 1992). These low mass objects can be subdivided into two types – the post-early AGB (P-EAGB) stars, which leave the AGB before thermal pulsing, and the AGB-manqué stars, that never ascend the AGB. Instead they move along the extended horizontal branch (EHB) as a subdwarf star, losing mass until eventually becoming a low mass white dwarf (Dorman et al., 1993). Their evolution is illustrated in Figure 1.3.

The stars then lose mass through what is thought to be a 'superwind'. The core contracts until electron degeneracy sets in. Once the central star is hotter than ~30,000 K, the ejected material is ionised, forming what is known as a planetary nebula (PN). The PN dissipates in ~100,000 years, leaving behind a hot (temperature > 100,000 K) white dwarf star.

1.2.2 Stars in close binary systems

The evolution of stars in binary systems that will one day become white dwarfs is described in detail in de Kool (1992), de Kool & Ritter (1993) and Iben & Livio (1993), and many other papers. Approximately half of all stars exist in binary systems, although half

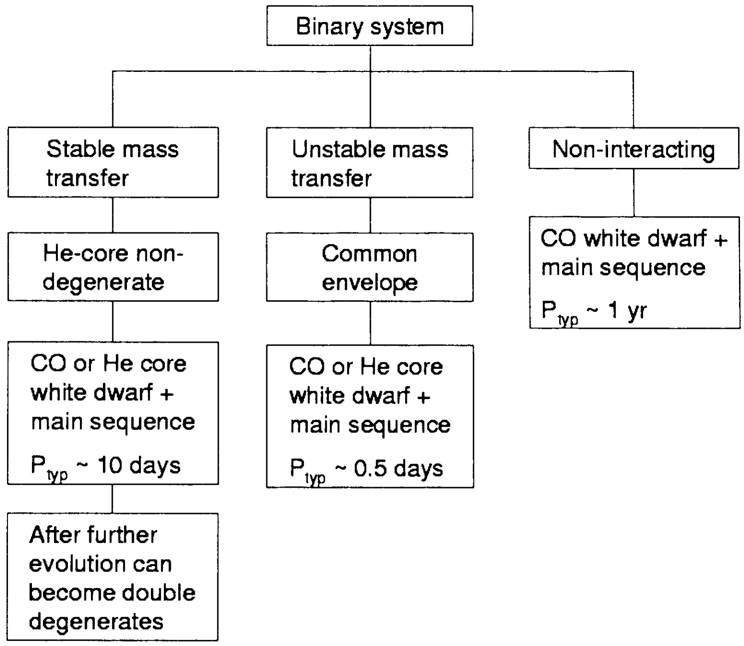

FIGURE 1.4. Overview of evolutionary paths leading to binary systems relevant to this thesis, adapted from de Kool & Ritter (1993).

again will never interact – these stars evolve as if they are isolated. There are three main ways in which a binary system might come to interact: firstly, through orbital shrinkage brought about by angular momentum loss due to a magnetic stellar wind or gravitational wave radiation, secondly, a low-mass companion may be drawn in to the envelope of the primary star by tidal dissipation, and thirdly, when a star expands during a giant phase it may fill its Roche lobe – the equipotential surface around the two stars which forms a figure-of-eight cross section – and matter spills onto the companion through the first Lagrangian point. It is this last scenario that is of interest to this thesis as it will alter the composition of the stars. Different forms of mass transfer can occur due to Roche lobe filling. Some of these are summarised in Figure 1.4, and the following description of these modes are summarised from de Kool (1992).

Mode II mass transfer occurs as the primary is transferring from the main sequence to the giant branch. The mass transfer is stable as the secondary is able to adjust its structure and accrete all the material, although the exception to this is if the mass ratio of the system is extreme, in which case a common-envelope may form and the two stars will eventually coalesce. The result of this mass transfer is a He-star primary, which will evolve to become a white dwarf. Eventually the system becomes a white dwarf plus main sequence binary with a typical orbital period of 10 days. As these binaries evolve further they can become double degenerate systems see, for example, Holberg et al. (1995) and

Marsh et al. (1995).

Mode III mass transfer occurs when the primary has a convective envelope while it is on the giant branch or as it ascends the AGB. The star fills its Roche lobe and matter is transferred to the secondary. The donor star expands in response to mass loss and the transfer is too rapid for the secondary to adjust its structure and it becomes surrounded by material, which is known as the common-envelope (CE). The system loses angular momentum due to the friction of the CE and the period shortens; some of the systems will eventually coalesce. If there is sufficient energy, the CE will be ejected, forming a PN. According to de Kool & Ritter (1993), about 10% of these systems will survive as binaries and most will have a period of less than a day. The mass of the primary will be approximately the same as the mass of its core before it entered the CE phase. If the mass transfer occurred after hydrogen shell burning, and the star is less massive than 0.48 $M_{\odot}$ (Bergeron et al., 1994, although this value varies according to the author), then helium burning cannot occur, resulting in a low-mass He-core white dwarf. More massive CO- or ONeMg-core white dwarfs can also be formed in this way. Further angular momentum will be lost through magnetic stellar wind braking and the emission of gravitational waves and the secondary may eventually fill its Roche lobe, resulting in a cataclysmic variable (CV).

1.3 White dwarfs

1.3.1 Basic properties

The first white dwarf to be discovered was Sirius B, which is the companion to the brightest star in the sky, Sirius. From the 'wobble' of the star in the sky, F.W. Bessel inferred the presence of a companion. However Sirius B was found to be 1,000 times less luminous than Sirius A, yet its temperature appeared higher. The suggested that the radius of the star was very small – typically a white dwarf has a similar size to the Earth, yet as its mass was found to be close to 1 $M_{\odot}$ this implied an extremely high density. Under this pressure the electrons in the core of the star mostly occupy the lowest energy levels and hence are degenerate. They behave like a gas with pressure related to density by $P \propto \rho^{\frac{5}{3}}$, in contrast to the cores of 'normal' stars, where the electrons behave like an ideal gas and so pressure is proportional to density and temperature. Due to the Pauli exclusion principle no two electrons can have the same quantum state within a certain volume, hence 'electron degeneracy pressure' prevents the core contracting any further.

The degenerate electrons can be approximated as supplying the pressure, while the non-degenerate ions hold the mass. The maximum mass that can be supported in this way was famously found by Chandrasekhar (1939) to be

$$M = \left(\frac{2}{\mu}\right)^2 1.4587 M_\odot$$

($\mu = A/Z$ and is ~2 for white dwarfs). Radius is related to mass in a white dwarf by:

$$R \propto \frac{1}{M^{\frac{1}{3}}}$$

hence adding mass to a white dwarf decreases its size. Improvements to Chandrasekhar's original theory have been made, for example Hamada & Salpeter (1961) included the effects of electrostatic interactions in their models, which results in a reduction of the maximum mass that a white dwarf can have. They also refined the mass-radius relation, under the assumption of zero temperature. In reality, however, this assumption is not valid. Evolutionary models, such as by Blöcker (1995), are now the state-of-the-art. These follow the cooling of the white dwarfs as they leave the AGB, and predict the radius of the white dwarf over time. Figure 1.5 shows one of their models, illustrating the cooling of a 0.605 $M_\odot$ star.

1.3.2 Classification

White dwarfs are classified according to their spectral characteristics. The system that is presently in use was proposed by Sion et al. (1983), and is based around a set of primary symbols, all beginning with the letter D for degenerate. These are shown in Table 1.1. Those stars that show weak features that normally characterise stars from another class have an additional letter, for example hydrogen dominated stars that also show weak He II lines are denoted DAO. A number between 0 and 9 can also be added to indicate the temperature; this value is given by:

$$\text{Temperature index} = \frac{50,400}{T}$$

DAOs must have a temperature above ~45,000 K in order for He II to be seen, and so have a temperature index of either 0 or 1.

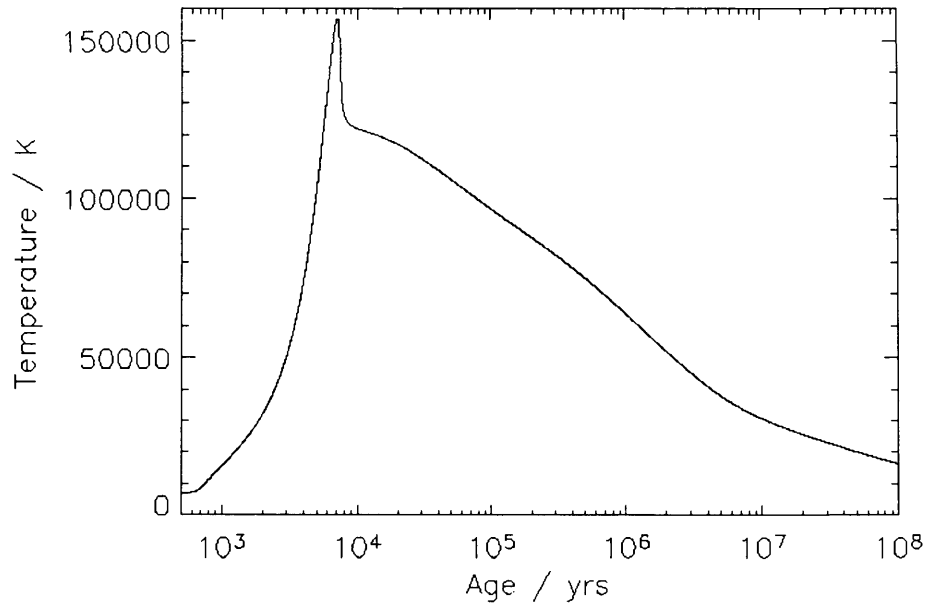

FIGURE 1.5. The cooling of a $0.605\,M_\odot$ white dwarf as it moves from the AGB, with an age of 0 corresponding to a radial pulsation period of 50 days. It takes approximately 10,000 years for the object to reach the tip of the white dwarf cooling sequence, during which time it gets hotter as it becomes more compressed.

Table 1.1. Primary symbols used to classify white dwarfs, reproduced from Sion et al. (1983).

Spectral type	Characteristics
DA	Only Balmer lines; no He I or metals present
DB	He I lines; no H or metals present
DC	Continuous spectrum, no lines deeper than 5% in any part of the electromagnetic spectrum
DO	He II strong: He I or H present
DZ	Metal lines only; no H or He
DQ	Carbon features, either atomic or molecular, in any part of the electromagnetic spectrum

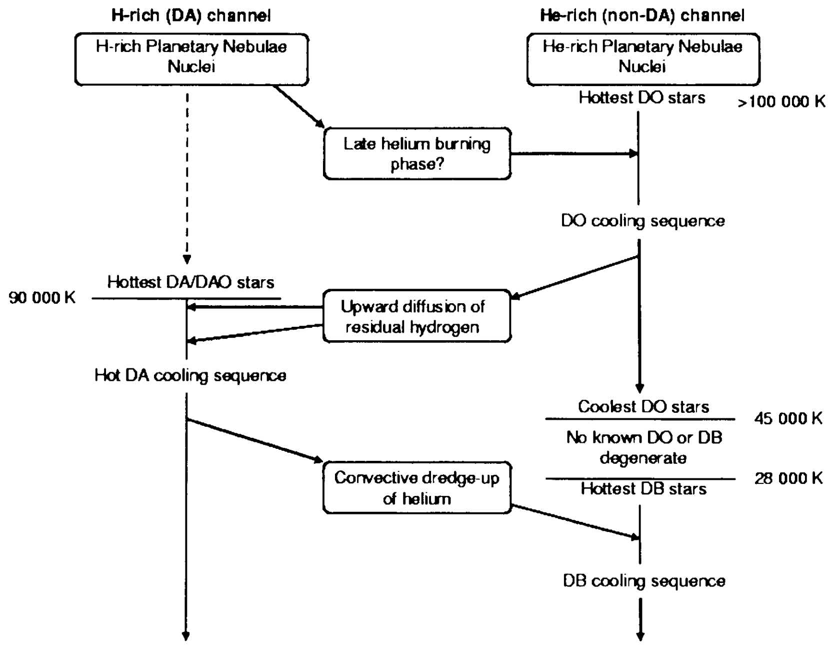

FIGURE 1.6. The H-rich and He-rich cooling channels, reproduced from Barstow (2003a).

1.3.3 Cooling

Hot white dwarfs are, in the main, separated into two distinct cooling sequences, the DAs, and the non-DAs (helium-dominated atmospheres) (Figure 1.6). The difference is thought to derive from the number of times the progenitor ascends the red giant branch, and the resultant mass loss. However, problems exist in our knowledge of white dwarf evolution. For the He-rich white dwarfs there is a continuous evolutionary sequence leading to the white dwarfs via the PG1159 stars, which have temperatures in excess of 100,000 K. In contrast, no H-rich white dwarfs are seen at a temperature greater than $\sim$80,000 K, so there is a gap in their evolutionary picture. This lead Fontaine & Wesemael (1987) to suggest that all the white dwarf progenitors lose their hydrogen-rich surface layer and evolve via the PG1159 stars in a single channel. Gravitational settling would then push the small amount of hydrogen that still existed in the atmosphere outwards, forming a thin hydrogen layer and masking the helium. However, Mendez (1991) found in his investigation of 115 central stars of planetary nebulae (CSPN) that only a third were hydrogen-deficient, and Napiwotzki & Schönberner (1995) similarly found that in their sample of 38 CSPN that the hydrogen-rich objects outnumber the hydrogen-deficient by 4 to 1, so contradicting the single channel theory, which predicts no H-rich CSPN. Looking further down the cooling sequence, the white dwarfs in the sample of

Fleming & Liebert (1986) showed a ratio of 7.1($\pm$2.9):1 between hydrogen-rich and -deficient objects with temperatures between 40,000 and 80,000 K. This falls as temperature drops, and by the time the effective temperature of the white dwarf reaches below 8,000 K the ratio is only 4.3($\pm$0.7):1. The picture is further complicated by the existence of a gap in the helium-rich sequence between $\sim$45,000 and 30,000 K. Objects above the temperature gap are known as the DOs and those below as the DBs, but no white dwarfs with helium-dominated atmospheres are seen between the two temperature limits. DAO white dwarfs, which contain both hydrogen and helium lines in their spectra, might be intermediate objects, transferring between the cooling sequences. It is therefore important to investigate the DAOs, in order to determine their evolutionary status. Chapter 2 introduces these white dwarfs in detail.

1.3.4 Mass distribution

There are currently more than 2,000 known white dwarfs (the most recent version of the Villanova Catalog of Spectroscopically Identified White Dwarfs contains 2249, McCook & Sion, 1999). Approximately 70% of these are identified to be of spectral type DA. A systematic investigation of the mass distribution of a large sample of these DAs, using the technique of fitting model white dwarf atmospheres to the hydrogen-Balmer lines seen in optical data, was conducted by Bergeron et al. (1992). They found that the mass distribution is strongly peaked, with the mode, containing $\sim$30% of all the stars in the sample, in the range 0.50-0.55 $M_{\odot}$. The mass distribution tails off towards both high and low mass with almost 10% of the objects having a mass low enough that their existence must be ascribed to binary star evolution. Subsequent studies, such as by Finley et al. (1997) and Napiwotzki et al. (1999) have reproduced these results, with small deviations due to differences in their samples and models used. The mass distribution of the helium-rich DB stars shows a similar peak to the DAs, at 0.55$\pm$0.10 $M_{\odot}$ (Oke et al., 1984).

1.4 White dwarf models

1.4.1 Atmospheric models

A large proportion of this thesis depends on the comparison of white dwarf model atmospheres with real data. The code that is used to create these models atmospheres is called TLUSTY (Hubeny & Lanz, 1995). This highly complex code solves the radiative transfer equation for a set of frequency points, as well as the equations of hydrostatic equilibrium (which states that the pressure gradient must be able to support the star against the force of gravity), radiative equilibrium (at each level the total radiation that is absorbed across the frequency range must equal the total emitted) and statistical equilibrium for chosen atomic energy levels (Hubeny & Lanz, 1995). A key feature of TLUSTY is that it allows departures from local thermodynamic equilibrium (LTE). Thermodynamic equilibrium occurs when there is no net flow of energy and all processes occur at the same rate as the opposite process, e.g. absorption and emission of photons (Carroll & Ostlie, 1996). Since, in a star, there is a net flow of energy outwards, and the temperature varies with depth, it can never be in perfect thermodynamic equilibrium. However, within a star, if significant temperature changes occur only over distances that are long compared to the mean free path of the particles and photons, then the system can be said to be in local thermodynamic equilibrium. This means that the particles and photons only 'see' a single temperature. Assuming LTE means that the Boltzmann and Saha equations can be used to calculate the proportions of atoms in different excitation and ionisation states respectively. However the assumption of LTE breaks down where the temperature gradient is steep, or where the mean free path is large, for example in the outer regions of the atmosphere where the density is less. When departures from LTE are allowed, the problem of calculating the stellar atmosphere becomes far more complex since a statistical equilibrium equation must be solved for each level of each ion; this is one of the reasons that TLUSTY is a state-of-the-art program.

TLUSTY also allows the effects of line blanketing to be included in the model calculation. This refers to the modification of the spectrum of the star by the absorption and re-emission of photons by atoms in the star's atmosphere, which, for the white dwarfs studied in this thesis, is mostly composed of hydrogen. In addition, heavy elements absorb a substantial proportion of the extreme ultraviolet flux and redistribute it to longer wavelengths. Importantly for the modelling of stellar atmospheres, the effect of this line blanketing is to increase the opacity of the atmosphere, which means that the temperature gradient must also increase. Therefore, the lower layers of the atmosphere must warm while the outer layers cool. Millions of lines must be considered if elements such as iron are to be included in the line blanketing calculations. To cope with this, TLUSTY uses the concept of superlevels, which involves the grouping together of levels that have similar energies and which are in Boltzmann equilibrium with each other (and hence have the same non-LTE departure coefficient). Opacities of these superlevels are described by 'Opacity Distribution Functions'. This involves taking the cross sections of all the levels that make up the superlevel and resampling them monotonically, with the peak at the mean wavelength of the lines. This has the advantage that the opacity can be treated with relatively few frequency points, and avoids problems with the missing of line cores that might occur if the opacity were simply sampled using insufficient frequency points.

The calculation of model atmospheres is very computationally intensive. A number of stages are required, with a simpler model being used as the input for the calculation of a more complex model atmosphere. The initial model is an H LTE grey model - a model where the opacity is frequency independent. Then, in subsequent model runs these assumptions are relaxed and further elements added. Models used for this thesis generally involved 4 steps: H+He, H+He+C, H+He+C+N+O+Si and H+He+C+N+O+Si+Fe+Ni, all in non-LTE. These built on existing H non-LTE models that had previously been calculated. TLUSTY uses the hybrid 'complete linearisation/accelerated lambda iteration' method to speed up calculations (Hubeny & Lanz, 1995), which is used as it combines the virtues of a high convergence rate with a short iteration time. The various equations are solved using an iterative process with the program going through a number of iterations until the model has converged to the point where temperature, electron density, populations and radiation intensity in a layer do not change significantly between iterations. Once the model atmosphere has been calculated the resulting atmospheric parameters (such as the temperature at each depth point) are read in by a companion program, SYNSPEC. This also takes as its input an extensive line list and solves the radiative transfer equation in detail, including these lines, at a user specified resolution, to produce the final synthetic spectrum.

When these models are described in this thesis, they are defined by the abundance of elements included within the atmosphere, and by their $T_{\rm eff}$ and log g. The *effective temperature* ($T_{\rm eff}$) is the temperature a black body must have if it is the same size as the white dwarf, in order to also have the same bolometric luminosity (de Loore & Doom, 1992), i.e.

$$L_{bol} = 4\pi R^2 \sigma T_{\rm eff}^4$$

The second parameter is the surface gravity (log g), which can be assumed to be constant over the part of the white dwarf atmosphere where lines are formed.

1.4.2 Evolutionary models

As a white dwarf cools, its $T_{\rm eff}$ will decrease and its log g will increase. The rate of cooling will depend on a stars composition, which in turn is dependant on mass lost as it evolves through the AGB. The models of Blöcker (1995) follow the evolution of stars through the red giant branch stage and along the AGB, using appropriate mass loss laws. As the period of radial pulsations in the models decreases from 100 days, the mass loss is reduced back to the giant branch rate at P = 50 days, which corresponds to an age of zero in the models. Once this mass loss rate is greater than that predicted for radiatively driven winds according to Pauldrach et al. (1988), the following mass loss rate equation from that paper was adopted:

$$\dot{M} = 1.29 \times 10^{-15} L^{1.86} \;\; [M_\odot/yr]$$

i.e. the mass loss rate during the white dwarf stage is assumed to be proportional to luminosity to the power 1.86. As the white dwarf fades over time, the mass loss rate will therefore reduce. This law was then used for the remainder of the post-AGB evolution. The calculations of Blöcker resulted in evolutionary tracks for post-AGB carbon-oxygen core white dwarfs between 0.53 and 0.94 $M_\odot$, which had been evolved from main sequence stars of initial mass between 1 and 7 $M_\odot$. Similarly Driebe et al. (1998) calculated tracks for helium core white dwarfs. They evolved their model stars, all having initial mass of 1 $M_\odot$, from the pre-main sequence phase to the top of the RGB. To simulate mass transfer during Roche lobe overflow, mass loss rates were assumed that did not destroy the thermal equilibrium of the star. The resultant evolutionary models have masses ranging from 0.179 to 0.414 $M_\odot$.

The evolutionary models take the form of tracks in the $T_{\rm eff}$ - log g plane. Each different mass white dwarf takes a slightly different track. Hence, if the $T_{\rm eff}$ and log g of a real white dwarf is known, its mass can be determined by comparing its parameters to the those of the models. This is illustrated in Figure 1.7. Since the evolutionary models also contain details of the stars luminosity and radii, these can also be determined for real objects. In addition, a distance estimate is found by calculating the absolute magnitude of the star from its luminosity using $M - M_\odot = -2.5 \log \frac{L}{L_\odot}$ (where M is the absolute magnitude and L luminosity, subscript $\odot$ means the value for the Sun is used). Then, the distance is obtained using $m - M = -5 + 5 \log d$ (m is apparent magnitude, which must be obtained from the literature, and d is the distance).

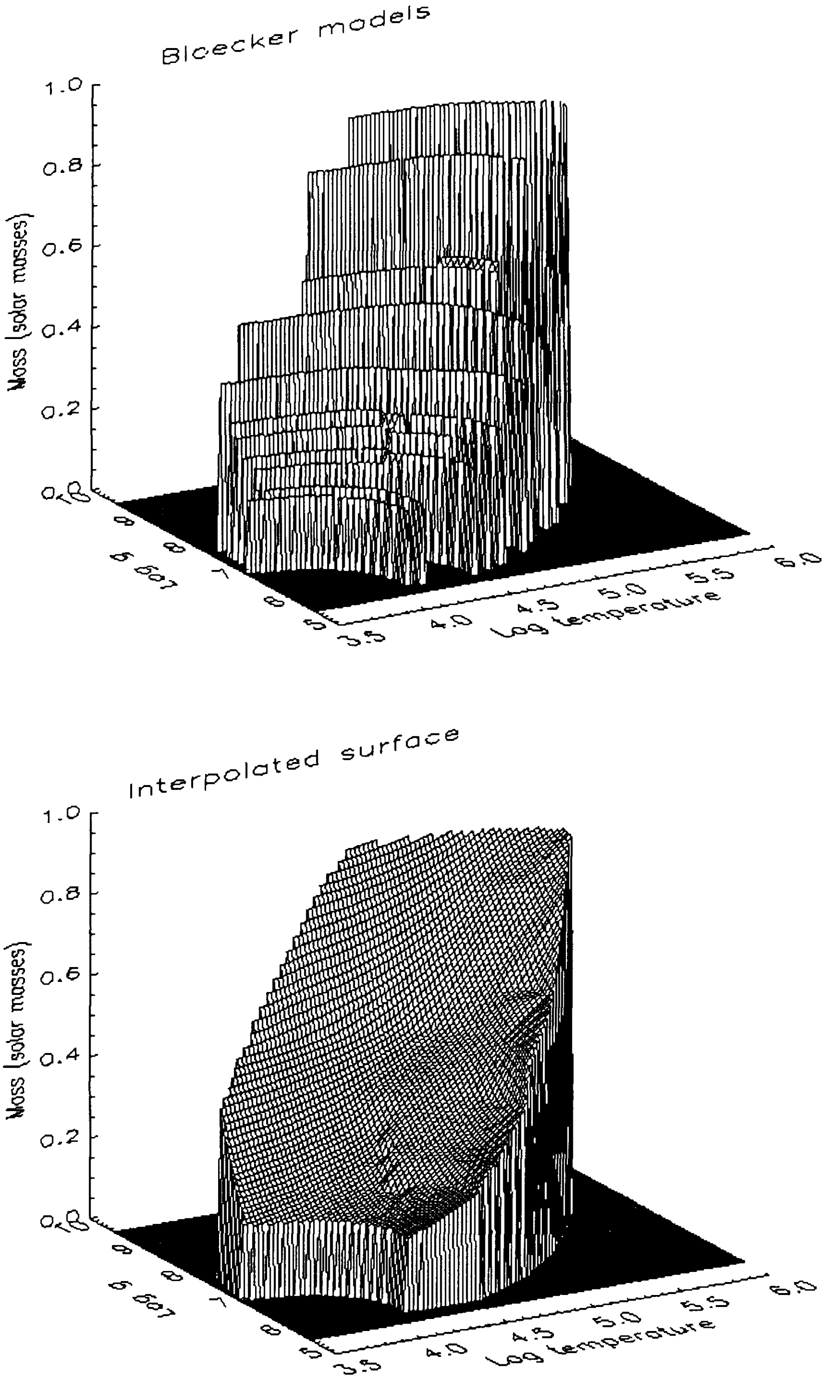

FIGURE 1.7. The evolutionary tracks of Blöcker (1995) and Driebe et al. (1998) for both CO- and He-core white dwarfs (top). Their models were calculated for a number of discrete masses of white dwarfs. By linearly interpolating between the tracks (bottom), the mass of a white dwarf can be determined from T_{eff} and $\log g$.

Chapter 2

Introduction to DAO white dwarfs

2.1 DAO white dwarfs

Those white dwarfs where weak He II lines are present in their optical spectra in addition to the hydrogen Balmer lines are known as DAOs. The prototype of these stars is HZ 34 (see Koester et al., 1979, Wesemael et al., 1993). Radiative levitation, a process which is used to explain the presence of trace heavy elements in white dwarf atmospheres, seems the most natural way in which the gravitational settling of helium can be prevented, and therefore to explain the presence of these He lines. However, radiative forces are unable to support sufficient helium, by a factor of at least 10 by number, to reproduce the observed helium abundances of DAOs (Vennes et al., 1988). The only previous spectroscopic investigation of a large sample of these objects was by Bergeron et al. (1994), who suggested a number of alternative explanations for the presence of helium in the spectra of these stars:

2.1.1 Intermediate objects

As discussed in Chapter 1, it had been suggested that all white dwarfs may evolve via a single channel. This requires that objects switch between the helium- and hydrogen-rich cooling sequences, which could happen if a small amount of hydrogen is mixed into an otherwise helium atmosphere. Gravitational settling would create a thin hydrogen layer at the surface, with the boundary with the helium layer described by diffusive equilibrium. This would give the star the appearance of a DA, but with weak helium features. However, Napiwotzki & Schönberner (1993) attempted to reproduce the line profile of the He II at 4686 Å in the DAO S 216 using both stratified and homogenous composition models and found that a better match was provided by the latter. The spectrum of only one object analysed by Bergeron et al. was better reproduced by a model with a stratified rather than homogeneous configuration. This object, PG 1305-017, is a possible example of a transitional white dwarf. The fact that it was unique in a sample of 14 was cited as evidence that the transition between the two cooling sequences must occur quickly. The helium line profile of a second object (PG 1210+533) was not reproduced well by either layered or homogeneous models, and is also strange as its helium abundance, as measured from optical spectra taken over a period of 15 years, appears to vary.

2.1.2 High temperature, low gravity objects

Most of the DAOs studied by Bergeron et al. had a high temperature, but low gravity. This led them to claim that 'hot, low surface gravity, single DA white dwarfs are necessarily DAO stars'. The lowest mass white dwarfs that can be formed through evolution via the AGB is $\sim$0.5 $M_\odot$ (Driebe et al., 1998). Therefore, the low mass of a number of the white dwarfs implies that they may not have ascended the AGB and instead evolved to a white dwarf through the EHB – the EGB-manqué stars. In order to explain the enhanced helium abundance in the line forming regions of this group of stars, Bergeron et al. invoked mass loss. There is some evidence that this explanation may be the true one; as these DAOs have low gravity their radius is comparitively large, and they are also hot. Therefore, they are relatively luminous compared to most white dwarfs, and the mass loss rate in radiatively driven winds is a strong function of luminosity (Abbott, 1982). Calculations have shown that the helium abundance in DAOs can be reproduced, in theory, by introducing mass loss to counter gravitational settling (Unglaub & Bues, 1998, 2000). In their models, they assume a mass loss rate from the white dwarf. If this wind originates from the bottom of the atmosphere, there must be a net flow of material to the surface, with the velocity of the flow dependent on the depth. By adding this velocity onto the diffusion velocity of the elements in their models, they found that the settling of helium was retarded; at a mass loss rate of 1×10^{-13} $M_\odot$ yr^{-1}, the helium sinks on a time scale similar to the cooling time scale of the white dwarf, while with a mass loss rate of 1×10^{-13} $M_\odot$ yr^{-1}, the helium abundance will reduce to that obtained with diffusion calculations in 20,000 years. The abundance of heavy elements in the line forming region of the stars should also be increased. However, Unglaub & Bues (2000) included the introduction of a 'wind limit'. Stars that have evolved past this limit, which can be approximated as a line at constant log g = $\sim$7.0 for DAOs, should not be experiencing mass loss, and hence DAO white dwarfs should eventually evolve into DAs. Therefore, because of this limit, mass loss would not be expected in DA white dwarfs, which have typical log g of 7.8. Unfortunately, the DAOs of Bergeron et al. also should not be experiencing mass loss, although the DAO CSPN of Napiwotzki (1999) are above the limit (Unglaub & Bues, 2000). However, Napiwotzki (1999) found a good correlation between luminosity and helium abundance in their sample of DAO CSPN and the DAOs of Bergeron et al. (1994). Dreizler et al. (1995) have found observational evidence for a wind in observations of one DAO (HS 2115+1148). The optical spectra of this object contains shallow absorption lines due to ultrahighly excited ionisation states of C, N, O and Ne, which have been interpreted as being due to an extremely hot, fast wind. The existence of the remnants of planetary nebulae around two other DAOs, and the fact that many of the white dwarfs that are surrounded by planetary nebulae, which are formed when the progenitor star sheds mass, are of DAO spectral type, also suggests that mass loss may be linked to the presence of helium (Bergeron et al., 1994).

2.1.3 The DAO+dM binaries

In the sample of Bergeron et al. (1994), three objects (RE 1016-053, PG 1413+015 and RE 2013+400) had 'normal' temperatures and gravities for white dwarfs, yet still had detectable helium lines in their optical spectra. Two reasons were suggested for this: firstly, as the progenitor star passes through the CE phase, mass loss will occur. This may lead to the star being hydrogen poor allowing a weak process, such as mass loss, to mix helium into the line forming region of the white dwarf. Secondly, these DAOs might be accreting from the wind of their companions. This seems the most likely explanation for a fourth DAO+dM binary, RE 0720-318, which was not included in the sample of Bergeron et al. (1994). Dobbie et al. (1999) used EUV photometry and phase resolved spectroscopy to identify likely non-uniformities in the surface abundance of helium, which is consistent with models of accretion.

2.2 The Balmer line problem

The 'Balmer line problem' is the phenomenon where the higher order Balmer lines (e.g. δ and ϵ) require a higher temperature model to fit their profiles than the lower order (e.g. β and γ) lines (Napiwotzki, 1992). By comparison of objects with similar parameters but where different strengths of the effect were seen, Bergeron et al. (1994) were able to exclude T_{eff} and log g effects as the cause of the problem. It is also not confined to the DAOs; Bergeron et al. (1994) found a hot DA (PG 0948+534) that exhibited the problem. A possible explanation of this problem was identified by Werner (1996). He created a number of models to try to reproduce the spectrum of an sdO star, for which the temperature was known through other means, and compared the temperature structure of each. In the nLTE models that did not contain C, N and O, the outer layers of the atmosphere exhibit a high temperature plateau, which is attributed to heating by H and He II lines. The introduction of C, N and O, with their line opacities represented by Doppler profiles, makes the surface of the atmosphere cooler by $\sim$50%. However, there is a strong increase in the temperature before the line forming region of the H and He lines is reached and so the Balmer line profiles are not strongly affected by including these elements in this way. In contrast, when the C, N and O line opacities are represented by Stark broadening profiles, this strong temperature increase is not seen and there is a smoother increase of temperature with depth; this effect is attributed to cooling by photon escape from the wings of the Stark profiles. This means that the cores of the hydrogen lines are formed in cooler temperatures, making them deeper. Using the models incorporating Stark broadened C, N and O, discrepencies between the strengths of the observed Balmer lines with the models in both an sdO star and a DAO white dwarf (S 216) were claimed to essentially disappear. If this is the cause of the Balmer line problem, then since the higher order Balmer lines are formed deepest in the white dwarf atmosphere, they are least affected by the difference in temperature structure due to the neglect of Stark broadened C, N and O and should yield a value closest to the 'correct' temperature (Napiwotzki, 1999).

2.3 The DAO sample

Table 2.1 contains a list of DAO white dwarfs and their coordinates, obtained through searching through the literature, and in the catalogues that are available (McCook & Sion, 1999, the white dwarf database (http://procyon.lpl.arizona.edu/WD), Abell, 1966, Kwitter et al., 1988). There are 43 stars in the list, hence DAOs make up <2% of all known white dwarfs. Interestingly, out of the 43 DAOs, only 5 have a declination less than 0°, and 3 of those have δ>-10°. It is therefore possible that there are many Southern Hemisphere white dwarfs that are DAOs but that are not yet identified as such. The objects for which data have been obtained and analysed for this thesis are indicated in bold in the table. Hence, the sample is biased towards objects observable from the Northern Hemisphere and might exclude objects with very weak He features, since they may not be correctly identified as DAOs.

Table 2.2 lists all the objects in the sample, what data have been obtained for them, and if they are associated with a planetary nebula or are known to be binaries. The

Table 2.1. List of DAO white dwarfs. Those in bold are analysed in this thesis. Unless otherwise stated, coordinates are taken from the White Dwarf Database (http://procyon.lpl.arizona.edu/WD/).

WD number	Alternative names	R.A. J2000	Dec J2000	
WD 0127+581	SH 2-188	$01^h30^m39^s$	$+58°21'57''$	
WD 0134+181	PG 0134+181	$01^h37^m22^s$	$+18°22'39''$	
WD 0231+050	PG 0231+051	$02^h33^m42^s$	$+05°18'36''$	*
WD 0322+452	HDW 3	$03^h26^m14^s$	$+45°24'22''$	
WD 0346-011	GD 50	$03^h48^m49^s$	$+00°58'22''$	
WD 0441+467**	**LS V+4621/SH 2-216/S 216**	$04^h44^m43^s$	$+46°49'30''$	
WD 0500-156	**A 7**	$05^h03^m07^s$	$-15°36'07''$	
WD 0505+012	**HS 0505+0112**	$05^h08^m31^s$	$+01°16'39''$	*
WD 0615+556	**PuWe 1**	$06^h19^m34^s$	$+55°36'43''$	
	K 2-2	$06^h52^m27^s$	$+09°58'19''$	***
WD 0718-316	**RE 0720-318**	$07^h20^m46^s$	$-31°46'54''$	
WD 0823+316	**Ton 320**	$08^h27^m04^s$	$+31°30'05''$	
WD 0834+500	**PG 0834+500**	$08^h37^m37^s$	$+49°52'29''$	
WD 0846+249	**Ton 353**	$08^h49^m05^s$	$+24°45'08''$	
	A 31	$08^h53^m46^s$	$+08°54'35''$	****
WD 0950+139	**EGB 6**	$09^h52^m58^s$	$+13°44'32''$	
WD 1013-050	**RE 1016-053**	$10^h16^m28^s$	$-05°20'29''$	
	NGC 3587	$11^h14^m48^s$	$+55°01'14''$	*
WD 1136+667	**HS 1136+6646**	$11^h39^m06^s$	$+66°30'18''$	*

* Coordinates obtained from Simbad (http://simbad.u-strasbg.fr/sim-fid.pl).
** This object is also somtimes listed as WD 0439+466.
*** Kwitter et al. (1988). **** Abell (1966). ***** McCook & Sion (1999).

following briefly summarises information that has previously been published about the objects. Temperatures, gravities and helium abundances for a number of the objects can be found in Bergeron et al. (1994) and Napiwotzki (1999), and these are listed in Table 2.3.

A7, PuWe 1 and A31

Ciardullo et al. (1999) used an HST snapshot survey to find resolved binary companions to CSPN. They looked at 113 such objects to find stars in close proximity that could be physically associated. The survey looked for objects with small separations in uncrowded fields of view but was limited by a lack of proper motion information. Only 10 likely binaries were found along with 6 possible associations. A31 was identified as having a probable companion, at a distance of less than 115 AU. A7 was one of the possible

Table 2.1. Continued...

WD number	Alternative names	R.A. J2000	Dec J2000	
WD 1202+608	**Feige 55**	$12^h04^m38^s$	$+60°32'05''$	
WD 1210+533	**PG 1210+533**	$12^h13^m23^s$	$+53°03'55''$	
WD 1214+267	**LB 2**	$12^h16^m34^s$	$+26°29'37''$	
	A 35	$12^h53^m32^s$	$-22°52'23''$	*
WD 1253+378	**HZ 34**	$12^h56^m14^s$	$+37°32'28''$	
WD 1305-017	**PG 1305-017**	$13^h08^m16^s$	$-01°59'05''$	
WD 1413+015	**PG 1413+015**	$14^h15^m35^s$	$+01°17'17''$	
	NN SER	$15^h52^m56^s$	$+12°54'47''$	
	A 39	$16^h27^m06^s$	$+27°54'21''$	****
WD 1751+106	A 43	$17^h53^m32^s$	$+10°37'26''$	
WD 1822+008	SH 2-68	$18^h24^m58^s$	$+00°51'37''$	
	IC 1295	$18^h54^m37^s$	$-08°49'49''$	*
WD 1851+329	**NGC 6720/HD 175353**	$18^h53^m37^s$	$+33°01'54''$	
	A 61	$19^h18^m35^s$	$+46°14'34''$	****
WD 1957+225	**NGC 6853/M 27**	$19^h59^m39^s$	$+22°43'15''$	
WD 2011+398		$20^h13^m09^s$	$+40°02'17''$	*****
WD 2013+400	**RE 2013+400**	$20^h13^m09^s$	$+40°02'17''$	
WD 2033+034	HS 2033+0327	$20^h35^m45^s$	$+03°37'44''$	
WD 2114+239	A 74	$21^h16^m53^s$	$+24°12'17''$	
WD 2115+118		$21^h18^m18^s$	$+12°01'33''$	
WD 2212+656		$22^h13^m26^s$	$+65°54'54''$	
WD 2218+706	**DeHt 5**	$22^h19^m33^s$	$+70°56'00''$	
WD 2226+210	**NGC 7293**	$22^h29^m18^s$	$+21°20'52''$	
WD 2342+806	**GD 561/SH 2-174**	$23^h45^m01^s$	$+80°56'51''$	

* Coordinates obtained from Simbad (http://simbad.u-strasbg.fr/sim-fid.pl).
** This object is also somtimes listed as WD 0439+466.
*** Kwitter et al. (1988). **** Abell (1966). ***** McCook & Sion (1999).

binaries, while PuWe 1 was listed as having a doubtful association. The separations of those two objects from their suggested companions was <11520 AU in the case of A7, and 1620 AU for PuWe 1.

HS 0505+0112

This object is strange in that it contains C IV absorption lines in its optical spectrum (Heber et al., 1996) and so is a DAOZ. It is unique in being the only DAO in this sample to show metal lines.

Table 2.2. Objects in the sample showing for which wavelength regions the data have been obtained. Also shown is whether the object is associated with a planetary nebula or if it is known to be part of a binary system.

		Source			
Object	WD number	Optical	FUSE	PN?	Binary?
PG 0134+181	WD 0134+181	√			
S 216	WD 0441+467	√	√	√	
A 7	WD 0500-156	√	√	√	√?
HS 0505+0112	WD 0505+012	√	√		
PuWe 1	WD 0615+556	√	√	√	√?
RE 0720-318	WD 0718-316	√	√		√
Ton 320	WD 0823+317	√	√		
PG 0834+500	WD 0834+501	√	√		√
TON 353	WD 0846+249	√			
A 31		√	√	√	
EGB 6	WD 0950+139		√		
RE 1016-053	WD 1013-050	√			√
NGC 3587			√		
HS 1136+6646	WD 1136+667	√	√		√
Feige 55	WD 1202+608	√	√		√
PG 1210+533	WD 1210+533	√	√		
LB 2	WD 1214+267	√	√		
HZ 34	WD 1253+378	√	√		
PG 1305-017	WD 1305-017	√			
PG 1413+015	WD 1413+015	√			√
A 39		√	√	√	
NGC 6720			√		
NGC 6853	WD 1957+225		√		
RE 2013+400	WD 2013+400	√	√		√
DeHt 5	WD 2218+706	√	√	√	
NGC7 293	WD 2226-210		√		
GD 561	WD 2342+806	√	√	√	

PG 0834+500 and GD561

Both these objects were included in the sample of Saffer et al. (1998) that searched for radial velocity variations. PG 0834+500 was identified as having a companion, while no velocity shifts were found in observations of GD 561.

Table 2.3. Table listing previously determined parameters of stars in the sample, from Bergeron et al. (1994) (B) (using homogeneous and stratified models) and Napiwotzki (1999) (N) (fitting only the higher order Balmer lines).

Object	Source	$T_{\rm eff}$ / K	Log g	Log $\frac{\rm He}{\rm H}$(homogeneous) or Log $\frac{M_H}{M_\odot}$ (stratified)
PG 0134+181	B (homogeneous)	56400 ±1500	7.40 ±0.11	-2.98 ±0.30
	B (stratified)	56300 ±1300	7.40 ±0.11	-14.59 ±0.20
S 216	B (homogeneous)	83800 ±1700	7.17 ±0.13	-1.71 ±0.18
	B (stratified)	72100 ±2300	6.97 ±0.15	-14.24 ±0.24
	B (homogeneous)	77300 ±3400	7.31 ±0.14	-2.06 ±0.24
	B (stratified)	70500 ±2100	7.19 ±0.15	-14.46 ±0.24
	N	83200 ±3300	6.74 ±0.19	-1.95 ±0.06
A 7	N	99000 ±18000	7.03 ±0.43	-1.49 ±0.37
PuWe 1	N	93900 ±6200	7.09 ±0.24	-1.70 ±0.20
Ton 320	B (homogeneous)	68800 ±1800	7.68 ±0.12	-2.74 ±0.27
	B (stratified)	72300 ±1800	7.68 ±0.12	-14.98 ±0.21
PG 0834+500	B (homogeneous)	60400 ±1900	7.11 ±0.12	-2.18 ±0.23
	B (stratified)	56500 ±1500	6.98 ±0.12	-14.23 ±0.19
TON 353	B (homogeneous)	66100 ±2400	7.11 ±0.19	-2.88 ±0.52
	B (stratified)	67200 ±2900	7.09 ±0.19	-14.20 ±0.33
A 31	N	84700 ±4700	6.63 ±0.30	-1.53 ±0.13
RE 1016-053	B (homogeneous)	56400 ±1200	7.74 ±0.07	-3.26 ±0.22
	B (stratified)	57500 ±1300	7.73 ±0.07	-15.01 ±0.15
NGC 3587	N	93900 ±5600	6.94 ±0.31	-1.07 ±0.13
Feige 55	B (homogeneous)	58300 ±1500	7.15 ±0.11	-2.92 ±0.31
	B (stratified)	58000 ±1500	7.17 ±0.12	-14.23 ±0.21
	B (homogeneous)	55100 ±1300	6.96 ±0.10	-2.91 ±0.28
	B (stratified)	55000 ±1200	6.97 ±0.10	-13.93 ±0.19

RE 0720-318, RE 1016-053, PG 1413+015 and RE 2013+400

These objects are all pre-cataclysmic variables. As described in §2.1.3, RE 0720-318 is likely to be accreting material from the wind of its companion (Dobbie et al., 1999). RE 1016-053 was observed by Tweedy et al. (1993) and a reflection effect was seen due to reprocessing of the white dwarf flux on the surface of a companion. The continuum of the secondary was undetected, however. PG 1413+015 is an eclipsing binary system. Fulbright et al. (1993) found the companion to be of spectral type M3 V-M5 V, and a reflection effect is also observed. RE 2013+400 was found by Barstow et al. (1995) to have a period of 0.71 days. A reflection effect was also seen in this object.

Table 2.3. Continued...

Object	Source	$T_{\rm eff}$ / K	Log g	Log $\frac{\rm He}{\rm H}$(homogeneous) or Log $\frac{M_H}{M_\odot}$ (stratified)
PG 1210+533	B (homogeneous)	44800 ±400	7.89 ±0.04	-2.08 ±0.05
	B (stratified)	46600 ±400	7.91 ±0.04	-15.68 ±0.06
LB 2	B (homogeneous)	65700 ±1400	7.67 ±0.11	-2.51 ±0.23
	B (stratified)	65100 ±1500	7.65 ±0.11	-15.12 ±0.18
HZ 34	B (homogeneous)	79900 ±3600	6.61 ±0.20	-1.33 ±0.24
	B (stratified)	60700 ±2400	6.28 ±0.17	-13.39 ±0.27
	N	90800 ±3900	6.60 ±0.20	-1.59 ±0.09
PG 1305-017	B (homogeneous)	45700 ±600	7.70 ±0.12	-0.72 ±0.07
	B (stratified)	44400 ±400	7.76 ±0.10	-15.98 ±0.16
PG 1413+015	B (homogeneous)	48100 ±1700	7.69 ±0.11	-2.57 ±0.40
	B (stratified)	49300 ±1100	7.70 ±0.10	-15.10 ±0.20
A 39	N	117000 ±11000	6.28 ±0.22	-0.85 ±0.10
NGC 6720	N	101200 ±4600	6.88 ±0.26	-1.14 ±0.09
NGC 6853	N	108600 ±6800	6.72 ±0.23	-1.12 ±0.09
RE 2013+400	B (homogeneous)	47800 ±2400	7.69 ±0.16	-2.62 ±0.63
	B (stratified)	48900 ±1600	7.71 ±0.15	-15.13 ±0.29
DeHt 5	N	76500 ±5800	6.65 ±0.19	<-2.69
NGC 7293	N	103600 ±5500	7.00 ±0.22	-1.43 ±0.15
GD 561	B (homogeneous)	65300 ±2000	6.71 ±0.15	-2.40 ±0.33
	B (stratified)	63000 ±2500	6.67 ±0.16	-13.59 ±0.27

EGB 6

EGB 6 is a large planetary nebula, the central star of which (WD 0950+139) is associated with a compact region of emission (Dopita & Liebert, 1989). The central star has a known infrared excess, compared to the flux that is expected from a white dwarf, corresponding to an upper limit of M4 V on the spectral type of a companion (Liebert et al., 1989). No variations in the infrared flux were found by Fulbright et al., who conducted JHK photometry of the central region. If the system is a close binary, flux from the white dwarf that is incident on the surface of the companion will be reprocessed and re-emitted. As the stars orbit each other, the proportion of the surface of the secondary that is reprocessing flux which is visible will change, so infrared variations would be expected. Therefore, this system might either have a long period, or might have an inclination that is very close to 0°.

NGC 3587, NGC 6720, NGC 6853 and NGC 7293

These objects are all associated with planetary nebulae: NGC 3587 is also known as the Owl Nebula, NGC 6720 as the Ring Nebula, NGC 6853 as the Dumb-bell nebula and NGC 7293 as the Helical Nebula.

HS 1136+6646

HS 1136+6646 was first observed by Heber et al. (1996) and identified as a spectroscopic binary with dK companion. When HS 1136+6646 was observed in 2001 the white dwarf spectrum showed strong emission features due to a reflection effect that was not originally observed. As it is a close binary it must have been through a common envelope stage and will eventually become a cataclysmic variable. When viewed at the correct point in its orbit the surface of the companion that produces the emission features is facing away from the Earth. A spectrum taken at that point is used in the analysis in this thesis, although some contamination from the secondary is still likely.

Feige 55

Feige 55 is a double-degenerate binary, first identified as such by Holberg et al. (1995). They found that the period of the system was $\sim$1.49 days. J- and K-band photometry put an upper limit on the mass of a main sequence secondary of 0.1 $M_{\odot}$, while the mass function gave a lower limit of 0.25 $M_{\odot}$, suggesting that the companion is degenerate.

PG 1210+533

PG 1210+533 has been observed a number of times over a period of more than 15 years, and the helium abundance measured from these spectra changes over time. Bergeron et al. (1994) found that neither homogeneous or stratified H+He models could reproduce the profile of the He II λ4686 line. Saffer et al. (1998) could not find any evidence of velocity shifts that might identify PG 1210+533 as a binary, althought they could not conclusively rule it out.

PG 1305-017

This is the only object where Bergeron et al. (1994) found that the stratified models would better reproduce the data than the homogeneous models. It is therefore possible that this is an example of a transitional object on the way to becoming a DA.

DeHt5

WD 2218+706 has been included in this study although there are no helium lines visible in the optical spectrum. However Barstow et al. (2001a) found a He II line at 1640 Å using an HST STIS observation, so technically it is a DAO. They found a helium abundance of 3×10^{-5} that of hydrogen, with an upper limit of only 2.3×10^{-4} at the 3σ confidence level.

HS 2115+1148

As described in §2.1.2, Dreizler et al. (1995) have found observational evidence for a wind in observations of HS 2115+1148.

Chapter 3

Analysis of optical data for a sample of DAO white dwarfs

3.1 Introduction

3.1.1 Aims

This chapter describes the use of optical data to determine the effective temperature, gravity and helium abundance of 22 objects. The stellar mass and radius are determined from these parameters using evolutionary models. The profiles of the helium lines in the spectra of the objects are also used to draw conclusions about the atmospheric structure. The relatively large size of the sample means that a comparison with the population of the more common DAs can be made. A further motivation for this work is to obtain the fundamental parameters for these stars using state-of-the-art models, since Bergeron et al. (1994), the only other large DAO optical study, used models that assumed LTE and neglected the effects of heavy elements.

3.1.2 Fundamental parameters from optical data

The fitting of the hydrogen-Balmer line profiles in optical spectra to determine the temperature and gravity of a white dwarf is a well-established technique (see, for example, Holberg et al., 1986, Bergeron et al., 1992). In DAOs, the presence of helium lines in the spectra, the strongest being He II at 4686 Å, also provides a means of measuring the helium abundance in the line forming region of the white dwarf. In addition, the relative strengths of the helium absorption lines gives a further constraint on the temperature of the objects, with neutral helium not seen in objects hotter than ~50,000 K. However, caution has to be applied to the intepretation of optical spectra. Firstly there exists the so-called 'Balmer line problem' (see §2.2). A second problem with the use of optical spectra is the weakness of the neutral hydrogen Balmer lines in hot white dwarfs. The high temperature in the white dwarf atmosphere causes some of the hydrogen to become ionised, so decreasing the strength of the lines. Taking into account the Balmer line problem, the higher order lines should be relied upon to give the correct temperature measurement, but these are also the weakest.

3.2 Observations

Table 3.2 lists the data analysed in this chapter. For a complete list of DAOs for which optical or far-UV data have been obtained, see Table 2.2. The spectra that were obtained from the 2.3m Steward Observatory Bok telescope on Kitt Peak, Arizona were recorded in two observing runs. The data from the first of these runs (21-22 March 2001) were recorded by myself, Jay Holberg and David Sing (both from the Lunar and Planetary Laboratory at the University of Arizona, U.S.A.) and reduced by myself. The data from the second run (20-21 December 2001) were taken and reduced by Jay Holberg and David Sing. Table 3.1 lists the DAO spectra recorded during each run.

The spectra were obtained using the Boller & Chivens Spectrograph at the Ritchey-Chretien f/9 focus, which is a Cassegrain focus used for observations at visible wavelengths. Data were recorded on a 1200×800 15 μm pixel CCD, used in combination with a 1200 line mm^{-1} grating and a 1."25 slit. Observations lasted 1200 s. Exposures of a He-Ar lamp were taken between observations of white dwarfs in order to later determine the wavelength solution. The standard stars Feige 55 and G 191-B2B were observed regularly to provide the flux calibration.

The Standard Image Reduction and Analysis Facility (IRAF) software package was used to perform the data reduction. The bias frames were combined using the zerocombine procedure. Flat field spectra were combined using flatcombine and a high order polynomial used to fit the shape of the response. These were removed from the data using the ccdproc procedure. The wavelength solution was found by identifying lines in the spectra of the He-Ar observations and entering their wavelengths into the identify procedure. As the wavelength of these lines and where they lie in the spectal image were known, it was possible to determine the wavelength solution of the whole spectrum, then dispcor was used to apply the solution to the spectra. The flux calibration

Table 3.1. List of DAO spectra recorded using the 2.3m Bok telescope at Kitt Peak during the two observing runs in 2001.

	Number of spectra taken.	
Object	21-22 March	20-21 December
S 216	1	1
A 7	3	
HS 0505+0112	2	1
PuWe 1	2	
Ton 320	2	
PG 0834+500	2	
A 31	2	
HS 1136+6646*	2	1
PG 1210+533	2	
A 39	3	
GD 561		3

* As the HS 1136+6646 spectrum of 21/12/2001 was recorded at a point in its orbit when no emission lines were seen, only this observation was used for the analysis in this chapter.

was performed by comparing the uncalibrated observations of the standard stars to the flux of the standard spectra (D.K. Sing, private communication), using the setairmass, standard, sensfunc and calibrate procedures. Since the standard stars were observed in similar conditions to the observations of the target stars, atmospheric effects should be removed from the spectra in this process. To perform the wavelength and flux calibrations, the He-Ar lamp and closest standard star exposure in time to a DAO observation was used. The final spectra ranged in wavelength between 3846 and 4996 Å.

In addition, the data used by Bergeron et al. (1994), the spectra of DeHt 5 (WD 2218+706) from Barstow et al. (2001a) and spectrum of RE 0720-318 from Barstow et al. (1995) are analysed here. The 2001 Kitt Peak data have a resolution of ~2 Å (FWHM), determined from the width of emission lines in the spectrum of HS 1136+6646, while for the Bergeron et al. observations the resolution is lower: ~8Å (FWHM). There are two spectra of DeHt 5, the resolution of which are 1.5Å (FWHM) and 8Å (FWHM). For RE 0720-318, the resolution was 3-4 Å. Measurement errors were estimated from the scatter in the data.

Table 3.2. Objects for which optical data have been obtained. Also listed are literature references and if the object is associated with a planetary nebula or has a companion.

Object	WD number	Source	Ref.	PN?	Binary?
PG 0134+181	WD0134+181	1	a		
S 216	WD0441+467	1,2	a,b	√	
A 7	WD0500-156	2	b	√	√?
HS 0505+0112	WD0505+012	2			
PuWe 1	WD0615+556	2	b	√	√?
RE 0720-318	WD0718-316	3			√
Ton 320	WD0823+317	1,2	a		
PG 0834+500	WD0834+501	1,2	a		√
TON 353	WD0846+249	1	a		
A 31		2	b	√	
RE 1016-053	WD1013-050	1	a		√
HS 1136+6646	WD1136+667	2	c		√
Feige 55	WD1202+608	1	a		√
PG 1210+533	WD1210+533	1,2,4	a,d		
LB 2	WD1214+267	1	a		
HZ 34	WD1253+378	1	a		
PG 1305-017	WD1305-017	1	a		
PG 1413+015	WD1413+015	1	a		√
A 39		2	b	√	
RE 2013+400	WD2013+400	1	a		√
DeHt 5	WD2218+706	5	b,e	√	
GD 561	WD2342+806	1,2	a,b	√	

1 Observations from Bergeron et al. (1994) (Bergeron, private communication), **2** Observations made using the Steward Observatory 2.3 m telescope on Kitt Peak, Arizona in 2001, **3** See Barstow et al. (1995), **4** Observations by F. Wesemael, J. Holberg and K. Kidder (Bergeron, private communication), **5** Observations of WD2218, originally published in Napiwotzki (1999).

a Bergeron et al. (1994), **b** Napiwotzki & Schönberner (1995), Napiwotzki (1999), **c** Holberg et al. (2001), **d** Wesemael et al. (1985), Holberg (1987), Kidder (1991), **e** Barstow et al. (2001a).

Table 3.3. Heavy element abundances used in homogeneous models

Element	Abundance/H abundance
C	4.0
N	1.6
O	9.6
Si	3.0
Fe	100.0
Ni	5.0

Abundances are $\times 10^{-7}$.

3.3 Models

Grids of stellar atmosphere models were used to fit the optical data, created using the programs TLUSTY and SYNSPEC (see Hubeny & Lanz, 1995). These allow model white dwarf atmospheres to be created with different effective temperatures, gravities and helium abundances. The range of these parameters were chosen to encompass the values that would be expected in the white dwarfs. The temperature varied between 40,000 and 100,000 K in 10,000 K steps while log g ranged from 6.5 to 8.0 in steps of 0.5. As the models were created to deal with DAO white dwarfs the helium abundance was also varied, as described below.

3.3.1 Homogeneous models

The homogeneous models have a uniform composition throughout the white dwarf atmosphere. They are mostly composed of hydrogen, with only a small amount of helium needed to create the observed lines. In the models the ratio of helium to hydrogen abundance varied from log $\frac{\mathrm{He}}{\mathrm{H}}$ = -5 to -1 in steps of 1. Models with higher abundance did not converge. Hot white dwarfs are observed to contain significant quantities of heavy elements at abundance levels similar to the well studied DA G 191-B2B (Barstow et al., 2003b). Heavy elements in the quantities measured by Barstow et al. (2000) for G 191-B2B were therefore included in the models. Table 3.3 lists the abundances used. The Stark broadening of the hydrogen-Balmer lines is dealt with using the tables of Lemke (1997), but Stark broadening profiles for heavy elements are not included.

3.3.2 Stratified models

The layered model atmospheres are mostly composed of helium, with a thin layer of hydrogen at the surface. The boundary between the hydrogen and helium is described by the balance between the concentration gradient and gravitational settling, as detailed in Jordan & Koester (1986) and Vennes et al. (1988). A program (Barstow, private communication) was used to calculate the helium abundance at discrete levels in the white dwarf atmosphere for a particular gravity and temperature. The method used to obtain this abundance distribution is described in detail in Barstow & Hubeny (1998) and references therein, but involves the use of a combined equation of mass conservation and hydrostatic equilibrium from Vennes et al. (1988), which describes the mass fraction of hydrogen as a function of the number ratio of H and He at different depths. The program uses an iterative process to find the number fraction of He at each depth point, that gives the required overall mass fraction of helium, and this was used as part of the input to TLUSTY. To simplify the calculations, no heavy elements were included. This will bias the measurements of $T_{\rm eff}$ and log g, since line blanketing by heavy elements influences the shape of the Balmer line profiles (Barstow et al., 1998). However, Bergeron et al. (1993) found that this does not strongly affect the He II line at 4686 Å. The ranges for the temperature and gravity are identical to those used in the homogeneous models. In this grid, the parameter that describes the hydrogen/helium composition is log $\frac{M_H}{M_\odot}$, and this varied between -17 and -13 in steps of 1.

3.4 Determination of temperature, gravity and helium abundance

Analysis was performed using the spectral fitting package XSPEC (Shafer et al., 1991). This uses a χ^2 minimisation technique to determine the model parameters that give the best agreement with the data. The Balmer lines from H_β through to H_ϵ were simultaneously fit. An independant normalisation coefficient was applied to each line to ensure that the results did not depend on the local slope of the continuum and to reduce the effect of systematic errors in the flux calibration of the spectra. In addition, where the flux calibration was particularly poor, a slope correction was applied to the data – see §3.5.1. 68% (1σ) confidence intervals for each parameter were derived from the $\Delta\chi^2$ distribution with three free parameters as described by Lampton et al. (1976).

3.5 Results

3.5.1 Potential sources of errors in the results

A possible source of error in the results is the Balmer line problem, where the core of the model H_β line is not deep enough when compared to the data, and so the line would be better fitted with a lower temperature model. A check was carried out in order to determine if different temperatures are in fact needed to fit each individual Balmer line. The spectrum of PG 0134+181 and an observation of S 216 were analysed with the temperature of each line allowed to vary independently. Log g was also allowed to be varied by XSPEC, but had the same value for each line. The helium abundances were fixed to within the 1σ error boundary obtained from the original fit as only the Balmer lines were fitted in this case. The results of these fits are listed in Table 3.4 with the spectra plotted in Figure 3.1. As previously found by Napiwotzki (1999) the best fit model to the higher order lines had a higher temperature than that found for the lower order lines. Also, the log g for the fit with independent temperatures is lower than that obtained where all the temperatures are the same. Looking at PG 0134+181, the $T_{\rm eff}$ for the same temperature fit is roughly the mean of the individual temperatures, as might be expected. However, as noted by Barstow et al. (2001a) when analysing spectra of the central star of DeHt 5, neither the temperatures or the gravities actually disagree with each other statistically - all are within or close to the 1σ error boundaries of each other. In contrast, S 216, which on visual inspection appears the object worst affected by the Balmer line problem, is best fitted by very different temperatures, to the extent that the temperature for H_ϵ has exceeded the upper limit of the model grid. The χ^2_{red} for the separate temperature fit is half that of the single temperature fit, however, so there is a possibility that the fit is becoming affected by noise. Napiwotzki (1999) obtained a temperature for this object of 83200 $\pm$3300 K using only the higher order lines. A similar fit where the H_δ and H_ϵ temperatures are kept the same, and using the log g obtained from fitting all the lines with separate temperatures yields 93960 $^{+3206}_{-2976}$ K. Since the temperatures obtained for the H_δ and H_ϵ lines do not seem to agree closely, the use of the higher order lines to determine the $T_{\rm eff}$ of the object, as suggested by Napiwotzki (1999) doesn't seem valid in this case; the temperature obtained from fitting the higher order lines together appears to be dominated by H_δ, and the error boundaries are small compared to the uncertainty in the measurements from individual lines. The approach adopted by Bergeron et al. (1994) in order to avoid the problem was to ignore the central 10 Å of each Balmer line, as the core is formed in the upper atmosphere where line blanketing effects by heavy elements are important. However, tests of a number of the spectra using this modification to the

Table 3.4. Results of fits when temperature is kept the same for all the Balmer lines (upper log g and $T_{\rm eff}$ in the table) and when each line is allowed to adopt the $T_{\rm eff}$ that gives the minimum χ^2.

	PG0134+181	S216
Log g	7.20 $^{+0.11}_{-0.11}$	7.19 $^{+0.07}_{-0.05}$
$T_{\rm eff}$ / K	54682 $^{+1179}_{-1690}$	67106 $^{+1281}_{-1475}$
DOF	332	563
χ^2_{red}	1.111	1.209
Log g	6.91 $^{+0.19}_{-0.18}$	6.89 $^{+0.07}_{-0.07}$
H_β $T_{\rm eff}$ / K	48877 $^{+3055}_{-1251}$	55035 $^{+2068}_{-2033}$
H_γ $T_{\rm eff}$ / K	52766 $^{+3576}_{-3084}$	65831 $^{+3262}_{-2997}$
H_δ $T_{\rm eff}$ / K	67647 $^{+9456}_{-7151}$	91879 $^{+8121}_{-8915}$
H_ϵ $T_{\rm eff}$ / K	64120 $^{+10610}_{-7784}$	100000 $^{+0}_{-8514}$
DOF	329	560
χ^2_{red}	1.027	0.633

fitting procedure produced no significant differences in the best fitting temperature but, unexpectedly, the measured log g increased, the opposite to what is seen when the Napiwotzki method is used! This is presumably because the fit is no longer constrained by the narrow core. The use of improved models at a later date, for example incorporating C, N and O Stark broadening, may resolve the issue.

Some of the spectra used in this analysis are of poor quality due to bad observing conditions. Normally the flux calibration is obtained from looking at a standard star with a known spectrum immediately after the target, but this assumes that conditions did not vary between the observations. If this is not the case, the problem is dealt with in the analysis stage by applying a slope correction to each feature. This should be equivalent to using a standard star in good observing conditions, but causes the spectra to appear discontinuous. To check this, the results from a couple of affected objects are looked at here. One of the worst affected spectra is an observation of A 7, which was observed three times in total. The three spectra are shown in Figure 3.2 and the results from the fits to the spectra have already been listed in Table 3.5. The best fitting temperature for the bad spectrum is higher than the other two, which agree very closely. However, there is no statistical difference in the three temperatures and all agree within the 1σ errors. The same is true for log g and log $\frac{\rm He}{\rm H}$. As a further check, these results were compared to those already published. Temperatures and gravity have been found for this object a number of times. Napiwotzki & Schönberner (1995) found a temperature of 99,000 $\pm$18,000 K and log g 7.03 $\pm$0.43. However they derived their temperatures

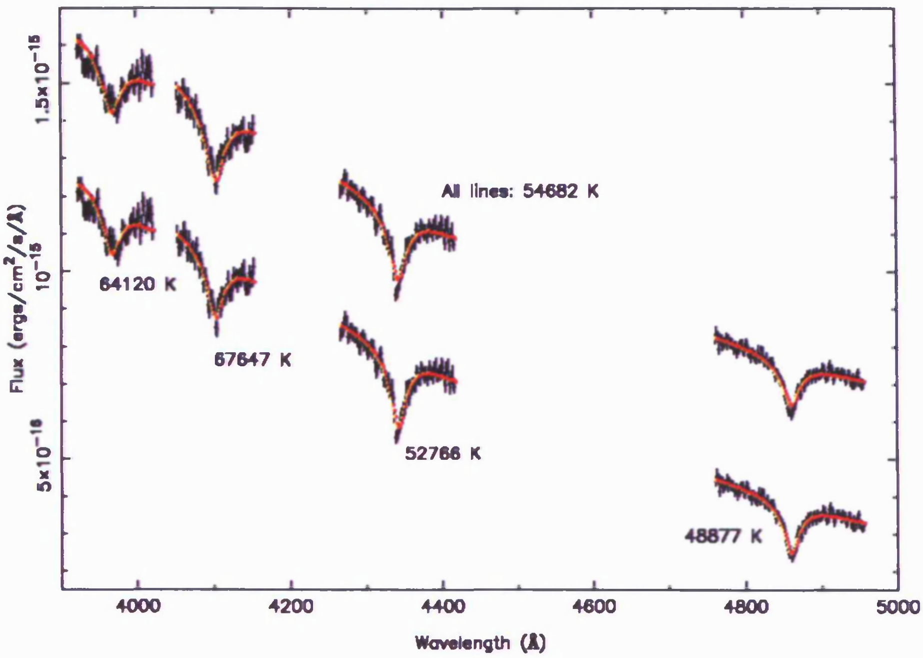

PG0134+181

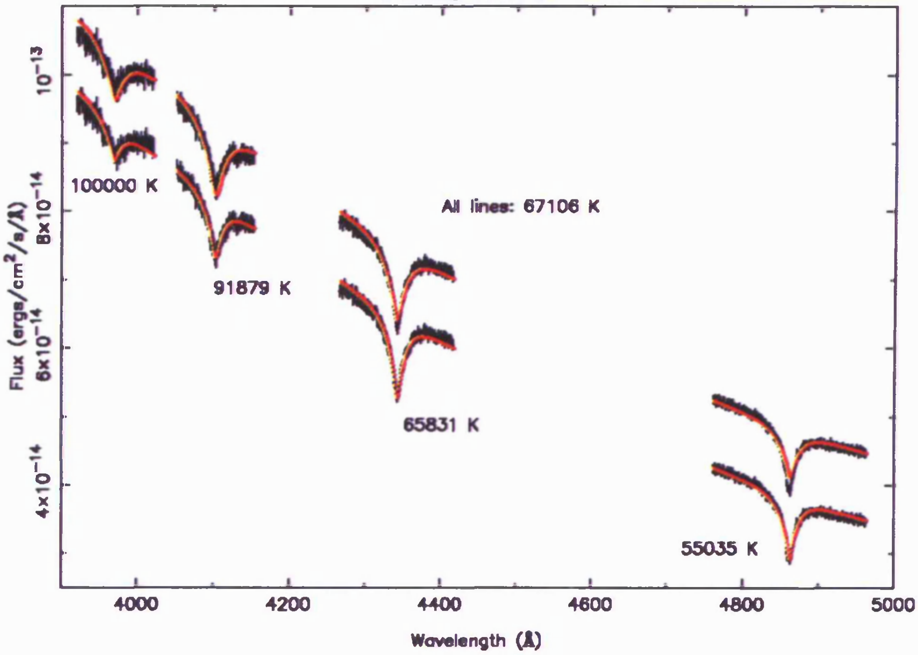

S216

FIGURE 3.1. Plots of the best fitting homogeneous model atmospheres to the Balmer lines of PG0134+181 and S216. In each case the upper data (black error bars) are overplotted in red with a model where the temperature indicated in the plot is used for each line. The lower data, which have been offset downwards, are overplotted with a model where each line has an independant temperature; the temperature used for each is shown next to the line.

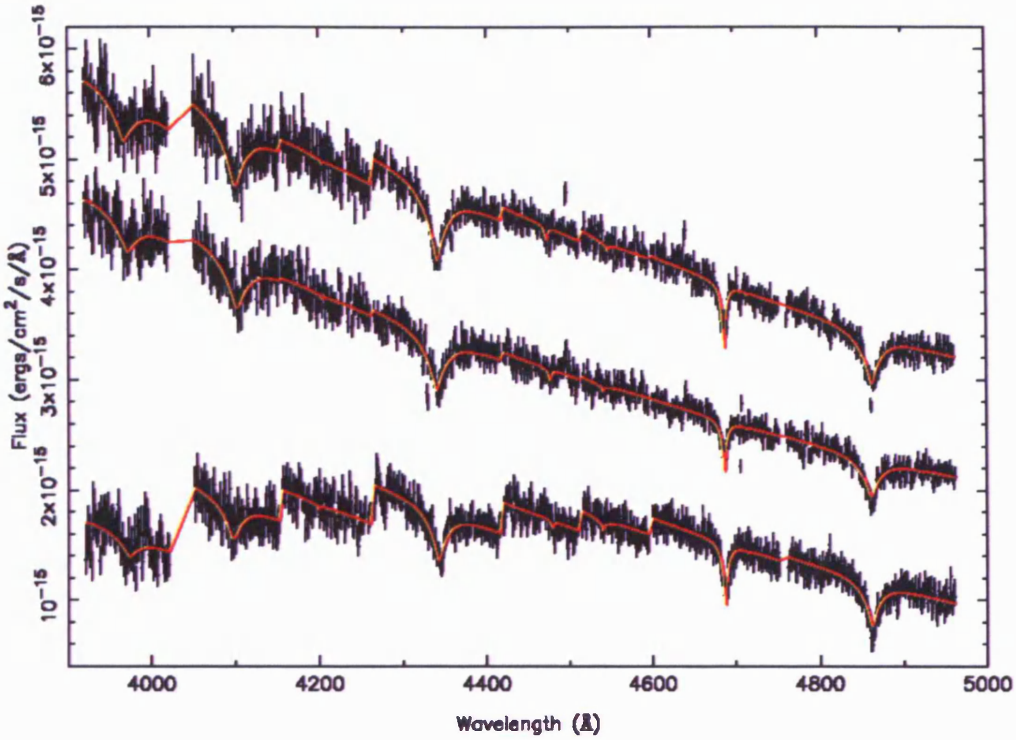

FIGURE 3.2. The three observations of A7. Best fitting effective temperatures were, from top to bottom: 64079 $^{+2834}_{-2276}$ K, 65063 $^{+2986}_{-3072}$ K and 71724 $^{+6637}_{-4069}$ K. The upper and lower spectra have been offset slightly to avoid overlapping. The best fitting homogeneous model atmospheres are overlaid in red. Discontinuities are due to the slope correction that has been applied to correct for the poor flux calibration.

from the fits of only H_δ and H_ϵ in order to avoid the Balmer line problem. Mendez et al. (1985) and Wesemael et al. (1985) found temperatures of 75,000 $\pm$10,000 K and 60,000 $\pm$10,000 K, and a log g of 7.0 $\pm$0.5 and 7.0 respectively, both of which agree with the results of this chapter. Another affected object is GD 561, which was observed at Kitt Peak in 2001 and also by Bergeron et al. (1994). The Kitt Peak observations required some slope correction, although not to the same extent as those for the observations of A 7. The results for all the spectra of GD 561 agree closely. It will therefore be assumed that the best fitting parameters obtained from the poorer quality spectra are reliable.

3.5.2 Homogeneous and stratified models

Table 3.5 lists the best fitting parameters and their 68% confidence intervals for all the observations of each star and for the homogeneous and stratified models. Please note that since the stratified models did not include heavy elements, the $T_{\rm eff}$ and log g measurements may be biased. One observation of PG 1210+533 is not included as the data contained only one of the Balmer lines – more than one line profile is required to obtain a unique determination of temperature and gravity. The number of degrees-of-freedom (DOF) and the minimum χ^2_{red} (= χ^2/DOF) that was achieved are also listed. χ^2_{red} would be expected to be 1 if the model reproduces the data well, but since the variance of the data influences the value of χ^2 of each data bin and the variance, obtained from the scatter in the data, was only an estimate, this was not always achieved, for example in the fit to the second spectrum of S 216. For this reason, the absolute value of χ^2_{red} is not used to judge the ability of a certain model to reproduce the data. An example spectrum of each object is shown in Figure 3.3 along with the the best fitting homogeneous and stratified models. Where available, the spectra shown are those taken in 2001 using the 2.3m telescope on Kitt Peak. Visual inspection of the expanded regions suggests that the stratified models do not reproduce the detail of the spectra as well as homogeneous models. A more objective approach to compare the two is with the F test:

The F distribution is the ratio of two independent χ^2 divided by their respective degrees of freedom and there is a different F distribution for each pair of degrees of freedom. The F distribution is used to test if the variances of two populations are equal and is commonly used in astrophysics to test if one model reproduces real data better than another with a high significance, since small differences in the χ^2 may result from random scatter in measurements. This is commonly done by using a look up table that lists the value of F that is required if a chosen significance is sought. However, the IDL programming language provides a function (F_PDF) that allows the ratio of the two χ^2 to be entered along with the number of degrees of freedom of each, and returns a significance value. The represents the confidence with which it can be said that one model better reproduces the data than the other and the final column of Table 3.5 lists these 'confidence' values. A confidence value of 50 % indicates that the models reproduce the data equally well (i.e. this is the value that is obtained if the χ^2 are equal), while if the value is high, one model has done a much better job of reproducing the data than the other. It can be seen from the table that the homogeneous model atmospheres give a slightly superior χ^2_{red} compared to the stratified atmospheres in most cases. For only a few obects (HS 0505+0112, HS 1136+6646, Feige 55, PG 1210+533 and RE 2013+400) the homogeneous model is better at greater than the 90% level. PG 1305+015 is the only one that seems sure to be stratified. However, the value of using the overall χ^2_{red} to distinguish between models is limited since it is the He II line at 4686Å, and the region around it, that is most sensitive to the differences between the stratified and homogeneous models, but this will only make a small contribution to the total χ^2. Therefore, the F test was also per-

Table 3.5. Best fitting parameters to the data using homogeneous and stratified models. The final column is the confidence with which the model that gave the lowest χ^2_{red} can be said to better reproduce the data. The confidence value is given in bold where the stratified model gave the lower χ^2_{red}.

	HOMOGENEOUS MODELS				STRATIFIED MODELS					
Object	$T_{\rm eff}$ / K	Log g	Log $\frac{He}{H}$	χ^2_{red}	$T_{\rm eff}$ / K	Log g	Log $\frac{M_H}{M_\odot}$	χ^2_{red}	DOF	Conf / %
PG0134+181	54682^{+1179}_{-1690}	$7.20^{+0.11}_{-0.11}$	$-2.80^{+0.25}_{-0.25}$	1.110	53097^{+1201}_{-1123}	$7.22^{+0.13}_{-0.09}$	$-14.17^{+0.13}_{-0.19}$	1.140	594	62.7
S216	69014^{+1613}_{-1203}	$6.90^{+0.08}_{-0.10}$	$-2.11^{+0.20}_{-0.17}$	1.106	59147^{+1181}_{-835}	$7.13^{+0.07}_{-0.04}$	$-14.56^{+0.11}_{-0.16}$	1.145	479	64.8
	73641^{+1263}_{-919}	$6.95^{+0.03}_{-0.07}$	$-1.87^{+0.69}_{-0.05}$	4.118	65797^{+391}_{-746}	$6.90^{+0.03}_{-0.02}$	$-14.28^{+0.05}_{-0.04}$	4.093	479	**52.7**
	67106^{+1281}_{-1475}	$7.19^{+0.07}_{-0.05}$	$-2.31^{+0.10}_{-0.10}$	0.837	61554^{+946}_{-880}	$7.21^{+0.03}_{-0.07}$	$-14.66^{+0.11}_{-0.07}$	0.955	989	98.1
	67254^{+1423}_{-774}	$7.27^{+0.04}_{-0.08}$	$-2.46^{+0.12}_{-0.19}$	1.101	61562^{+1421}_{-551}	$7.22^{+0.08}_{-0.06}$	$-14.63^{+0.10}_{-0.18}$	1.124	945	62.5
A7	71724^{+6637}_{-4069}	$7.16^{+0.20}_{-0.23}$	$-1.00^{+0.00}_{-0.18}$	0.867	61914^{+2844}_{-2890}	$6.85^{+0.30}_{-0.23}$	$-14.76^{+0.32}_{-0.22}$	0.831	988	**74.7**
	65063^{+2986}_{-3072}	$7.29^{+0.16}_{-0.14}$	$-1.37^{+0.24}_{-0.24}$	1.163	59230^{+2339}_{-1705}	$7.28^{+0.08}_{-0.11}$	$-15.14^{+0.16}_{-0.18}$	1.174	994	55.9
	64079^{+2834}_{-2276}	$7.24^{+0.13}_{-0.13}$	$-1.51^{+0.18}_{-0.09}$	1.171	59317^{+1465}_{-1197}	$7.24^{+0.07}_{-0.04}$	$-15.01^{+0.11}_{-0.05}$	1.191	979	60.4
HS0505+0112	60081^{+1746}_{-608}	$7.17^{+0.10}_{-0.12}$	$-1.00^{+0.00}_{-0.05}$	1.385	54500^{+1463}_{-945}	$7.09^{+0.02}_{-0.06}$	$-15.03^{+0.05}_{-0.06}$	1.569	962	97.3
	61513^{+3507}_{-2088}	$7.10^{+0.17}_{-0.19}$	$-1.00^{+0.00}_{-0.08}$	0.940	55235^{+1881}_{-1788}	$7.07^{+0.06}_{-0.08}$	$-15.06^{+0.10}_{-0.06}$	1.027	962	91.5
	68087^{+1489}_{-3158}	$7.63^{+0.16}_{-0.15}$	$-1.00^{+0.00}_{-0.02}$	1.246	59852^{+1119}_{-2076}	$7.60^{+0.10}_{-0.04}$	$-16.00^{+0.03}_{-0.03}$	1.355	930	89.9
PuWe 1	79252^{+9620}_{-3005}	$6.89^{+0.20}_{-0.15}$	$-2.26^{+0.56}_{-0.31}$	1.040	67191^{+4810}_{-3732}	$6.95^{+0.19}_{-0.19}$	$-14.44^{+0.15}_{-0.52}$	1.036	992	**52.4**
	69184^{+5356}_{-3311}	$7.14^{+0.23}_{-0.21}$	$-2.51^{+0.29}_{-0.33}$	1.094	65082^{+3706}_{-4295}	$7.01^{+0.30}_{-0.20}$	$-14.33^{+0.22}_{-0.53}$	1.096	982	51.1
RE 0720-318	54011^{+1646}_{-1547}	$7.68^{+0.13}_{-0.13}$	$-2.61^{+0.19}_{-0.19}$	1.831	55558^{+1881}_{-1199}	$7.65^{+0.08}_{-0.11}$	$-14.99^{+0.19}_{-0.04}$	1.946	650	78.1
Ton 320	64784^{+3117}_{-2510}	$7.33^{+0.16}_{-0.12}$	$-2.63^{+0.27}_{-0.27}$	0.840	60709^{+2465}_{-1589}	$7.33^{+0.08}_{-0.12}$	$-14.62^{+0.22}_{-0.20}$	0.862	235	57.8
	59760^{+3056}_{-2545}	$7.22^{+0.15}_{-0.14}$	$-2.40^{+0.19}_{-0.20}$	1.071	56731^{+2093}_{-1752}	$7.44^{+0.06}_{-0.15}$	$-15.11^{+0.40}_{-0.12}$	1.121	985	76.3
	66661^{+2145}_{-3344}	$7.26^{+0.11}_{-0.15}$	$-2.32^{+0.22}_{-0.18}$	1.187	60435^{+2004}_{-1470}	$7.37^{+0.05}_{-0.11}$	$-14.96^{+0.16}_{-0.15}$	1.216	987	64.8
PG0834+501	56925^{+1673}_{-1748}	$7.17^{+0.13}_{-0.12}$	$-2.16^{+0.22}_{-0.27}$	1.081	54109^{+1280}_{-1279}	$7.35^{+0.04}_{-0.15}$	$-14.93^{+0.48}_{-0.12}$	1.149	235	68.0
	56814^{+1929}_{-1521}	$6.91^{+0.08}_{-0.11}$	$-2.43^{+0.20}_{-0.20}$	1.404	56376^{+1517}_{-1147}	$6.82^{+0.04}_{-0.05}$	$-14.07^{+0.10}_{-0.08}$	1.482	988	80.2
	55672^{+1446}_{-1603}	$6.89^{+0.09}_{-0.10}$	$-2.63^{+0.20}_{-0.20}$	1.132	54257^{+1832}_{-1042}	$6.88^{+0.07}_{-0.09}$	$-14.11^{+0.10}_{-0.09}$	1.192	986	79.1
Ton 353	62057^{+4593}_{-3171}	$7.19^{+0.19}_{-0.11}$	$-3.01^{+0.38}_{-0.35}$	0.643	60420^{+5008}_{-2912}	$7.16^{+0.18}_{-0.20}$	$-14.18^{+0.13}_{-0.28}$	0.688	230	69.6

Table 3.5. continued...

	HOMOGENEOUS MODELS				STRATIFIED MODELS					
Object	$T_{\rm eff}$ / K	Log g	Log $\frac{He}{H}$	χ^2_{red}	$T_{\rm eff}$ / K	Log g	Log $\frac{M_H}{M_\odot}$	χ^2_{red}	DOF	Conf / %
A31	68242^{+4081}_{-2041}	$7.13^{+0.12}_{-0.13}$	$-1.53^{+0.10}_{-0.18}$	1.323	60248^{+2377}_{-1689}	$7.20^{+0.07}_{-0.12}$	$-15.04^{+0.13}_{-0.09}$	1.337	989	56.6
	81209^{+7727}_{-8175}	$6.77^{+0.18}_{-0.15}$	$-1.47^{+0.24}_{-0.12}$	1.008	69590^{+4984}_{-3242}	$6.61^{+0.13}_{-0.04}$	$-14.05^{+0.10}_{-0.33}$	1.024	985	59.8
RE1016-053	53409^{+1257}_{-617}	$7.99^{+0.01}_{-0.07}$	$-2.99^{+0.20}_{-0.35}$	0.935	55091^{+1674}_{-775}	$8.00^{+0.00}_{-0.04}$	$-13.35^{+0.28}_{-0.88}$	0.974	479	67.3
HS1136+6646	61787^{+787}_{-622}	$7.35^{+0.07}_{-0.07}$	$-2.46^{+0.11}_{-0.05}$	0.885	60010^{+946}_{-847}	$7.46^{+0.03}_{-0.03}$	$-15.00^{+0.05}_{-0.03}$	0.961	1991	96.7
Feige 55	53557^{+429}_{-434}	$6.96^{+0.03}_{-0.05}$	$-2.80^{+0.12}_{-0.08}$	1.481	53158^{+1067}_{-594}	$6.92^{+0.08}_{-0.04}$	$-14.01^{+0.11}_{-0.12}$	1.666	479	90.1
	54339^{+900}_{-793}	$6.95^{+0.14}_{-0.06}$	$-2.64^{+0.18}_{-0.19}$	1.640	53447^{+1217}_{-1506}	$6.94^{+0.20}_{-0.04}$	$-14.08^{+0.06}_{-0.20}$	1.783	469	81.7
PG1210+533	46457^{+904}_{-854}	$7.87^{+0.09}_{-0.10}$	$-1.13^{+0.10}_{-0.10}$	1.043	46938^{+925}_{-1551}	$7.89^{+0.05}_{-0.03}$	$-16.00^{+0.02}_{-0.02}$	1.176	997	97.1
	47329^{+762}_{-1038}	$7.83^{+0.10}_{-0.10}$	$-1.35^{+0.10}_{-0.07}$	1.643	47498^{+1333}_{-1415}	$7.91^{+0.05}_{-0.04}$	$-16.00^{+0.04}_{-0.04}$	2.216	216	98.6
	45696^{+576}_{-569}	$7.73^{+0.06}_{-0.07}$	$-2.00^{+0.05}_{-0.06}$	0.480	44637^{+492}_{-493}	$7.80^{+0.04}_{-0.07}$	$-15.27^{+0.09}_{-0.04}$	0.879	495	100.
	46328^{+201}_{-614}	$7.75^{+0.03}_{-0.02}$	$-1.38^{+0.04}_{-0.04}$	1.743	45521^{+253}_{-283}	$7.96^{+0.02}_{-0.01}$	$-16.00^{+0.01}_{-0.00}$	2.389	1010	100.
	45880^{+205}_{-399}	$7.79^{+0.05}_{-0.04}$	$-1.36^{+0.04}_{-0.05}$	1.700	45665^{+604}_{-319}	$7.95^{+0.02}_{-0.01}$	$-16.00^{+0.00}_{-0.00}$	2.395	1022	100.
LB2	60294^{+3135}_{-2107}	$7.60^{+0.10}_{-0.27}$	$-2.35^{+0.23}_{-0.26}$	1.067	58875^{+1445}_{-1347}	$7.33^{+0.07}_{-0.04}$	$-14.71^{+0.09}_{-0.16}$	1.017	235	**64.3**
HZ34	75693^{+6396}_{-4490}	$6.51^{+0.14}_{-0.01}$	$-1.68^{+0.25}_{-0.21}$	0.666	63046^{+1541}_{-2558}	$6.63^{+0.10}_{-0.09}$	$-14.10^{+0.11}_{-0.14}$	0.701	479	71.2
PG1305-017	51713^{+1720}_{-891}	$7.90^{+0.10}_{-0.17}$	$-1.14^{+0.14}_{-0.17}$	1.339	44592^{+2265}_{-1626}	$8.00^{+0.00}_{-0.09}$	$-16.42^{+0.08}_{-0.05}$	1.112	241	**92.5**
PG1413+015	47951^{+761}_{-1396}	$7.82^{+0.12}_{-0.09}$	$-2.63^{+0.31}_{-0.29}$	1.044	48659^{+1070}_{-1095}	$7.72^{+0.11}_{-0.06}$	$-15.00^{+0.22}_{-0.06}$	1.162	471	87.7
A39	68591^{+5832}_{-2968}	$6.79^{+0.13}_{-0.15}$	$-1.00^{+0.00}_{-0.17}$	1.259	61331^{+2861}_{-2758}	$6.68^{+0.11}_{-0.11}$	$-14.37^{+0.13}_{-0.10}$	1.353	961	86.8
	75101^{+6049}_{-6334}	$6.63^{+0.17}_{-0.13}$	$-1.00^{+0.00}_{-0.17}$	1.024	64129^{+3824}_{-3364}	$6.64^{+0.12}_{-0.10}$	$-14.19^{+0.12}_{-0.13}$	1.049	986	64.8
	73661^{+7678}_{-7432}	$6.86^{+0.18}_{-0.19}$	$-1.00^{+0.00}_{-0.13}$	0.832	60770^{+2945}_{-2613}	$6.69^{+0.23}_{-0.13}$	$-14.55^{+0.07}_{-0.16}$	0.836	980	53.0
RE2013+400	47610^{+1134}_{-767}	$7.90^{+0.10}_{-0.10}$	$-2.80^{+0.12}_{-0.28}$	1.001	48473^{+642}_{-601}	$7.81^{+0.10}_{-0.06}$	$-15.00^{+0.15}_{-0.03}$	1.303	449	99.7
DeHt5	56082^{+1038}_{-1391}	$6.77^{+0.04}_{-0.07}$	$-4.85^{+0.63}_{-0.15}$	1.490	56022^{+969}_{-1035}	$6.77^{+0.06}_{-0.07}$	$-13.15^{+0.12}_{-0.10}$	1.565	866	76.5
	58904^{+2390}_{-1570}	$7.38^{+0.33}_{-0.16}$	$-5.00^{+1.02}_{-0.00}$	1.853	56769^{+1604}_{-1690}	$7.38^{+0.35}_{-0.15}$	$-13.03^{+0.03}_{-1.06}$	1.613	190	**83.0**
GD561	63625^{+3438}_{-1236}	$6.87^{+0.17}_{-0.12}$	$-2.54^{+0.27}_{-0.31}$	1.049	60229^{+2316}_{-1972}	$6.88^{+0.11}_{-0.09}$	$-14.04^{+0.20}_{-0.10}$	1.067	474	57.3
	66257^{+5319}_{-2148}	$6.98^{+0.20}_{-0.10}$	$-2.93^{+0.33}_{-0.51}$	0.429	64553^{+3955}_{-4318}	$6.97^{+0.17}_{-0.16}$	$-13.99^{+0.28}_{-0.20}$	0.425	957	**55.7**
	64986^{+3790}_{-2265}	$7.03^{+0.13}_{-0.16}$	$-3.21^{+0.30}_{-0.36}$	1.165	63992^{+2805}_{-1896}	$6.91^{+0.11}_{-0.09}$	$-13.62^{+0.14}_{-0.39}$	1.181	954	58.3
	62547^{+4652}_{-2065}	$6.87^{+0.22}_{-0.19}$	$-2.75^{+0.34}_{-0.35}$	1.071	58235^{+2624}_{-2928}	$6.90^{+0.09}_{-0.11}$	$-14.15^{+0.09}_{-0.22}$	1.061	953	**55.8**

Table 3.6. χ^2_{red} for the 4600–4750 Å region. Confidence values are in bold where the stratified model gave the lower χ^2_{red}.

	χ^2_{red}			
Object	Homogeneous	Stratified	DOF	Confidence / %
PG 0134+181	1.477	1.812	65	79.4
S 216	0.560	1.140	49	99.3
	1.334	2.836	49	99.5
	0.729	1.252	121	99.8
	1.161	1.574	115	94.8
A 7	0.587	0.649	117	70.6
	1.175	1.214	121	57.1
	1.745	1.808	120	57.7
HS 0505+0112	1.739	3.475	90	99.9
	1.418	2.209	92	98.3
	2.452	2.992	93	83.1
PuWe 1	1.042	1.093	121	60.3
	1.049	1.095	117	59.2
RE 0720-318	2.399	2.863	95	80.5
Ton 320	1.322	1.761	15	70.7
	1.013	1.286	119	90.3
	1.627	1.821	119	73.0
PG 0834+501	1.252	2.470	15	90.0
	1.440	1.996	117	96.1
	1.019	1.537	116	98.6
Ton 353	0.772	1.418	15	87.5
A 31	1.164	1.322	119	75.6
	0.951	0.968	115	53.8

formed on the values of χ^2_{red} found for the 4600–4750Å region only. Table 3.6 lists these values and shows that the homogeneous models are preferred at better than 90% confidence for the following objects: S 216, HS 0505+0112, PG 0834+501, HS 1136+6646, Feige 55, PG 1210+533, PG 1413+015 and RE 2013+400, as well as for single observations of Ton 320 and DeHt 5. Interestingly, apart from for one spectrum, the observations of PG 1210+533 are reproduced well by homogeneous models, in contrast to the results of Bergeron et al. (1994). In most other cases the homogeneous models are preferred, although not with a high confidence level. For some this is extremely marginal, for example in the case of PuWe 1. Therefore, from these results, stratified atmospheres are ruled out at the 90% level in less than half the objects.

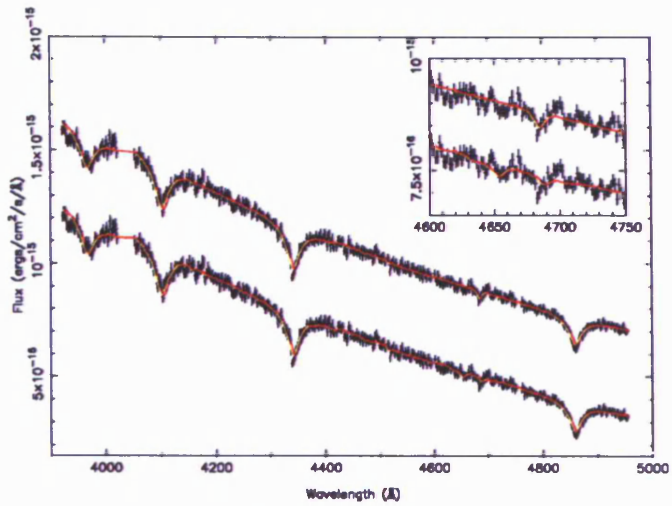

PG 0134+181

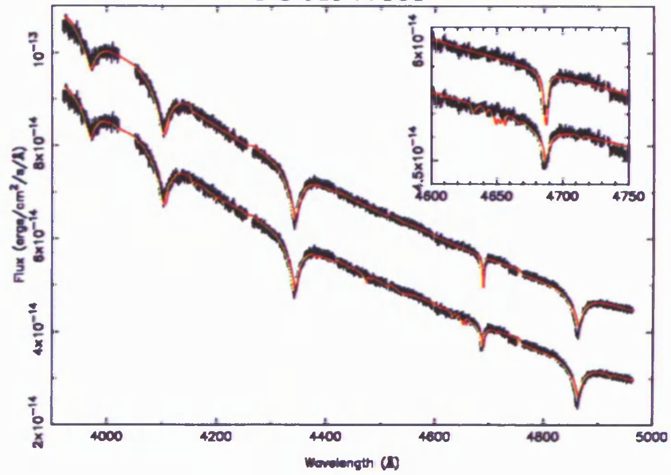

S 216

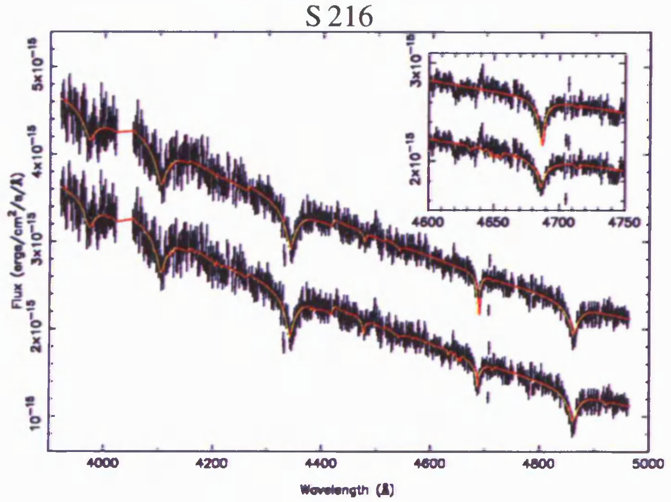

A 7

FIGURE 3.3. Homogeneous and stratified model fits (red lines) to the optical data (black error bars) for each object. (Top - homogeneous models, bottom - stratified models, offset for clarity). Discontinuities in the spectra are due to the slope correction that has been applied to correct for poor flux calibration.

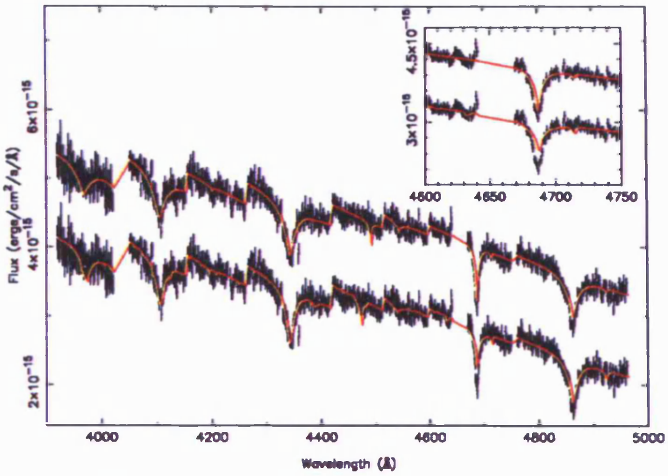

HS 0505+0112

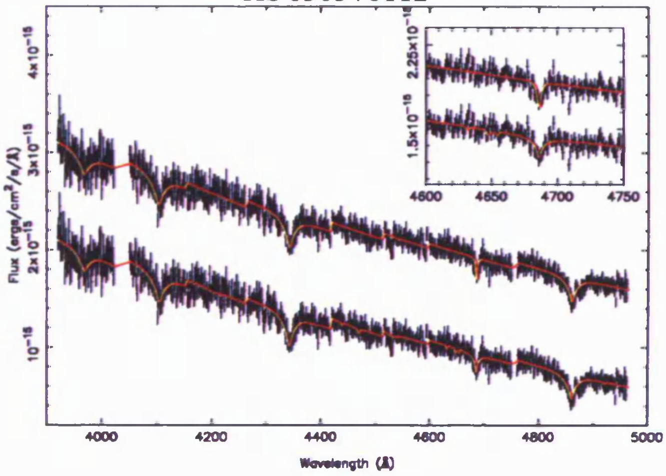

PuWe 1

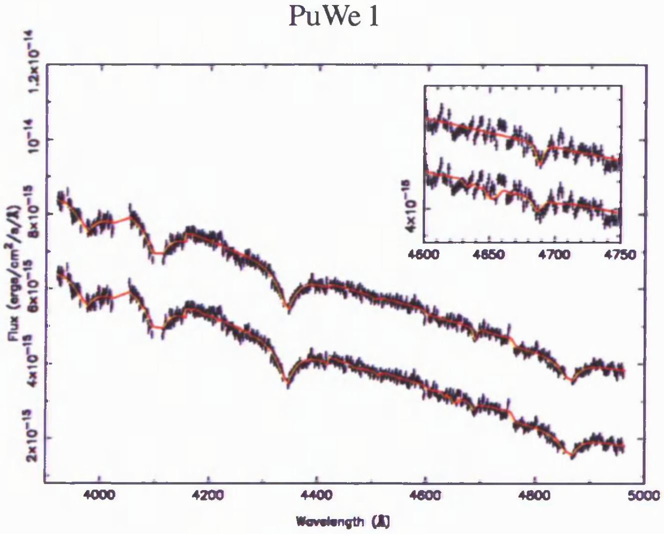

RE 0720-318

FIGURE 3.3. continued...

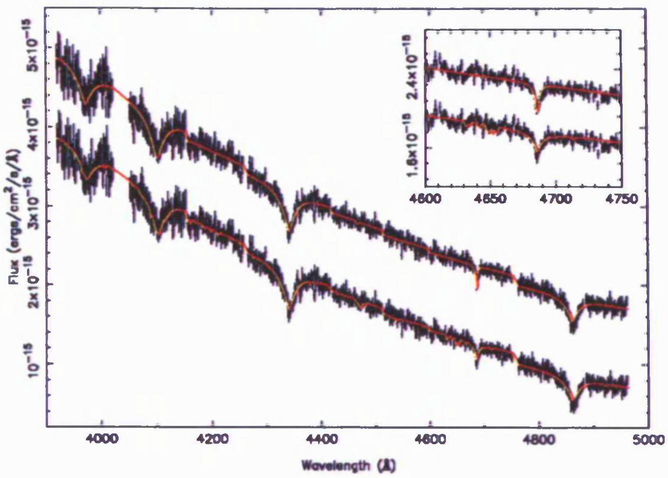

Ton 320

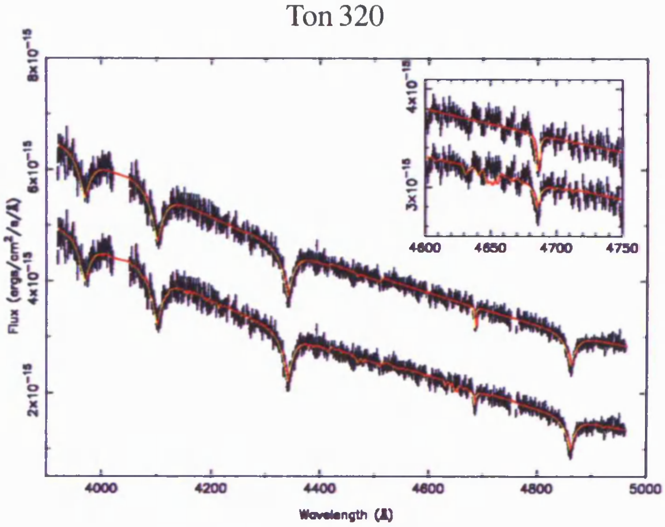

PG 0834+500

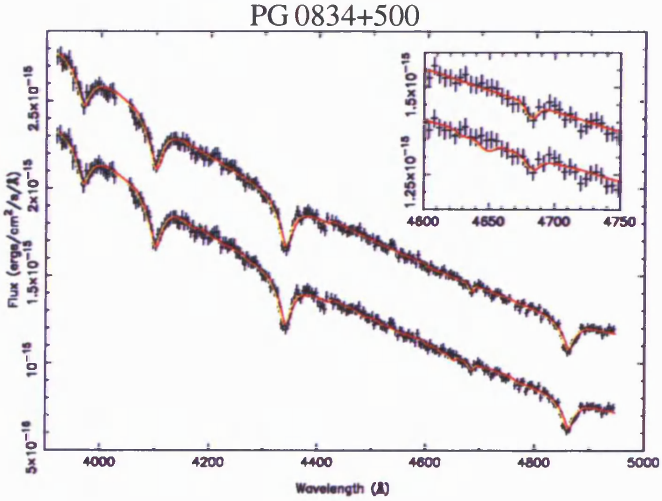

Ton 353

FIGURE 3.3. continued...

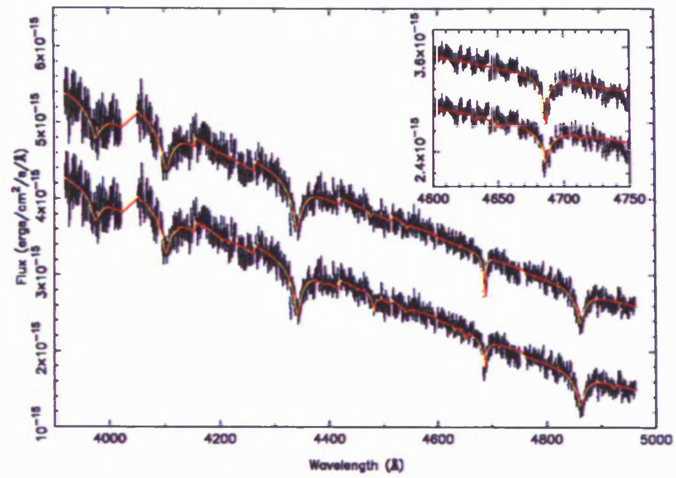

A 31

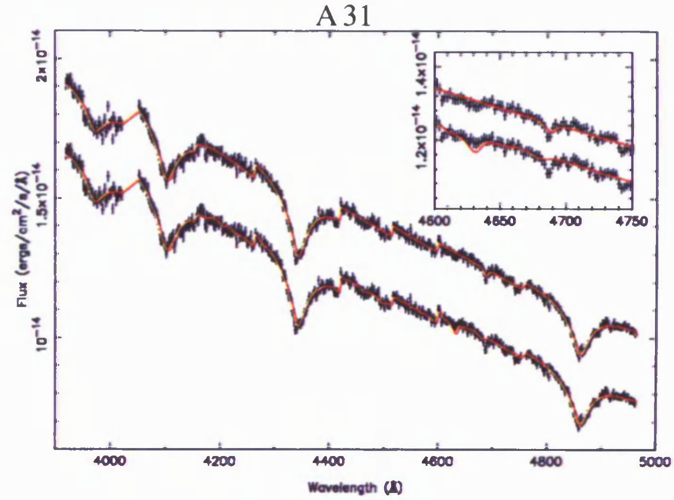

RE 1016-053

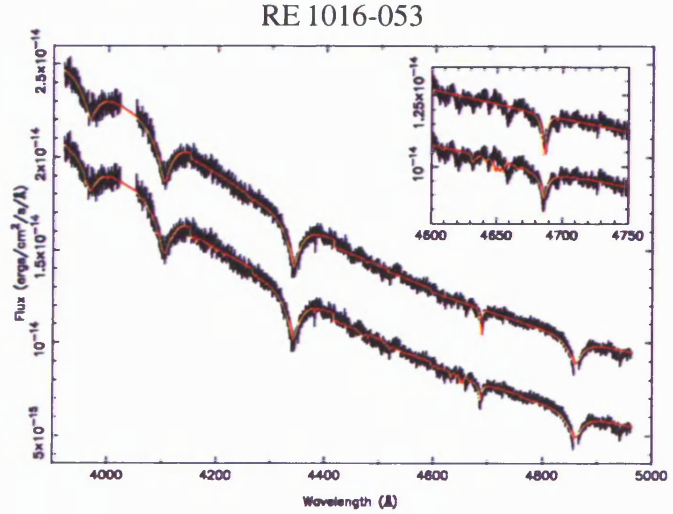

HS 1136+6646

FIGURE 3.3. continued...

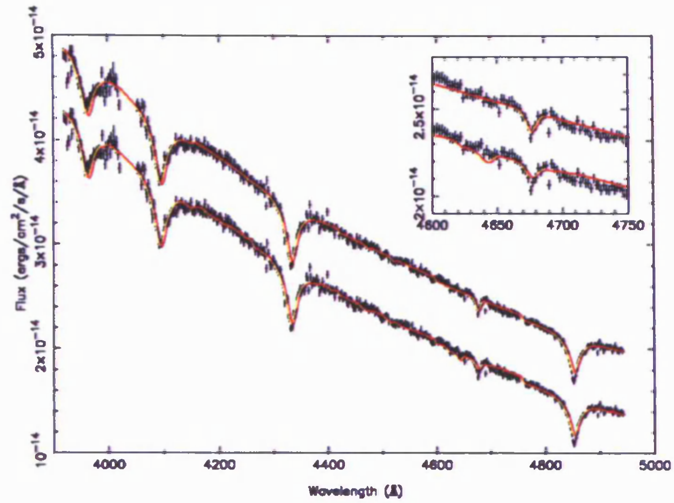

Feige 55

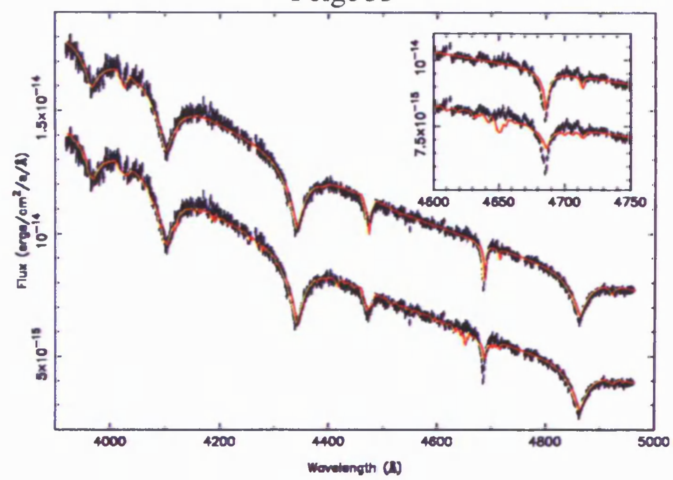

PG 1210+533

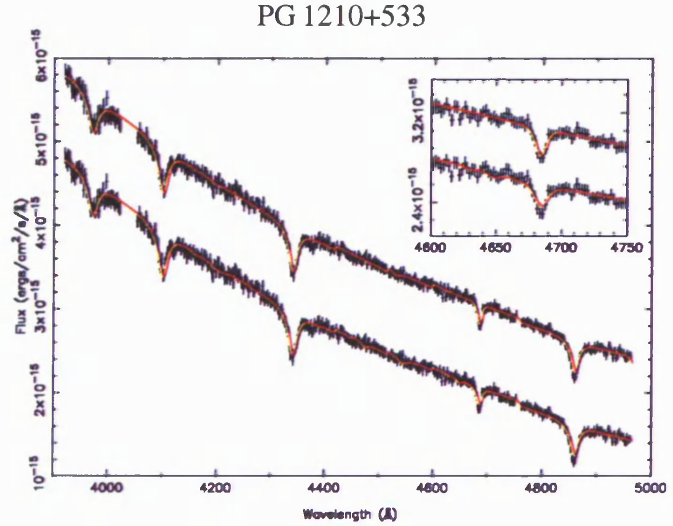

HZ 34

FIGURE 3.3. continued...

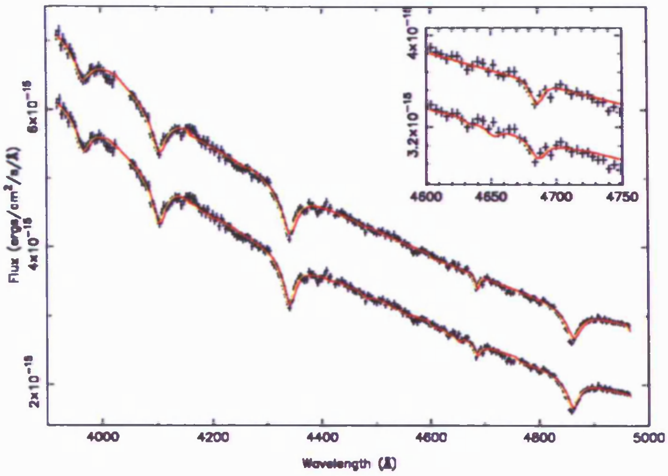

LB 2

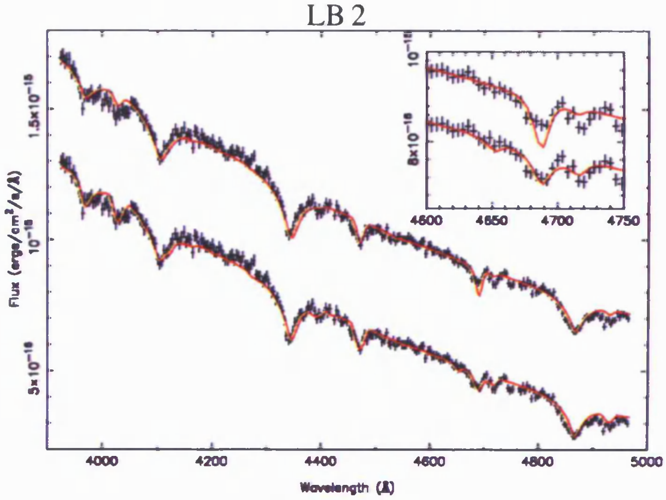

PG 1305-017

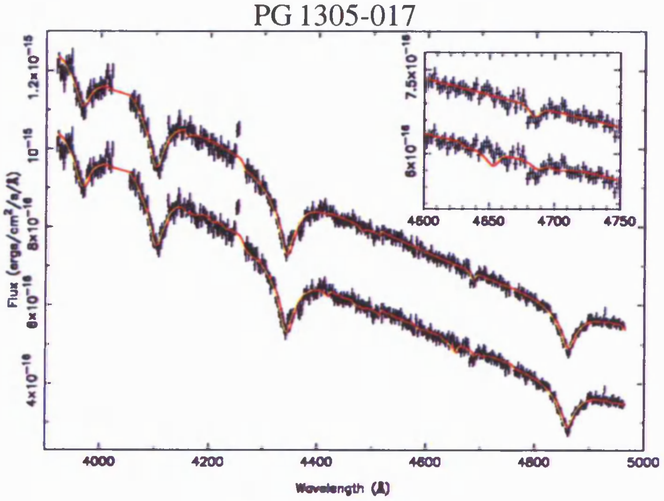

PG 1413+015

FIGURE 3.3. continued...

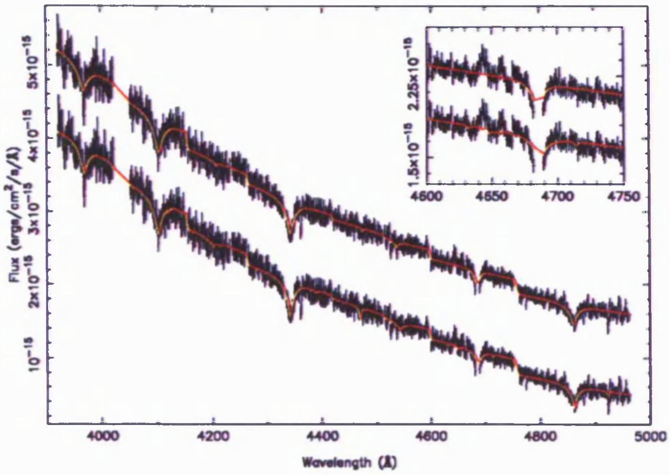

A 39

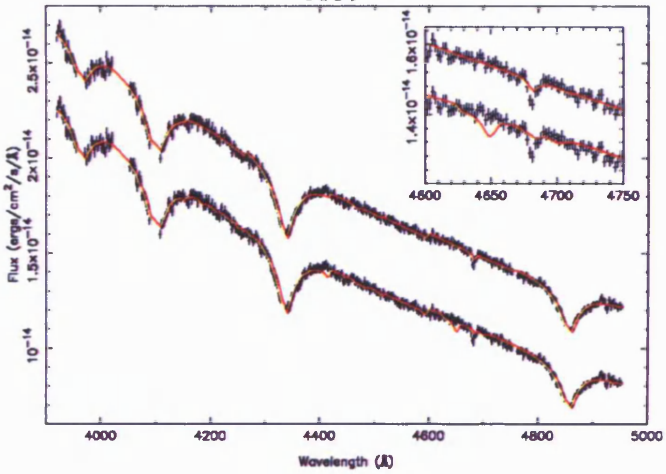

RE 2013+400

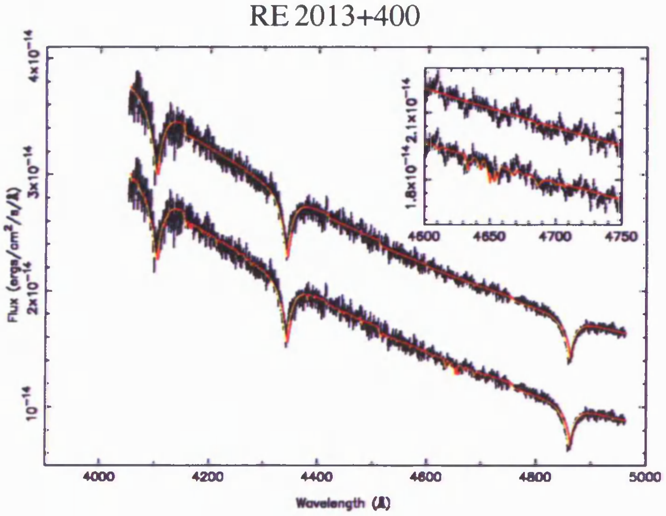

DeHt 5

FIGURE 3.3. continued...

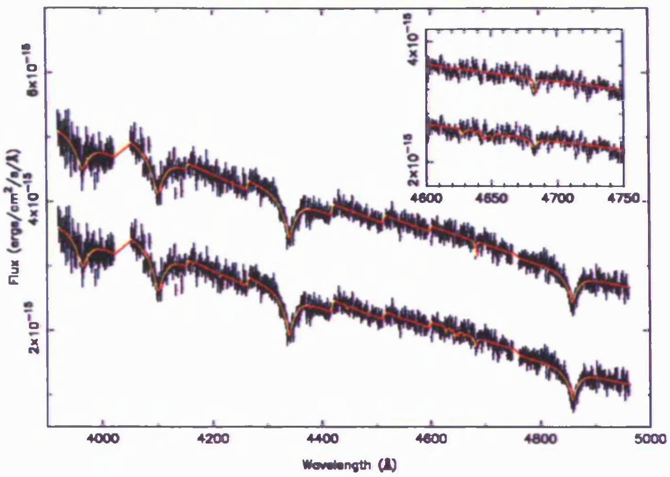

GD 561

FIGURE 3.3. continued...

3.5.3 Multiple observations

Objects with multiple observations provide a way of comparing the formal uncertainties with the actual scatter in the measurements. There are three objects where 4 observations or more have been obtained – S 216, PG 1210+533 and GD 561 and the results for each are plotted in Figure 3.4. Only scatter in temperature and gravity is looked at for PG1210+533 because of its varying helium abundance. For PG 1210+533, the best fitting temperatures and gravities agree well within the error boundaries. This object is at the lower end of the temperature range for the objects in the sample. At the higher temperatures the GD 561 results also agree well with each other, but S 216 appears to be the exception, with relatively small error bars yielding no overlap between any observation. S 216 is a bright object, resulting in a high signal-to-noise spectra. In this case the systematic errors in the analysis may outweigh the observational errors, resulting in an underestimate of the uncertainties of the measurements. The Balmer line problem is seen in S 216 and this may also have contributed to the large scatter in the best fitting parameters. Errors in $T_{\rm eff}$ and log g may therefore be underestimated in fits to the highest signal-to-noise data. The S 216 results suggest that temperature cannot be determined more accurately than to a few thousand degrees, and log g to within $\sim$0.1. Measurement of the helium abundance is most sensitive to the strength of the He II line at 4686 Å and the helium abundance measurements seem to agree well within confidence intervals.

The best fitting parameters for each observation are now averaged to give a single set of measurements for each object. The homogeneous results are used, apart from for

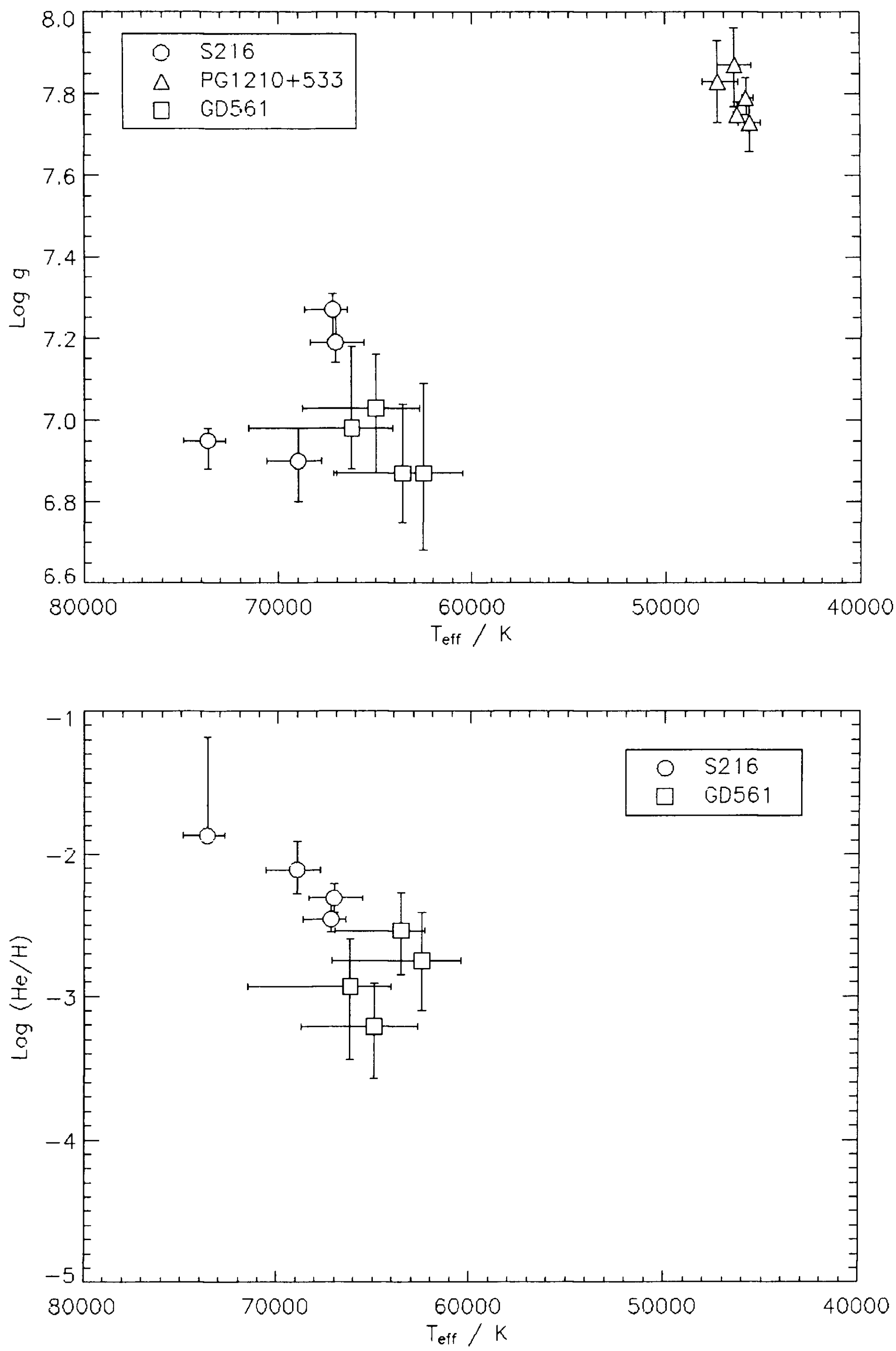

FIGURE 3.4. Upper panel shows scatter in log g and $T_{\rm eff}$, lower panel scatter in log $\frac{\rm He}{\rm H}$ and $T_{\rm eff}$.

Table 3.6. continued...

Object	χ^2_{red} Homogeneous	Stratified	DOF	Confidence
RE 1016-053	0.997	1.406	49	88.4
HS 1136+6646	0.858	1.120	265	98.5
Feige 55	1.527	2.661	49	97.3
	1.642	2.775	49	96.5
PG 1210+533	1.164	2.033	116	99.9
	2.608	3.710	29	82.6
	1.095	4.172	49	100.
	3.246	8.193	119	100.
	2.770	7.511	119	100.
LB 2	1.761	2.568	15	76.3
HZ 34	0.749	1.052	49	88.1
PG1305-017	3.399	1.909	15	**86.2**
PG 1413+015	0.856	1.762	49	99.4
A 39	1.603	1.847	116	77.7
	1.104	1.213	112	69.0
	0.882	0.992	112	73.2
RE 2013+400	1.064	3.205	49	100.
DeHt 5	1.646	1.857	118	74.3
	3.015	1.376	13	91.5
GD 561	0.940	1.191	49	79.5
	0.414	0.407	114	**53.6**
	1.659	1.833	115	70.3
	0.846	0.878	112	57.8

PG 1305-017 as it was best fit by the stratified models. Table 3.7 shows these results. The helium abundance for PG1210+533 is not listed as it varies between observations.

3.6 Discussion

3.6.1 Comparison of results with those of Bergeron et al. (1994)

Since Bergeron et al. (1994) used LTE models containing only hydrogen and helium, the new results from this chapter, which has used non-LTE models that included heavy elements, provide an opportunity to investigate the differences between the predictions of the different models. Figure 3.5 compares the results from Bergeron et al. (1994) with the parameters obtained from fitting the same spectra with the new models. The

Table 3.7. Mean best fitting model parameters to the data. For PG 1305-017, the best fit stratified model parameters are shown, and the value in the Log $\frac{He}{H}$ column is log $\frac{M_H}{M_\odot}$. If, during the fitting procedure, a parameter has reached the edge of the model grid, its error is quoted as zero.

Object	T_{eff} / K	±	Log g	±	Log $\frac{He}{H}$	±
PG 0134+181	54682	1412	7.20	0.11	-2.80	0.26
S 216	69254	1234	7.08	0.06	-2.19	0.15
A 7	66955	3770	7.23	0.17	-1.29	0.15
HS 0505+0112	63227	2088	7.30	0.15	-1.00	0.00
PuWe 1	74218	4829	7.02	0.20	-2.39	0.37
RE 0720-318	54011	1596	7.68	0.13	-2.61	0.19
TON 320	63735	2755	7.27	0.14	-2.45	0.22
PG 0834+501	56470	1651	6.99	0.11	-2.41	0.21
TON 353	62057	3816	7.19	0.15	-3.01	0.36
A 31	74726	5979	6.95	0.15	-1.50	0.15
RE 1016-053	53409	881	7.99	0.03	-2.99	0.26
HS 1136+6646	61787	700	7.34	0.07	-2.46	0.08
Feige 55	53948	671	6.95	0.07	-2.72	0.15
PG 1210+533	46338	647	7.80	0.07	-	-
LB 2	60294	2570	7.60	0.17	-2.53	0.25
HZ 34	75693	5359	6.51	0.04	-1.68	0.23
PG 1305-017	44592	1919	8.00	0.00	-16.42	0.07
PG 1413+015	47961	1031	7.82	0.10	-2.63	0.30
A 39	72451	6129	6.76	0.16	-1.00	0.01
RE 2013+400	47610	933	7.90	0.10	-2.80	0.18
DeHt 5	57493	1612	7.08	0.16	-4.93	0.22
GD 561	64354	2909	6.94	0.16	-2.86	0.35

plots show that for log g and log $\frac{He}{H}$, the LTE models of Bergeron et al. (1994) yield similar results to the non-LTE models; although there is scatter in the data, particularly in log g, the trend appears to follow the line of equal gravity or abundance. However, the temperature found using the newer models tends to be lower than those of Bergeron et al., with the discrepancy increasing with temperature – at a temperature of $\sim$45,000 K the results are the same within the error boundaries, but the trend line shows that by $\sim$80,000 K the non-LTE models give temperatures that are more than 5,000 K lower. To make sure that these deviations are not due to systematic errors in the analysis, the spectra of three objects were reanalysed using a grid of LTE H+He models that was created for this purpose. The objects were chosen as each falls into one of the three clusters of points seen in the T_{eff} comparison shown in Figure 3.5. In performing these fits, it was found that the cores of the Balmer lines had a strong influence on the results; when the line

Table 3.8. Results of fitting LTE H+He models to the spectrum of three objects compared to the analysis of Bergeron et al. (1994).

	Fits with LTE H+He models			Bergeron et al. (1994) results		
Object	$T_{\rm eff}$ / K	Log g	Log $\frac{\rm He}{\rm H}$	$T_{\rm eff}$ / K	Log g	Log $\frac{\rm He}{\rm H}$
S 216	76948 $^{+2395}_{-2799}$	7.37 $^{+0.13}_{-0.13}$	-2.00 $^{+0.12}_{-0.10}$	77300 $\pm$ 3400	7.31 $\pm$ 0.14	-2.06 $\pm$ 0.24
Ton 320	70412 $^{+4031}_{-2843}$	7.68 $^{+0.19}_{-0.19}$	-2.53 $^{+0.22}_{-0.21}$	68800 $\pm$1800	7.68 $\pm$0.12	-2.74 $\pm$0.27
Feige 55	59588 $^{+616}_{-1744}$	7.28 $^{+0.12}_{-0.11}$	-2.56 $^{+0.17}_{-0.18}$	58300 $\pm$1500	7.15 $\pm$0.11	-2.92 $\pm$0.31

cores were included in the fits the $T_{\rm eff}$ dropped by up to 10,000 K in comparison to when they were excluded. This is in contrast to fits performed with the nLTE models, where excluding the line cores made no significant difference to the best fitting temperature (see §3.5.1). This implies that the LTE models do not reproduce the shape of the Balmer line cores as well as the non-LTE models do. As fitting the line cores using non-LTE models has already been found to not having a strong affect on the results, and since Bergeron et al. (1994) excluded the line cores from their fits, that approach is also adopted here. The results are given in Table 3.8 and also plotted in Figure 3.5, and show that the results of the new fits are consistent with those of Bergeron et al. (1994), although again there is some scatter in the log g and log $\frac{\rm He}{\rm H}$ comparisons.

Napiwotzki et al. (1999) investigated the differences between LTE and non-LTE models by generating model spectra under LTE conditions, adding noise and then fitting the resultant data using non-LTE models. They found that the non-LTE result will be $>$10,000 K lower if $T_{\rm eff}$ is found to be 80,000 K using LTE models, and log g $\sim$0.3 lower. However, the differences should decrease at lower temperatures, as is observed. Barstow et al. (1998) have also investigated the effect of transferring from LTE pure H to non-LTE heavy element models, although the hottest object they studied was $\sim$70,000 K. They report a decrease in $T_{\rm eff}$ by 4,000-7,000 K and minimal change in log g, which is in good agreement with the results from this chapter. In contrast, the stratified models that were used to obtain the parameters of PG 1305-017 yield a lower temperature under the assumption of LTE than under non-LTE conditions. This is also true of the homogeneous model fits to this object, although these were discarded because they did not reproduce the He II λ4686 Å line as well as the stratified models. As there is only one object in the sample that appears to have a layered composition, it is not possible to decide if this is a characteristic of stratified atmospheres or statistical error; a study such as that carried out by Napiwotzki et al. (1999) is required to investigate this.

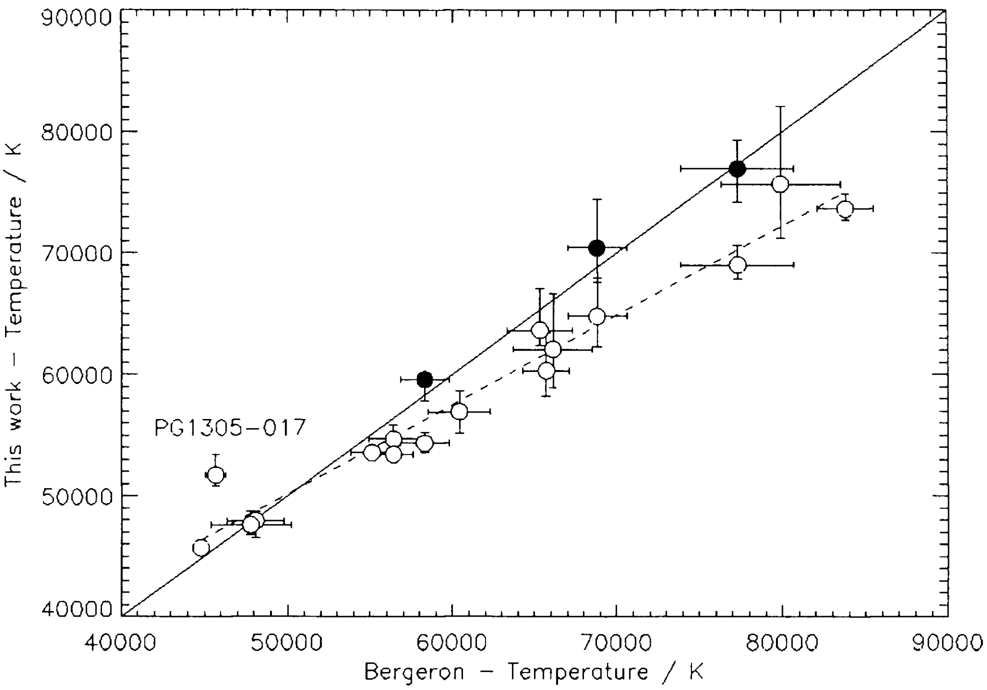

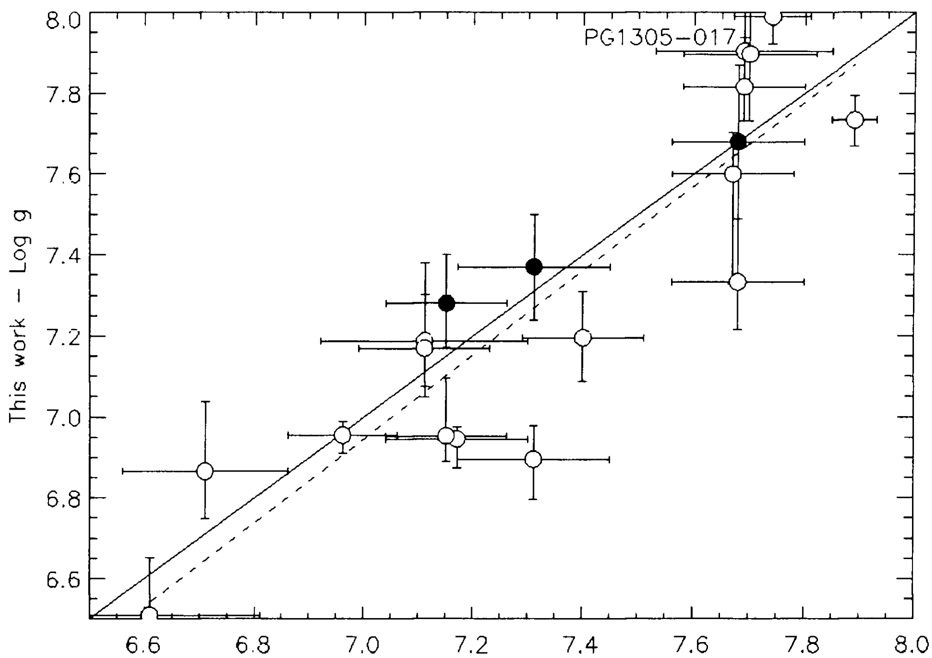

FIGURE 3.5. Comparison of the best fitting model parameters to the data of Bergeron et al. (1994) obtained using non-LTE homogeneous models that include heavy elements, to those obtained by Bergeron et al. using LTE H+He models. Also shown are a comparison between fits that used LTE H+He models compared to the Bergeron et al. values; these are indicated by filled circles. The solid line indicates equal parameters from both sets of models, and the dashed line shows the actual trend in the results.

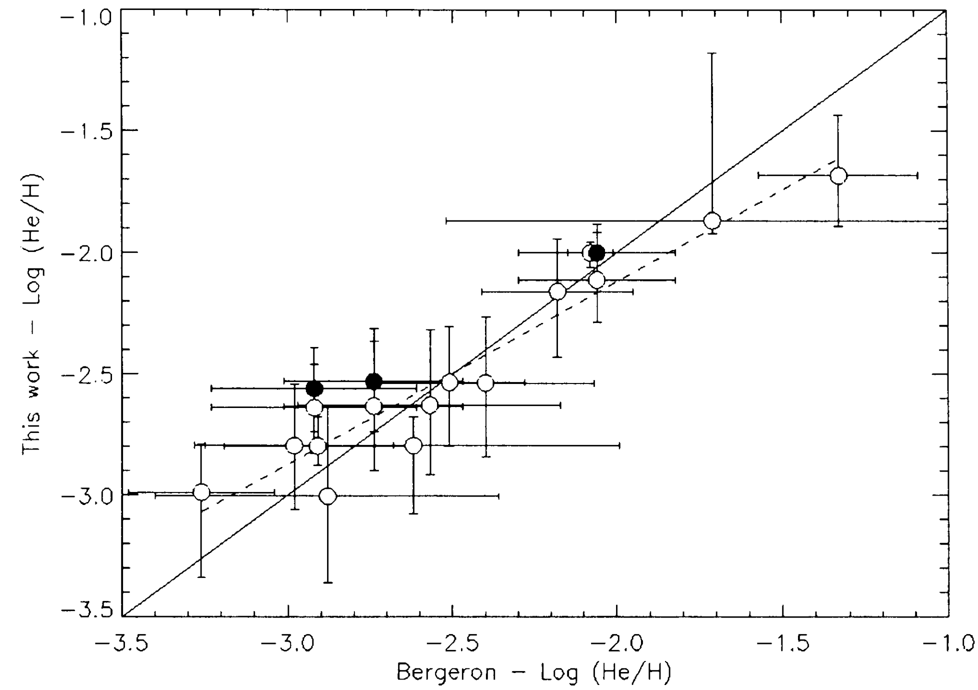

FIGURE 3.5. continued...

3.6.2 The DAO population

The temperatures and gravities obtained from the fits to the data can be used to compare the white dwarfs to theoretical evolutionary models. Figure 3.6 plots $T_{\rm eff}$ against $\log g$ with the post-AGB 0.530 and 0.605 $M_\odot$ white dwarf evolutionary tracks of Blöcker (1995) and the 0.414 $M_\odot$ post-CE track of Driebe et al. (1998) shown for comparison. As might be expected, the objects that are associated with planetary nebulae mostly appear to be hotter, and hence younger, than those where the PN is not seen. Most of the objects are seen to fall between the 0.414 $M_\odot$ track for a He-core white dwarf and the 0.530 $M_\odot$ track, which has a CO-core. Therefore, these may have evolved via the EHB rather than the AGB, or may be post-CE binaries. The temperatures and gravities from Table 3.7 have also been used to compare the objects to the evolutionary tracks for different mass white dwarfs. By interpolating between the theoretical tracks it is possible to infer the mass, radius and luminosity of the white dwarfs from the models and these are shown in Table 3.9.

The mass distribution of the DAO white dwarfs is shown in Figure 3.7. For comparison the DA distributions of Napiwotzki (1999) have also been plotted. Although,

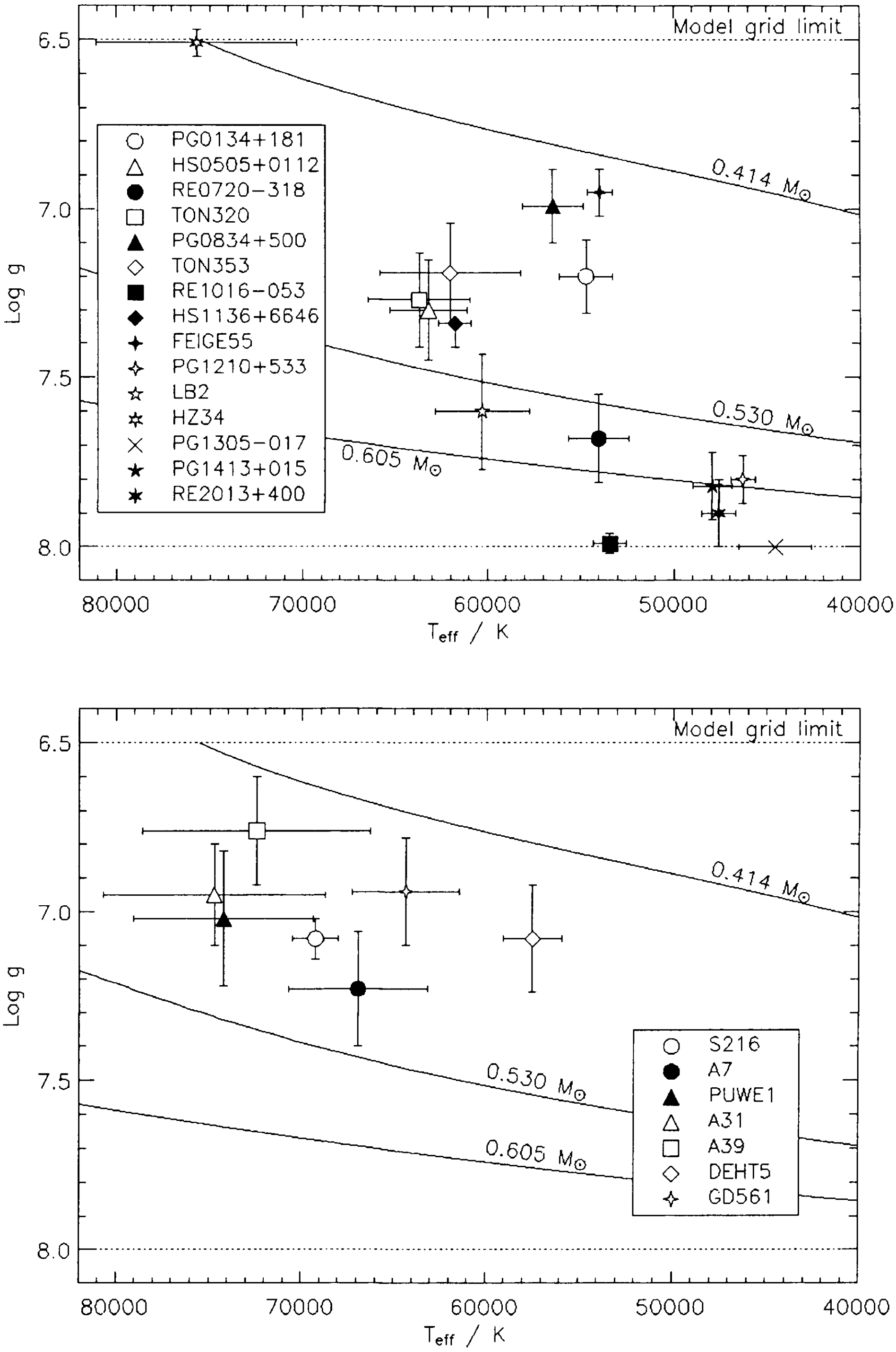

FIGURE 3.6. The best fitting temperatures and gravities. To prevent the plots being crowded the objects are separated into those not associated with planetary nebualae (upper plot) and those that are (lower plot). Filled symbols are used where the object is known or suspected to be in a binary system. PG1305-017, which appears to have stratified H+He, is represented by a cross. Also shown are evolutionary tracks for 0.414, 0.530 and 0.605 $M_\odot$ white dwarfs.

Table 3.9. Results from comparison with evolutionary models

Object	V	Radius / $R_\odot$	±	Mass / $M_\odot$	±	d / pc	±	Log L / $L_\odot$	±
PG 0134+181	17.14[1]	0.029	0.029	0.480	0.015	845	11	0.818	0.112
S 216	12.90[2]	0.033	0.002	0.496	0.009	152	5	1.362	0.067
A 7	15.60[2]	0.029	0.005	0.508	0.020	443	18	1.165	0.185
HS 0505+0112	15.20[3]	0.026	0.004	0.509	0.018	333	6	0.995	0.152
PuWe 1	15.70[2]	0.036	0.007	0.499	0.026	610	21	1.546	0.212
RE 0720-318	16.10[5]	0.018	0.002	0.566	0.046	321	5	0.390	0.109
Ton 320	15.74[6]	0.027	0.004	0.507	0.017	442	7	1.037	0.149
PG 0834+501	15.79[1]	0.035	0.004	0.453	0.049	562	7	1.059	0.103
TON 353	16.71[6]	0.029	0.004	0.495	0.019	741	13	1.061	0.172
A 31	15.60[2]	0.039	0.006	0.491	0.025	629	25	1.620	0.200
RE 1016-053	14.10[7]	0.014	0.000	0.694	0.014	99	0.4	0.147	0.036
HS 1136+6646	13.60[3]	0.025	0.002	0.511	0.007	151	1	0.917	0.062
Feige 55	13.61[1]	0.037	0.003	0.439	0.015	208	2	1.007	0.065
PG 1210+533	14.12[6]	0.016	0.001	0.595	0.033	107	1	0.027	0.057
LB 2	15.63[8]	0.020	0.003	0.557	0.049	295	6	0.654	0.153
HZ 34	15.73[1]	0.059	0.002	0.417	0.018	1025	8	2.015	0.145
PG 1305-017	17.20[9]	0.014	0.000	0.684	0.003	369	2	-0.183	0.077
PG 1413+015	17.09[1]	0.016	0.001	0.608	0.046	423	5	0.077	0.083
A 39	15.60[2]	0.046	0.007	0.455	0.036	744	19	1.724	0.212
RE 2013+400	14.60[1]0	0.015	0.001	0.642	0.043	126	1	0.005	0.077
DeHt 5	15.40[2]	0.033	0.005	0.470	0.025	435	14	1.015	0.151
GD 561	14.52[11]	0.038	0.002	0.464	0.029	85	6	1.346	0.160

[1] Green et al. (1986) [2] Napiwotzki & Schönberner (1995) [3] Heber et al. (1996), estimated from B mag [4] From White Dwarf Database (http://procyon.lpl.arizona.edu/WD/) [5] From Simbad (http://simbad.u-strasbg.fr/sim-fid.pl) [6] Kidder (1991) [7] Barstow et al. (1993) [8] Cheselka et al. (1993) [9] Estimated from the flux of the optical spectrum [10] Barstow et al. (1995) [11] Greenstein (1974)

other mass distributions have been published with larger samples, for example Finley et al. (1997), this is the only one that has used non-LTE white dwarf model atmospheres and the evolutionary models of Blöcker (1995) and Driebe et al. (1998) to determine mass. However, their sample was extreme-ultraviolet selected, and so, since low mass white dwarfs that may be detected at great distances in optical surveys are not seen in the EUV due to interstellar absorption, there is a lack of objects at the lower end of the distribution. In the DAO distribution a very sharp peak is seen between 0.45 and 0.5 $M_{\odot}$. In comparison, the DAs have a peak in their mass distribution between 0.55 and 0.65 $M_{\odot}$. The very lowest mass DAOs (between 10 and 15% of the sample) are of too low a mass to have been formed within the age of the galaxy raising the possibility that some may have gone through common envelope-evolution and be part of close binary systems. However, in Chapter 6 a search for binarity in the objects for which FUSE data are available is conducted. This investigation fails to detect binarity in any objects that were not known binaries. The limit of mass below which white dwarfs must be in binary systems is uncertain, but is quoted as between 0.45 and 0.5 $M_{\odot}$ by Bergeron et al. (1992). Of the objects with mass $\sim$0.45 $M_{\odot}$ or below, both Feige 55 and PG 0834+500 are known binaries. GD 561 does not show any sign of binarity, but it is possible that some of the objects have very faint companions that haven't been detected yet. The lowest mass object, HZ 34 is also not a known binary. If we assume that those with mass between 0.45 and 0.5 $M_{\odot}$ evolved from EHB stars, then just under 50% are post-EHB. In addition, over 20% of the DAOs have a mass that coincides with, or is greater than, the position of the peak of the DA mass distribution. In summary, the mass distribution of the DAOs peaks at a lower mass than the DAs but tails off towards both high and low mass, with none of the DAOs having a mass above 0.7 $M_{\odot}$ or below 0.35 $M_{\odot}$. Therefore, the population of DAOs seems to include white dwarfs formed in binary systems, post-EHB stars and post-AGB stars. A final summary of the likely evolutionary paths of the DAOs can be found in §10.8.

Figure 3.8 shows the distribution of $T_{\rm eff}$ and log g for the sample of DAO white dwarfs, and the DAs for comparison. The majority of the DAOs have a temperature in the range $\sim$50,000-70,000 K, and in general the DAOs seem to be hotter than the DAs – this is unsurprising as DAOs must be hotter than $\sim$45,000 K in order for He II to be detected. The dips in the distribution between 55,000 and 60,000 K, and 65,000 and 70,000 K are less than the counting statistics involved in looking at a small number of objects, and are probably not real. The log g distribution is very interesting and appears to be bimodal with a peak at around log g = 7.0, and another at log g = 7.75 - 8.0. There is also a very strong peak in the DA distribution at log g = 7.75 - 8.0, so the higher

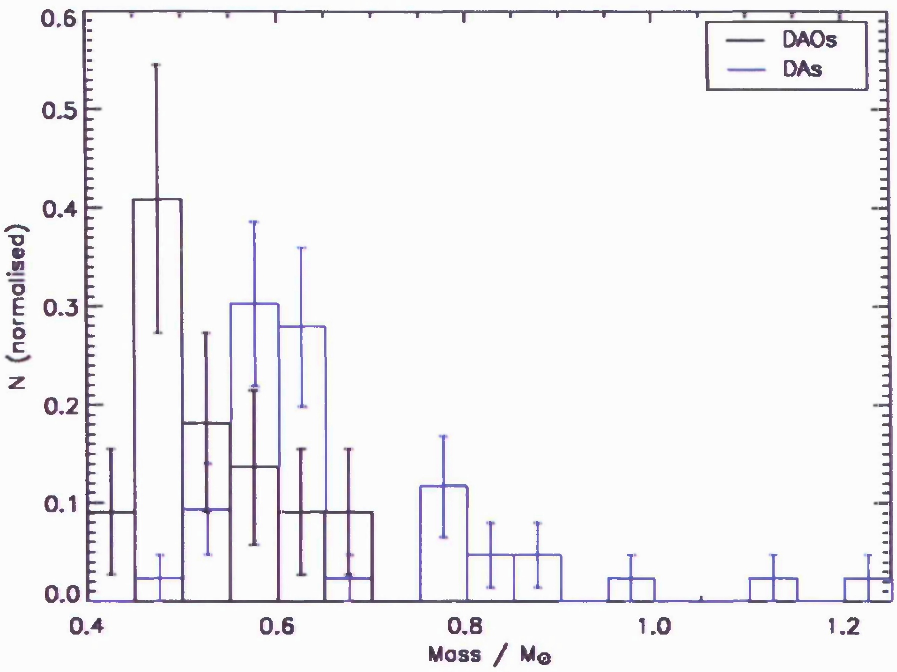

FIGURE 3.7. The distribution of masses obtained from the optical data, and for the DAs of Napiwotzki et al. (1999).

gravity DAOs fall into the same log g bin as the peak of DAs. They are: RE 1016-053, PG 1210+533, PG 1305-017, PG 1413+015 and RE 2013+400. These objects are either unusual – PG 1305-017 is the only one that appears to be stratified and PG 1210+533 exhibits a changing helium abundance over many years – or are post-CE, pre-cataclysmic binaries, and so may form a separate sub-class of DAOs. In contrast, the low log g DAOs have no counterparts in the DA distribution. These objects include the low mass probable post-EHB and binaries in their number. Therefore, two groups of DAOs can be defined: the low log g, and the high log g stars.

3.7 The helium abundance and distribution in DAOs

Relationships between the helium abundance and the temperature, gravity and luminosity of DAOs have been noticed by Bergeron et al. (1994) and Napiwotzki (1999). The large sample of DAOs studied here presents an excellent opportunity to look for trends such as these. Fig. 3.9 shows how helium abundance depends on temperature and gravity; PG1210+533, with its varying helium abundance, is not considered here. There is

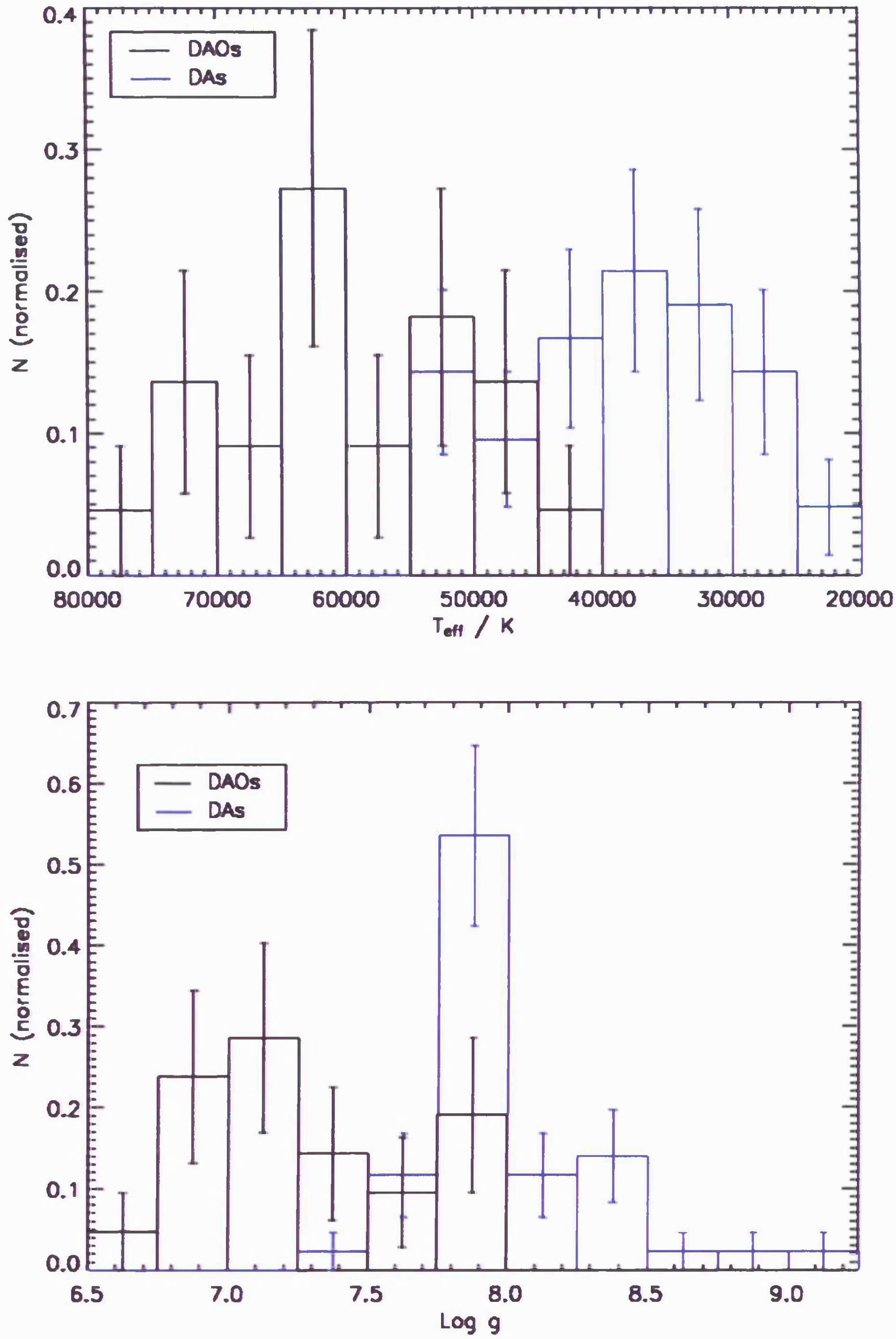

FIGURE 3.8. Temperature and log g distribution for the DAOs from this study, and the DAs of Napiwotzki et al. (1999).

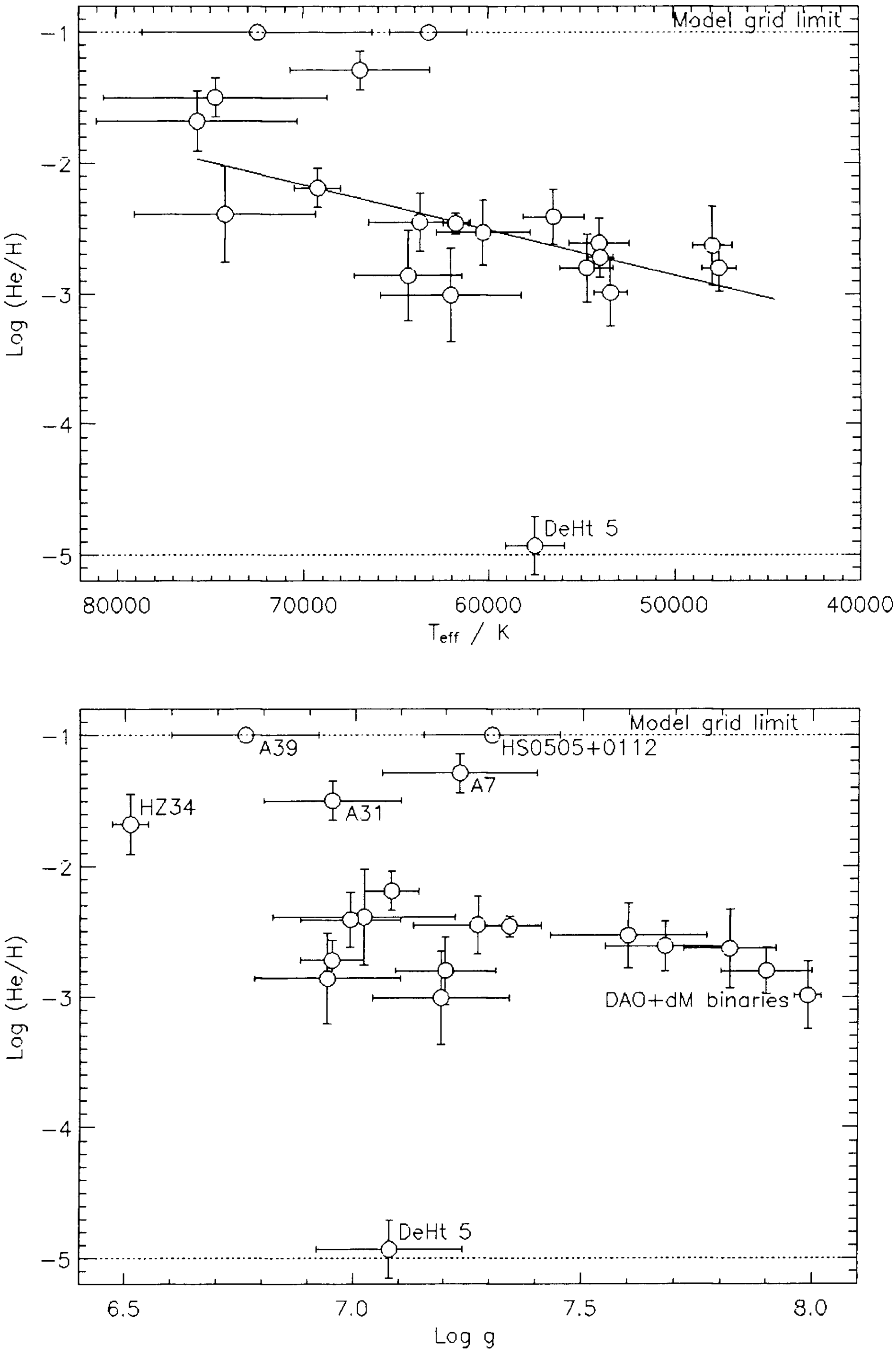

FIGURE 3.9. Dependance of helium abundance on T_{eff} and log g.

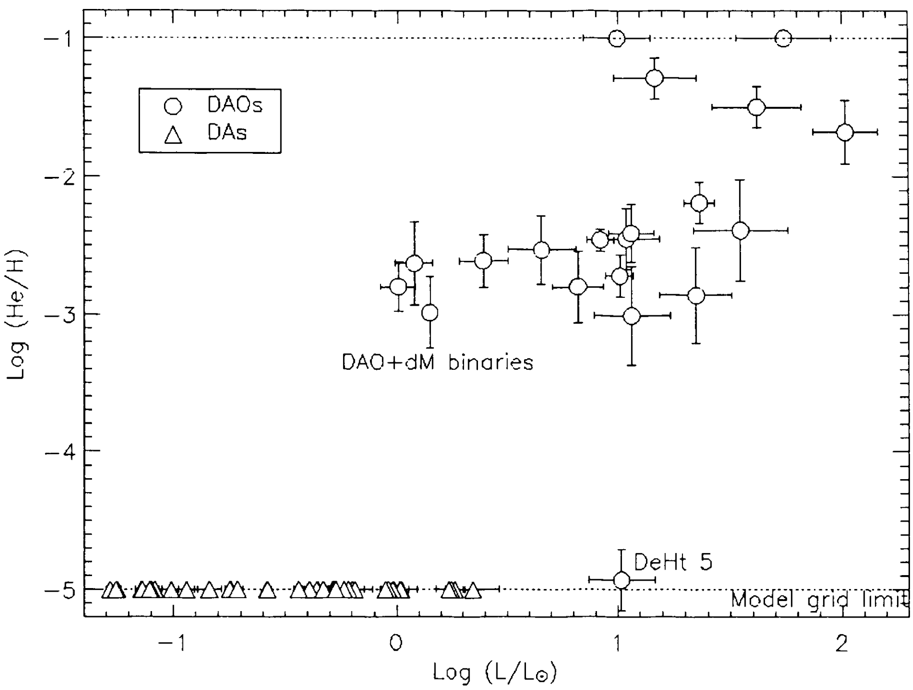

FIGURE 3.10. Dependance of helium abundance on luminosity. The DAs of Napiwotzki et al. (1999) are also shown with a nominal log $\frac{\mathrm{He}}{\mathrm{H}}$ of -5.

perhaps a suggestion of a correlation between log $\frac{\mathrm{He}}{\mathrm{H}}$ and T_{eff}, but no trend is apparent in the log $\frac{\mathrm{He}}{\mathrm{H}}$ - log g plot. However, in this plot, it is easy to separate the DAOs into groups; those denoted as DAO+dM binaries have log g greater than 7.5, whereas most have a lower gravity than this and log $\frac{\mathrm{He}}{\mathrm{H}}$ between approximately -2 and -3. A further group exists with similar log g, but higher helium abundance. These high He abundance objects don't appear related to each other, although 3 of the 5 are associated with planetary nebulae. DeHt 5 has the lowest $\frac{\mathrm{He}}{\mathrm{H}}$ in the sample, even though its gravity appears to associate it with the low log g objects. In figure 3.10 the helium abundances are plotted against log luminosity, which depends on both the temperature and gravity of the object. Also plotted are the DAs from Napiwotzki et al. (1999), each with a nominal log $\frac{\mathrm{He}}{\mathrm{H}}$ of -5. The DAO+dM binaries all have luminosities that are similar to those seen in the DAs, while all the others are more luminous - with the low helium abundance of DeHt 5 unusual for its luminosity. As mass loss rate is related to luminosity in a radiatively driven wind, it is possible that these high luminosity objects are experiencing mass loss (Abbott, 1982). Unglaub & Bues (1998) used an equation taken from Blöcker (1995) (see

§1.4.2) to predict mass loss rate from an objects luminosity:

$$\dot{M} = 1.29 \times 10^{-15} L^{1.86}$$

In a later paper (Unglaub & Bues, 2000) calculations of mass loss were performed as the stellar parameters varied with time, according to evolutionary models. They also used a second estimate of the mass loss rate that included a cut off, below which no wind would be expected, and introduced some dependance on the composition of the objects, so that mass loss would continue for PG 1159 stars up to log $g \sim 8$, for example, because of their high metal abundance. For DAOs, however, mass loss would be expected to cease by log $g \sim 7$, which coincides with the peak in the DAO log g distribution. Beyond this the transition from DAO to DA would be rapid. It is possible, therefore, that DeHt 5 is an example of an object making this transition.

Using the above equation, the mass loss rate for the objects in the DAO sample were calculated and are shown in Table 3.10. Although the mass loss rates have large uncertainty, some interesting results can be seen. PG 1305-017 has the lowest predicted mass loss at $5.9 \pm 1.9 \times 10^{-16}$ $M_{\odot}$ yr^{-1}, and out of the 22 objects in the sample, it is the only one that appears to have stratified a helium atmosphere, although in a number of cases it is difficult to distinguish between the homogeneous and layered models. If even very weak mass loss ($>10^{-16}$ $M_{\odot}$ yr^{-1}) is occurring, it would prevent the diffusive equilibrium that is assumed in the stratified models from occurring. However, PG 1305-017 has passed the wind limit, so mass loss should not be occurring anyway. The highest mass loss rates are predicted for HZ 34 and A 39, both of which have high helium abundance. Overall, the log mass loss rate correlates with helium abundance to the same extent as the log luminosity, since the two are closely related, but a strong correlation is not necessarily expected as the effect on mass loss of different metallicities in the objects is not properly known. For the subset of DAOs with high log g binaries, mass loss should have ceased. The existence of helium in their spectra must instead be explained in other ways, for example through stripping of mass during a common envelope phase or through accretion from their companion. However, there is no obvious explanation for the helium observed in PG 1210+533, which is not a known binary.

3.8 Conclusions

Out of a sample of 22 objects, only one has a helium distribution that is best described by diffusive equilibrium. The other 21 objects appear to have homogeneously distributed

Table 3.10. Mass loss rate for the DAO white dwarfs.

Object	Log $\frac{He}{H}$	$\pm$	Mass loss rate / $10^{-14}\,M_{\odot}\,yr{-1}$	$\pm$
PG 0134+181	-2.80	0.26	4.3	2.1
S 216	-2.19	0.15	44.	13.
A 7	-1.29	0.15	19.	15.
HS 0505+0112	-1.00	0.00	9.1	6.0
PuWe 1	-2.39	0.37	97.	89.
RE 0720-318	-2.61	0.19	0.69	0.32
TON 320	-2.45	0.22	11.	7.0
PG 0834+501	-2.41	0.21	12.	5.3
TON 353	-3.01	0.36	12.	9.0
A 31	-1.50	0.15	130.	115.
RE 1016-053	-2.99	0.26	0.24	0.037
HS 1136+6646	-2.46	0.08	6.5	1.7
Feige 55	-2.72	0.15	9.6	2.7
PG 1210+533	-	-	0.14	0.035
LB 2	-2.53	0.25	2.1	1.4
HZ 34	-1.68	0.23	720.	450.
PG 1305-017	-16.42	0.07	0.059	0.019
PG 1413+015	-2.63	0.30	0.18	0.064
A 39	-1.00	0.01	220.	210.
RE 2013+400	-2.80	0.18	0.13	0.044
DeHt 5	-4.93	0.22	10.	6.5
GD 561	-2.86	0.35	41.	28.

helium, in the line forming regions at least. In general the DAOs have a lower mass than the more common DAs, and may require binary evolution to form within the age of the galaxy, or may have evolved along the EHB - please see §10.8 for a summary of the likely evolutionary paths of these objects. A subset of DAOs have a higher gravity than the rest, and masses that would be thought of as normal for DA white dwarfs. These seem to be either unusual, for example with stratified H+He or variable helium abundance, or are pre-CV, post-CE sytems and so may be accreting from the wind of their companions or the visible helium in their spectra might be the result of the modification of their composition during the common envelope stage. The lower log g white dwarfs are mostly not known to have companions. The helium lines that are seen in their spectra may be related to their high luminosities. As mass loss rate is related to luminosity in radiatively driven winds, this may hint at mass loss being the mechanism that is acting to prevent gravitational settling of helium.

Chapter 4

The Far Ultraviolet Spectroscopic Explorer (FUSE)

4.1 Introduction

A significant proportion of this thesis is based on observations made by the Far Ultraviolet Spectroscopic Explorer. This chapter describes the UV missions that preceded FUSE, the capabilities of the satellite, the observations of DAO white dwarfs that have been obtained, and the method used to reduce the data.

4.2 Observing the ultraviolet universe

Although observations of stellar sources at visible wavelengths are possible from the ground, absorption by the atmosphere means that the ultraviolet (UV) universe must be observed from space. Even there it is only possible because the interstellar medium is non-uniform and contains partially ionised material that is transparent to UV photons. The UV wavelength region can be split into a number of sections; these are the extreme-UV (EUV), extending approximately beween 10 and 900 Å, the far-UV (FUV), between 900 and 1600 Å and the near-UV longwards of this limit.

In 1975, the Extreme Ultraviolet Telescope was flown, attached to an Apollo capsule, which detected unambiguously for the first time an EUV source; this was the hot white dwarf HZ 43 (Barstow & Holberg, 2003). In the late 1970s and early 1980s, the Einstein and European X-ray Astronomy Satellite (EXOSAT) satellites were launched. Although X-ray missions, their spectral sensitivity extended into the EUV. An important result from these satellites was that the soft X-ray flux of white dwarfs was significantly lower than was expected, based on pure hydrogen models (Barstow & Holberg, 2003). This was initially thought to be due to the presence of helium in the white dwarf atmospheres. The amount of helium that can be supported by radiative levitation was found to be too small to explain the observed lack of flux, and instead the idea of stratified atmospheres was suggested, which would consist of a thin hydrogen layer, where the Balmer lines are formed, on top of a mostly helium atmosphere (Vennes et al., 1988). In 1990, the Roentgen Satellite (ROSAT) was launched, carrying with it the wide field camera (WFC), which performed the first EUV sky survey, between 60 and 200 Å. Only 125 white dwarfs were detected by ROSAT, compared to the 1,000-2,000 that were expected (Barstow, 1989). It was found that the flux observed in photometric data was always lower than predicted by H+He models. Instead, trace heavy elements, levitated in the white dwarf atmosphere by radiative forces, were proposed to be supplying the opacity (Barstow, 1993). Two years after ROSAT, the Extreme Ultraviolet Explorer (EUVE) was launched. It also carried out a sky survey, but extended the wavelength region covered up to 760 Å, the results of which largely reflected those of ROSAT (Barstow & Holberg, 2003).

One of the earliest satellites to observe the FUV wavelength region was Copernicus (also known as the Orbiting Astronomical Observatory 3), which obtained far- and near-UV spectral scans, mostly of bright stars, between 1972 and 1981. The Voyager satellites, which began their journey to the outer planets in the late 1970s, carried on board UV cameras that were primarily to be used to study the atmospheres of the gas giant planets. An observation of HZ 43, made shortly after Voyager 2 left Jupiter, recorded the region of the Lyman series of hydrogen between 900 and 1200 Å for the first time (Holberg et al., 1980). In 1978, the International Ultraviolet Explorer (IUE) was launched, operating between 1200 and 3000 Å. IUE was especially important in discovering white dwarfs in binary systems, which were masked out by their companion stars at optical wavelengths and was also useful in identifying the heavy elements that exist within a white dwarf atmosphere (Barstow & Holberg, 2003). Since IUE was turned off in 1996, the FUV longwards of 1200 Å has only been accessible using instruments aboard the Hubble Space Telescope (HST). Initially, it carried the Goddard High Resolution Spectrometer (GHRS), which provided very high resolution spectra but only in a narrow wavelength range during each observation, and the Faint Object Spectrometer (FOS), with which low resolution observations could be made across the UV wavelength range. In 1997 the GHRS was replaced by the Space Telescope Imaging Spectrograph (STIS). This is currently providing very high resolution data in the spectral region beteen 1200

Table 4.1. Wavelength ranges of the FUSE detector segments, from the FUSE observers guide (see http://fuse.pha.jhu.edu/analysis)

Channel	Segment A	Segment B
SiC 1	1090.9–1003.7	992.7–905.0
LiF 1	987.1–1082.3	1094.0–1187.7
SiC 2	916.6–1005.5	1016.4–1103.8
LiF 2	1181.9–1086.7	1075.0–979.2

and 2000 Å (Barstow & Holberg, 2003). The only current mission that can provide access to the spectral region shortwards of 1200 Å, where most of the hydrogen Lyman lines reside, is FUSE:

4.3 FUSE

The Far-Ultraviolet Spectroscopic Explorer (FUSE) was launched on June 24, 1999 on a Delta II rocket as part of NASA's Origins programme. It orbits at approximately 760 km above the surface of the Earth at an inclination of 25° to the equator, and one orbit takes about 100 minutes. FUSE provides high resolution spectra in wavelengths between 905 and 1187Å and is the only current mission giving access to this region of the electromagnetic spectrum. The design and performance of FUSE have been published elsewhere, e.g. Moos et al. (2000), Sahnow et al. (2000), so the following is just a brief summary of the main points.

The design of the FUSE instrument is quite unusual (see Figure 4.1) and creates a number of problems in the reduction of the data. It consists of four separate co-aligned optical paths (channels). Each channel has a mirror, a Focal Plane Assembly, a diffraction grating and part of a detector. Light from a target enters the apertures of all the channels at the same time. Two of the mirrors and two of the gratings are coated with SiC, the others with LiF over a layer of aluminium. This is necessary in order to provide coverage over the whole FUSE wavelength range since the reflectivity of the Al+LiF is low below about 1020Å. FUSE has two microchannel plate detectors (1 and 2), each divided into two segments (A and B) that are separated by a small gap. Light from a SiC and a LiF channel falls onto each detector. This results in 8 individual spectra, two of which cover the 900 – 1000Å wavelength region, four in the 1000 – 1100Å range and the other two in the 1100 – 1200Å region. Table 4.1 gives the exact wavelength ranges covered by each.

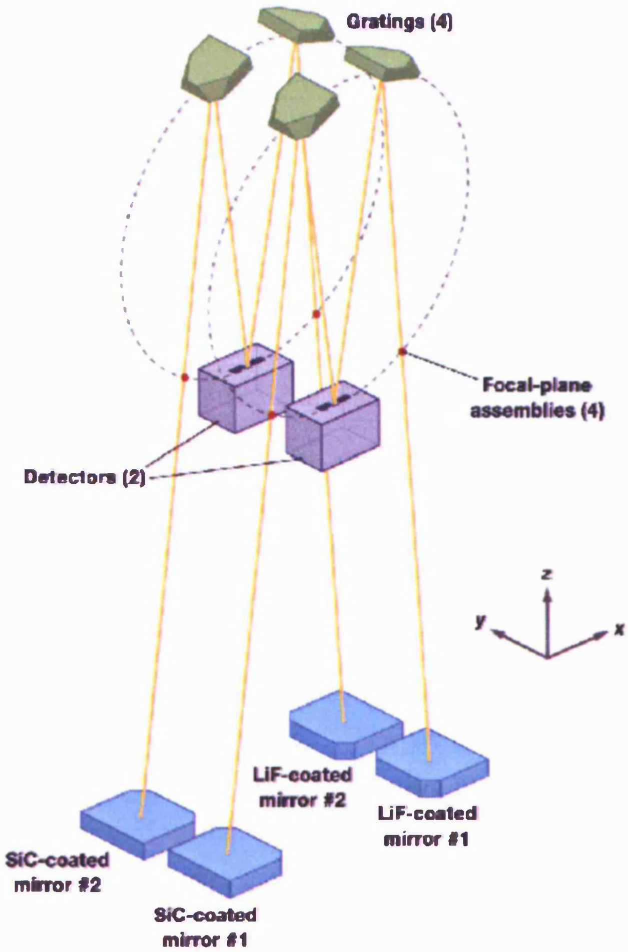

FIGURE 4.1. Diagram of the FUSE optical setup, (figure taken from the FUSE website, http://fuse.pha.jhu.edu).

There is no internal wavelength calibration source on FUSE, so molecular hydrogen lines and low ionization atomic lines have been used to obtain the wavelength calibration. However, particularly in early versions of the FUSE calibration pipeline, the wavelength solution has been poor, with shifts in the position of spectral features seen between channels. Drift of the source in the aperture can also cause wavelength shifts in the same channel between exposures. There are a number of different apertures available for use on FUSE and these are listed in Table 4.2. Problems are encountered when thermal changes rotate the mirrors slightly, causing the target to move out of the aperture when the HIRS and MDRS modes were used, so virtually all observations have been carried out using the LWRS aperture. Loss of flux is still evident in some of the data, however. In this aperture the spectral resolution was found to be 20,000 for the LiF 1 channel, determined using molecular hydrogen lines in observations of the central star of the planetary

Table 4.2. FUSE apertures, adapted from the FUSE Instrument and Data Handbook (see http://fuse.pha.jhu.edu/analysis)

Aperture	Dimensions / arcsecs	Description
HIRS	1.25×20	High resolution
MDRS	2.0×20	High throughput
LWRS	30×30	Large square

nebula S 216. This is the only aperture and channel for which the resolution has been calculated.

FUSE has two modes for recording data – time-tagged event lists (ttag data) or as spectral image histograms (hist data). The advantage of ttag data is the time of arrival of each photon is known, so the count rate from the target at all times during the observation can be seen. The hist mode is used where the source is bright and too many events would be recorded in ttag mode. As FUSE is in a low-Earth orbit emission lines from the Earth's atmosphere are sometimes seen. The strongest of these 'airglow' lines is hydrogen-Lyman emission. These lines are not removed in the data reduction stage but instead are dealt with during the data analysis. A particular problem with FUSE spectra is the presence of the 'worm', which is a shadow cast by the electron repeller grid located above the detector surface, and manifests itself by a decrease in flux by up to 50%, particularly in the LiF 1B segment. The amount of flux loss varies according to whether the image produced by the grating coincides with the grid wires, and is also affected by the position of the target in the aperture and so cannot easily be removed by the calibration software. For this reason the section of the LiF 1B segment most affected by the worm is not used if any flux decrease is seen. In December 2001 FUSE lost two of its four reaction wheels. Since then the FUSE team have developed a new system for pointing the satellite using magnetic torquing and most of the sky is now again visible to FUSE. The reduced control over pointing means that occasionally the target can drift out of the aperture. In ttag mode the position of the target on the detector is recorded and corrected for. In hist mode only the time when the target was out of the aperture is known, and this is taken away from the exposure time.

4.4 FUSE data reduction

4.4.1 The CalFUSE pipeline

Raw FUSE data is first processed by the CalFUSE calibration software. This removes instrument effects, extracts the spectra and applies the flux and wavelength calibrations. Typically spectra downloaded from the archive have been processed using version 1.8.7 of the program. Version 2 of the program contains a number of improvements over 1.8.7, for example the heliocentric correction was being applied in the wrong direction, enhancing the wavelength shift caused by the Earths motion around the Sun, rather than removing it. Therefore the raw data were obtained and processed using a locally installed version of CalFUSE (version 2.0.5). The pipeline automatically accounts for spacecraft jitter, detects when FUSE has entered the south Atlantic anomaly, removes the effects of gain sag, removes the background etc. A full summary of the CalFUSE calibration software can be found on the FUSE website reference pages (http://fuse.pha.jhu.edu/analysis/pipeline_reference.html). Subsequently new versions of the pipeline have been released, and the most recently downloaded data have been processed using v2.4.0. There does not appear to be a significant difference between the calibrated spectra produced by the two versions.

4.4.2 Local pipeline

Data that has passed through the CALFUSE pipeline still requires some work before a final spectrum is produced. For each exposure there are 8 spectra for each aperture, representing the possible instrument channel/detector segment combinations, although only the data for the aperture in use contains a useful spectrum. A suite of IDL and FORTRAN programs were developed by myself, to take these files and produce a single combined spectrum. Obtaining the final product involves the following steps:

- The exposures for each segment are cross correlated, and a wavelength correction is calculated to account for drift between exposures.
- A co-added spectrum for each segment is then produced with each exposure weighted according to exposure time. If the target has drifted out of the aperture for any of the exposures then that exposure is not included.
- The spectrum for each segment is then inspected. The edges of the spectra are normally the noisiest, and have the poorest wavelength solution so these are removed.

If the worm is noticeable in a segment then the section of data with reduced flux is not used.

- The segments are cross correlated to find and correct for wavelength shifts. The spectra are shifted to line up with the LiF 1A segment, which is the segment used in the pointing of the satellite and should have the best flux and wavelength calibrations. In segments that cover the same wavelength range this is normally straightforward as there are heavy element and interstellar lines that can be used to line up the spectra. Where there is little overlap between segments this step is less certain, but measurement of the radial velocity of absorption features can be used to check the wavelength solution.

- The segments are then co-added onto a single wavelength scale, typically with 0.02 Å binning, which oversamples the true resolution by $\sim$2.5 times. The data are weighted according to their signal to noise, calculated over a running mean of 20 Å.

4.5 DAO white dwarfs observed by FUSE

Table 4.3 lists the objects for which FUSE data have been downloaded from the archive (http://archive.stsci.edu/mast.html). For a complete list of DAOs for which optical or far-UV data have been obtained, see Table 2.2.

A number of the objects have been observed more than once by FUSE. Table 4.4 gives the observation ID of each, along with exposure length. Observations that missed the target are not listed. Some objects were observed with an aperture used for measuring the background, and these are also not included. In the following chapters observations will be referred to by the name and observation number listed in the table.

Table 4.3. Objects in the FUSE sample.

Object	WD number	PN?	Binary?
S 216	WD 0441+467	√	
A 7	WD 0500-156	√	√?
HS 0505+0112	WD 0505+012		
PuWe 1	WD 0615+556	√	√?
RE 0720-318	WD 0718-316		√
TON 320	WD 0823+317		
PG 0834+500	WD 0834+501		√
A 31		√	
EGB 6	WD 0950+139		
NGC 3587			
HS 1136+6646	WD 1136+667		√
Feige 55	WD 1202+608		√
PG 1210+533	WD 1210+533		
LB 2	WD 1214+267		
HZ 34	WD 1253+378		
A 39		√	
NGC 6720			
NGC 6853	WD 1957+225		
RE 2013+400	WD 2013+400		√
	WD 2115+118		
DeHt 5	WD 2218+706	√	
NGC7 293	WD 2226-210		
GD 561	WD 2342+805	√	

Table 4.4. List of FUSE observations for the stars in the sample.

Object	Obs. no.	Obs. ID	Date	Start time	Length / ks	Aperture
S 216	1	I8190102000	14/02/2000	19:52	7.881	LWRS
	2	I8190103000	15/02/2000	07:30	7.932	LWRS
	3	I8190105000	16/02/2000	08:31	7.757	LWRS
	4	M1070402000	09/01/2001	17:37	3.381	MDRS
	5	M1070403000	09/01/2001	22:52	4.829	HIRS
	6	M1070404000	10/01/2001	15:28	6.246	LWRS
	7	M1070405000	23/01/2001	16:13	9.187	MDRS
	8	M1070406000	24/01/2001	03:36	9.191	HIRS
	9	M1070407000	25/01/2001	14:48	6.955	LWRS
	10	M1070408000	25/01/2001	19:58	6.285	MDRS
	11	M1070409000	26/01/2001	04:13	5.805	HIRS
	12	P1041002000	22/01/2000	07:13	118.352	MDRS
	13	P1041003000	22/01/2000	17:03	13.731	LWRS
A 7		B0520901000	05/10/2001	09:00	11.525	LWRS
HS 0505+0112		B0530301000	02/01/2001	08:48	7.303	LWRS
PuWe 1	1	B0520701000	11/01/2001	01:30	6.479	LWRS
	2	S6012201000	15/02/2002	22:35	8.194	LWRS
RE 0720-318		B0510101000	13/11/2001	08:48	17.723	LWRS
TON 320		B0530201000	21/02/2001	20:09	9.378	LWRS
PG 0834+500		B0530401000	04/11/2001	18:33	9.394	LWRS
A 31		B0521001000	25/04/2001	08:31	8.434	LWRS
EGB 6	1	A0340101000	08/01/2000	13:30	11.546	LWRS
	2	A0341101000	08/05/2000	20:20	9.485	LWRS
NGC 3587		B0520501000	23/03/2001	14:20	10.209	LWRS
HS 1136+6646	1	B0530801000	12/01/2001	20:31	6.217	LWRS
	2	S6010601000	29/01/2002	15:33	7.879	LWRS

Table 4.4. continued...

Object	Obs. no.	Obs. ID	Date	Start time	Length / ks	Aperture
Feige 55	1	P1042101000	26/02/2000	12:00	13.763	MDRS
	2	P1042105000	29/12/1999	14:31	19.638	MDRS
	3	S6010101000	28/01/2002	18:05	10.486	LWRS
	4	S6010102000	31/03/2002	15:00	11.907	LWRS
	5	S6010103000	01/04/2002	07:35	11.957	LWRS
	6	S6010104000	01/04/2002	23:03	12.019	LWRS
PG 1210+533		B0530601000	13/01/2001	00:05	4.731	LWRS
LB 2		B0530501000	14/02/2001	19:02	9.197	LWRS
HZ 34		B0530101000	16/01/2001	19:56	7.593	LWRS
A 39		B0520301000	26/07/2001	10:41	6.879	LWRS
NGC 6720		B0690201000	08/06/2001	13:35	28.364	LWRS
NGC 6853	1	M1070301000	23/09/2000	03:45	16.113	MDRS
	2	M1070302000	24/09/2000	04:41	16.411	HIRS
	3	M1070303000	28/05/2001	19:05	7.561	LWRS
	4	M1070304000	29/05/2001	01:01	7.514	MDRS
	5	M1070305000	29/05/2001	12:16	7.750	HIRS
	6	P1043301000	05/06/2000	08:03	16.732	LWRS
	7	M1070306000	28/07/2001	13:07	7.445	LWRS
	8	M1070307000	28/07/2001	17:54	7.169	MDRS
	9	M1070308000	29/07/2001	04:24	7.092	HIRS
	10	M1070309000	01/08/2001	00:22	7.668	LWRS
	11	M1070310000	01/08/2001	06:39	6.920	MDRS
	12	M1070311000	01/08/2001	13:18	6.332	HIRS
	13	M1070313000	31/10/2002	05:31	8.451	MDRS
	14	M1070319000	03/11/2002	05:03	3.092	HIRS
RE 2013+400		P2040401000	10/11/2000	02:26	11.483	LWRS
HS 2115+1148		C0960101000	02/07/2002	16:58	10.167	LWRS
DeHt 5		A0341601000	15/08/2000	18:39	6.055	LWRS
NGC 7293	1	P1980202000	11/10/2001	23:15	5.085	HIRS
	2	C1770401000	02/10/2002	14:20	8.747	LWRS
GD 561		B0520401000	08/09/2001	17:15	5.365	LWRS

Chapter 5

Molecular hydrogen absorption in FUSE spectra

5.1 Introduction

Molecular hydrogen (H_2) is probably the most abundant material in the universe by mass after atomic hydrogen, helium and their ions (Shull & Beckwith, 1982). It has been observed in a large number of the observations made by FUSE and the width of the narrow H_2 lines have been used to find the wavelength resolution of the LWRS aperture. However, the H_2 attenuates significant flux and masks out features in the spectrum of a target. This chapter aims to measure the H_2 in the observations of DAO white dwarfs and CSPN observed by FUSE. Once the H_2 absorption is accounted for, the white dwarf spectra can be analysed.

Useful reviews of the physics behind the formation and existence of molecular hydrogen can be found in Shull & Beckwith (1982) and Duley & Williams (1984). The following summarises the relevant information for this work from those texts.

5.1.1 Formation of molecular hydrogen

Although it had been predicted that H_2 might exist in interstellar space since the 1930s, it wasn't until a sounding rocket carrying a UV spectrometer was flown in 1970 that it was actually detected, in the line of sight towards ξ Persei. The Copernicus satellite, launched in 1972, showed that H_2 was common in the interstellar medium, and that it seemed to coincide with obscured lines of sight. Hydrogen is very abundant in the interstellar medium, and so it might be expected that interactions between H atoms would result in the H_2 that is seen. However, in a gas phase reaction the molecule is formed in an excited state and it is unlikely that it will stabilise, through emission of a photon, before the molecule dissociates. Other, similar reactions have the same problem. Since H_2 is dissociated by the interstellar radiation field at a much higher rate than that with which it is formed due to these reactions, this route must be relatively insignificant in the creation of the interstellar H_2. An alternative way that H_2 could be formed is on the surface of grains. A hydrogen atom collides with and sticks to a grain and is held there until another atom is adsorbed. Once the molecule is formed the excess energy is distributed between ejecting the molecule from the grain, rotational-vibrational excitation and the grain itself. Through this mechanism it is possible to form H_2 at a high enough rate to explain the amount seen in the interstellar medium, and also accounts for the fact that it is seen in regions that are obscured by dust.

H_2 is also observed within planetary nebulae, in dense patches called cometary knots. These knots occur within the region ionised by the central star. The H_2 can be detected through observations in the infra-red at $2.12\,\mu$m, for example in the Helix Nebula (NGC7293) (O'Dell & Handron, 1996) and the Ring Nebula (NGC6720) (Speck et al., 2003), with shocked gas regions and excitation by UV and X-rays from the central stars in photodissociation regions competing to explain this emission.

5.1.2 Rotational excitation of H_2

Vibrational excitation of H_2 will only occur in shocked regions of the interstellar medium or in regions exposed to a large UV field, due to the large energy required. Rotationally excited states, though, are seen through electronic transitions in the H_2 Lyman and Werner bands that lie at wavelengths less than 1120Å and which therefore fall within the FUSE wavelength range. The strongest absorption lines are caused by the J = 0 and 1 rotational levels, the relative populations of which are determined from thermal proton collisions. The ratio of column densities between the two levels is given by:

$$\frac{N(J=1)}{N(J=0)} = \frac{g_1}{g_0} exp - \left(\frac{E_{0\to 1}}{kT}\right)$$

where g_0 and g_1 are the statistical weights of the J = 0 and 1 rotational states respectively. The levels with odd rotational quantum number (J) are nuclear triplet states (ortho-hydrogen), and have statistical weight $g_J = 3(2J+1)$ in the ground state. Levels with even J are singlet states (para-hydrogen) and have $g_J = (2J+1)$. $E_{0\to 1}$ is the sepa-

Table 5.1. Rotational energy levels and statistical weights of H_2 in the ground vibrational state, adapted from Duley & Williams (1984).

J	E(J) / eV	g_J
0	0.000	1
1	0.015	9
2	0.044	5
3	0.087	21
4	0.145	9
5	0.216	33
6	0.299	13
7	0.395	45

ration of the J = 0 and 1 energy levels – Table 5.1 lists the energy levels and statistical weights of the rotational levels up to J = 7. k is the Boltzmann constant and T is the kinetic temperature, which is typically $\sim$80 K for a diffuse cloud. The distribution of the populations of higher-J levels is dominated by collisions, excitation during formation and UV pumping. These populations can also be described by a Boltzmann distribution, but with a temperature that must be higher than the kinetic temperature if these high J states are to be seen. Measurements of the column densities of the individual rotational states therefore allow a 'kinetic' and an 'excitation' temperature to be determined from the above relationship.

5.1.3 The Doppler parameter

The movement of the H_2 molecules will modify the profile of the absorption lines and must be taken into account when measuring column densities. The absorption energy of an electronic transition in a molecule that is moving away from the observer will be red-shifted relative to the rest frame and similarly molecules moving in the opposite direction will be blue-shifted. This reduces the depth of the absorption line, but also broadens it. The speed of movement of molecules in a cloud that does not experience external forces will relax into a Maxwellian distribution. Therefore, in addition to a column density, H_2 absorption is parameterised with the Doppler parameter $b = \frac{2kT}{m_{H_2}}$. Unfortunately the observer only has a two dimensional view of the H_2 absorption, and this may incorporate a number of different interstellar clouds that have different temperatures and Doppler parameters, so results can only be an average of the absorption from all the material in the line of sight.

5.2 Measurements of molecular hydrogen

Two methods are generally used for measuring molecular hydrogen absorption - curve of growth fitting and line profile fitting. Curve of growth fitting is the most commonly used and involves measuring the equivalent width (W_λ) of a number of lines and plotting a graph of log $\left(\frac{W_\lambda}{\lambda}\right)$ against log $(Nf\lambda)$, where λ is the central wavelength of the line, N the column density of the measured material and f the oscillator strength. N is not known, so the method relies on constructing theoretical curves of growth with different Doppler parameters and shifting the data points along the x-axis until a good fit with the theoretical curves is found. The blending of lines can make this inaccurate and it is often difficult to constrain the Doppler parameter closely. Line profile fitting can be more difficult than using a curve of growth as it requires a large grid of accurate models. The advantage, however, is that it is easier to constrain the Doppler parameter, can cope with blended lines, and can also give an indication of the goodness of fit that has been achieved. Line profile fitting has therefore been used in this work.

5.3 Models

To parameterise the H_2 in the line of sight towards the DAO white dwarfs the data must be compared to theoretical models. In addition to the H_2 absorption, an extinction model to account for obscuration due to dust is used. The models are described in the following sections.

5.3.1 Extinction model

The model of UV interstellar extinction was taken from Seaton (1979), who used observations by the OAO-2, Copernicus and TD-1 satellites to obtain an analytical expression for the absorption. If x is defined as $x = \frac{1}{\lambda}$ (wavelength λ in microns) then interstellar absorption in the range $7.14 \leq x \leq 10$ (i.e. 1000 - 1400Å) is given by:

$$A_\lambda = E_{B-V}\left(16.17 - 3.20x + 0.2975x^2\right)$$

where A_λ is the extinction in magnitudes at wavelength λ and E_{B-V} is the difference in extinction between the wavelengths of the B and V filters, also in magnitudes. A_λ can easily be converted into a decrease in flux using the standard definition of magnitudes. The extinction model therefore requires only one variable parameter, E_{B-V}.

5.3.2 H_2 models

The H_2 models used to fit the data were developed by Stephan McCandliss for use in analysing FUSE data (McCandliss, 2003). Templates are provided with Doppler parameter in the range b = 1 - 20 km s^{-1} and rotational states J = 0 - 15. The models have 0.01 Å sampling, which means that the templates with b = 1 km s^{-1} are undersampled and cannot be used for quantitative analysis. Column densities of up to 10^{21} cm^{-2} can be used for each rotational state and Doppler parameter, and these can be added together to form absorption spectra with many components. Figure 5.1 illustrates the transmission of far-UV flux through columns of 10^{18}-10^{21} cm^{-2}, produced from these models. Below a column density of 10^{19} the individual lines can mostly be resolved, but above this the line blending is severe and can obscure the hydrogen Lyman lines in the spectrum of the white dwarf that we wish to observe. The models were converted into multiplicative table models that can be used in the spectral analysis package XSPEC. A separate model was created for each rotational state, each having two variable parameters - the Doppler parameter, which can vary between 2 and 20 km s^{-1} and log (column density), varying between 10 and 21. As the models consist of multiplication factors between 0 and 1, corresponding to the proportion of flux that will be transmitted at each wavelength, more complicated models, incorporating many different rotational states, can be formed by multiplying the models together.

5.4 Fitting technique

As the background source in all the H_2 spectra is a white dwarf, care must be taken to only fit the H_2 absorption lines and not to allow the neutral hydrogen Lyman lines or heavy element absorption lines that come from the white dwarf to interfere with the fit. Three spectral ranges were chosen - these were: 1045-1065Å, 1090-1120Å and 1140-1150Å. Choosing only wavelengths above 1045Å avoids the white dwarf's Lyman lines. The section between 1065 and 1090Å is normally very noisy because only one FUSE segment falls in that wavelength range and so it is not used. The majority of the H_2 lines fall below 1120Å and so that is used as the upper limit for the second range. Unless the column density is extremely high no H_2 lines are seen in the third range. Instead this is used to normalise the white dwarf model. XSPEC is used to perform the fitting, which finds the best fitting set of parameters by minimising the χ^2 statistic. Initially a white dwarf atmospheric model is added, to provide the continuum level for the H_2 fits. The parameters for the white dwarf model are taken from the fits

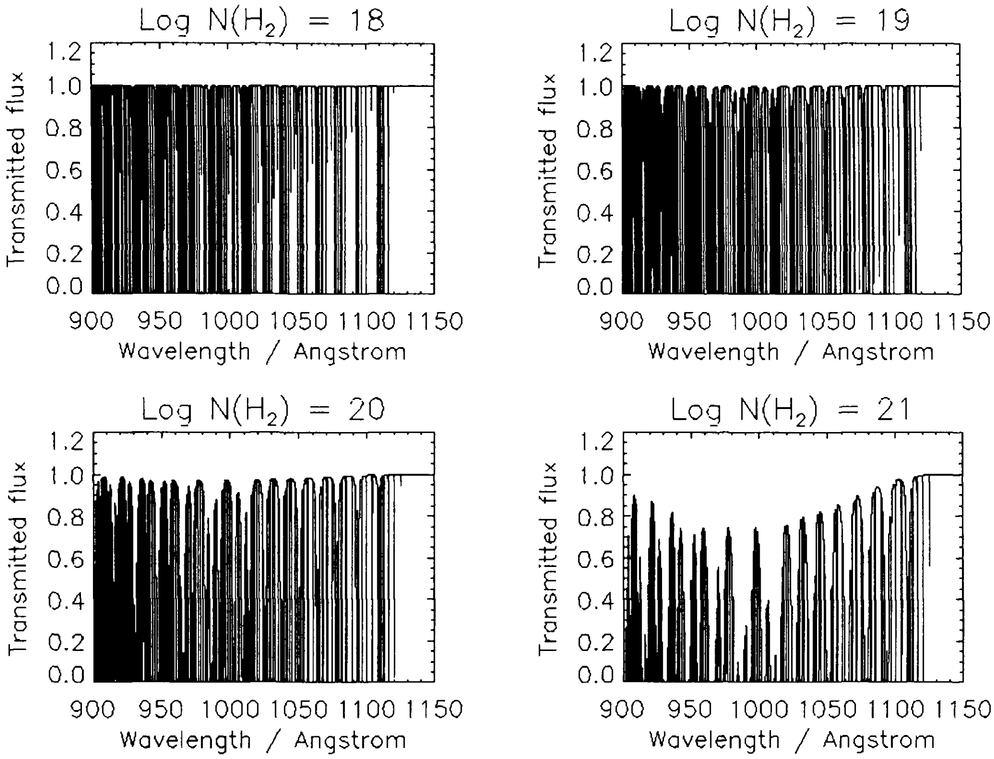

FIGURE 5.1. The proportion of flux transmitted when passing through molecular hydrogen with varying column density.

to optical data (see Chapter 3) or from the literature, and were constrained to within 1σ error limits where they are available. The interstellar extinction model is then added and sections of data containing photospheric heavy element lines in the white dwarf model are ignored. First, two H_2 components are added, with J = 0 and 1. These are by far the strongest H_2 lines seen in all the spectra. XSPEC is then allowed to find the best fitting parameters. After that components are added one at a time with higher values of J. The Doppler parameter is assumed to be the same for all components so the addition of each rotational level adds only a single free parameter to the fit. Rotational levels are added until lines due to that state cannot be seen, and adding new levels does not produce an improvement in the χ^2_{red} at the 99% confidence level, determined from the F-test. Ideally a good fit to the data produces a χ^2_{red} of $\sim$1, however due to the complicated nature of what is being fit – for example there may be multiple clouds of H_2 in the line of sight, and the fact that the atmospheric model will not perfectly reproduce the white dwarf spectrum due to the Balmer/Lyman temperature problem (Barstow et al., 2003b and see also later chapters), a χ^2_{red} of 2-3 was taken to be satisfactory for this work. After the H_2 components have been added, any remaining absorption lines due to heavy elements

Table 5.2. Objects where H_2 was not detected.

Object
HS 0505+0112
RE 0720-318
NGC 3587
HS 1136+6646
Feige 55
PG 1210+533
LB 2
RE 2013+400

in the white dwarf atmosphere or other interstellar absorption are then ignored from the final fit. 1σ errors were then obtained using the $\Delta\chi^2$ distribution with the required number of free parameters, depending on the number of rotational levels of H_2 used. As a χ^2_{red} of 1 was not achieved in some cases, these errors may be underestimated. In some cases a satisfactory fit was not obtained using a single set of H_2 models that had the same value for the Doppler parameter. Additional components were added to improve the fit to these spectra – this is discussed in detail in section 5.5.2.

5.5 Results and analysis

H_2 was not detected in the spectra of a number of the DAOs and these are listed in Table 5.2. At the signal to noise of the FUSE data this places an upper limit on the H_2 column density of 10^{13}-10^{14} cm^{-2}. Most of the spectra were fit with models that shared the same Doppler parameter, and these are described in section 5.5.1. Those requiring H_2 models with different Doppler parameters are then discussed in section 5.5.2.

5.5.1 Single component fits

Table 5.3 lists the parameters obtained for those objects for which satisfactory fit has been obtained using a single value for the Doppler parameter. Multiple observations exist for one object - EGB 6. Unfortunately the first observation of EGB 6 couldn't be used as the data above 1120 Å were poor. As the wavelength resolution of FUSE is ~0.05 Å, if the Doppler parameter b $< \sim$7 km s^{-1} the broadness of the H_2 lines will be mostly due to the instrument response. However, the depth of the lines will also be affected by the broadening so it is possible to measure b more accurately than that, as long as the

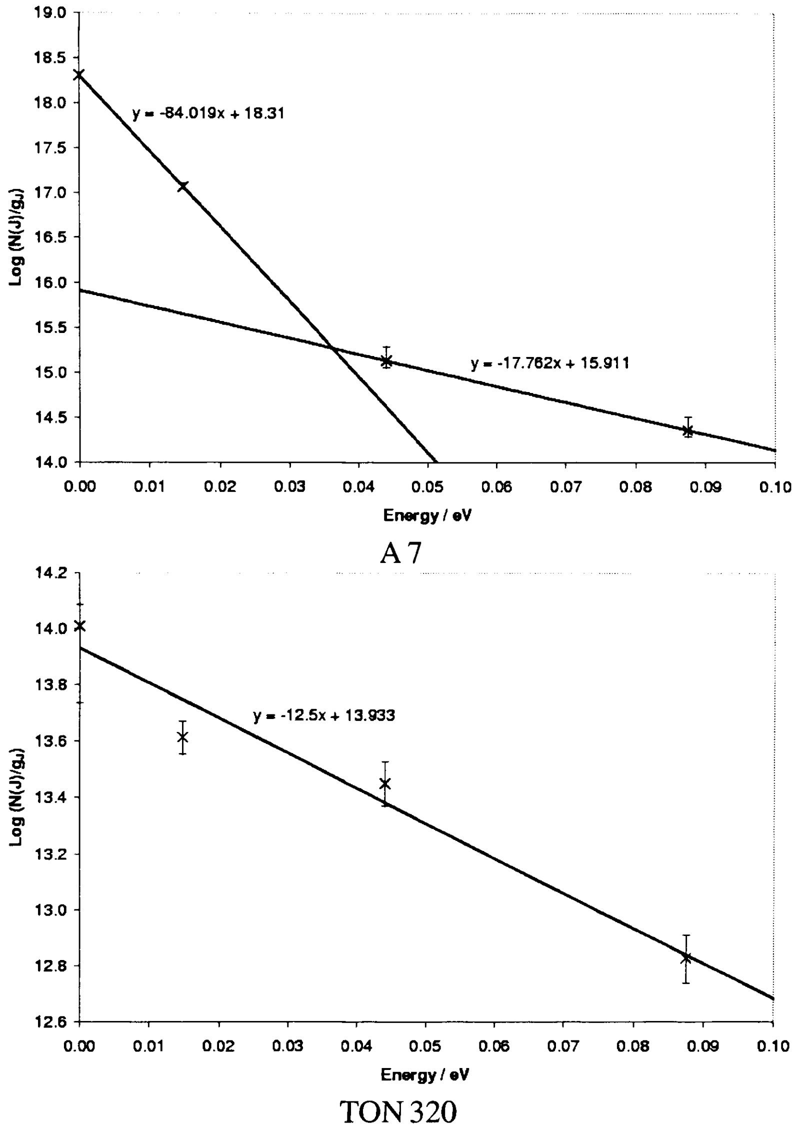

FIGURE 5.2. Plots showing the Boltzmann distributions of the objects fitted using a single Doppler parameter. The equations of the lines through the points were calculated using linear regression and these are shown on the plots.

absorption lines are not saturated. Figure 5.2 shows the column densities divided by the statistical weight for each rotational level, against the rotational level energy. Since the population of the levels have a Boltzmann distribution, the J = 0 and 1 states can be fitted with a single straight line, and the higher J states with a second line. In some cases a single line can be drawn through all the points.

Table 5.3. Table of results - single component fits

Object	E(B-V)	b / km s^{-1}	Log column density, J =					Source of WD parameters
			Total	0 4	1 5	2 6	3 7	
A 7	$0.003^{+0.006}_{-0.003}$	$2.09^{+0.12}_{-0.09}$	$18.49^{+0.03}_{-0.01}$	$18.31^{+0.04}_{-0.02}$	$18.03^{+0.04}_{-0.02}$	$15.83^{+0.16}_{-0.12}$	$15.68^{+0.14}_{-0.07}$	1
TON 320	$0.001^{+0.015}_{-0.001}$	$13.80^{+2.34}_{-2.52}$	$14.88^{+0.04}_{-0.06}$	$14.01^{+0.08}_{-0.25}$	$14.57^{+0.06}_{-0.06}$	$14.15^{+0.08}_{-0.08}$	$14.15^{+0.08}_{-0.09}$	1
PG 0834+500	$0.000^{+0.010}_{-0.000}$	$2.35^{+0.08}_{-0.15}$	$18.17^{+0.03}_{-0.05}$	$17.74^{+0.06}_{-0.03}$	$17.96^{+0.04}_{-0.07}$	$15.95^{+0.09}_{-0.14}$	$15.30^{+0.12}_{-0.10}$	1
A 31	$0.046^{+0.009}_{-0.011}$	$2.82^{+0.09}_{-0.18}$	$18.76^{+0.03}_{-0.02}$	$18.39^{+0.03}_{-0.06}$	$18.42^{+0.03}_{-0.04}$	$17.62^{+0.06}_{-0.11}$	$17.48^{+0.10}_{-0.07}$	1
EGB 6 obs 2	$0.028^{+0.009}_{-0.003}$	$8.48^{+0.60}_{-0.42}$	$15.63^{+0.04}_{-0.03}$	$14.86^{+0.03}_{-0.09}$	$15.46^{+0.05}_{-0.04}$	$14.69^{+0.07}_{-0.07}$	$14.33^{+0.11}_{-0.12}$	1

1 From optical chapter

Table 5.3. continued...

Object	E(B-V)	b / km s^{-1}	Log column density, J =					Source of
			Total	0	1	2	3	WD parameters
				4	5	6	7	
HZ 34	$0.034^{+0.008}_{-0.006}$	$18.94^{+1.06}_{-3.42}$	$14.31^{+0.29}_{-0.44}$	$14.01^{+0.08}_{-0.27}$	$14.40^{+0.07}_{-0.05}$			1
A 39	$0.053^{+0.016}_{-0.009}$	$3.71^{+0.23}_{-0.24}$	$19.93^{+0.02}_{-0.04}$	$19.59^{+0.04}_{-0.03}$	$19.64^{+0.03}_{-0.08}$	$18.19^{+0.07}_{-0.07}$	$17.86^{+0.14}_{-0.15}$	1
				$15.13^{+0.26}_{-0.24}$				
NGC 6720	$0.056^{+0.009}_{-0.004}$	$3.35^{+0.08}_{-0.09}$	$19.21^{+0.02}_{-0.00}$	$18.72^{+0.03}_{-0.02}$	$19.01^{+0.02}_{-0.01}$	$17.78^{+0.06}_{-0.06}$	$17.50^{+0.05}_{-0.07}$	2
				$14.73^{+0.13}_{-0.08}$				
WD 2115+118	$0.000^{+0.005}_{-0.000}$	$2.00^{+0.16}_{-0.00}$	$18.82^{+0.04}_{-0.02}$	$18.15^{+0.09}_{-0.05}$	$18.69^{+0.05}_{-0.03}$	$17.50^{+0.10}_{-0.13}$	$16.56^{+0.14}_{-0.29}$	3
DeH t5	$0.1863^{+0.020}_{-0.015}$	$4.58^{+0.24}_{-0.17}$	$20.07^{+0.03}_{-0.02}$	$19.74^{+0.05}_{-0.04}$	$19.79^{+0.04}_{-0.03}$	$17.91^{+0.21}_{-0.29}$	$17.68^{+0.21}_{-0.18}$	1
				$16.54^{+0.29}_{-0.30}$	$16.52^{+0.34}_{-0.34}$	$15.39^{+0.25}_{-0.25}$	$15.47^{+0.19}_{-0.18}$	
NGC 7293	$0.009^{+0.005}_{-0.009}$	$3.23^{+0.05}_{-0.05}$	$17.81^{+0.03}_{-0.04}$	$17.58^{+0.02}_{-0.06}$	$17.41^{+0.06}_{-0.02}$	$15.91^{+0.04}_{-0.06}$	$15.06^{+0.12}_{-0.06}$	2

1 From optical chapter

2 Napiwotzki & Schönberner (1995)

3 No physical information available, so used $T_{\rm eff}$ = 65,000 K, log g = 7.0 and He/H = $10^{-2.5}$

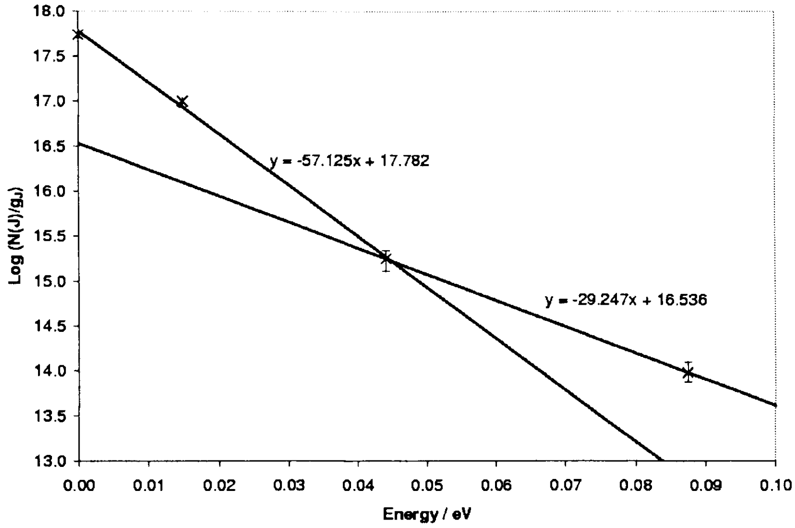

PG 0834+500

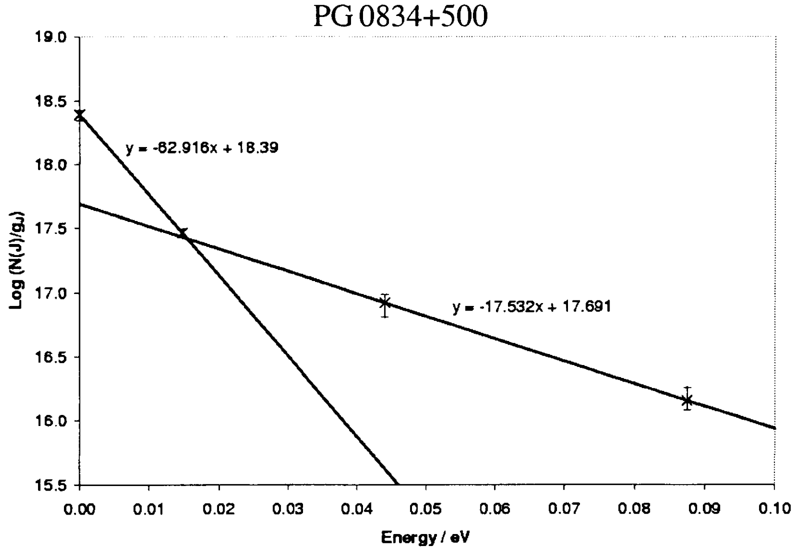

A 31

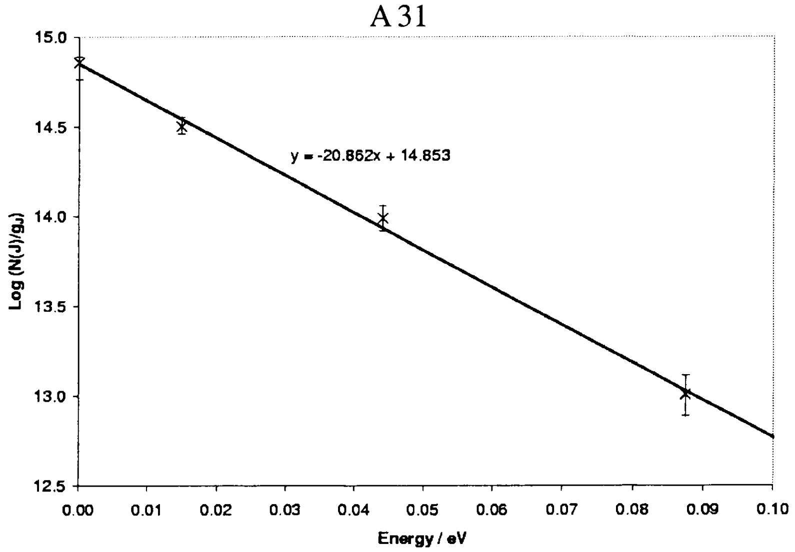

EGB 6 obs 2

FIGURE 5.2. continued...

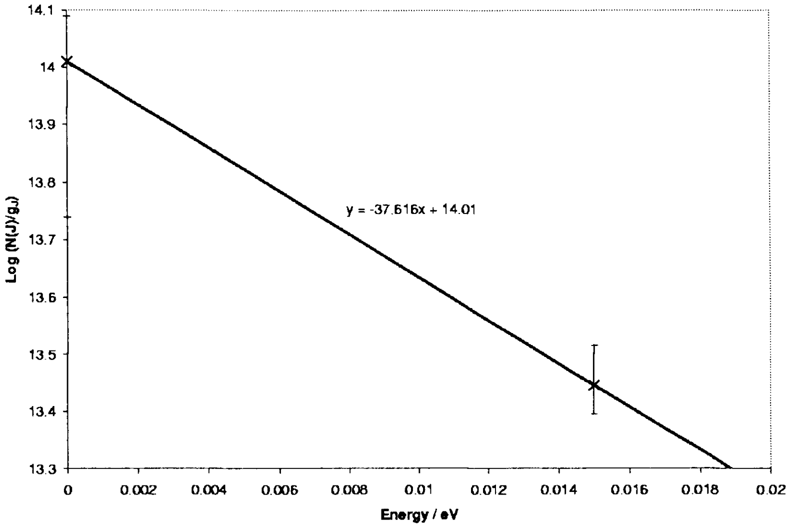

HZ 34

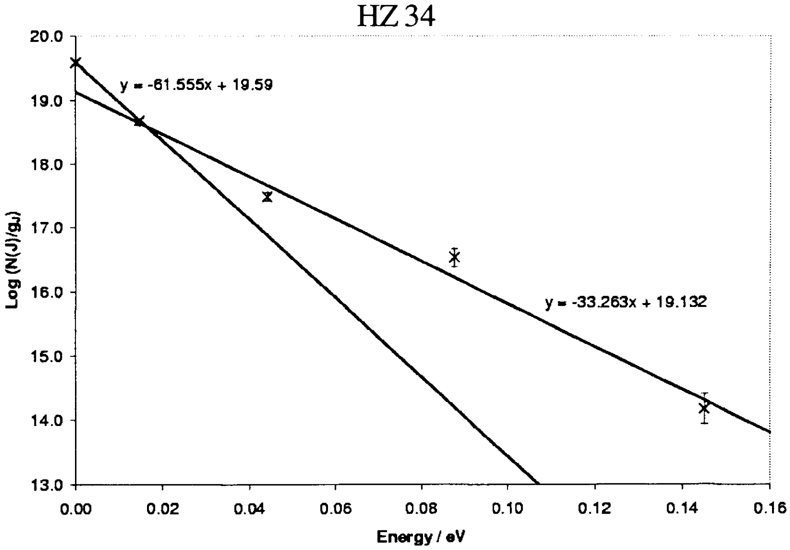

A 39

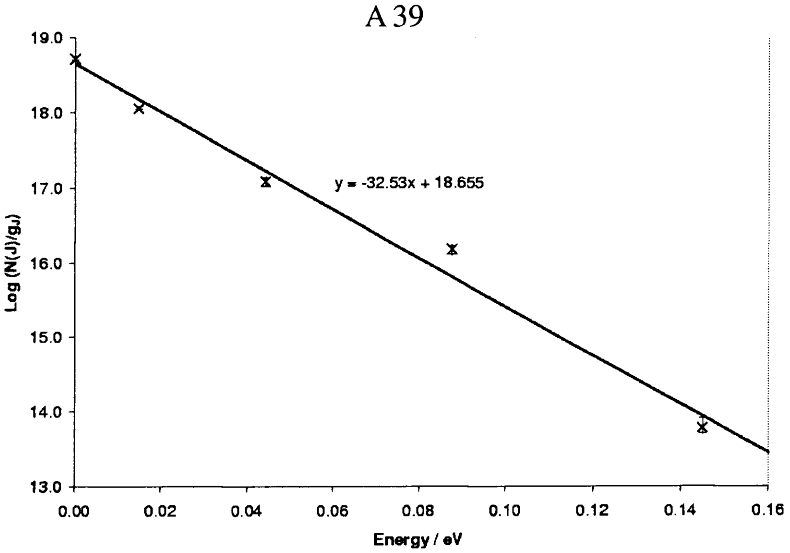

NGC 6720

FIGURE 5.2. continued...

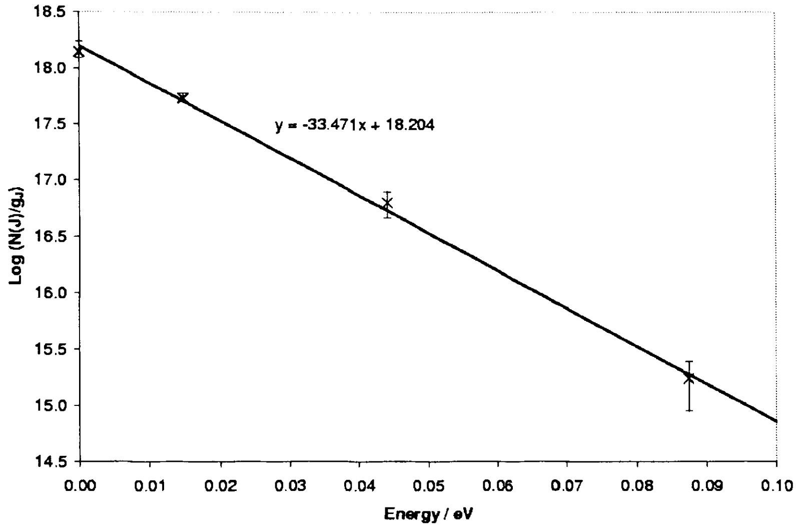

WD 2115+118

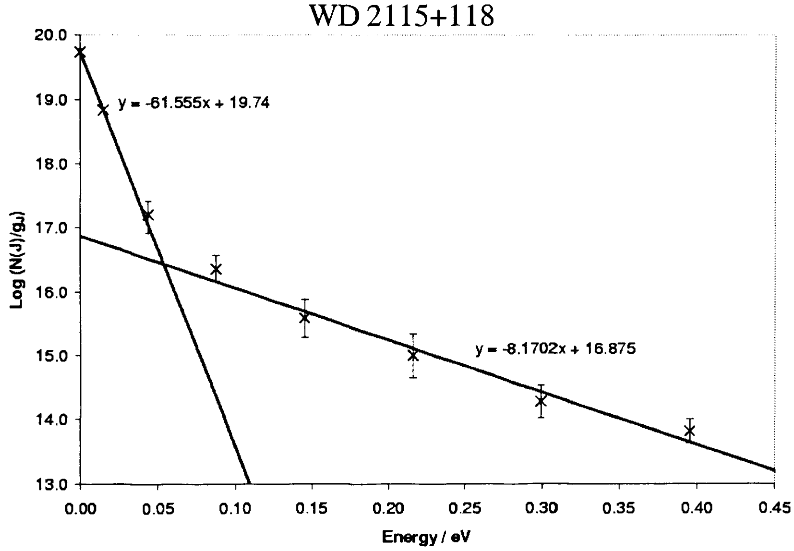

DeHt 5

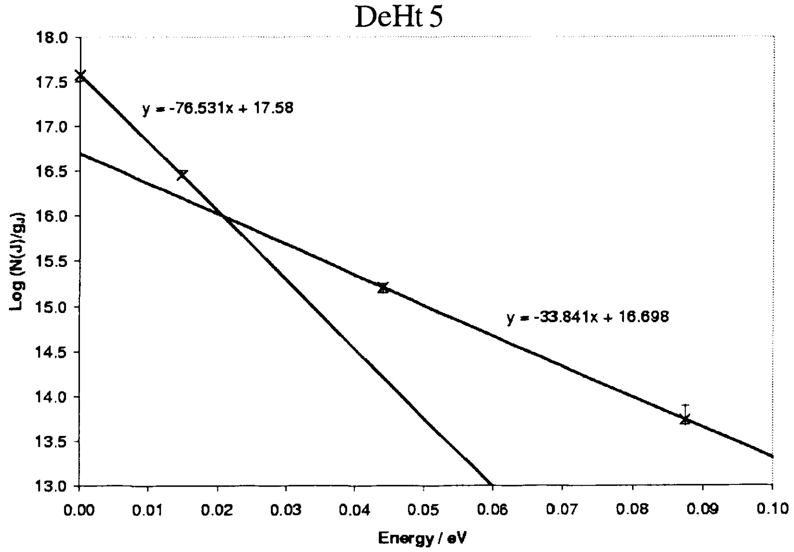

NGC 7293

FIGURE 5.2. continued...

Table 5.4. Kinetic and excitation temperatures.

Object	b / $km\,s^{-1}$	Kinetic temperature / K	Excitation temperature / K
A 7	2.1	60	234
TON 320	13.8	403	-
PG 0834+500	2.4	88	172
A 31	2.8	80	287
EGB 6 obs 2	8.5	242	-
HZ 34	18.9	131	-
A 39	3.7	82	152
NGC 6720	3.4	155	-
WD 2115+118	4.6	151	-
DeHt 5	4.6	82	617
NGC 7293	3.2	96	149

Kinetic and excitation temperatures

From the gradient of the lines the kinetic and excitation temperatures can be calculated. These are listed in Table 5.4.

Rotational levels up to J = 7 are seen in the spectrum of DeHt 5, hence it must have an extremely high excitation temperature. High population of the upper J levels can be due to UV excitation, so it may be that these are diffuse clouds that are close to the white dwarf. The objects where the level populations can be fitted with a single temperature tend to have a high Doppler parameter. If the Doppler parameter, is high the velocities of the molecules must also be high, and hence in these cases collisional excitation might be dominating over UV excitation. The results from neither the Ring or Helix Nebulae observations (NGC 6720 and NGC 7283 respectively) appear to show any evidence that the H_2 absorption is associated with the planetary nebula.

5.5.2 Two component fits

NGC 6853 (M 27)

NGC 6853 is unique in this sample in having two distinguishable H_2 clouds in the line of sight. The lines due to each are separated by about 45 $km\,s^{-1}$ (McCandliss et al., 2000) and the Doppler parameters are low so the distributions are easy to resolve. NGC 6853 has been observed many times by FUSE. Only observations that use the LWRS aperture

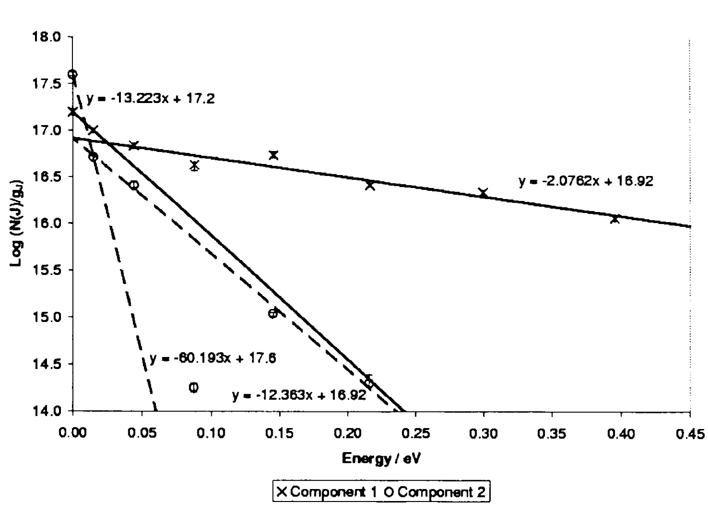

FIGURE 5.3. Populations of the rotational levels of the combined LWRS spectra of NGC6853 up to J = 7. The solid lines are trend lines for component 1, dashed line for component 2.

are analysed here, since for these the wavelength resolution is known. All the LWRS observations were combined together, with a cross-correlation used to make sure the exposures lined up. This produced a very high signal-to-noise spectrum from which rotational levels up to J = 14 could be identified in one of the clouds. The results are shown in Table 5.5, with the cloud with the high J levels called component 1, the other component 2. The two components were separated by a redshift of $\sim 1.4 \times 10^{-4}$, which corresponds to a velocity of ~43 km s^{-1}.

Simultaneously fitting such a large number of parameters is very difficult, and the column density for the J = 3 rotational level of component 2 can be seen to be clearly unreasonable when the results are plotted (Figure 5.3). The most likely explanation of this is that the lines due to this level coincide with other lines, making the column density difficult to measure. Unfortunately, the final χ^2_{red} for the fit was extremely high (~60). This was partly due to the high signal-to-noise, since a slight deviation of the model from the data produced a large χ^2 for that wavelength bin. The Doppler parameter for one component was below the model limit of 2 so a number of the absorption features were fitted with lines that were too broad, and the fits to both components will have been very sensitive to the assumed resolution of the data. Fitting individual observations of NGC6853 gave an improved χ^2_{red} as the data was noisier. It was not possible to identify as many rotational levels, however, and the results did not agree well with the combined observation, probably because the lines that were being fit were blended.

Table 5.5. Results from the H_2 fit to the combined LWRS FUSE spectrum of NGC6853.

E(B-V)	Component	b / km s^{-1}	Log column density, J =				
			Total	0	1	2	3
				4	5	6	7
				8	9	10	11
				12	13	14	
				0	1	2	3
				4	5		
$0.001^{+0.008}_{-0.001}$	1	$2.86^{+0.02}_{-0.03}$	$18.68^{+0.01}_{-0.02}$	$17.20^{+0.03}_{-0.03}$	$17.96^{+0.02}_{-0.03}$	$17.54^{+0.03}_{-0.03}$	$17.96^{+0.03}_{-0.07}$
				$17.70^{+0.03}_{-0.03}$	$17.94^{+0.04}_{-0.02}$	$17.46^{+0.02}_{-0.04}$	$17.72^{+0.02}_{-0.04}$
				$16.71^{+0.03}_{-0.11}$	$17.23^{+0.02}_{-0.03}$	$15.26^{+0.04}_{-0.04}$	$15.58^{+0.04}_{-0.05}$
				$14.16^{+0.05}_{-0.04}$	$14.28^{+0.04}_{-0.04}$	$13.33^{+0.10}_{-0.10}$	
	2	$2.00^{+0.00}_{-0.00}$	$18.01^{+0.01}_{-0.02}$	$17.60^{+0.02}_{-0.02}$	$17.67^{+0.01}_{-0.03}$	$17.11^{+0.05}_{-0.02}$	$15.58^{+0.05}_{-0.06}$
				$16.00^{+0.01}_{-0.02}$	$15.82^{+0.10}_{-0.04}$		

White dwarf parameters obtained from Napiwotzki & Schönberner (1995).

Remaining objects

Fitting the remainder of the objects observed by FUSE with a single Doppler parameter did not give a satisfactory result. The broad J = 0 and 1 features are always predicted to be too narrow at the core of the lines while the wings are too wide. The higher J lines are not broad enough to be able to see if the same problem affects them. Adding in extra components with J = 0 and 1 with a lower Doppler parameter improves the fit. For example, Figure 5.4 shows a section of GD561 with a single (red) and dual (green) Doppler parameter fit overlaid. The χ^2_{red} for the dual fit is better than for the single fit by ~0.4. Table 5.6 lists the parameters obtained with these two component fits, and Figure 5.5 shows the log $\frac{N(J)}{g_J}$ vs energy distributions for each of the objects. As for the single component fits, lines are drawn through the points, although there is no reason to expect a Boltzmann distribution in these cases unless these models reflect the true physical situation. S 216 has been observed many times and a combined LWRS spectrum is used to fit the H_2 here. It is clear with this high signal to noise data that even adding the components with lower Doppler parameter, it is still not possible to accurately reproduce the data and so these results are only a parameterisation.

Possible explanations for the line profiles

The approach of using two components with different Doppler parameters could be a reflection of the true physical situation if there are two H_2 clouds in the line of sight with similar redshifts but different Doppler parameters, or different temperatures. An example of such a situation might be if part of the H_2 cloud is heated by the white dwarf. These fits still do not seem to reproduce the observed data fully, which may just be indicative of the complexity of the situation, for example there may be a range of temperatures and velocities of H_2 molecules. Other causes of discrepancies between the models and the data might be problems with the models themselves, or heavy element absorption that is not resolved by FUSE which is changing the line profiles, although this seems unlikely as the problem is seen in a number of absorption lines and appears to be symmetrical, occurring on both sides of the line profile. The H_2 models came from an exterior source and it is difficult to check their accuracy, but they produce good matches to the data for the objects with single component fits. Another explanation may be that the velocities of the H_2 molecules are not in random motion, for example if they are contained within circumstellar material. Then, the core of the line might be deeper and the wings less broad. This is demonstrated in Figure 5.6. Rotational levels up to J = 7 are seen in all these objects suggesting proximity to a UV source. Unfortunately it is not possible

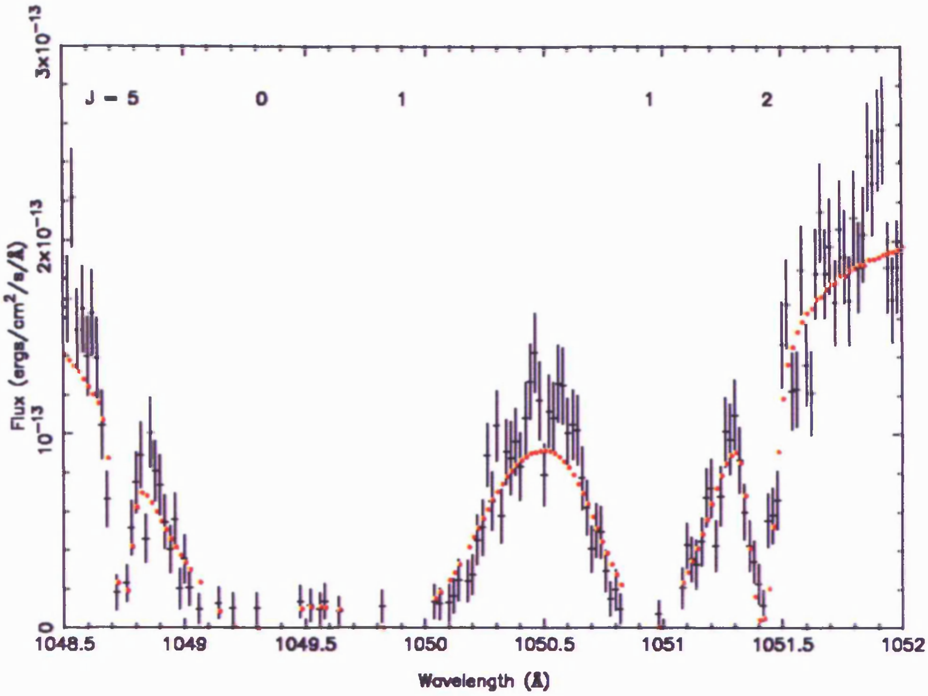

DeHt 5

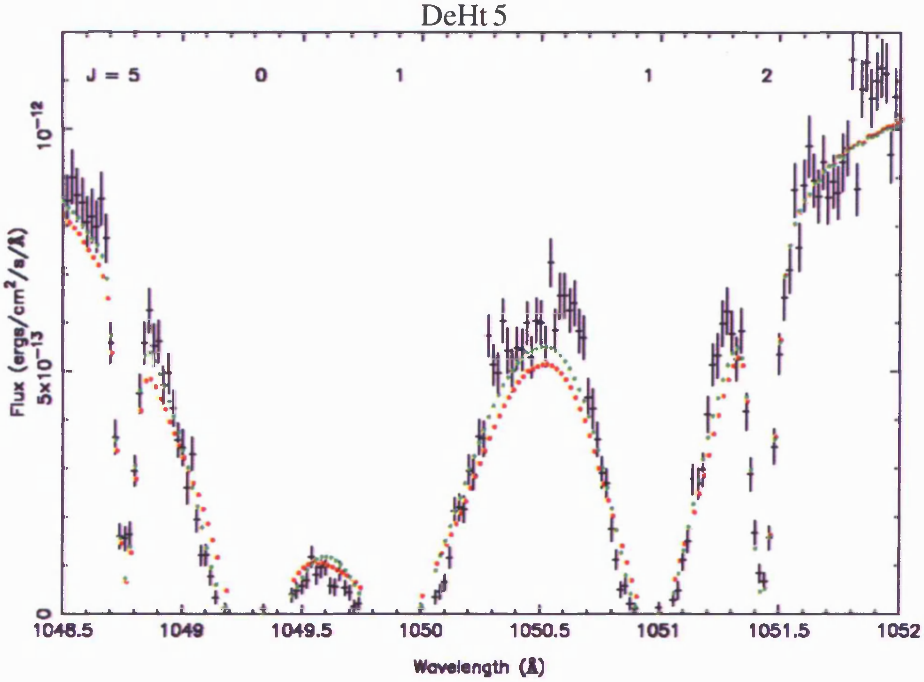

GD 561

FIGURE 5.4. A section of the FUSE spectra of DeHt 5 and GD561. The two have similar total column densities and in both rotational levels up to J = 7 are seen. The red dots are a white dwarf model absorbed by H_2 rotational levels that all share the same Doppler parameter. This reproduces the spectrum of DeHt 5 reasonably well (χ^2_{red} = $\sim$1.6), but not so well for GD561 ($\chi^2_{red} > 3$). The green dots overlaid on the spectrum of GD561 have additional J = 0 and 1 components added that have a lower Doppler parameter, which improves the fit. Marked above the lines are the rotational levels that have caused the absorption.

Table 5.6. Table of results - duel component fits

Object	E(B-V)	b / km s^{-1}	Log column density, J =				
			Total	0	1	2	3
				4	5	6	7
				0	1		
S 216 comb	0.096 $^{+0.002}_{-0.02}$	2.99 $^{+0.04}_{-0.02}$	19.36 $^{+0.00}_{-0.01}$	19.01 $^{+0.00}_{-0.01}$	19.03 $^{+0.00}_{-0.01}$	18.17 $^{+0.01}_{-0.01}$	17.54 $^{+0.01}_{-0.02}$
				15.80 $^{+0.03}_{-0.02}$	15.79 $^{+0.04}_{-0.03}$	14.73 $^{+0.02}_{-0.12}$	14.63 $^{+0.02}_{-0.02}$
		2.00 $^{+0.09}_{-0.00}$	19.65 $^{+0.01}_{-0.01}$	19.51 $^{+0.01}_{-0.00}$	19.08 $^{+0.00}_{-0.01}$		
PuWe 1	0.097 $^{+0.015}_{-0.010}$	3.47 $^{+0.21}_{-0.19}$	19.73 $^{+0.05}_{-0.04}$	19.62 $^{+0.06}_{-0.05}$	19.04 $^{+0.05}_{-0.06}$	18.05 $^{+0.09}_{-0.09}$	17.32 $^{+0.18}_{-0.15}$
				14.46 $^{+0.25}_{-0.28}$			
		2.00 $^{+3.55}_{-0.00}$	19.53 $^{+0.06}_{-0.10}$	18.90 $^{+0.19}_{-0.16}$	19.42 $^{+0.04}_{-0.13}$		
GD 561	0.053 $^{+0.015}_{-0.007}$	4.52 $^{+0.10}_{-0.13}$	19.72 $^{+0.03}_{-0.03}$	19.12 $^{+0.09}_{-0.10}$	19.59 $^{+0.01}_{-0.03}$	17.59 $^{+0.11}_{-0.15}$	17.52 $^{+0.14}_{-0.12}$
				16.78 $^{+0.11}_{-0.28}$	16.58 $^{+0.05}_{-0.19}$	15.45 $^{+0.10}_{-0.18}$	15.33 $^{+0.11}_{-0.14}$
		2.37 $^{+2.89}_{-0.37}$	19.21 $^{+0.04}_{-0.11}$	19.42 $^{+0.02}_{-0.07}$	19.00 $^{+0.02}_{-0.03}$		

White dwarf parameters obtained from optical chapter.

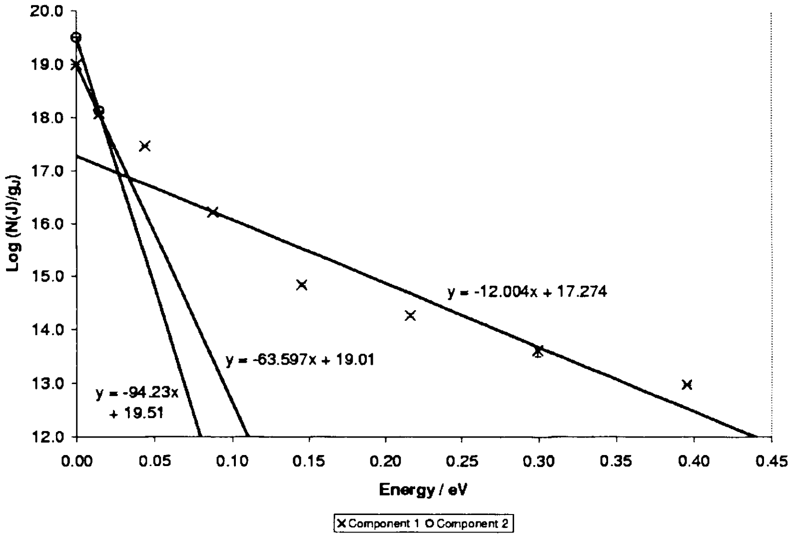

S216

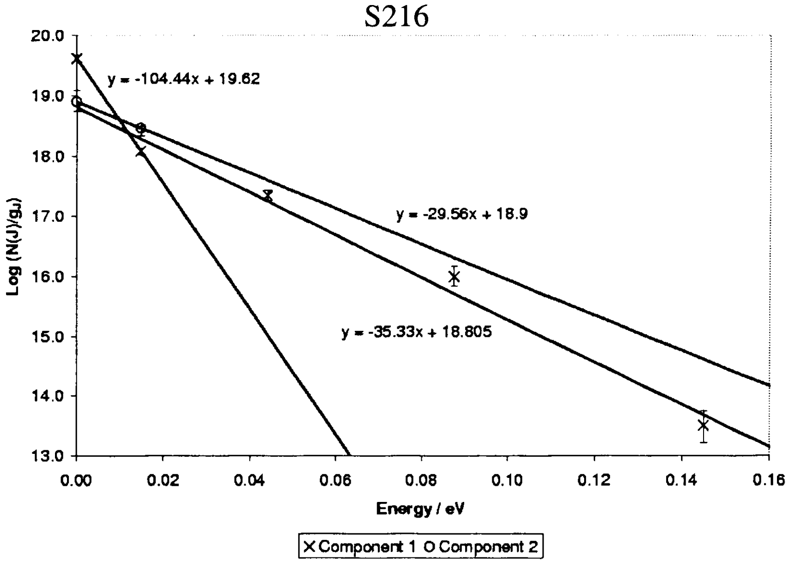

PuWe 1

FIGURE 5.5. Plots showing the Boltzmann distributions of the objects fitted using two Doppler parameters. The equations of the lines through the points were calculated using linear regression and these are shown on the plots. In each case, component 2 is the set of rotational levels with the lower Doppler parameter.

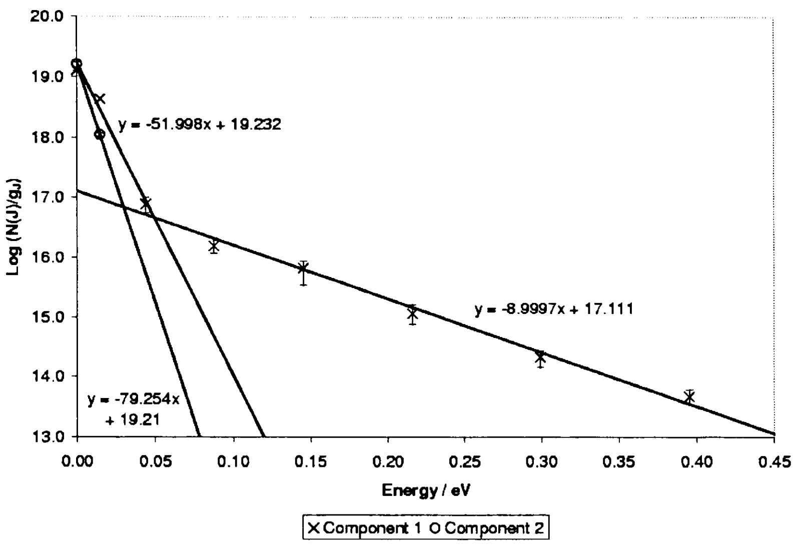

GD561

FIGURE 5.5. continued...

to deconvolve the velocity distribution from the H_2 models in order to test this, but is something that could be investigated in the future.

S 216

S 216 is one of the objects that are better fitted with two Doppler parameters, and was also the object used to measure the resolving power of FUSE. According to the FUSE website (http://fuse.pha.jhu.edu/support/guide/guide_v4.0.html#INRES), this was done by constructing a curve of growth and obtaining a Doppler parameter of 3 ± 1 km $^{-1}$. Figure 5.7 shows the best fitting model with the Doppler parameter set to this value. This clearly does not provide a good fit to the line profiles. The instrument resolution was obtained, however, by deconvolving the profile created by such a Doppler parameter from the measured line widths. Fortunately this is unlikely to affect the calculated instrument resolution greatly, since the high J, unsaturated lines that would have been used to measure line widths are too narrow for this problem to be seen, but for work that is very sensitive to the resolution, such as measuring the Doppler parameter of H_2 lines, this may be important. It also highlights the limitations of curve of growth fitting.

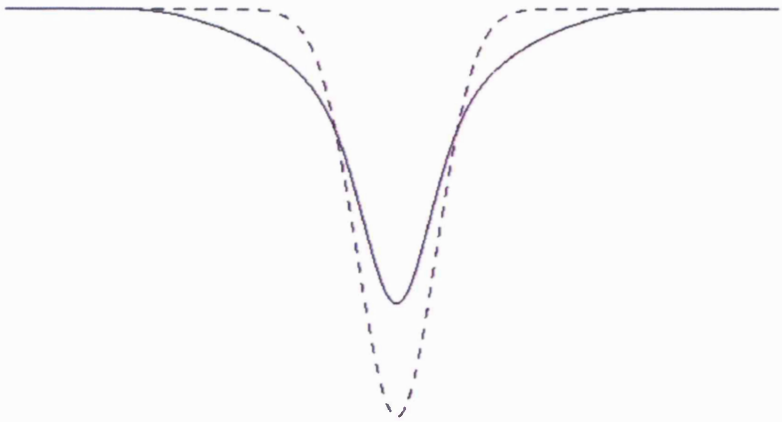

FIGURE 5.6. Example line profiles: the solid line is a simulation of an absorption profile for molecules that have a Maxwellian velocity distribution and are travelling in random directions. The dashed line is for molecules that share a common direction of motion, and with a Gaussian distribution of velocities about the mean. The lines have been smoothed by a Gaussian to make comparison with the FUSE data easier, although the axes are arbitrary since they depend on density of material, temperature and speed of the molecules.

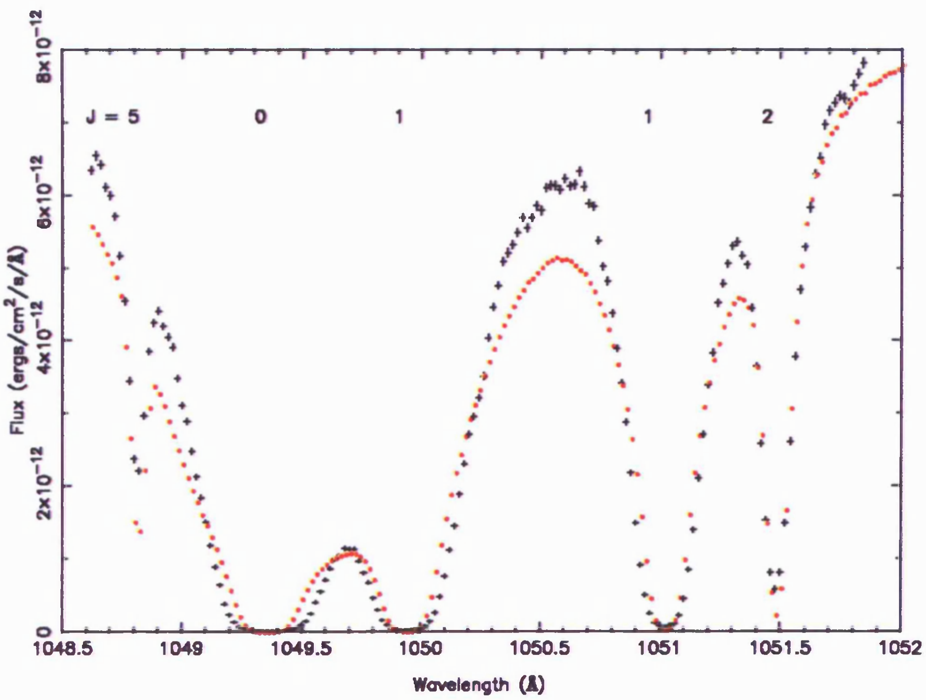

FIGURE 5.7. Section of the combined FUSE spectrum of all LWRS observations of S216. Data are shown by the black error bars. Overlaid is the best fitting model with a Doppler parameter of 3 km s^{-1}.

5.6 Conclusions

A parameterisation of the H_2 absorption in the DAO FUSE spectra has been obtained, allowing the white dwarf spectra to be separated from the ISM H_2 component for analysis. It is clear, however, that the models used in this analysis are simplistic compared to what is actually being observed. Further investigation using different models, as well as high resolution and signal-to-noise data are needed to fully understand some of the line profiles.

Chapter 6

A search for binaries using FUSE

6.1 Introduction

White dwarfs above $\sim$0.5 $M_{\odot}$ in mass have had time to evolve as single stars to a white dwarf via the AGB within the age of the galaxy (Driebe et al., 1998). Stars which do not ascend the AGB, can evolve along the EHB as EHB-manqué objects, forming lower mass objects. Alternatively, low mass He-core white dwarfs can form in close binary systems, after the CE phase has stripped mass away from the progenitor. As many of the DAOs are less massive than 0.5 $M_{\odot}$, it is important to determine whether or not they are in binary systems in order to determine their evolutionary history. FUSE observations consist of a number of exposures that are normally co-added to form a single, high signal-to-noise spectrum; this chapter reports the use of these individual exposures to search for radial velocity shifts in photospheric heavy element lines, which would indicate binarity. Such shifts are seen, for example, in the exposures of HS 1136+6646 (see Figure 6.1). This object has recently been found to be a binary with orbital period $\sim$1 day. Although the shifts are obvious in the case of HS 1136+6646, using the high wavelength resolution of FUSE it is possible to look for much smaller variations in the wavelengths of lines.

6.2 Probability of detection of radial velocity shifts

The ability to detect radial velocity shifts using FUSE depends on a number of factors; sensitivity to particular periods will depend on the separation in time of the exposures, while the mass of the white dwarf and secondary and the inclination of the system will

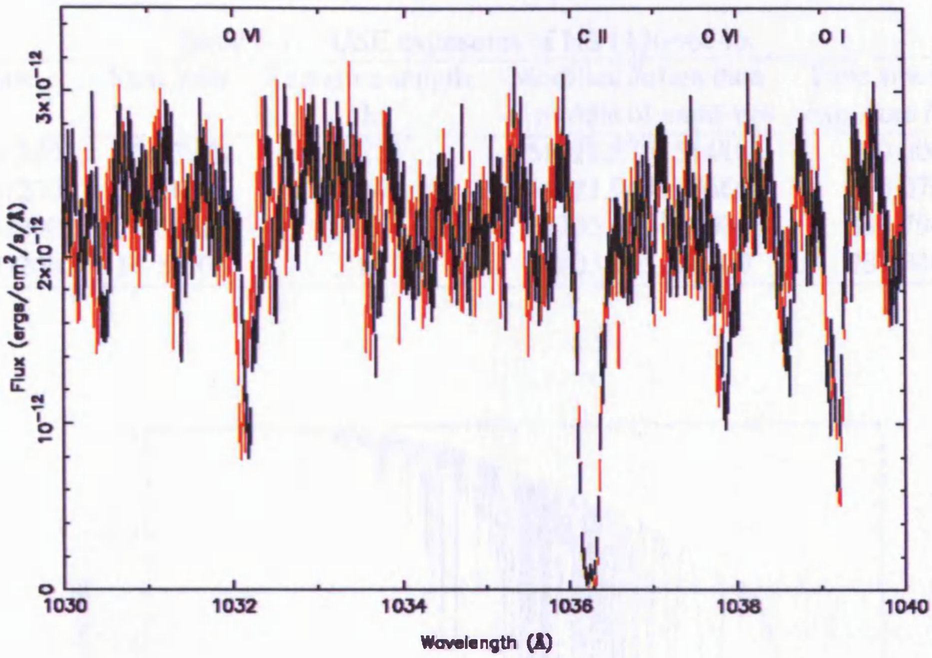

FIGURE 6.1. The two exposures from observation 1 of HS 1136+6646. The middle of the exposures were separated by 1.68 hrs. Marked are the strong O VI photospheric lines, which show a shift between exposures, and the stationary C II and O I ISM lines. The wavelength shifts correspond to a change in velocity of $\sim$30 km s^{-1}.

affect the size of any radial velocity shifts. Therefore, any non-detection does not necessarily mean that an object is not in a binary system. To estimate the probability that FUSE would detect any radial velocity shifts under the assumption that the objects are in binary systems, a program was written by myself that calculates the change in radial velocity of a white dwarf with a dM companion during the length of time between the exposures of an object, for a range of periods. Since, when making a FUSE observation, neither the inclination or the point of the orbit relative to the observor which the system is in are known, the radial velocity changes were calculated for 501 inclinations between 0 and 90°, and for 500 starting positions of the objects. If the change in velocity during the time between two FUSE exposures of an object, assuming a particular initial configuration to the system, was greater than the accuracy to which it can be measured, then it should be possible to detect binarity in that case. Dividing the number of configurations where shifts can be measured by the total number tested then gives the probability of detecting radial velocity variations for a binary system with a given period. The mass of the primary was assumed to be 0.5 $M_{\odot}$, and the secondary 0.1 $M_{\odot}$, which are typical white dwarf and M dwarf masses respectively. The accuracy with which radial velocity could be measured was typically $\sim$1 km s^{-1}, but depended on the signal-to-noise of the data and

Table 6.1. FUSE exposures of HS 1136+6646.

Date	Start time	Exposure length / ks	Modified Julian date of middle of exposure	Time since first exposure / days
12/01/2001	20:33:08	3.225	51921.875151410	0.000
12/01/2001	22:16:04	2.940	51921.944995660	0.070
29/01/2002	15:31:13	3.915	52303.669494085	381.794
29/01/2002	16:37:08	3.921	52303.715246900	381.840

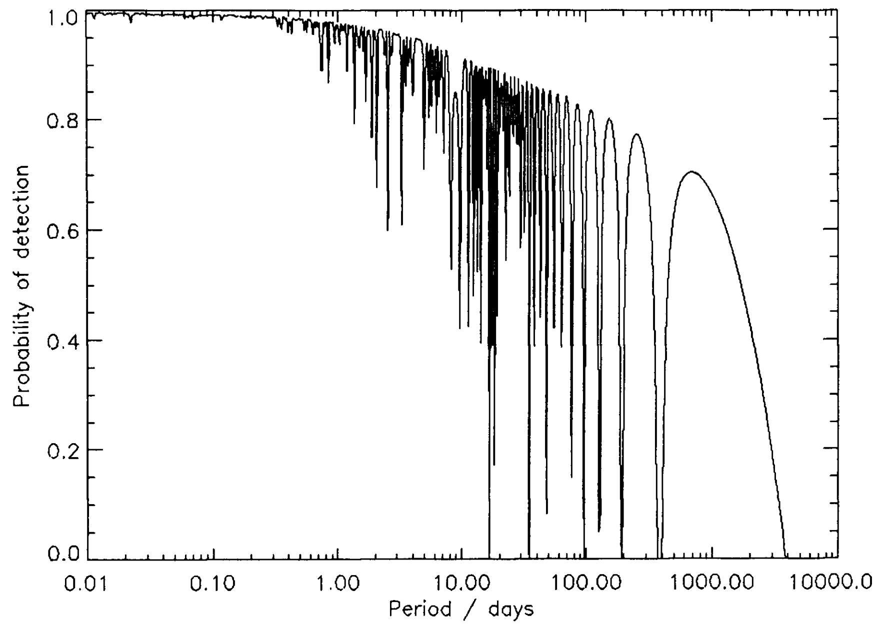

FIGURE 6.2. The probability of detecting radial velocity shifts between exposures of HS 1136+6646.

the number of lines being measured, and so varied with each object. HS 1136+6646 is used here as an example of its output. HS 1136+6646 was observed by FUSE as part of the B053 guest investigator programme (P.I. Barstow). It was subsequently reobserved under programme S601, which began after FUSE started having pointing problems, and looked at previously observed objects where additional observations or improved signal-to-noise would be helpful. Two exposures were taken for each observation, the details of which are listed in Table 6.1, and the calculated probability of detecting radial velocity shifts shown in Figure 6.2. The two observations of HS 1136+6646 were separated in time by over a year, and the individual exposures in each were about 6 ks and 4 ks apart. The ability to detect of radial velocity shifts is strongly affected by the period of

Table 6.2. ISM lines used to correct for wavelength calibration shifts between FUSE exposures, with rest frame wavelengths as listed by Morton (1991).

Species	Lab. wavelength / Å
O I	988.6549
Si II	989.8731
Si II	1020.6989
C II	1036.3367
C II	1037.0182
O I	1039.2304
Ar I	1048.2199
Fe II	1063.1764
Ar I	1066.6599

the system being observed – in this case if the period is approximately a year any shifts are very difficult to detect, as the white dwarf will have approximately the same radial velocity in each observation. The same is true if the period of the system is half a year, or a quarter etc. An additional constraint is the length of each exposure. This puts a limit on the lowest period system where binarity could be detected before any radial velocity shifts become smeared out. Exposures are typically $\sim$1 hr long due to the length of the unocculted part of the orbit of the FUSE 96 minute orbit.

6.3 Radial velocity measurement technique

FUSE observations suffer from wavelength calibration problems, as described in Chapter 4. As LiF 1A is the best calibrated channel it is used as the main reference for the radial velocity measurements. Even so, the wavelength scale can drift between exposures; this can be corrected for by reference to interstellar medium lines, the radial velocity of which should be the same in every exposure. The main lines used are listed in Table 6.2, with their rest frame wavelengths from Morton (1991). At least some of these lines were detectable in the spectra of every object. A Gaussian and a second order polynomial were used to model the line profile and continuum level respectively. The set of parameters that best reproduce the data were determined by a least-squares fitting routine that is part of the IDL language (CURVEFIT). In addition a 1σ error on the central wavelength was returned by the fitting function. As the true redshift of the ISM lines is not known, and the FUSE wavelength calibration is not reliable, the mean central wavelength of a line in all the exposures taken of an object is assumed to represent its real position.

Table 6.3. Strong photospheric lines used to measure radial velocities.

Species	Lab. wavelength / Å
P V	997.5240
O VI	1031.9310
O VI	1037.6130
Si IV	1066.6140
O IV	1067.7680
Fe VII	1073.9480

Table 6.4. Radial velocities measured for photospheric lines in the spectrum of HS 1136+6646.

Species	Radial velocity / km s^{-1}			
	Observation 1		Observation 2	
	Exposure 1	Exposure 2	Exposure 1	Exposure 2
O VI	74.81±1.78	47.01±1.32	34.27±1.38	58.77±1.59
O VI	75.84±2.12	44.55±1.77	33.69±1.48	59.32±2.31
O IV	72.15±2.05	45.20±2.10	35.52±1.90	56.81±2.16
MEAN	74.27±1.15	45.59±1.02	34.49±0.93	58.30±1.15

The shift of a line in each exposure relative to the mean position can then be found. Finally, for each exposure the mean of the shifts calculated for all the ISM lines is found. This value was then used to line up the wavelength scales of all the exposures. For HS 1136+6646 the maximum shift that was applied to an exposure wavelength scale was 0.011 Å, which corresponds to a change in velocity of only ~3 km s^{-1}. The central wavelengths of photospheric lines were then measured in a similar way. Table 6.3 lists the lines used, although again not all were present in all the objects, or were difficult to identify in the low signal-to-noise exposures. For example, Si IV can only be seen if the Ar I ISM line at 1066.6599 Å is not present. The wavelength shifts calculated from the ISM lines were applied to each measured central wavelength, and then the velocity of the lines were calculated. Table 6.4 shows the radial velocities found for HS 1136+6646 and Figure 6.3 shows the mean radial velocities in each exposure plotted against the time of exposure. It is easy to see, as expected, that the radial velocities change with time, but there are not enough exposures to determine the orbital period. In reality, the error on the radial velocities is probably greater than the formal errors obtained from the fitting function, since often differences of ~10 km s^{-1} were seen in the velocities of the different lines in a single exposure.

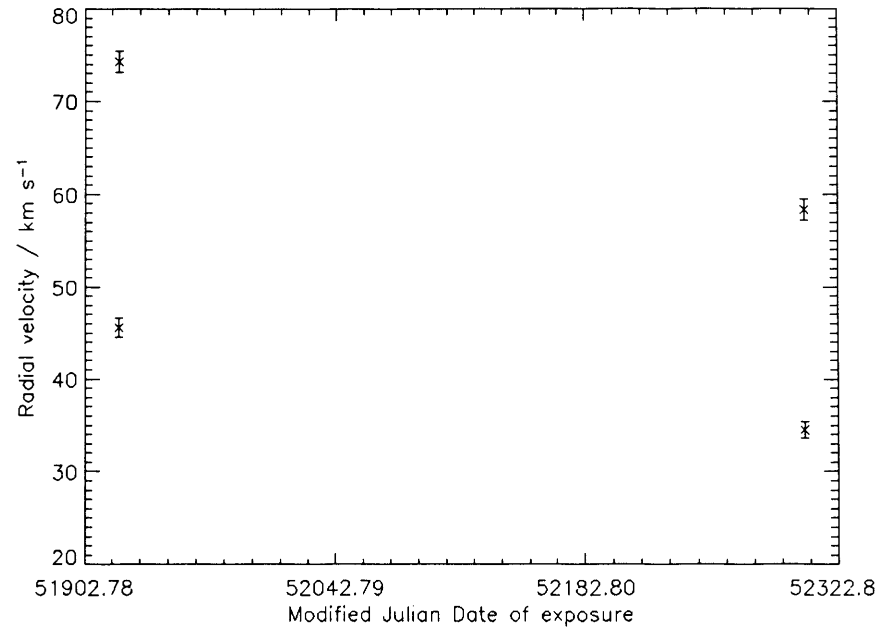

FIGURE 6.3. Mean radial velocity of the photospheric lines in the spectra of HS 1136+6646 plotted against time of exposure.

6.4 Significance of radial velocity differences

The measurement of radial velocity is only accurate to a few km s^{-1}, so it may be difficult to decide if any shifts are actually caused by the motion of the white dwarf within a binary system or if they are due to random errors. This may be a problem, for example, if exposures are close together, in which case any velocity shift due to binarity might be small. Therefore, some method of determining if radial velocity changes are significant, or just due to random error, is needed. To do this, a Monte Carlo routine was written by myself. If an object is a single star, the measured radial velocities should be constant, but with differences due to random errors. Therefore, if the object really is a single star then it should be possible to take a constant velocity, add random noise, and produce a set of radial velocities that look like the measured data. To test this, a constant velocity line was fitted to the measured radial velocities and the minimum χ^2 acheived was recorded. Then, a set of measurements was simulated by applying random Gaussian errors to a constant velocity. The size of the errors in the real data is affected by the quality of the data, since shorter exposures, i.e. with poor signal-to-noise, result in larger uncertainties in the measured wavelengths. Therefore, the measurement errors from the real measurements were used to determine the standard deviation of the Gaussian errors applied to the simulated data. Then a constant velocity line was fitted to the simulated data and the minimum χ^2 recorded. If the χ^2 from the simulated data is greater than the χ^2 from the real data, this suggests that the radial velocity of the object is constant. However, because the errors are random, then by chance the simulated χ^2 might be large, suggesting that the object's radial velocity is changing. Therefore, this was done 1,000,000 times and the number of occasions when the simulated χ^2 was equal to or less than the real χ^2 counted. Dividing this by the number of trials gives a measure of the proportion of times that the observed radial velocity variations would occur randomly if the object had a constant radial velocity. If this is less than 0.3% of the times, the object can be said to be part of a binary system with 3σ certainty.

6.5 Results

For NGC 6853, H_2 absorption prevented radial velocities being measured. For the other white dwarfs, plots of the measured radial velocities against modified Julian date and the periods to which the technique is sensitive are shown in Figure 6.4. Table 6.5 lists the results of the Monte Carlo tests and the best fitting radial velocities.

Radial velocity variations between exposures have been detected at the 3σ level in nine objects; these are S 216, RE 0720-318, Ton 320, PG 0834+500, EGB 6, HS 1136+6646, Feige 55, RE 2013+400 and NGC 7293. However, in some cases the results of the Monte Carlo tests appear erroneous:

6.5.1 S 216

In the case of S 216 the difference in radial velocities between exposures is never more than ~15 km s^{-1}, which is less than the resolution of FUSE. The measured radial velocities for a number of the exposures is shown in Figure 6.5. Fitting a sine wave to these data using the STARLINK package PERIOD yielded a χ^2 no better than 3, which was obtained with a period of just over a day, and so there does not appear to be any short term variation that would explain the scatter in the data points. For the best fitting line of constant velocity, the χ^2_{red} is 4.69, which is significantly worse than the best fit sine wave. However as the longest observation of S 216 lasted less than 10 ks, with the data spread over 3 years, it is not possible to tell if there is a real sinusoidal variation or due to inaccuracies in the radial velocity measurement technique.

Table 6.5. Results of the Monte Carlo analysis. Those objects that the calculations suggest have real radial velocity shifts at the 3σ level are underlined. The stars in bold are already known to have companions. The mass of each object is also shown.

Object	Number of exposures	Best fitting vel / km s^{-1}	Chance of variations occurring randomly	Mass / $M_{\odot}$
S 216	105	12.6	0.00000*	0.496 ± 0.009[1]
A 7	5	38.8	0.01540	0.508 ± 0.020[1]
HS 0505+0112	3	50.4	0.02695	0.509 ± 0.018[1]
PuWe 1	6	17.5	0.07894	0.499 ± 0.026[1]
RE 0720-318	5	-194.4	0.00000*	0.566 ± 0.046[1]
TON 320	9	33.8	0.00000*	0.507 ± 0.017[1]
PG 0834+500	3	-46.6	0.00001	0.453 ± 0.049[1]
A 31	4	80.8	0.01788	0.491 ± 0.025[1]
EGB 6	11	-2.5	0.00001	0.556 ± 0.058[3]
NGC 3587	4	37.1	0.33411	0.582 ± 0.009[2]
HS 1136+6646	4	53.2	0.00000*	0.511 ± 0.007[1]
Feige 55	41	4.2	0.00000*	0.439 ± 0.015[1]
PG 1210+533	2	-3.3	0.93316	0.595 ± 0.033[1]
LB 2	5	15.1	0.00882	0.557 ± 0.049[1]
HZ 34	4	6.7	0.56639	0.417 ± 0.018[1]
A 39**	3	2.2	0.36889	0.455 ± 0.036[1]
NGC 6720**	12	-14.5	0.01853	0.56 ± 0.02[4]
RE 2013+400	9	-15.2	0.00000*	0.642 ± 0.043[1]
HS 2115+1148***	3	-7.4	0.29493	0.465[5]
DeHt 5**	2	-40.9	0.65238	0.470 ± 0.025[1]
NGC 7293	26	0.0	0.00000*	0.57 ± 0.02[6]
GD 561	2	-12.5	0.61473	0.464 ± 0.029[1]

* In none of the Monte Carlo trials was the minimum χ^2 achieved by fitting a constant velocity line to the real data less than the χ^2 from fitting a constant velocity line to the simulated data.

** Velocity measurements made difficult by H_2 absorption.

*** Four exposures exist, but one was not used due to poor signal to noise.

1 From Chapter 3.

2 From Chapter 7.

3 Parameters used: $T_{\rm eff} = 70{,}000 \pm 7000$ K, $\log g = 7.5 \pm 0.25$ (Liebert et al., 1989).

4 Parameters used: $T_{\rm eff} = 101{,}200 \pm 4600$ K, $\log g = 6.88 \pm 0.26$ (Napiwotzki, 1999).

5 Parameters used: $T_{\rm eff} = 67{,}000$ K, $\log g = 6.9$ (Dreizler et al., 1995).

6 Parameters used: $T_{\rm eff} = 103{,}600 \pm 5500$ K, $\log g = 7.00 \pm 0.22$ (Napiwotzki, 1999).

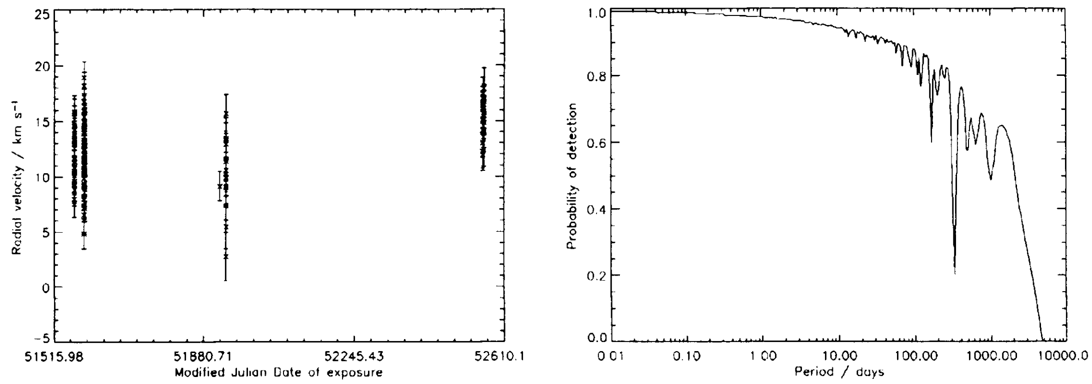

S 216

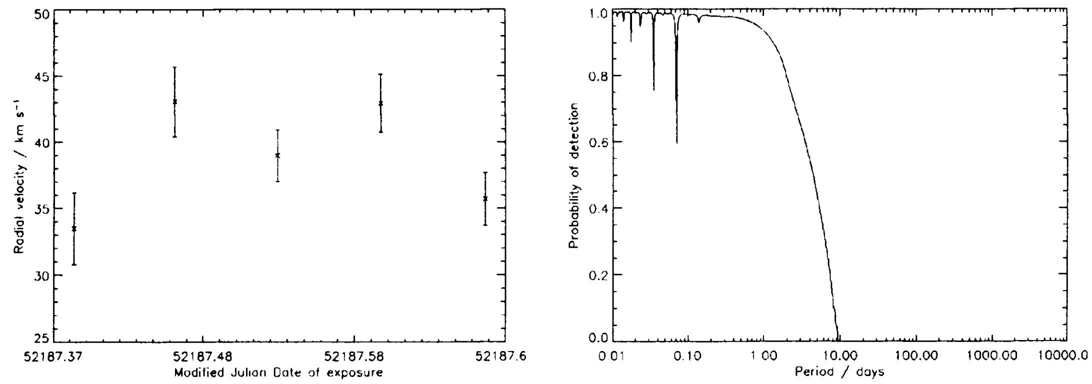

A 7

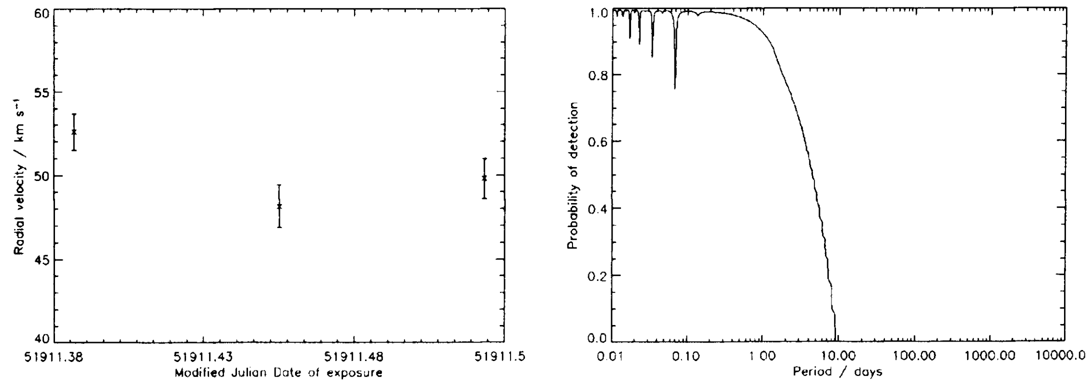

HS 0505+0112

FIGURE 6.4. The radial velocity of the photospheric lines in the exposures of each object, and the chance of detecting velocity shifts if they are in binary systems.

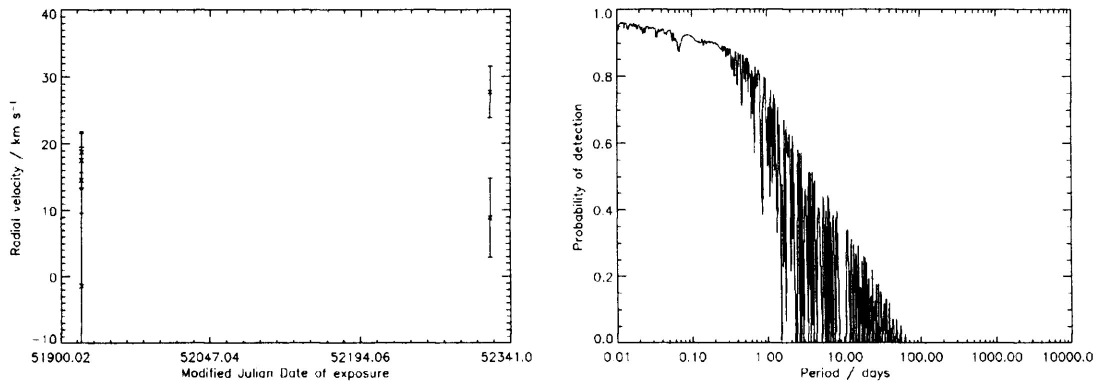

PuWe 1

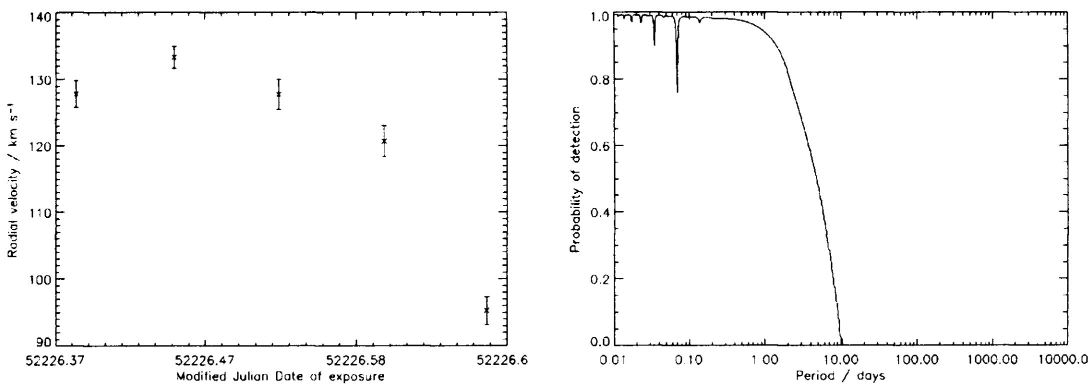

RE 0720-318

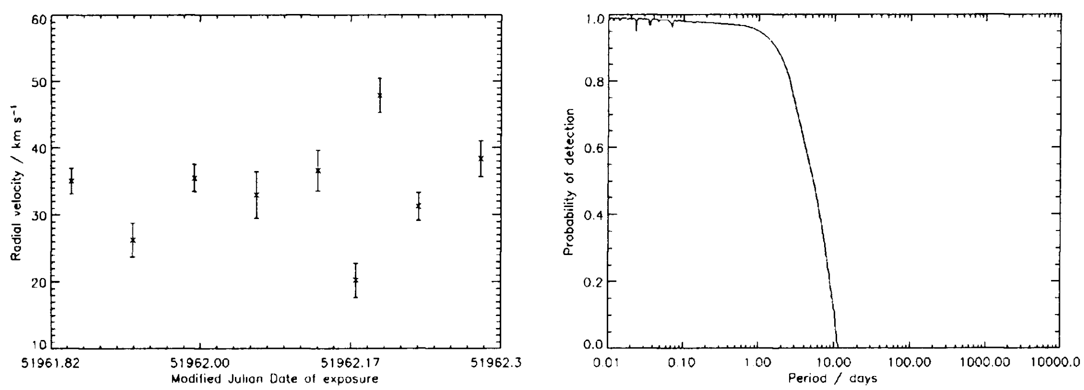

Ton 320

FIGURE 6.4. continued...

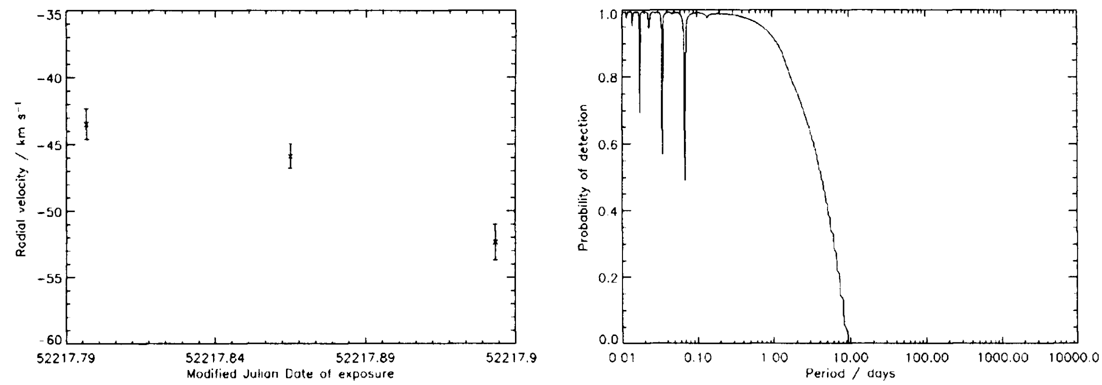

PG 0834+500

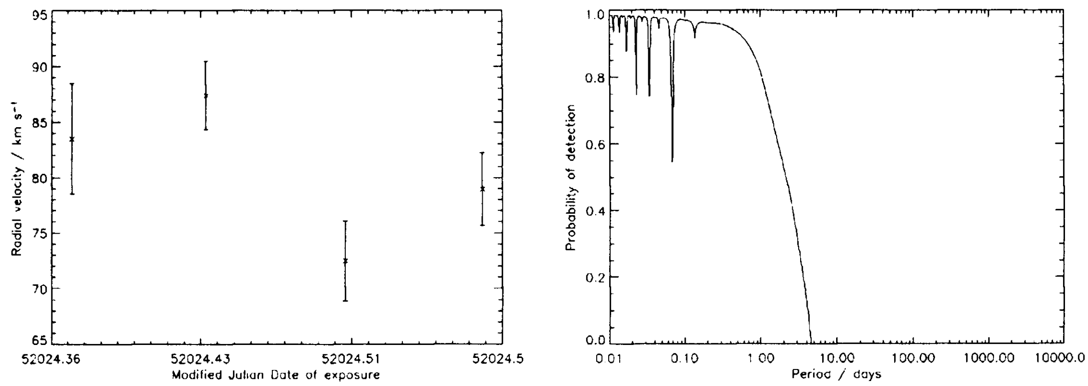

A 31

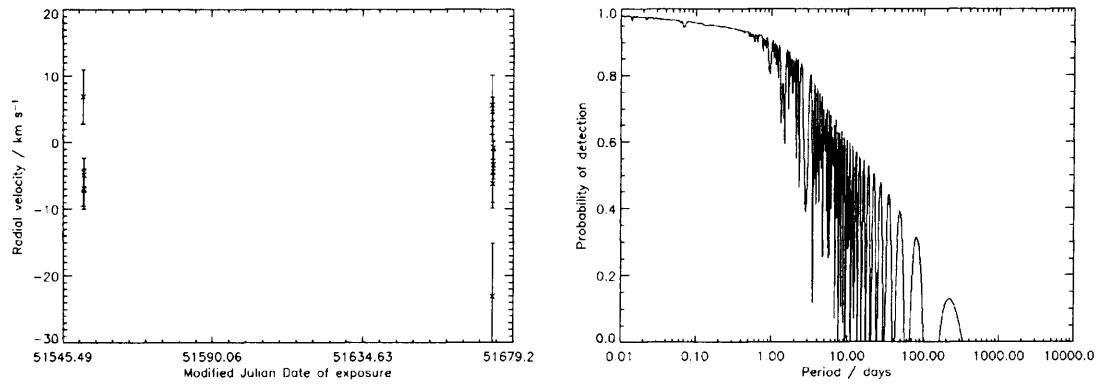

EGB 6

FIGURE 6.4. continued...

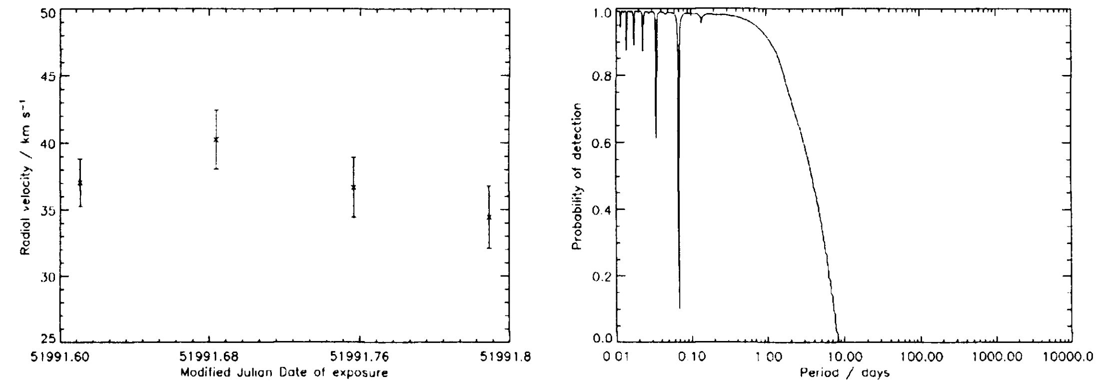

NGC 3587

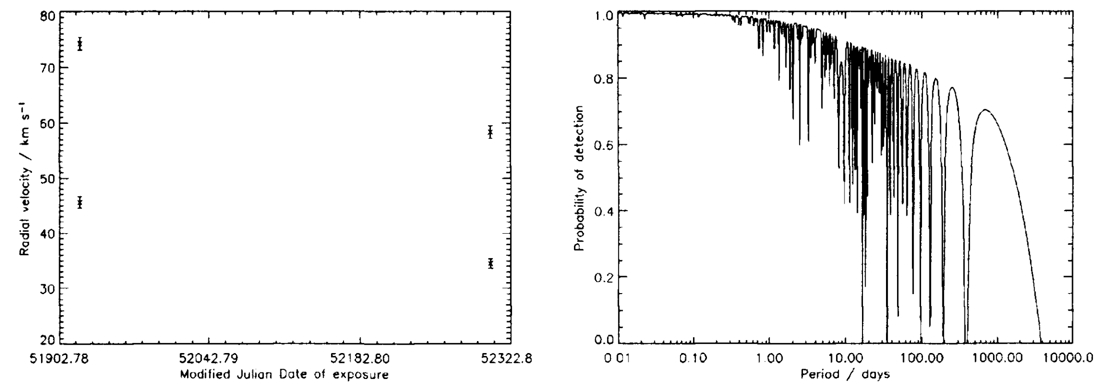

HS 1136+6646

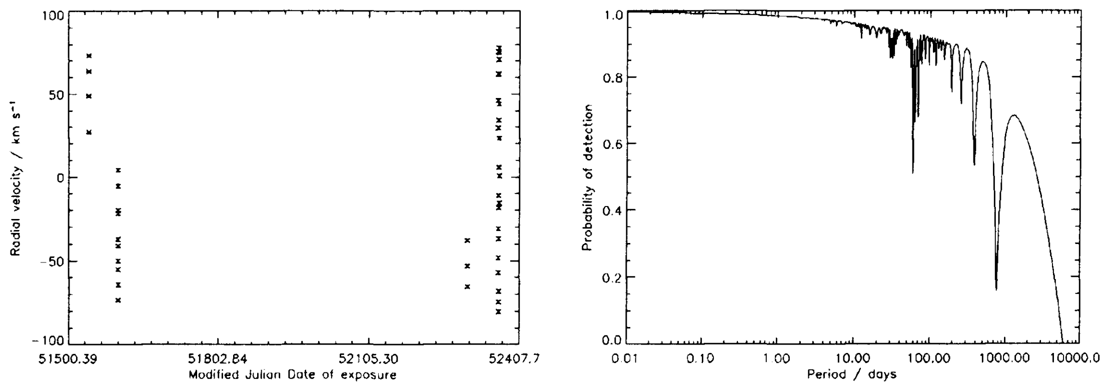

Feige 55

FIGURE 6.4. continued...

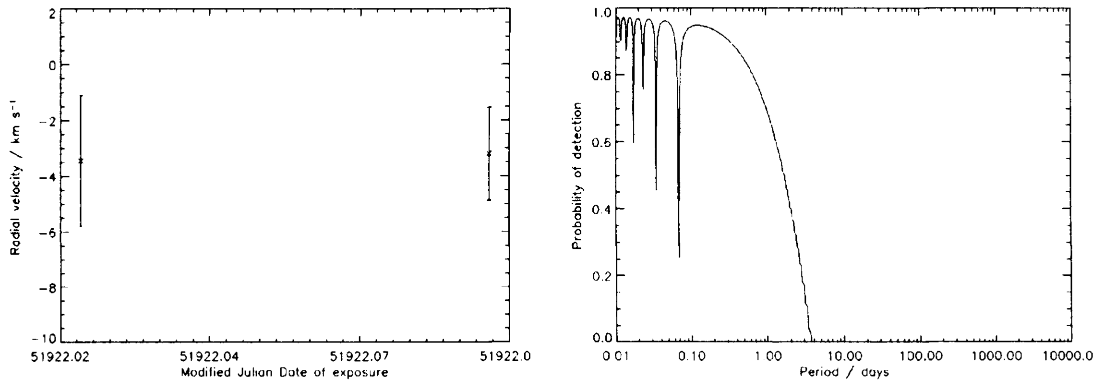

PG 1210+533

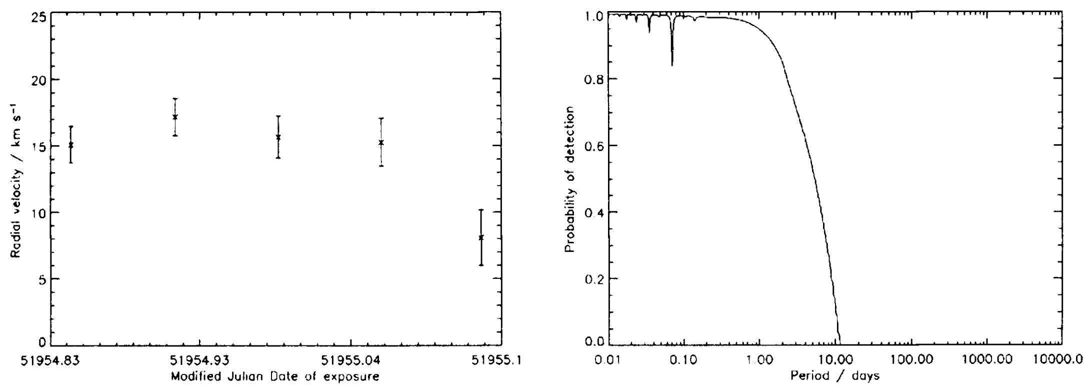

LB 2

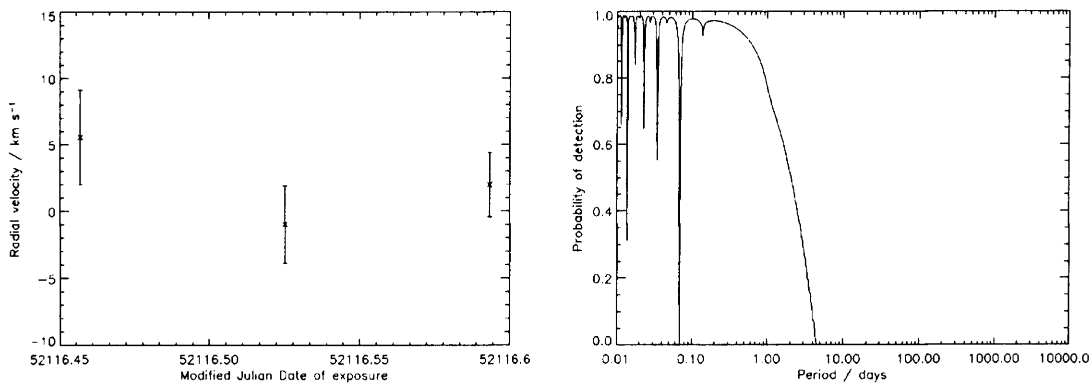

HZ 34

FIGURE 6.4. continued...

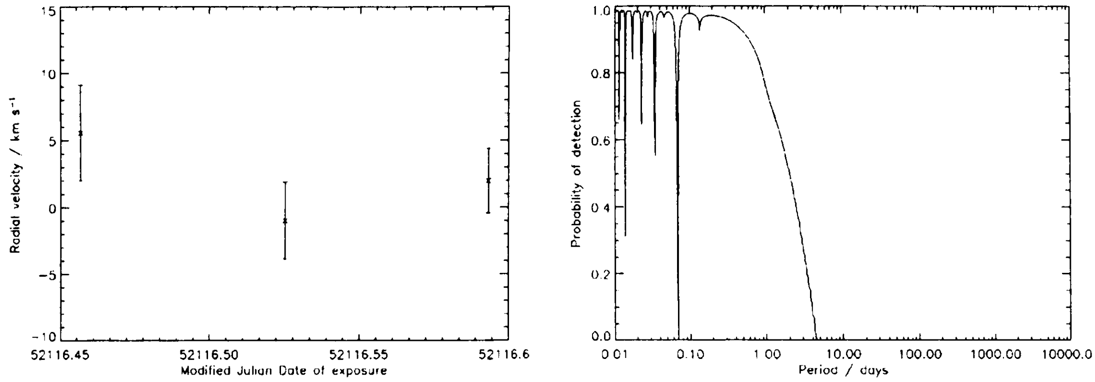

A 39

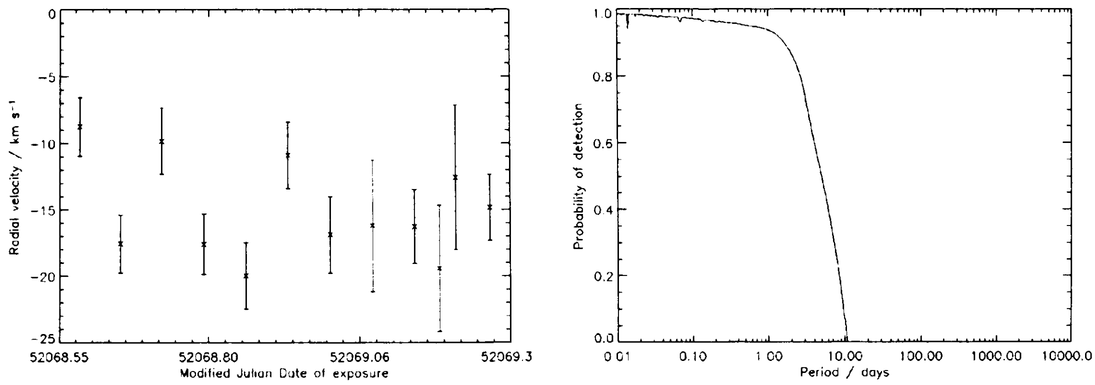

NGC 6720

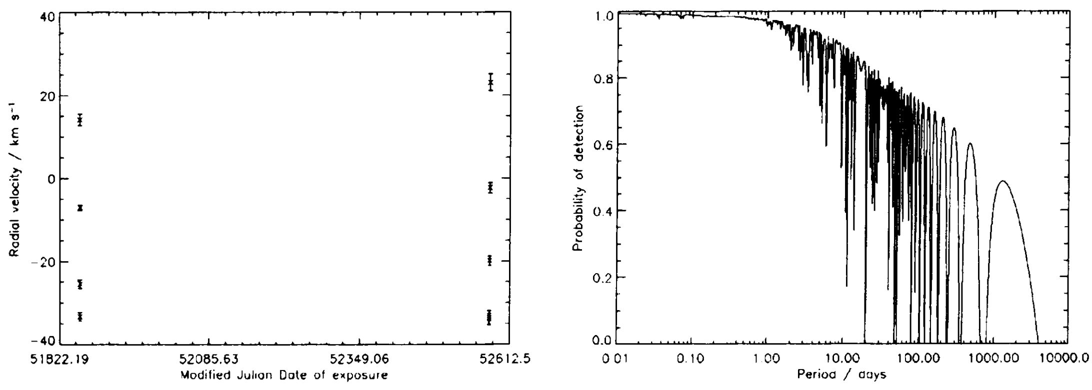

RE 2013+400

FIGURE 6.4. continued...

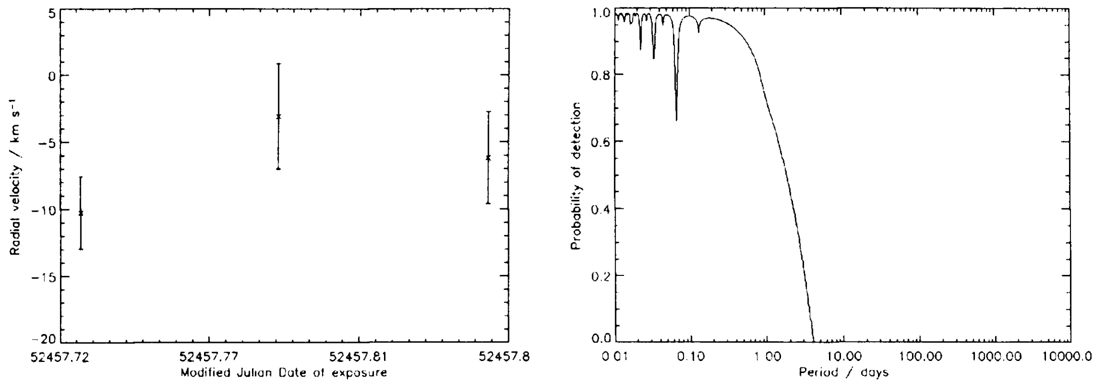

HS 2115+1148

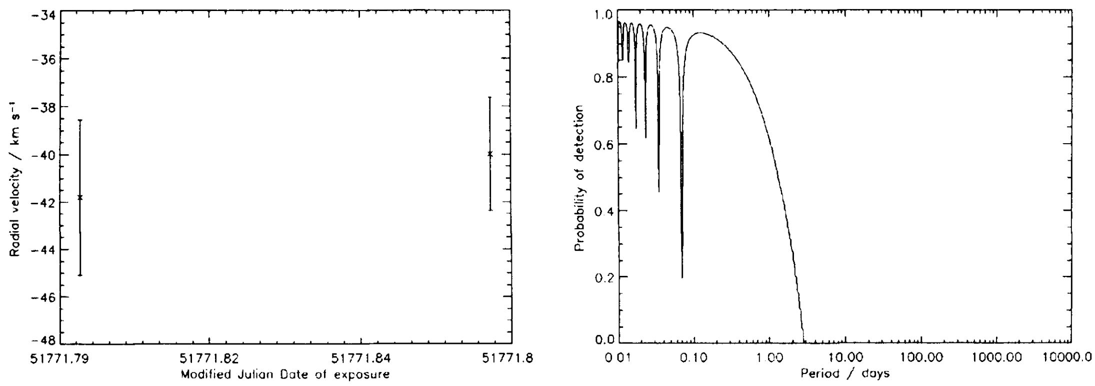

DeHt 5

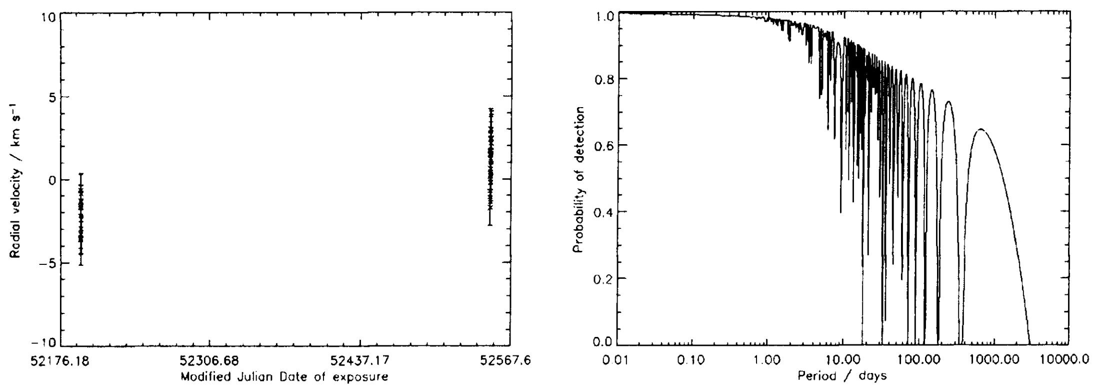

NGC 7293

FIGURE 6.4. continued...

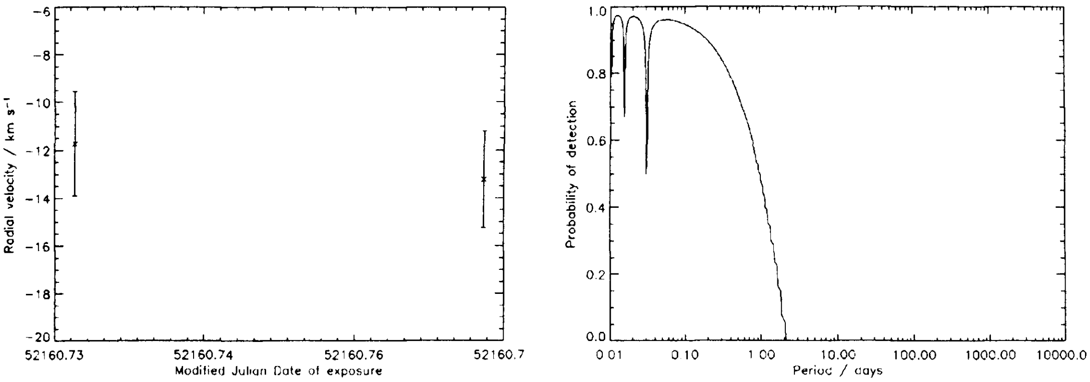

GD 561

FIGURE 6.4. continued...

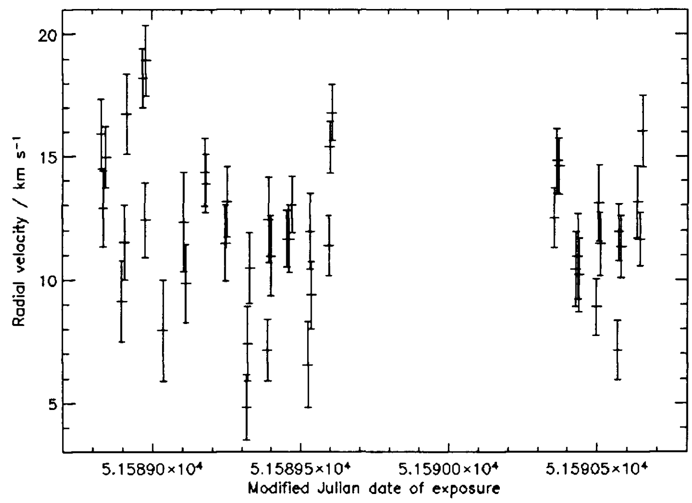

FIGURE 6.5. Radial velocities of the photospheric lines measured for exposures 1, 2 and 3 of S 216.

6.5.2 Ton 320

Upon visual inspection, the radial velocities determined from the exposures of Ton 320 do not appear to follow a sinusoidal variation. The best fitting sine wave has a significantly better χ^2_{red} of 4.33 compared to 9.05 for a constant velocity. However, the best fit sine wave has a period of 1.5 days, which is very similar to the time between the exposures.

6.5.3 EGB 6

In the case of EGB 6, the Monte Carlo test is likely to have been biased by a couple of inaccurate radial velocity measurements. This usually occurs where an exposure length is short, and hence the data have very poor signal-to-noise. However, EGB 6 has a known infrared excess and probably has an M dwarf companion, but lack of variation in the infrared flux suggests the inclination of the orbit must be close to 0°(Fulbright & Liebert, 1993). Therefore, although EGB 6 is likely to be a binary, no radial velocity variations should be seen.

6.5.4 NGC 7293

Two observations were made of NGC 7293, separated by over year. The measured radial velocities from exposures of this object are consistent within 10 km s^{-1}. However, the mean of the velocities measured for the first observation is slightly lower than that of the second observation. This is likely to have caused the fit to a constant velocity to have returned a high χ^2_{red}, producing the positive Monte Carlo result. The differences between the radial velocities from the two observations are extremely small (equivalent to a difference of ~0.01 Å in wavelength space) and are likely to be caused by inaccuracies in the measurement technique, e.g. due to a slight misalignment of the ISM lines.

6.5.5 PG 0834+500

PG 0834+500 has a known sdB companion, and so radial velocity shifts might be expected for this object (Saffer et al., 1998). However, only three exposures of PG 0834+500 were taken, and the differences in the measured radial velocities are less than 15 km s^{-1}. It is possible that the interstellar medium lines were not lined up accurately, resulting in the small shift seen, rather than this being a true detection of binarity. To discount this, the difference in the measured wavelengths between the C II 1036.3 Å ISM line and the O VI 1037.6 Å photospheric line was found for each exposure, and the results are shown in Figure 6.6. The wavelength difference plot shows the same shifts as were seen in radial velocities, suggesting they are real. Unfortunately, the observation was less than 0.2 days long and very little of the orbit is covered, so no period can be determined.

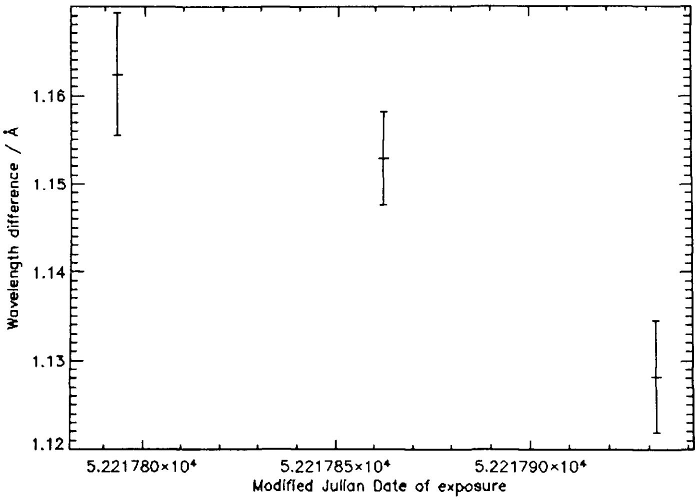

FIGURE 6.6. Difference in the measured wavelengths of the C II 1036.3 Å ISM line and the O VI 1037.6 Å photospheric line of PG 0834+500.

6.5.6 RE 0720-318, HS 1136+6646, Feige 55, and RE 2013+400

All these objects are known to be binaries. In the radial velocity measurements for each, shifts are very clear, and are much larger than the FUSE resolution. The short length of the FUSE observations means that in most cases a complete orbit is not covered. RE 0720-318 has a period of 1.26245 ± 0.00004 days (Vennes & Thorstensen, 1996), hence the FUSE observation spans only about a fifth of the orbit. However, the measured velocities agree well with the published ephemeris (Dobbie, private communication). The radial velocity shifts of HS 1136+6646 are obvious, but with only four exposures over a timespan of a year it is not possible to determine an orbital period. Feige 55 is a well studied double degenerate, with a period of 1.49303 ± 0.00011 days and a semi-amplitude of $77.4 \pm 7.0\,\mathrm{km\,s^{-1}}$ (Holberg et al., 1995). Kruk et al. (2003) have conducted a similar radial velocity analysis to that performed here, but on observations 4, 5 and 6 only. From this they determined a period of 1.4891 days and velocity semi-amplitude $80.377\,\mathrm{km\,s^{-1}}$. Using the STARLINK package PERIOD, a sine wave was fitted to the radial velocity measurements of all the exposures, yielding a period of 1.490 days, and a velocity semi-amplitude of $\sim 79\,\mathrm{km\,s^{-1}}$, both of which are in good agreement with the published values. Radial velocity variations are also clear for RE 2013+400, but the small number of exposures and large temporal separation of the observations makes it impossible to determine the period.

Out of the 9 objects for which positive Monte Carlo results have been obtained, only

5 can be said to definitely have radial velocity variations. In addition, EGB 6 is known to be a binary, although the Monte Carlo result appears erroneous. The results for the remaining three objects cannot be totally discounted from the evidence of these data, but the likelihood appears to be that they, too, are erroneous.

6.6 Discussion

6.6.1 The proportion of DAOs in binaries

Out of the 22 objects for which a search for radial velocity shifts has been attempted, binarity has been positively detected in only 5. In addition, EGB 6 is likely to be a binary, but is at an unfavourable inclination for the detection of velocity variations. No radial velocity shifts were seen in the exposures of A 7 and PuWe 1, both of which were listed as having possible companions by Ciardullo et al. (1999). This is expected, however, as the technique for the detection of binarity used here is not sensitive to the periods that these objects would have if they are in binary systems. Whether or not they are in binaries is, in any case, irrelevant to this thesis, since at such large separations they would not have interacted with their companions, and hence binarity can't have influenced the amount of helium in their atmospheres. As every object has a different number of exposures, each having different temporal separations and quality of data, it is difficult to quantify these results. However, it can be seen from Figure 6.4 that the probability of detecting radial velocity shifts for binaries with periods less than a day is greater than 95% in virtually all cases. Most post-CE binaries have a period less than one day (see, for example Hillwig et al., 2000), so assuming that all the DAOs are in close binary systems, radial velocity variations should have been observed in $\sim$20.

6.6.2 Implications for evolutionary scenarios

No radial velocity variations are seen for PG 1210+533, although this is based on only two exposures, hence there is still no indication of the source of the helium that is observed in this object. Both RE 0720-318 and RE 2013+400 were known binaries, and the proposed explanation for the helium that is seen in their spectrum is based on either accretion from their companion's wind or the loss of mass during the CE phase. This is also a plausible explanation for the remaining binaries, although they might also fit in with the low log g DAOs, which form the largest group. Many of the DAOs in the 0.45-0.5 $M_{\odot}$bin had no detectable radial velocity shifts and so they must have evolved

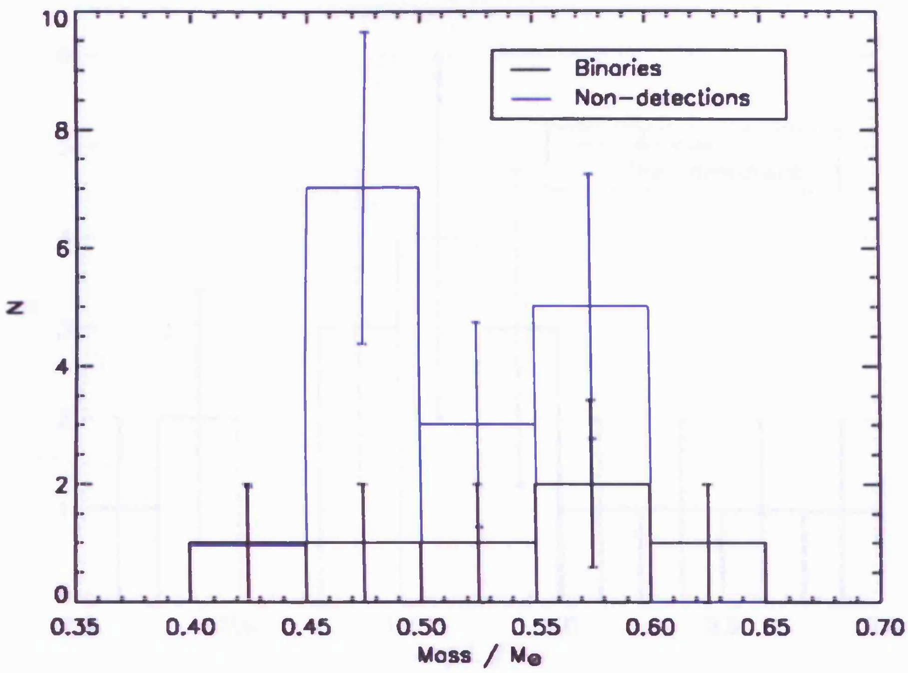

FIGURE 6.7. Comparison of the masses of the DAO white dwarfs for which binarity is detected with those for which no evidence of a companion has been found.

via the EHB rather, as suggested by Bergeron et al. (1994), otherwise they would not be massive enough to have evolved to as an isolated white dwarf within the age of the galaxy (Figure 6.7). No radial velocity shifts were seen in the exposures of HZ 34, which seems to have too low a mass even to have evolved as a single star via the EHB. However, this is based on optical data; if results from fitting the Lyman lines are used, this object falls into a higher mass bin – see Chapter 7. Therefore, the results of this chapter appear to be consistent with evolutionary theory, although the small sample size prevents any strong conclusions. The presence of helium in the line forming regions of the atmospheres of the low log g objects could be explained by a process such as mass loss. As mass loss is related to luminosity in a radiatively driven wind (Abbott, 1982), it might be expected that high luminosity DAOs do not need to be in binaries. In contrast, if a DAO has low luminosity, a different process, such as accretion of the wind from a companion, must be invoked in order to explain the presence of helium lines. This is indeed the case, as shown in Figure 6.8. RE 0720-318 and RE 2013+400 both inhabit the lowest two luminosity bins, along with PG 1210+533, whereas above 1.25 $L_{\odot}$ binarity was detected for no objects.

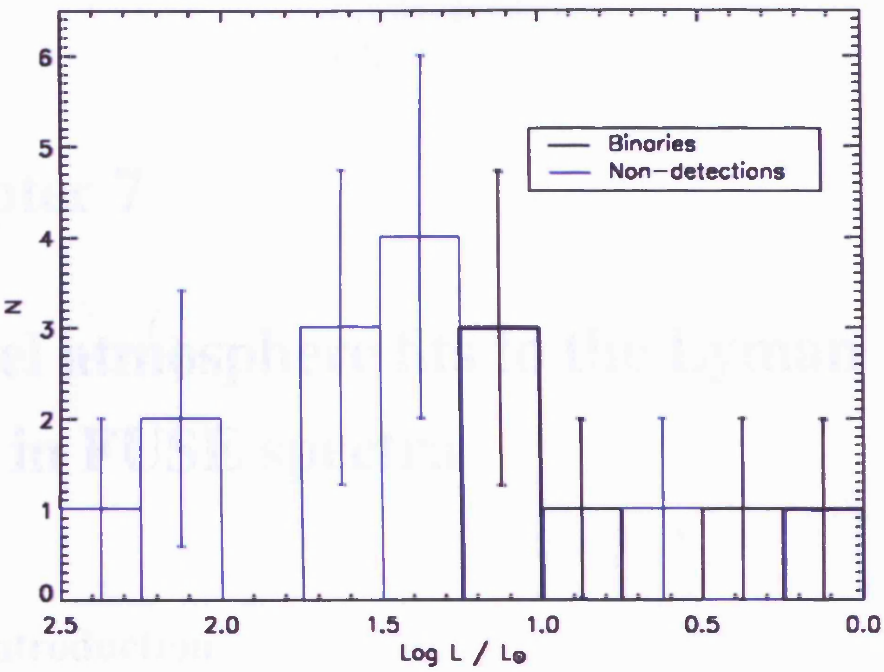

FIGURE 6.8. Comparison of the luminosities of the DAO white dwarfs for which binarity is detected with those for which no evidence of a companion has been found.

6.7 Conclusions

A search for radial velocity shifts of photospheric heavy element lines has been conducted using observations made by FUSE. Out of 22 objects, only 5 had detectable shifts, while a sixth is known to be a binary. Four times this number of detections would be expected if all the objects were in close binary systems. Shifts were not detected in the majority of the low mass objects, suggesting that they may have evolved via the EHB, although CE evolution can still be invoked to explain the low mass of some. The high luminosity objects (i.e. those with low log g) do not appear to require a companion to be DAOs, while those the lowest luminosities are either binaries or are unusual objects.

Chapter 7

Model atmosphere fits to the Lyman lines in FUSE spectra

7.1 Introduction

Although hydrogen Balmer line fitting to obtain the temperature and gravity of a white dwarf has been in use for many years, the Lyman lines, which are found in the far-UV have not been well exploited because of the need for satellite data. The ability to obtain the fundamental parameters of a white dwarf from the Lyman lines is important since it provides a check on the results from the Balmer lines and on the model atmospheres being used. In some cases optical data cannot be used, for example if a white dwarf has a bright companion or is in a CV, and in these cases the Lyman lines provide the best way to determine the fundamental parameters of the star.

7.2 Determination of temperature, gravity and helium abundance

The homogeneous model grid as described in Chapter 3 is also used for the analysis discussed here, but with the temperature range extended up to 120,000 K. As for the optical study, the parameters that give the best agreement between model and data are obtained by χ^2 minimisation using the XSPEC program. A simultaneous fit of the β, γ, δ and ϵ lines of the neutral hydrogen Lyman series, as well as the He II line at 1084.9 Å, is performed. The data are divided into three wavelength ranges, containing L_γ, L_δ and L_ϵ (934-990 Å), since the wings of these lines overlap, L_β (1000-1050 Å), and the He II

1084.9 Å line (1075-1095 Å). Unfortunately, the signal-to-noise of the data in the region of the helium line is usually low as it is only covered by the SiC 2B segment and the edge of SiC 1A, so the errors in the measurement of helium abundance are often large. Fits to the FUSE data are shown in Figure 7.1.

Since FUSE is a space based observatory the data aren't affected by the systematic atmospheric effects that are seen in ground-based observations, and a single model normalisation is applied across all three ranges. An extinction model is added to account for interstellar absorption (Seaton, 1979 – see Chapter 5 for details). In some cases the spectra are affected by H_2 absorption. Ideally the H_2 would be simultaneously fit at the same time as the white dwarf spectrum but in practise this is not possible because of the large number of variable parameters that would be required to specify the model, a number of which are strongly correlated. Instead, the results obtained in Chapter 5 are used to construct an H_2 absorption spectrum over the wavelength ranges being fit. The white dwarf model is then multiplied by this absorption, allowing the underlying DAO spectrum to be fitted. As a result, the errors derived for the fitted parameters will be underestimated since the H_2 is not being treated, as it strictly should be, as an uncertain quantity.

As FUSE is in a low-Earth orbit, emission lines due to the Earth's geocorona are often superimposed on the white dwarf spectrum. ISM absorption lines are also seen, and a particular problem is interstellar H I, which artificially deepens the cores of the Lyman lines. The central regions of the cores of the Lyman and helium lines are therefore excluded from the analyses to remove any contamination from geocoronal or interstellar absorption, together with any ISM lines, to prevent them from influencing the fit. Many photospheric lines due to heavy elements are also seen in FUSE spectra. Although, in principle, these could be included within the models, the FUSE spectral range has only recently become well studied and it is not certain that all the possible transitions have been included. Also, the reliability of the atomic data is untested. In addition, the distribution of heavy elements may be stratified (see, for example, Barstow et al., 2003b), whereas a homogeneous structure is assumed in the models. Finally, creating a grid of individual models for the differing composition of each DAO in the sample would be computationally very time-consuming. Instead, the composition of the G 191-B2B is taken to be typical for hot white dwarfs. The shape and depth of the Lyman lines, and hence the measured parameters, should not be strongly affected by this assumption (Barstow et al., 1998). Where strong photospheric features are seen, that spectral region was excluded from the fit, which prevents the fact that the models were not individually tailored to each object from influencing the result.

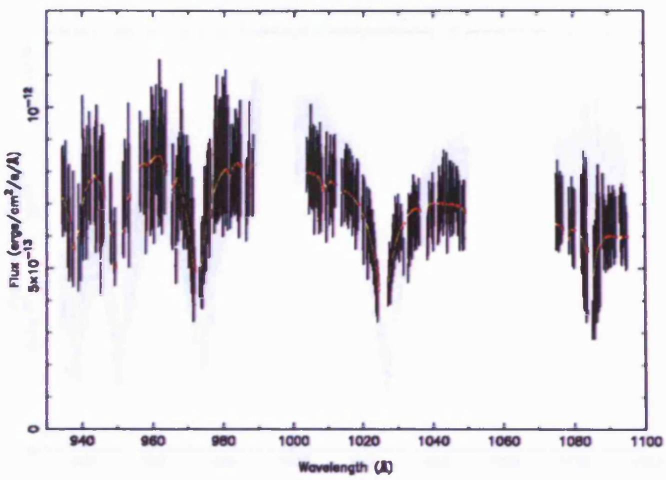

A 7

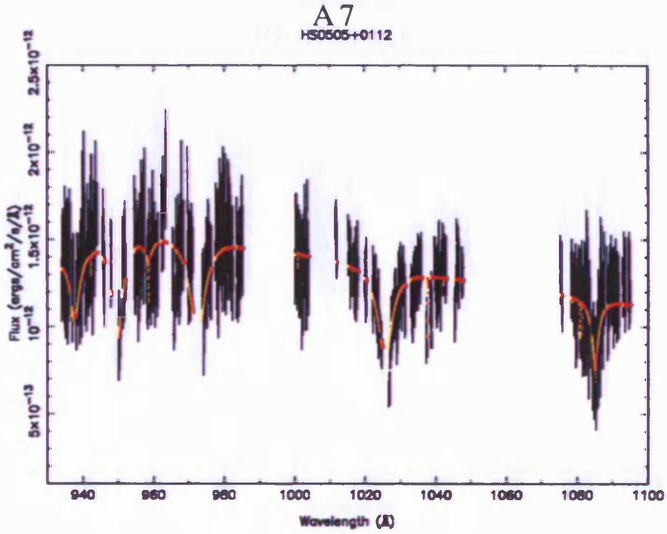

HS 0505+0112

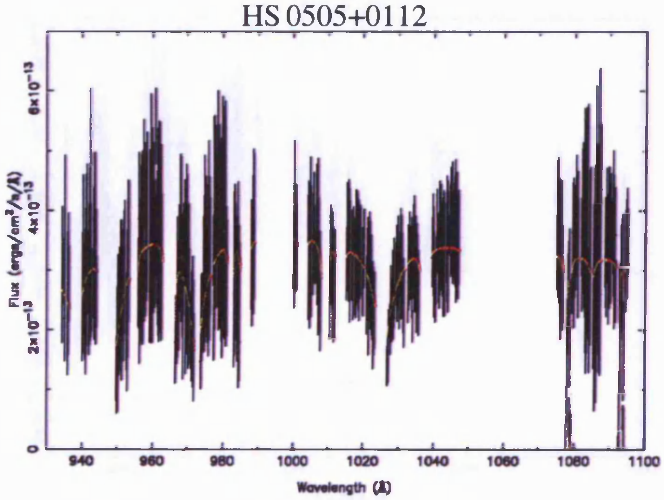

PuWe 1

FIGURE 7.1. Model fits (red lines) to FUSE data (black error bars) for each object. Interstellar and photospheric lines have been removed from the spectra to allow the fitting of the Lyman lines. In spectra where H_2 is seen, a molecular hydrogen model is included in the fit, and narrow H_2 lines are removed from the fit.

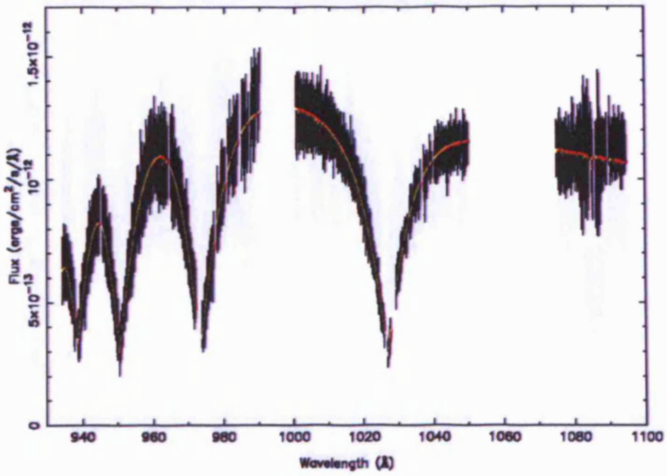

RE 0720-318

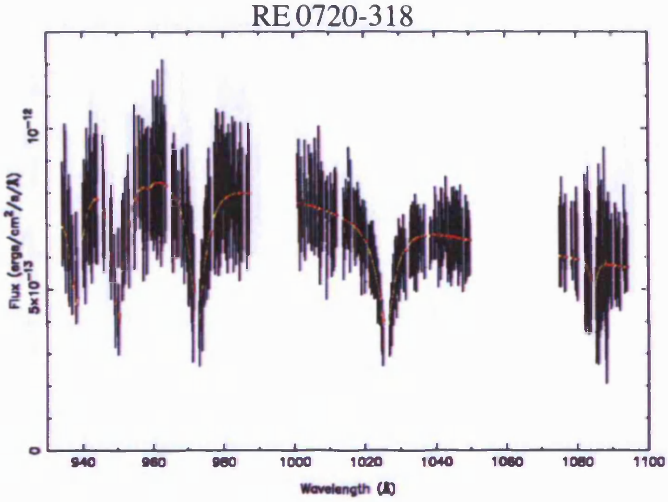

Ton 320

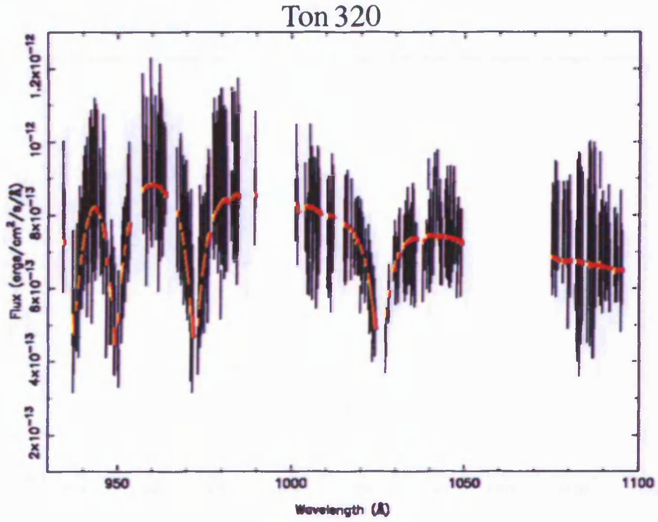

PG 0834+500

FIGURE 7.1. continued...

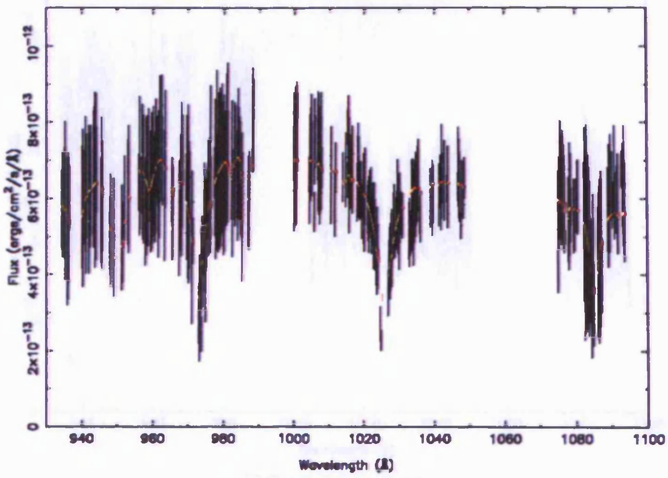

A 31

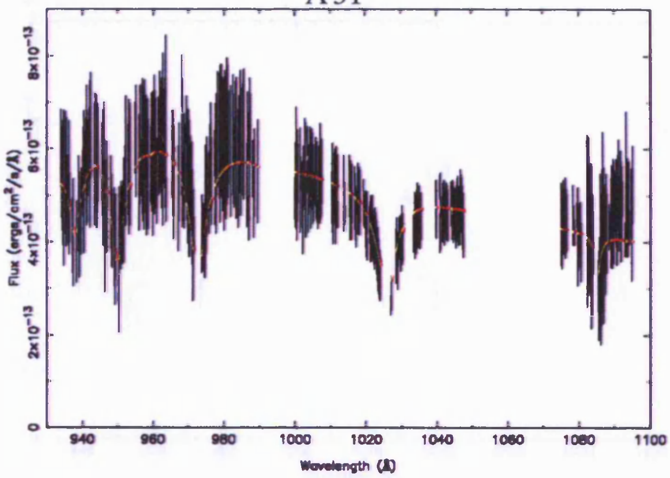

EGB 6

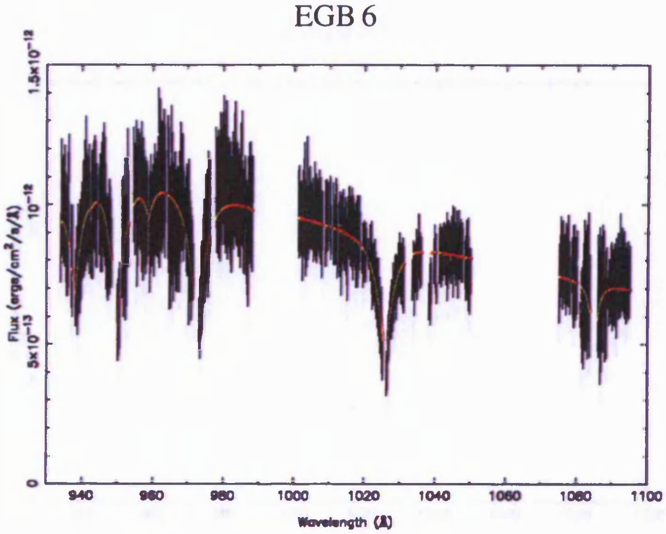

NGC 3587

FIGURE 7.1. continued...

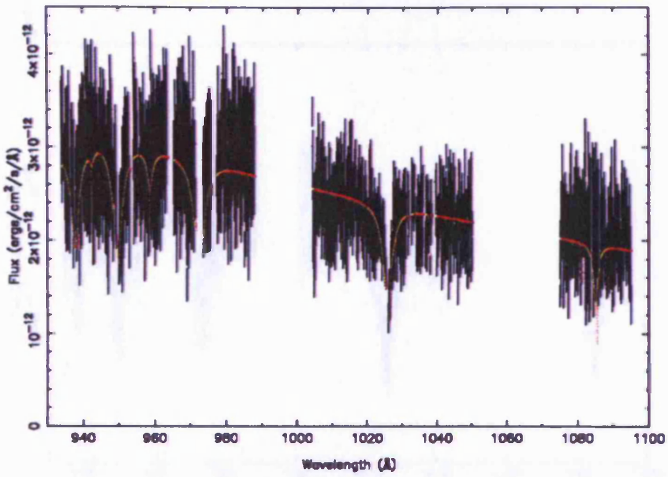

HS 1136+6646

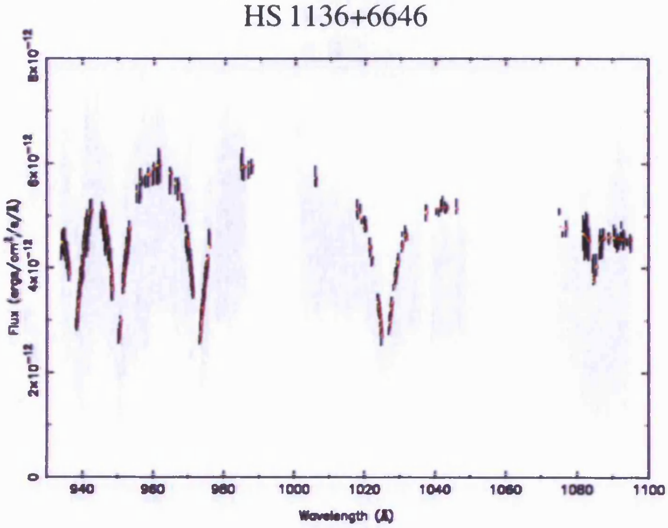

Feige 55

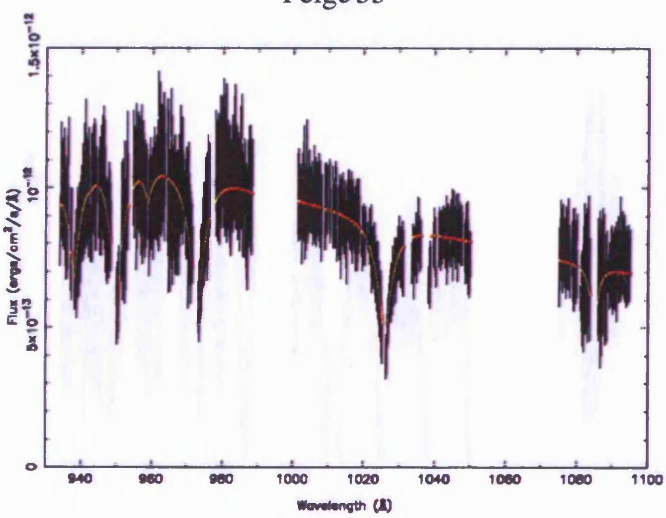

PG 1210+533

FIGURE 7.1. continued...

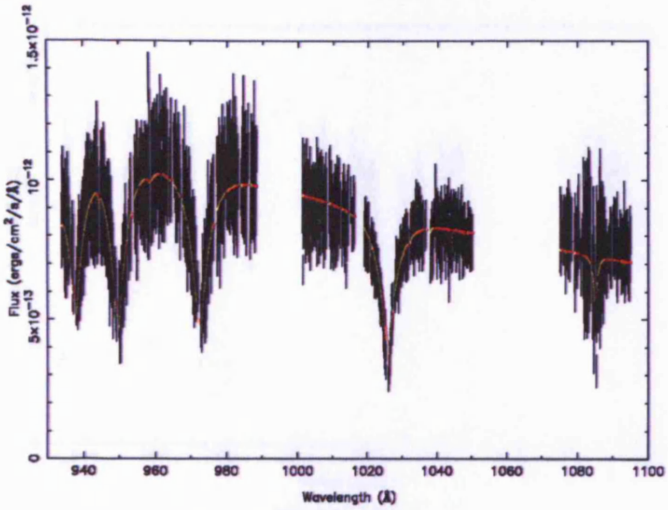

LB 2

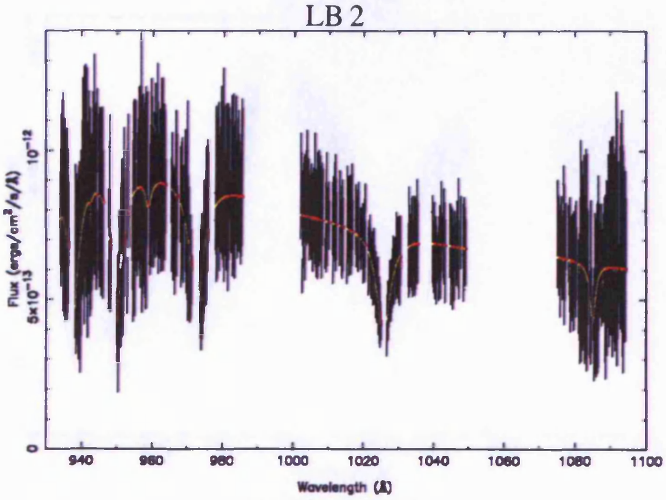

HS 34

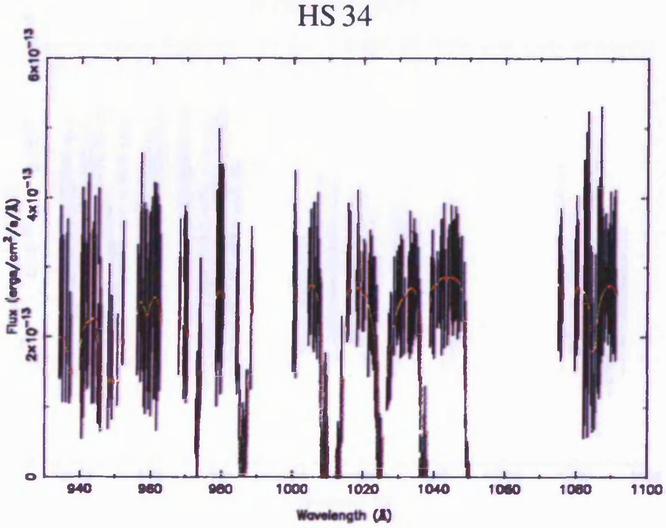

A 39

FIGURE 7.1. continued...

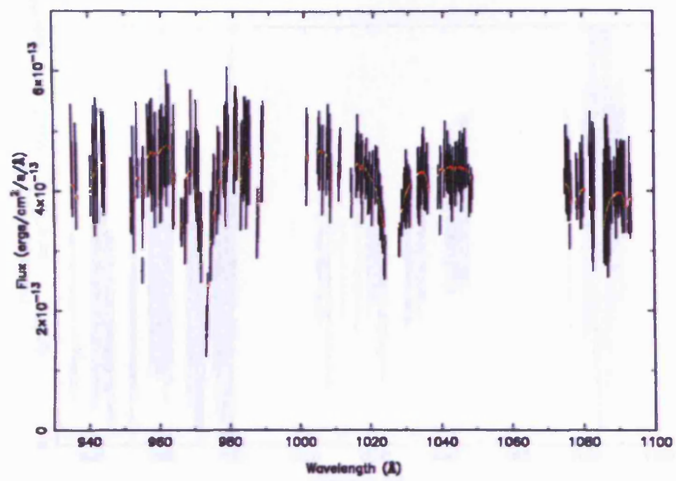

NGC 6720

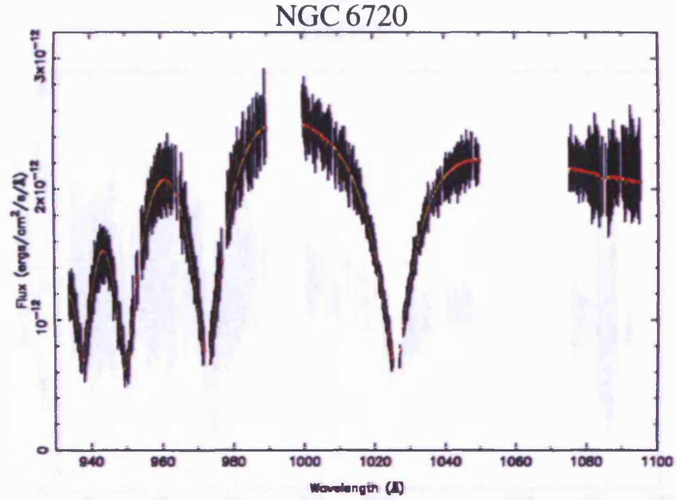

RE2013+400

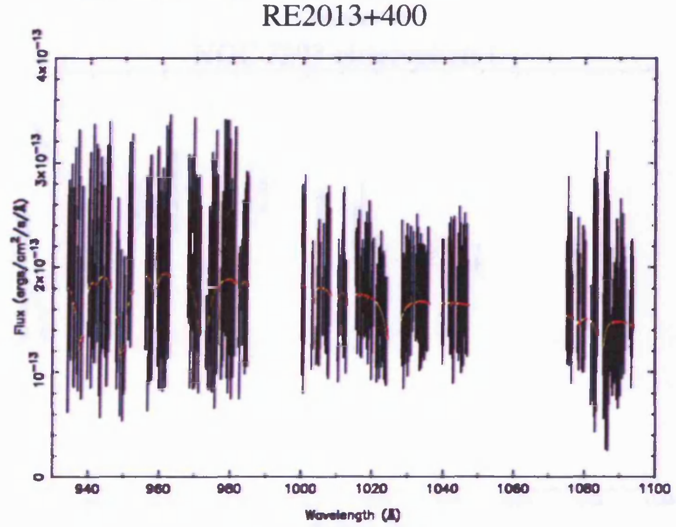

HS 2115+1148

FIGURE 7.1. continued...

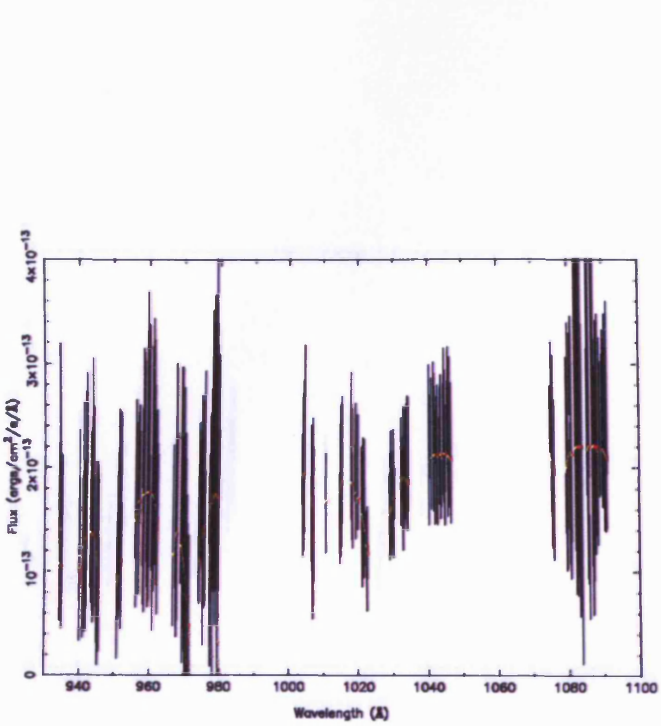

DeHt 5

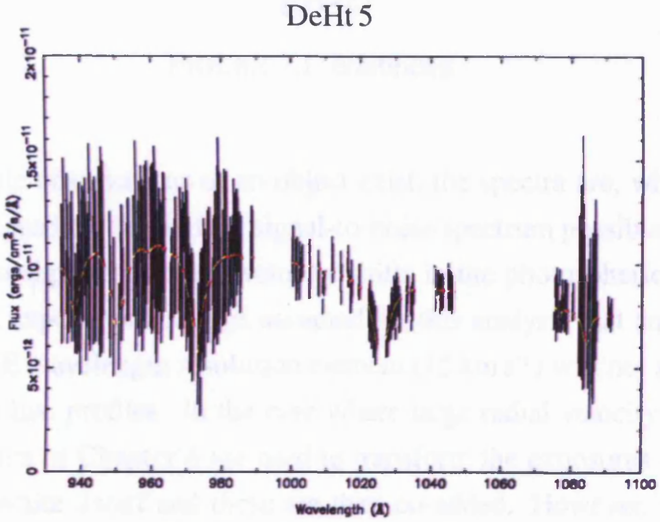

NGC 7293 observation 1

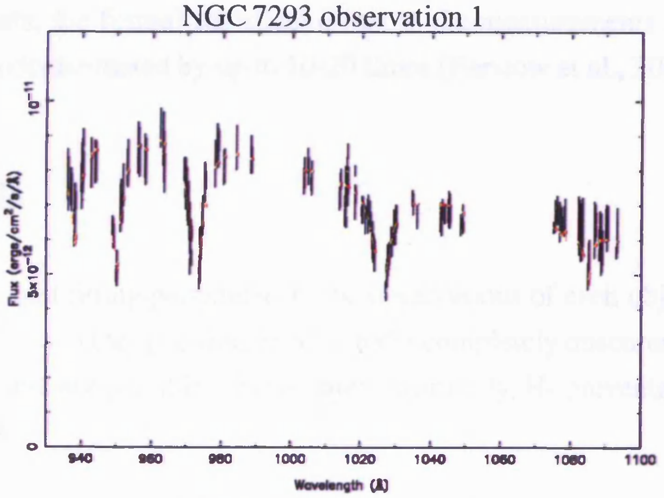

NGC 7293 observation 2

FIGURE 7.1. continued...

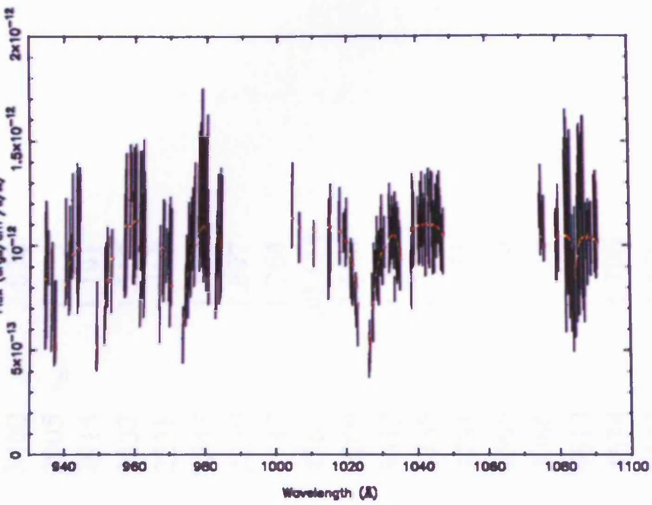

GD 561

FIGURE 7.1. continued...

Where multiple observations of an object exist, the spectra are, where possible, co-added in order to produce the highest signal-to-noise spectrum possible. This is straightforward where no significant radial velocity shifts in the photospheric absorption lines are seen between exposures, and it is assumed for this analysis that any shifts less than the size of a FUSE wavelength resolution element (15 km s^{-1}) will not significantly alter the broad Lyman line profiles. In the case where large radial velocity shifts have been detected, the results of Chapter 6 are used to transform the exposures into the frame of reference of the white dwarf and these are then co-added. However, when using high signal-to-noise data, the formal statistical errors in the measurements of $T_{\rm eff}$ and log g are likely to be underestimated by up to 10-20 times (Barstow et al., 2003b).

7.3 Results

Table 7.1 lists the best fitting parameters to the observations of each object. The number of H_2 absorption lines in the spectrum of NGC 6853 completely obscures the white dwarf spectrum, so a fit was not possible for this object. Similarly, H_2 prevented analysis of the spectrum of S 216.

Table 7.1. Best fitting parameters to the data using homogeneous models. Errors are not quoted where the $T_{\rm eff}$ or log g have exceeded the boundaries of the model grid since a χ^2 minimum had not been reached. Where log $\frac{\rm He}{\rm H}$ has reached the boundary of the grid, no errors in helium abundance are given.

Object	Note	$T_{\rm eff}$ / K	Log g	Log $\frac{\rm He}{\rm H}$	E(B-V)	DOF	χ^2_{red}
A 7		99227^{+2309}_{-2284}	$7.68^{+0.06}_{-0.06}$	$-1.70^{+0.09}_{-0.09}$	$0.001^{+0.003}_{-0.001}$	3067	1.799
HS 0505+0112		120000	7.24	-1.00	0.047	3460	3.820
PuWe 1		109150^{+10223}_{-13648}	$7.57^{+0.17}_{-0.28}$	$-2.59^{+0.55}_{-1.01}$	$0.090^{+0.007}_{-0.008}$	2905	1.533
RE 0720-318	*	53060^{+674}_{-560}	$7.83^{+0.03}_{-0.03}$	$-3.96^{+0.33}_{-0.56}$	$0.019^{+0.002}_{-0.002}$	4915	1.191
Ton 320		99007^{+3779}_{-4292}	$7.26^{+0.07}_{-0.08}$	$-2.00^{+0.06}_{-0.24}$	$0.000^{+0.002}_{-0.000}$	3333	1.513
PG 0834+500		120000	7.28	-4.99	0.033	2238	1.999
A 31		93887^{+4115}_{-2416}	$7.43^{+0.21}_{-0.11}$	-1.00	$0.045^{+0.006}_{-0.004}$	2347	1.487
EGB 6		120000	7.64	-1.84	0.000	2939	1.897
NGC 3587		107570^{+2096}_{-2410}	$7.16^{+0.06}_{-0.08}$	$-1.21^{+0.09}_{-0.10}$	$0.000^{+0.001}_{-0.000}$	4742	1.764
HS 1136+6646	*	120000	6.50	-1.00	0.001	4766	30.134
Feige 55	*	77514^{+612}_{-463}	$7.13^{+0.02}_{-0.02}$	$-2.59^{+0.05}_{-0.05}$	$0.023^{+0.001}_{-0.001}$	1269	2.500
PG 1210+533		47045^{+353}_{-338}	$7.87^{+0.04}_{-0.04}$	$-1.04^{+0.04}_{-0.06}$	$0.040^{+0.005}_{-0.005}$	5672	1.564
LB 2		87622^{+4036}_{-3423}	$6.96^{+0.04}_{-0.04}$	$-2.36^{+0.17}_{-0.17}$	$0.004^{+0.002}_{-0.003}$	4735	1.738
HZ 34		87004^{+7440}_{-3614}	$6.57^{+0.20}_{-0.07}$	$-1.73^{+0.15}_{-0.11}$	$0.000^{+0.002}_{-0.000}$	3781	1.351
A 39		87965^{+4670}_{-4733}	$7.06^{+0.13}_{-0.17}$	$-1.40^{+0.14}_{-0.15}$	$0.130^{+0.007}_{-0.005}$	4569	1.853
NGC 6720		120000	7.59	-1.28	0.068	2086	1.914
RE 2013+400	*	50487^{+1215}_{-272}	$7.93^{+0.02}_{-0.02}$	$-4.02^{+0.31}_{-0.85}$	$0.010^{+0.008}_{-0.002}$	4813	1.288
HS 2115+1148		120000	6.50	-1.00	0.051	4634	1.796
DeHt 5		59851^{+985}_{-2636}	$6.75^{+0.08}_{-0.12}$	-5.00	$0.160^{+0.011}_{-0.007}$	4643	1.640
NGC 7293	Obs. 1	120000	7.38	-1.54	0.009	1872	2.092
	Obs. 2	120000	7.30	-1.50	0.009	1031	5.053
GD 561		75627^{+7141}_{-3436}	$6.64^{+0.06}_{-0.07}$	$-2.77^{+0.22}_{-0.27}$	$0.089^{+0.005}_{-0.006}$	1634	1.962

* All the exposures for the object were shifted into the frame of reference of the white dwarf and co-added.

7.4 Discussion

The number of objects in the FUSE sample is only marginally smaller than the number of objects for which optical data have been obtained (21 compared to 22). Unfortunately, however, the $T_{\rm eff}$ found from the fits to the Lyman lines exceeds the boundary of the model grid in quite a few cases. This means that a χ^2 minimum has not been reached and the value of the other parameters are not necessarily accurate. In each case it is the upper boundary of temperature in the grid, at $T_{\rm eff}$ = 120,000 K, that has been reached. Although it is possible to create models that are hotter than this, the temperature would need to be significantly higher to reproduce the shallowness of the observed Lyman lines and effective temperatures this high are beyond the range normally expected for white dwarfs. There is no obvious cause for this problem, although at the moment it seems confined to the DAOs, since it did not manifest in the DA sample of Barstow et al. (2003c). As the parameters measured for these objects are unreliable they are excluded from the following analysis; this has the effect of reducing the sample size to 14.

The temperature distribution of this sample is shown in Figure 7.2, with the DA distribution of Napiwotzki (1999). The majority of the DAs have a temperature lower than 40,000 K. By definition, all the DAOs are hotter than this; any cooler and they would be DABs. However, the lowest temperature DAOs do overlap with the hotter part of the DA distribution. In this group are the close DAO+dM binaries, the unusual object PG 1210+533, and DeHt 5, which has a low helium abundance compared to the other DAOs. The majority of the DAOs fall into a second group of hotter objects, with $T_{\rm eff}$ >70,000 K. A number of these are hotter than 80,000 K according to the FUSE data, in contrast to the optical results where none were found to be that hot. The log g distibution (Figure 7.3) for DAOs from the FUSE results is flat over the whole range between log g = 6.5 and 8.0, whereas the DA distribution has a strong peak between 7.75 and 8.0, and has a tail towards higher gravities. The temperature and log g distributions therefore point to the DAOs being generally hotter and having lower gravity than the DAs. There isn't a clear peak at low gravity, as seen in the optical data, although the size of the sample is too small to decide if this is significant. Therefore, in contrast to the results of Chapter 3, when separating the DAOs into groups using the result of Lyman line fits, $T_{\rm eff}$ is a better diagnostic than log g.

Using evolutionary models, the $T_{\rm eff}$ and log g can be converted into a mass, radius and luminosity. These are listed in Table 7.2 and Figure 7.4 shows the mass distribution of the objects. The distribution is similar to that obtained from the optical data, for example approximately half the DAOs are in the range between 0.5 and 0.6 $M_\odot$ in

Table 7.2. Results from comparison with evolutionary models.

Object	V	Radius / $R_\odot$	$\pm$	Mass / $M_\odot$	$\pm$	d / pc	$\pm$	Log L / $L_\odot$	$\pm$
A 7	15.60[1]	0.0196	0.0011	0.673	0.018	357	13	1.522	0.066
PuWe 1	15.70[1]	0.0221	0.0049	0.663	0.058	439	16	1.791	0.275
RE 0720-318	16.10[2]	0.0158	0.0004	0.630	0.013	282	1	0.278	0.034
Ton 320	15.74[3]	0.0295	0.0023	0.578	0.014	572	5	1.873	0.102
A 31	15.60[2]	0.0247	0.0051	0.599	0.044	438	18	1.627	0.189
NGC 3587	13.50[1]	0.0332	0.0024	0.582	0.009	238	7	2.120	0.074
Feige 55	13.61[4]	0.0323	0.0007	0.518	0.002	213	1	1.527	0.022
PG 1210+533	14.12[3]	0.0152	0.0005	0.628	0.018	102	1	0.006	0.032
LB 2	15.63[5]	0.0394	0.0017	0.521	0.009	692	5	1.913	0.089
HZ 34	15.73[6]	0.0590	0.0072	0.477	0.026	1083	16	2.252	0.163
A 39	15.60[1]	0.0355	0.0057	0.531	0.027	615	16	1.829	0.282
RE 2013+400	14.60[7]	0.0145	0.0002	0.661	0.009	127	0.3	0.089	0.025
DeHt 5	15.40[1]	0.0448	0.0041	0.412	0.018	605	17	1.362	0.094
GD 561	14.52[8]	0.0525	0.0034	0.442	0.024	521	5	1.907	0.141

[1] Napiwotzki & Schönberner (1995)
[2] From Simbad (http://simbad.u-strasbg.fr/sim-fid.pl)
[3] Kidder (1991)
[4] Green et al. (1986)
[5] Cheselka et al. (1993)
[6] Greenstein (1984)
[7] Barstow et al. (1995)
[8] Greenstein (1974)

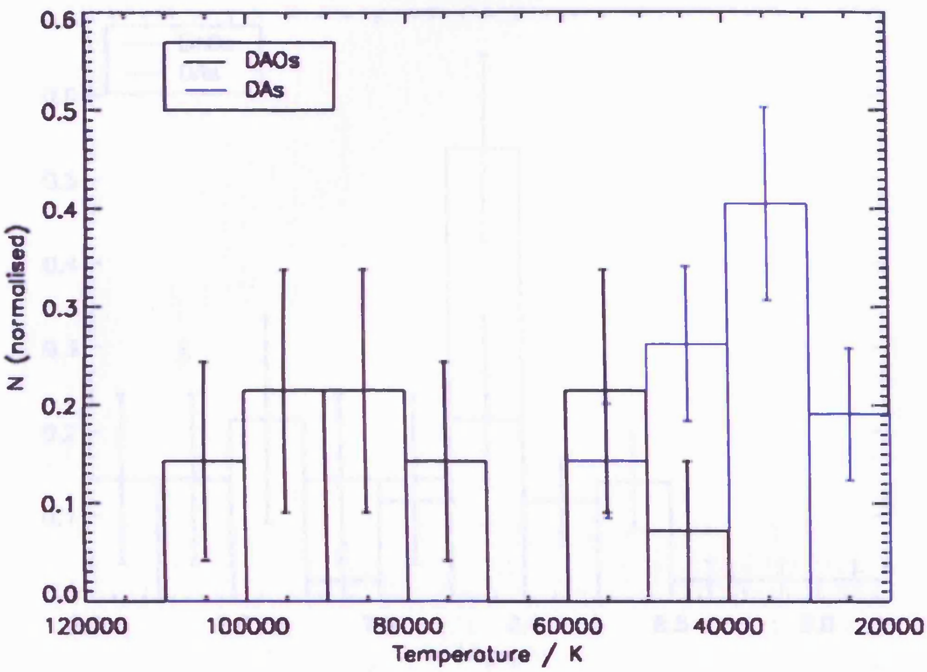

FIGURE 7.2. Temperature distribution for the DAOs from this study, and the DAs of Napiwotzki et al. (1999).

both distributions. However, the masses derived from the FUSE results tend to be higher than those from optical fits. In particular, in contrast to the result of Chapter 3, the mass of HZ 34 obtained from the results of the Lyman line fit is greater than 0.45 $M_{\odot}$. This is important since below that limit, it would be expected that HZ 34 had evolved in a close binary system, yet it does not show any evidence of binarity. However, the mass obtained in this Chapter is within the range where HZ 34 could have evolved from an EHB-manqué star. Overall, more than 50% of the objects are less massive than 0.6 $M_{\odot}$, which is proportionally less than was found using optical data. This is due to the exclusion of those objects whose $T_{\rm eff}$ exceeded the boundary of the model grid, most of which would most likely fall into the lower mass bins according to the results of Chapter 3.

If, as described in Chapter 2, mass loss is the mechanism that is acting against gravitational settling to push the helium towards the line forming region of the star, then a correlation between helium abundance and luminosity is expected. However, Figure 7.5 suggests that there is no strong relationship between the two, although luminosity does separate the DAOs from the DAs, which are shown on the plot with a nominal $\frac{\rm He}{\rm H}$ of 10^{-5}. The exceptions to this are the DAO+dM binaries, which have similar luminosities to the

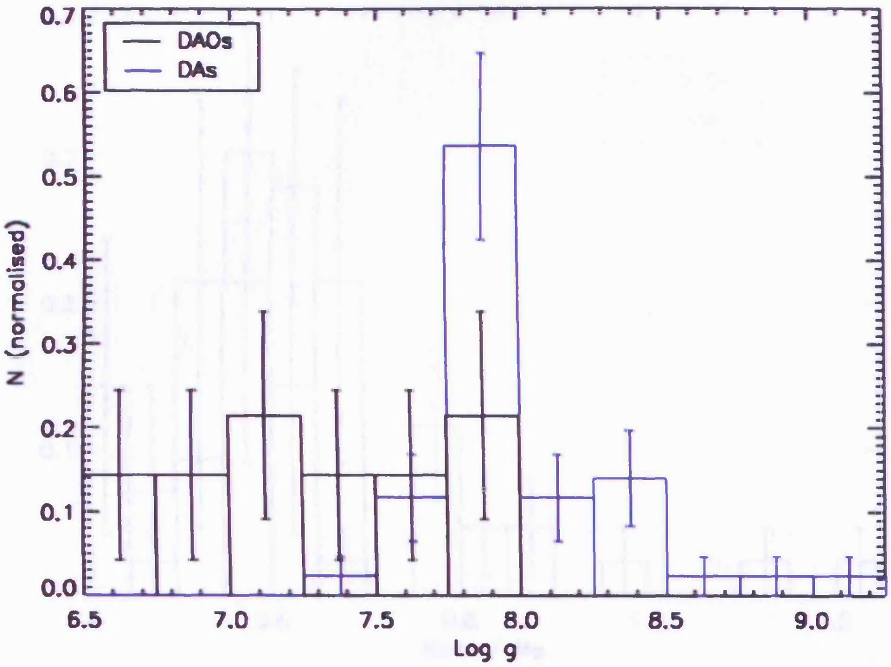

FIGURE 7.3. Log g distribution for the DAOs from this study, and the DAs of Napiwotzki et al. (1999).

DAs. However, if accretion from the winds of their companions is used to explain their high helium abundance, mass loss does not need to be invoked. There are two outlying points: DeHt 5 and PG 1210+533. PG 1210+533 is known to be unusual as it has a varying helium abundance, so it is possible that some other process is acting, e.g. accretion from the ISM. The luminosity of DeHt 5 sets it apart from the DAs, suggesting that if mass loss is believed, its evolution must differ from that of the other DAOs in some way to make it helium poor, since other objects with similar parameters do show helium lines (see Napiwotzki, 1999). The measured helium abundance can also be compared to log g and $T_{\rm eff}$ (Figure 7.6). Although there does not appear to be any correlation between log $\frac{\rm He}{\rm H}$ and log g, there is some suggestion of a relationship with $T_{\rm eff}$. In this case, DeHt 5 is no longer unusual, since it has a similar temperature to the DAs and the DAO+dM binaries. However, PG 1210+533 is still anomalous. The possibility of a correlation between $T_{\rm eff}$ and log $\frac{\rm He}{\rm H}$ was also noted by Napiwotzki (1999), but in their large sample of CSPN, luminosity was found to be more indicative of helium abundance.

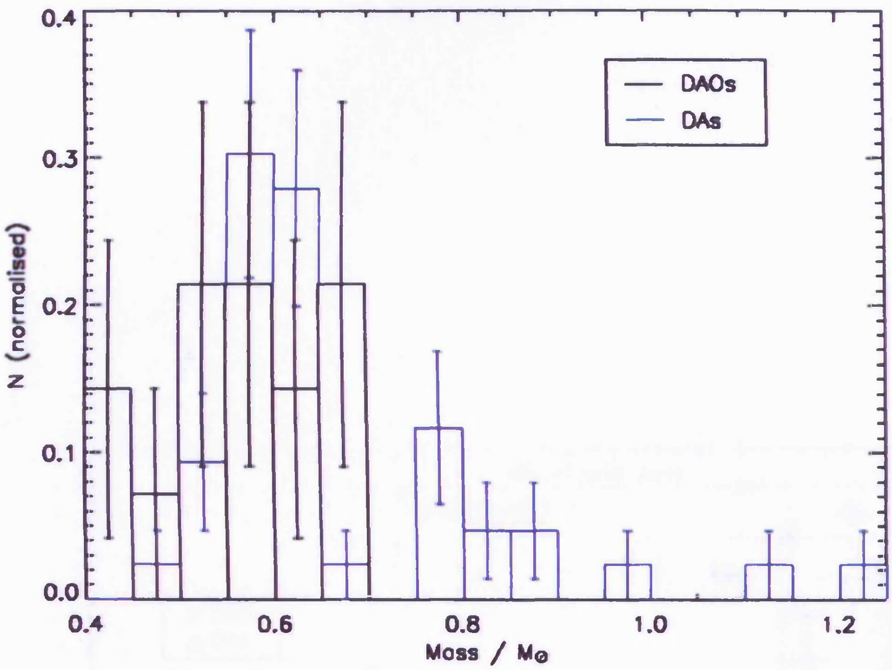

FIGURE 7.4. Mass distribution for the DAOs from this study, and the DAs of Napiwotzki et al. (1999).

7.5 Conclusions

The neutral hydrogen Lyman lines in FUSE data have been used to determine temperatures and gravities for 21 objects. For 7 of these an extremely high temperature model is needed in order to reproduce the observed Lyman lines profiles, which exceeded the bounds of the model grid. This meant that the results from only 14 objects were usable. The luminosities of the high temperature group of DAOs are significantly higher that those of the DAs, as might be expected if mass loss is the mechanism that is acting against gravitational settling in the helium rich objects. However, there appears to be a better correlation between log $\frac{\mathrm{He}}{\mathrm{H}}$ and T_{eff} than with luminosity. Note: some caution is required in the interpretation of these results; there are differences in the effective temperature of models that best fit the Lyman lines compared to the Balmer lines, and it is not known which is the more reliable value to use. See Chapter 8 for a comparison between the Balmer and Lyman results.

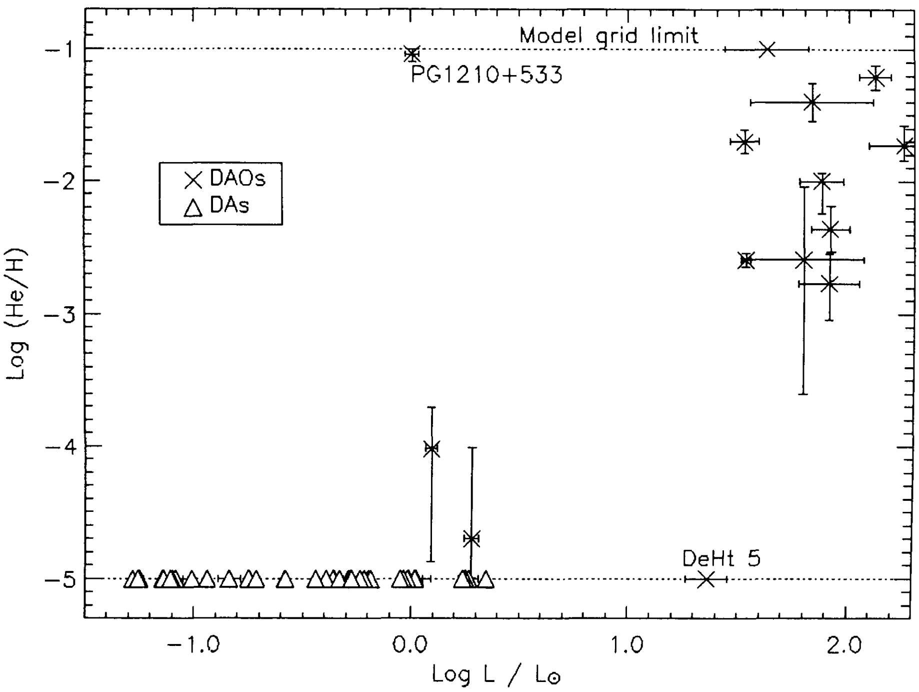

FIGURE 7.5. Plot of the helium abundance against log luminosity.

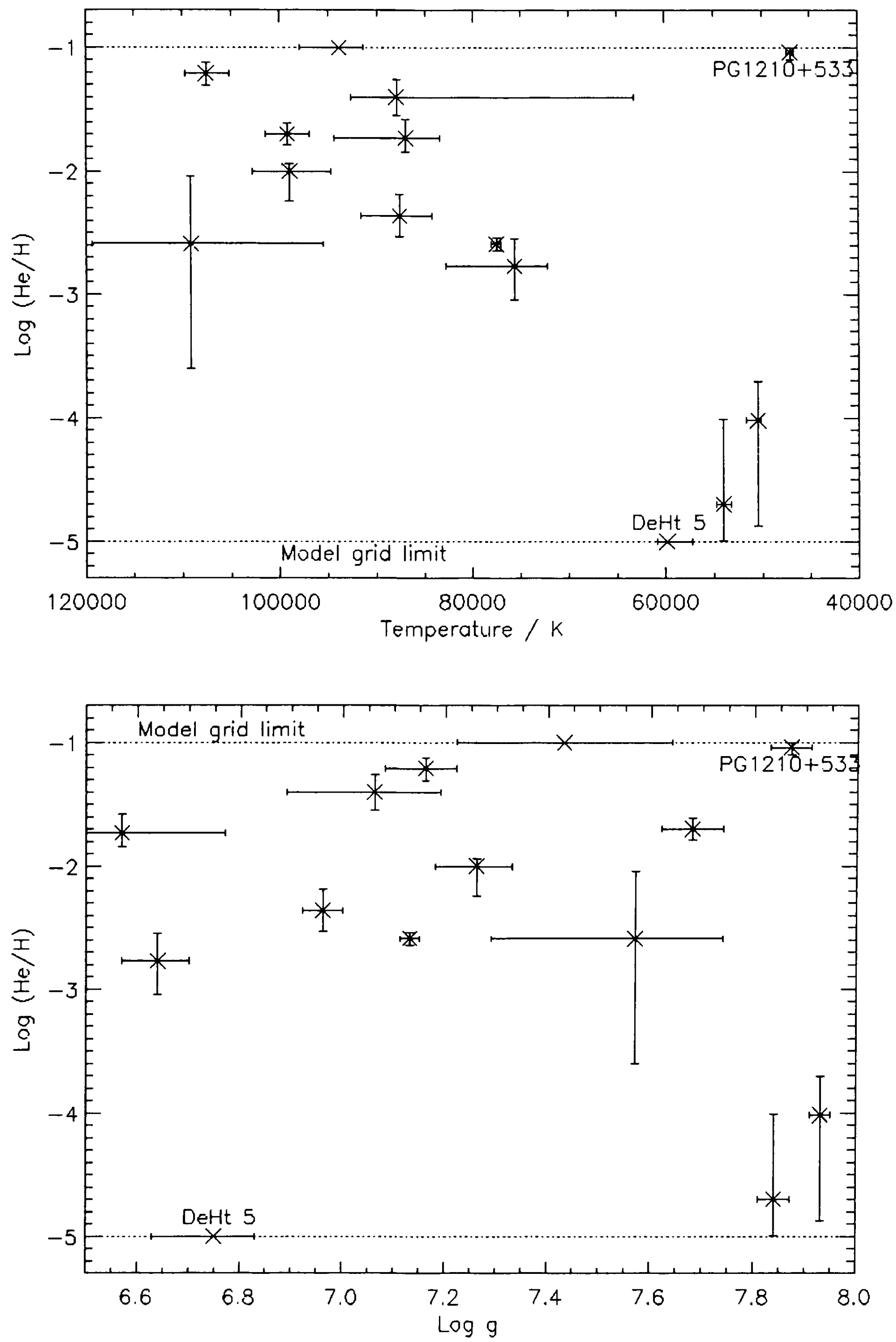

FIGURE 7.6. Plot of the helium abundance against T_{eff} (top) and log g(bottom).

Chapter 8

Comparison between the results obtained using optical and FUSE data

8.1 Introduction

Use of the Lyman lines to determine the fundamental parameters of white dwarfs is important where optical data cannot be used. To check the consistency of measurements made using the different region of the spectrum, Barstow et al. (2001c) used ground-based optical and UV data taken using HUT (Hopkins Ultraviolet Telescope), ORFEUS (Orbiting and Retrievable Far and Extreme Ultraviolet Spectrometers) and FUSE. They found that any disagreement between results obtained using the two wavelength regimes were likely to primarily be caused by systematic effects in the data reduction and analysis rather than because of problems with the models. However, objects hotter than 50,000 K were sparsely sampled, a problem that was later addressed by Barstow et al. (2003b). This later paper found that above 50,000 K the results started to diverge, with the Lyman lines systematically giving a higher temperature than a fit to the Balmer lines of the same object. It was not clear if it was the Lyman or the Balmer lines, or neither, that were giving the correct results, although it was possible to find an empirical relationship between the optical and far-UV results. Two objects did not fit into this relationship; the Lyman $T_{\rm eff}$ for RE 0457-281 was larger than the Balmer measurement at a level significantly higher than for the other objects, while conversely PG 1342+44 was the only object whose Lyman $T_{\rm eff}$ was significantly lower than that obtained from the Balmer lines. The measurements of log g agreed with each other well, apart from four outlying objects. Two of these had log g above 7.8, but the others had the lowest gravities in the sample. The measurement disagreements in the high gravity objects may have been caused by their unusual nature; GD 394 is photometrically variable in the EUV, and may experience episodic accretion, while WD 1620-391 shows quasi-molecular Lyman satellite lines, which were not included in the model atmosphere calculations. The two low gravity objects might represent a true departure from equal Balmer and Lyman log g measurements towards low gravity, although this couldn't be confirmed without including more low gravity objects in the sample. Both Barstow et al. (2001c) and Barstow et al. (2003b) looked at DAs only and it is therefore of interest to do the same comparison with DAO white dwarfs to see if the problem is present and at the same level. In addition, Barstow et al. (2003b) concluded that it was likely to be the detailed physics input into the models that was source of the problem, so the slightly different conditions found in a DAO white dwarf might give some further insight into the problem.

8.2 Results

Table 8.1 lists the mean best fitting parameters determined for those objects where both FUSE and optical data have been obtained, to allow direct comparison between the results from the two wavelength regions.

8.3 Discussion

8.3.1 Comparison of $T_{\rm eff}$ measurements

Figure 8.1 plots the temperatures obtained from the Balmer and Lyman line fits to each object. As with the previous DA study (Barstow et al., 2003b), below ~55,000 K there is good agreement between the Balmer and Lyman results. The three lowest temperature objects (PG 1210+533, RE 2013+400 and RE 0720-318) fall into the high log g group of DAOs, and are similar to the DAs in terms of their temperature and gravity. The FUSE and optical measurements also agree well for DeHt 5, which has a slightly lower mass than the others and a low He abundance, unusual in this sample of DAOs. The remainder of the sample all have higher Lyman $T_{\rm eff}$ measurements than from the Balmer analysis. Most of these form a possible trend of higher Lyman temperatures than Balmer, similar to, and continuing, the trend that is seen in the DAs. As the DAOs are, in general, hotter than the DAs, the average difference between the Lyman and Balmer measurements are slightly higher than that seen in the DAs. The trend is not totally clear, however, since there is considerable scatter in the data points. The magnitude of the differences between

Table 8.1. Mean best fitting parameters for objects where both optical and FUSE data have been obtained. Mean log $\frac{\mathrm{He}}{\mathrm{H}}$ is not listed for the optical data of PG 1210+533 as it is seen to vary between observations. 1σ confidence intervals are given, apart from where the temperature or gravity of the object is beyond the range of the model grid and hence a χ^2 minimum has not been reached.

	OPTICAL						**FUSE**					
Object	T_{eff} / K	±	Log g	±	Log $\frac{\mathrm{He}}{\mathrm{H}}$	±	T_{eff} / K	±	Log g	±	Log $\frac{\mathrm{He}}{\mathrm{H}}$	±
A 7	66955	3770	7.23	0.17	-1.29	0.15	99227	2296	7.68	0.06	-1.70	0.09
HS 0505+0112	63227	2088	7.30	0.15	-1.00	-	120000	-	7.24	-	-1.00	-
PuWe 1	74218	4829	7.02	0.20	-2.39	0.37	109150	11812	7.57	0.22	-2.59	0.75
RE 0720-318	54011	1596	7.68	0.13	-2.61	0.19	53060	614	7.83	0.03	-3.96	0.43
TON 320	63735	2755	7.27	0.14	-2.45	0.22	99007	4027	7.26	0.07	-2.00	0.12
PG 0834+500	56470	1651	6.99	0.11	-2.41	0.21	120000	-	6.50	-	-2.00	-
A 31	74726	5979	6.95	0.15	-1.50	0.15	93887	3153	7.43	0.15	-1.00	-
HS 1136+6646	61787	700	7.34	0.07	-2.46	0.08	120000	-	6.50	-	-1.00	-
Feige 55	53948	671	6.95	0.07	-2.72	0.15	77514	532	7.13	0.02	-2.59	0.05
PG 1210+533	46338	647	7.80	0.07	-	-	47045	345	7.87	0.04	-1.04	0.05
LB 2	60294	2570	7.60	0.17	-2.53	0.25	87622	3717	6.96	0.04	-2.36	0.17
HZ 34	75693	5359	6.51	0.04	-1.68	0.23	87004	5185	6.57	0.20	-1.73	0.13
A 39	72451	6129	6.76	0.16	-1.00	-	87965	4701	7.06	0.15	-1.40	0.14
RE 2013+400	47610	933	7.90	0.10	-2.80	0.18	50487	575	7.93	0.02	-4.02	0.51
DeHt 5	57493	1612	7.08	0.16	-4.93	0.22	59851	1611	6.75	0.10	-5.00	-
GD 561	64354	2909	6.94	0.16	-2.86	0.35	75627	4953	6.64	0.06	-2.77	0.24

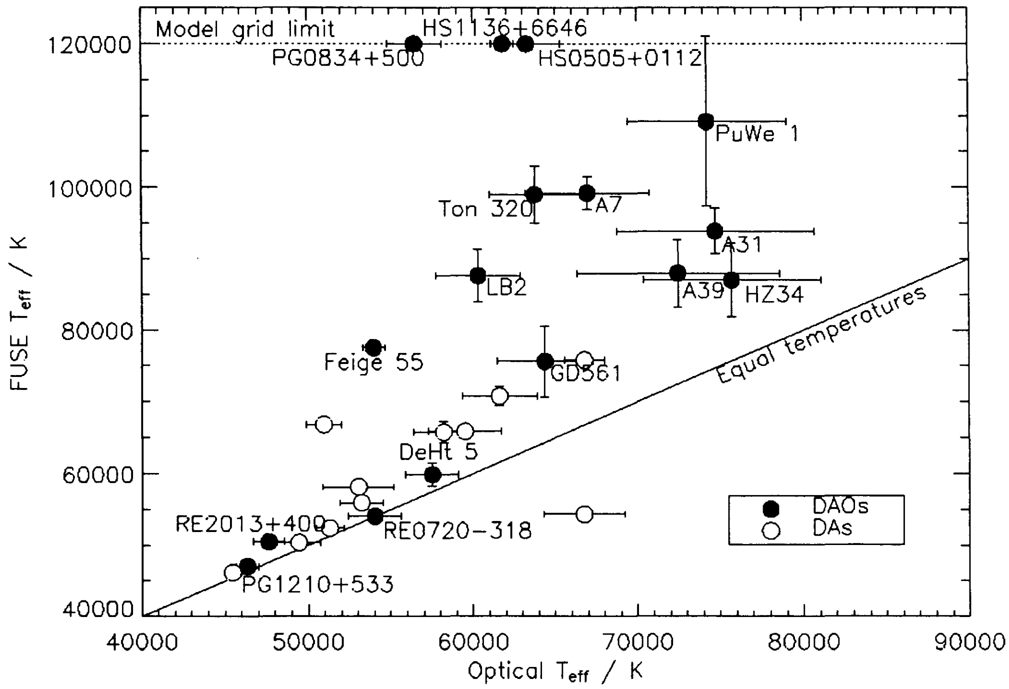

FIGURE 8.1. Comparison of the temperatures obtained from fits to FUSE and optical data. The results for DAs, from Barstow et al. (2003b), are also shown.

the measurements does not appear to have a straightforward correlation with the gravity or helium abundance of the objects (Figure 8.2), although the difference in the measured temperatures appear less at high and low gravity. The objects labelled in the upper plot of Figure 8.2 are unusual and are discussed below. The three lowest helium abundance objects show good agreement between temperatures, but as the DAs of Barstow et al. (2003b) all, by definition, have little or no helium in their line forming regions, this seems unlikely to be significant. For the higher abundance objects, there doesn't appear to be any relationship between abundance and the difference in temperature.

Three of the objects seem unusual when compared to the others in the sample – these are PG 0834+500, HS 1136+6646 and HS 0505+0112. The $T_{\rm eff}$ for all of these has exceeded the upper limit of the model grid in the Lyman analysis, yet the optical data yielded temperatures of ~60,000 K. The optical and FUSE spectra for these objects are completely inconsistent with the models; this is illustrated in Figure 8.3 – if a model is created with parameters as determined from the optical data the Lyman lines are clearly much stronger than that seen in the FUSE data. Also, in the real data there is no decrease in flux as the Lyman series converges, as is present in the model. The 120,000 K model is

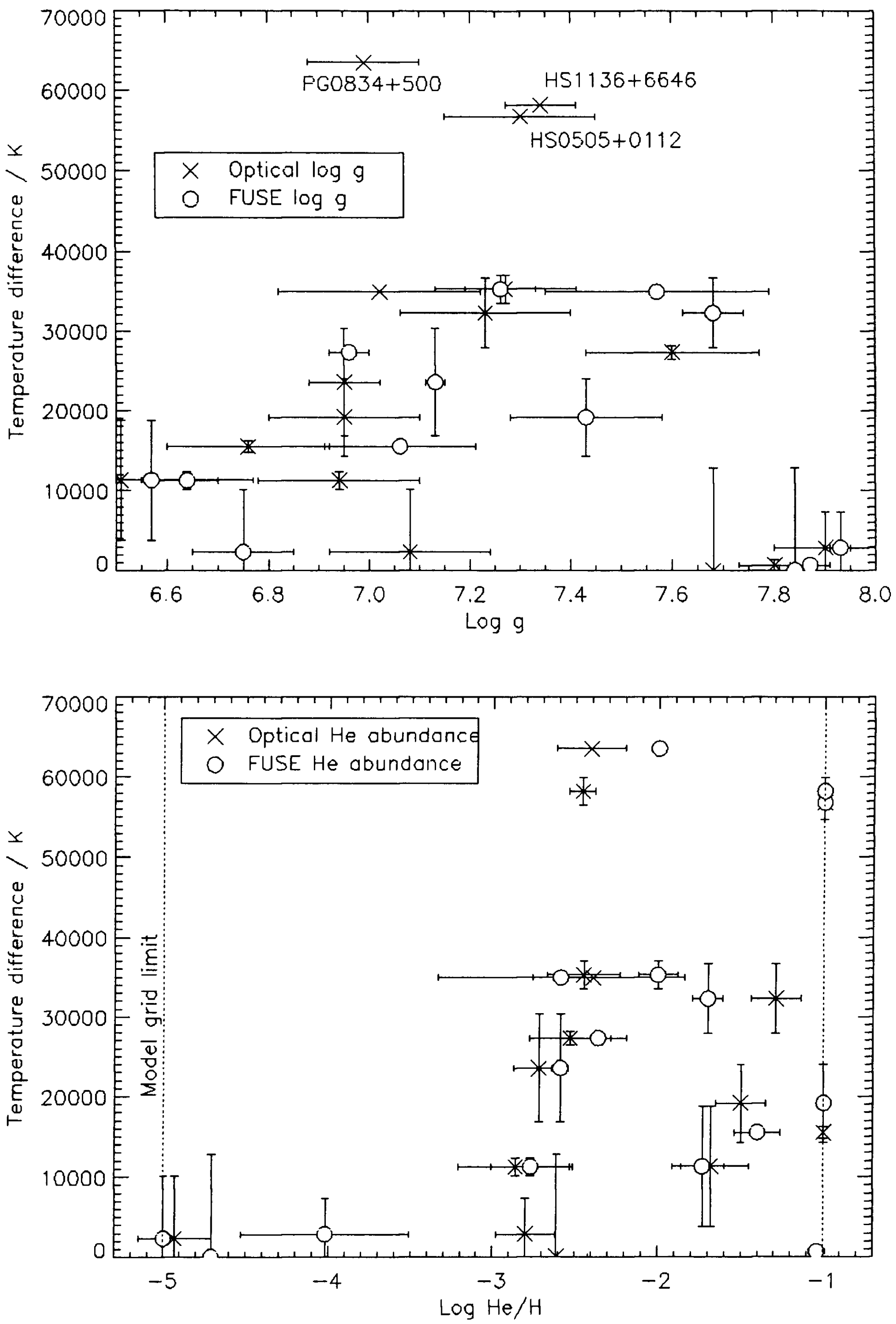

FIGURE 8.2. The difference in $T_{\rm eff}$ measured using the Lyman and Balmer lines, compared to gravity and helium abundance. The results of Barstow et al. (2003b) for DAs are also shown on the log g plot.

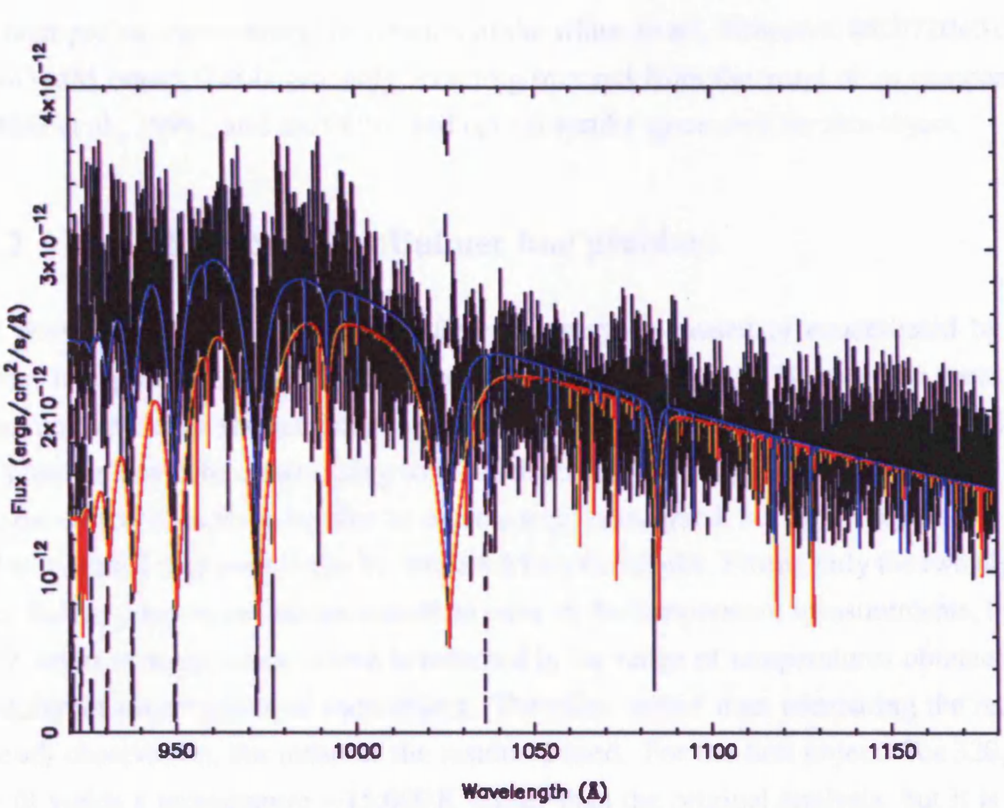

FIGURE 8.3. FUSE spectrum of HS 1136+6646 with atmospheric models with $T_{\rm eff}$ 60,000 K (red) and 120,000 K (blue) overplotted. Log g = 7.5 and log $\frac{\rm He}{\rm H}$ = -2 in both cases.

a closer match to the FUSE data, but it is similarly impossible to reconcile this with the optical results. The optical spectra of HS 0505+0112 all suffer from strong atmospheric effects, and the spectrum of HS 1136+6646 was fluxed so that it was consistent the FUSE spectra. However, comparison of the optical and FUSE spectra of PG 0834+500 with model atmospheres suggests that the relative flux levels of the two spectra are consistent for a white dwarf, so it seems unlikely that another source is contaminating the data. Of these three objects, both HS 1136+6646 and PG 0834+500 are known binaries. It is possible that these objects could be linked by accretion; HS 0505+0112 is peculiar compared to the other DAOs as it shows C IV in its optical spectrum, which is unusual in a hydrogen-rich star. This could be explained if it were accreting material, for example from the ISM. There is also possible evidence of accretion onto HS 1136+6646 (see Sing et al., 2003 for a discussion of observations of HS 1136+6646) – photometric observations, taken using the JKT on La Palma, show low amplitude variations with a period of ~2 hours superimposed on the larger variations which occur as the binary system revolves. This could be due to accretion onto a magnetic spot or pole with the two hour period representing the rotation of the white dwarf. However, RE 0720+318 is a DAO+dM binary that is probably accreting material from the wind of its companion (Dobbie et al., 1999), and the FUSE and optical results agree well for this object.

8.3.2 The influence of the Balmer line problem

It is possible that the temperature differences may be caused or exacerbated by the Balmer line problem, which is described in Chapter 3. As the Balmer line measurements underestimate the temperatures as compared to the Lyman line fits, the Balmer line problem could be contributing to the Balmer/Lyman temperature problem. To test this, the optical data for a number of objects were reanalysed, but with only H_δ, H_ϵ and the He II 4686 Å line used in the fit. Table 8.2 lists the results. Fitting only the two higher order Balmer lines increases the statistical error on the temperature measurements, by up to 5-6 times in some cases, which is reflected in the range of temperatures obtained for the different observations of each object. Therefore, rather than comparing the results for each observation, the mean of the results is used. For the first object, Ton 320, the new fit yields a temperature $\sim$15,000 K higher than the original analysis, but it is still $\sim$20,000 K cooler than the Lyman temperature. Fitting only the higher order lines actually decreased the temperature for A 31. This is due to one of the observations producing a much higher temperature than the other when all the lines were fit – inspection of the two spectra suggests that the core of H_γ is slightly filled in in the second spectrum, most likely due to noise, biasing the result. RE 2013+400 is one of the objects where the Balmer and Lyman temperatures agree, but fitting only H_δ and H_ϵ decreases the temperature, and reduces the level of agreement. In the case of GD 561, fitting the higher order lines has produced a temperature that agrees with the Lyman fit. However, the results are also in statistical agreement with the temperature determined using all the Balmer lines. Therefore, although in some cases fitting only the higher order Balmer lines produces a result that is closer to that obtained from the Lyman lines, in others it actually makes the agreement worse and so cannot fully resolve the problem. The abundance of heavy elements in the photosphere could also influence the fit if the models contained abundances that were too high or too small. However, Barstow et al. (2003b) found that varying the abundances by a factor of 10 from the G 191-B2B values did not make a significant difference to the best fitting temperature. From the results in Table 8.2, it is also clear that using only the weak H_δ and H_ϵ lines can introduce large uncertainties in the results and multiple observations of an object are needed to obtain a reliable temperature if this method of fitting is adopted.

Table 8.2. Comparison of the best fitting parameters to the H_δ, H_ϵ and He II 4686 Å line compared to fits to all the Balmer lines, and the temperature obtained from FUSE data.

	All Balmer lines			**H_δ, H_ϵ and He II only**			**FUSE**
Object	$T_{\rm eff}$ / K	Log g	Log $\frac{\rm He}{\rm H}$	$T_{\rm eff}$ / K	Log g	Log $\frac{\rm He}{\rm H}$	$T_{\rm eff}$ / K
Ton 320	64784^{+3117}_{-2510}	$7.33^{+0.16}_{-0.12}$	$-2.63^{+0.27}_{-0.27}$	86244^{+11556}_{-12103}	$7.10^{+0.19}_{-0.20}$	$-2.52^{+0.31}_{-0.28}$	
	59760^{+3056}_{-2545}	$7.22^{+0.15}_{-0.14}$	$-2.40^{+0.19}_{-0.20}$	74871^{+9968}_{-13516}	$7.28^{+0.23}_{-0.21}$	$-2.23^{+0.19}_{-0.20}$	
	66661^{+2145}_{-3344}	$7.26^{+0.11}_{-0.15}$	$-2.32^{+0.22}_{-0.18}$	74690^{+8093}_{-6051}	$7.45^{+0.18}_{-0.17}$	$-2.20^{+0.19}_{-0.19}$	
MEAN	63735 ±2755	7.27 ±0.14	-2.45 ±0.22	78602 ±5996	7.28 ±0.11	-2.48 ±0.10	99007 ±4027
A31	68242^{+4081}_{-2041}	$7.13^{+0.12}_{-0.13}$	$-1.53^{+0.10}_{-0.18}$	69019^{+6416}_{-11919}	$7.43^{+0.20}_{-0.17}$	$-1.72^{+0.19}_{-0.19}$	
	81209^{+7727}_{-8175}	$6.77^{+0.18}_{-0.15}$	$-1.47^{+0.24}_{-0.12}$	69872^{+10628}_{-3893}	$7.93^{+0.07}_{-0.32}$	$-1.94^{+0.26}_{-0.18}$	
MEAN	74726 ±5979	6.95 ±0.15	-1.50 ±0.15	69446 ±5428	7.68 ±0.18	1.83 ±0.14	93887 ±3153
RE 2013+400	47610^{+1134}_{-767}	$7.90^{+0.10}_{-0.10}$	$-2.80^{+0.12}_{-0.28}$	44994^{+2922}_{-2098}	$7.86^{+0.14}_{-0.17}$	$-2.27^{+0.30}_{-0.28}$	50487 ±575
GD 561	63625^{+3438}_{-1236}	$6.87^{+0.17}_{-0.12}$	$-2.54^{+0.27}_{-0.31}$	72525^{+7300}_{-7743}	$6.99^{+0.23}_{-0.20}$	$-2.52^{+0.27}_{-0.27}$	
	66257^{+5319}_{-2148}	$6.98^{+0.20}_{-0.10}$	$-2.93^{+0.33}_{-0.51}$	60072^{+16470}_{-7792}	$7.37^{+0.32}_{-0.51}$	$-3.00^{+0.27}_{-0.42}$	
	64986^{+3790}_{-2265}	$7.03^{+0.13}_{-0.16}$	$-3.21^{+0.30}_{-0.36}$	82040^{+13502}_{-6973}	$6.83^{+0.16}_{-0.16}$	$-2.16^{+0.27}_{-0.36}$	
	62547^{+4652}_{-2065}	$6.87^{+0.22}_{-0.19}$	$-2.75^{+0.34}_{-0.35}$	78762^{+21238}_{-8952}	$6.96^{+0.33}_{-0.32}$	$-2.63^{+0.33}_{-0.29}$	
MEAN	64354 ±2909	6.94 ±0.16	-2.86 ±0.35	73350 ±5415	7.04 ±0.15	-2.58 ±0.18	75627 ±4953

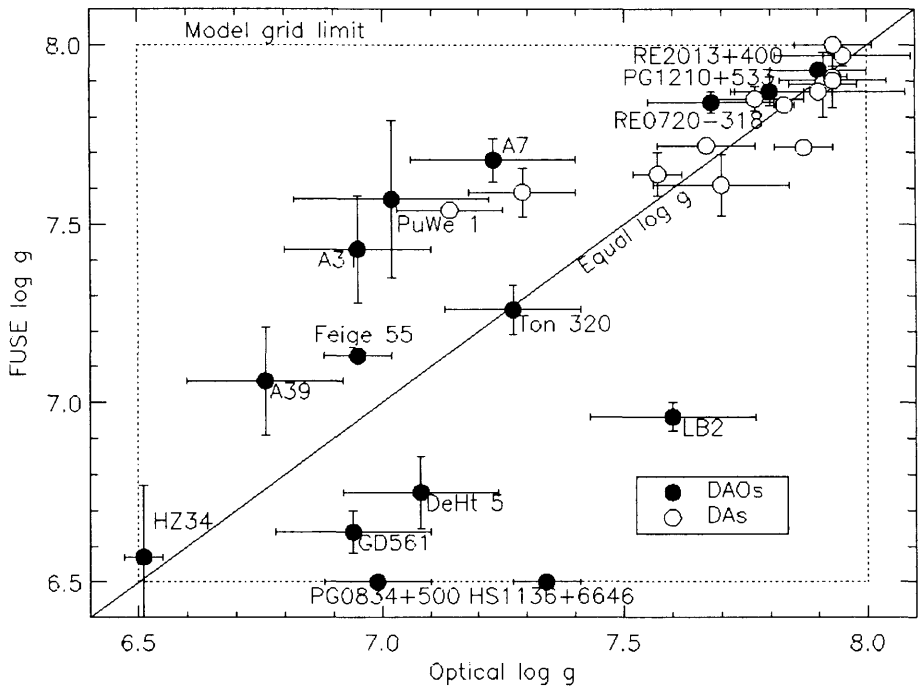

FIGURE 8.4. Comparison of the gravities obtained from fits to FUSE and optical data. The results of Barstow et al. (2003b) for DAs are also shown.

8.3.3 Comparison of log g and log $\frac{\text{He}}{\text{H}}$ measurements

The log g measurements are plotted in Figure 8.4. Considerable scatter is seen in these measurements, with the log g from the Lyman fit greater than the Balmer fit in some cases, and less in others. The three lowest temperature objects that had consistent optical and far-UV temperatures also agree well in log g, and are comparable with the results of Barstow et al. (2003b) for DAs. DeHt 5, however, has a Lyman log g that is $\sim$0.25 lower than the Balmer value. PG 0834+500 and HS 1136+6646, which exceeded the upper limit of the model grid in temperature, also have log g beyond the lowest model atmosphere gravity. However, the Lyman lines are barely visible in these objects so the measurement of log g is unlikely to be reliable. The other objects seem to be scattered either side of the line of equal gravity, with slightly more with higher Lyman log g than Balmer. However, with the small number of objects this may simply be a statistical anomaly. The results from fitting only the higher order Balmer lines did not affect the log g measurements, apart from in the case of A 31. However, this had the effect of changing the Balmer result from a value that was lower than the Lyman value, to one that is higher. It is possible that the differences may simply be due to statistical scatter

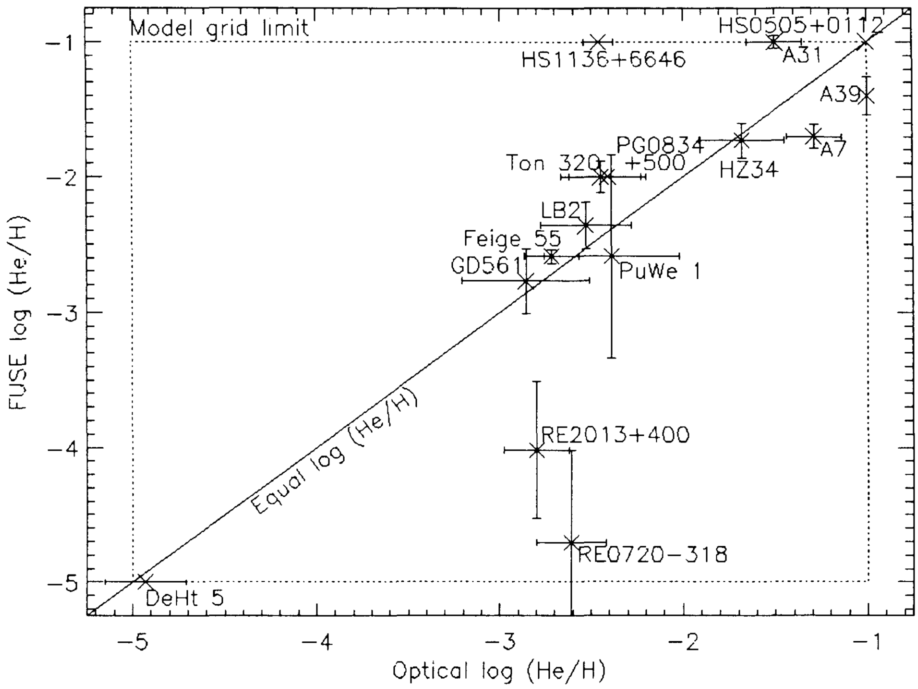

FIGURE 8.5. Comparison of the helium abundances obtained from fits to FUSE and optical data.

in the results, especially if the errors on the measurements are underestimated (Barstow et al., 2001c). A larger sample is needed to determine if this is the case, however.

The DAs studied by Barstow et al. (2003b) do not have a large enough abundance of helium to be detected (if, indeed, any is present). Therefore, this sample of DAOs is the first opportunity to discover if the He abundances measured in the two wavelength regimes are consistent. Although theory predicts that helium should be stratified in the atmosphere of a white dwarf (Vennes et al., 1988), the results of Napiwotzki & Schönberner (1993), Bergeron et al. (1994) and Chapter 3 of this thesis suggest that models containing homogeneously distributed helium better reproduce the line profile of the He II 4686 Å line in the optical data. However, the helium line that is measured in the FUSE data will be formed in a different region of the atmosphere and so a comparison of the abundances found from optical and FUSE data provides an opportunity to study directly the distribution of He in the white dwarf atmosphere. The helium abundances are plotted in Figure 8.5 and show good agreement between the different abundance measurements. This is slightly surprising as the the different temperatures in the models will affect the measured helium abundance.

There are three obvious outlying objects, however – HS 1136+6646, RE 0720-318 and RE 2013+400. The FUSE helium abundance measurement of the first of these objects cannot be relied upon, however, since a χ^2 minimum was not acheived in the fit. Both the other two objects have a lower helium abundance in the FUSE measurement than that obtained from the optical data and both are pre-CV, post-common envelope systems. The difference might be due to the change of helium abundance with depth in the white dwarf atmosphere, or alternatively could be due to the fact that the object was observed at different times at the different wavelengths, since surface inhomogeneities in helium abundance have been observed on the surface of RE 0720-318 by Dobbie et al. (1999).

8.4 Conclusions

Below ~55,000 K the temperatures obtained from fits to the Balmer lines of DAOs seem to agree well with the results of Lyman line fits. Above this temperature, the $T_{\rm eff}$ measured from far-UV data tends to be higher than that obtained from optical observations, with the best agreement found at high and low log g. Although there is considerable scatter in the results, the magnitude of the differences appears larger than that observed in DAs. The reason for the differences is not clear, although it appears possible to rule out the Balmer line problem as the cause. There is also a group of three objects which have extremely shallow Lyman line features, two of which are known to be in binary systems, and whose far-UV spectra can only be fit with a model atmosphere that is hotter than 120,000 K. .

There is considerable scatter in the measurements of log g, and there doesn't appear to be a clear trend. It is possible that the measurement errors are underestimated and that the deviations from the line of equal log g are simply random scatter. The optical and FUSE measurements of helium abundance agree well, apart from in two objects. This suggests that the helium and hydrogen are homogeneously mixed through both the optical and far-UV line forming regions, although the disrepancy between temperatures makes the results uncertain. Two objects, both DAO+dM binaries, have lower helium abundance measured from far-UV data compared to the optical, and this may be due to inhomogeneity in the surface abundance of helium in these objects.

Chapter 9

Heavy element abundances in the atmospheres of DAO white dwarfs

9.1 Introduction

Far- and extreme-ultraviolet spectra of hot white dwarfs often contain many heavy element absorption lines. The abundance of these elements have, in the past, usually been estimated by visually matching line strengths in an appropriate stellar model atmosphere to those observed. This was normally accomplished by varying the heavy element abundances in an atmospheric model within a small range using a spectral synthesis program such as SYNSPEC. A fully converged model was then calculated to check the results. This becomes more difficult to do where there are large numbers of lines of a particular species, and also does not allow a formal error to be assigned to the abundance. To address this problem, Barstow et al. (2003c) constructed a grid of models which covered the range of temperatures and gravities that might be expected for hot white dwarfs, and which contained heavy elements with abundances between 0.01 and 100 times those found in the well studied DA G 191-B2B. They then used a χ^2 minimisation technique, as is commonly used in the fitting of the Balmer and Lyman lines, to find the element abundances in the UV spectra of 25 DA white dwarfs. Carbon and nitrogen were found in all the hottest stars, but were only detected in three white dwarfs that were cooler than ~50,000 K. Oxygen was also not seen in the cooler stars, although the results were poorly constrained because the measurements were based only on O V. The abundance of silicon showed a strong dependance on temperature, with a decline between 55,000 and 40,000 K but was the only element detected in the two coolest objects in the sample. A minimum in Si abundance is predicted by the radiative levitation calculations of Chayer et al. (1995b), but at a temperature 30,000 K hotter than found by Barstow et al. (2003c). Iron and nickel were also detected in the higher temperature objects, but not below 50,000 K. The ratio of Fe to Ni was found to be near constant at 20, which is close to the cosmic value. In the few objects cooler than 50,000 K where heavy elements were seen, they were often stratified. For the hottest white dwarfs abundance seemed to most strongly depend on gravity and although the measured abundances did not match the predicted values very well, they did reflect what would be expected if radiative levitation were the dominant mechanism acting against gravity and preventing the heavy elements from sinking (see Chayer et al., 1995b, Schuh et al., 2002).

Helium is, by definition, overabundant in the line-forming regions of DAOs as compared to the DAs. Whatever mechanism that is causing this might also affect the observed heavy element abundances. Insight into the nature of this mechanism might therefore be gained from studying the strength of absorption of different elements. The temperature of the white dwarf will also affect the ionisation balance of the elements, so the detection, or non-detection, of certain species can be used to constrain the temperature of the white dwarf, and may be useful in determining which of the Balmer and Lyman line temperatures are correct.

9.2 Models and fitting technique

The FUSE spectral range contains absorption lines due to a large number of heavy elements. If, when fitting a FUSE spectrum, the abundance of each element were considered separately, the large number of free parameters and data points would make the fit very difficult. In addition, calculating a model grid in which the abundance of every element was varied individually would be computationally prohibitive. Instead, a grid of models was created using TLUSTY and SYNSPEC, which had $T_{\rm eff}$ ranged between 40,000 and 120,000 K in 10,000 K steps, log g between 6.5 and 8.0 in steps of 0.5, log $\frac{\rm He}{\rm H}$ between -5 and -1 in steps of 1 and heavy element abundance between 10^{-1} and $10^{1.5}$ times the G 191-B2B abundances (Table 3.3), with each grid point having abundances a factor $10^{0.5}$ different to the adjacent point. Models with a higher heavy element abundances than this did not converge, therefore SYNSPEC was used to further increase the abundances by a factor of 10. Scaling the abundances in this way is only valid while it can be assumed that the structure of the white dwarf atmosphere will not be significantly affected by the change. As the abundances that are being used are so high, this assumption is not necessarily valid. However, these abundances were needed to reproduce the strengths of some the absorption lines. The implications of this are discussed later. These

Table 9.1. Wavelength ranges used for spectral fitting, and the main species contained in that region.

Species	λ / Å
N IV	920.0–926.0
N III	990.5–992.5
O VI	1031.0–1033.0
O VI	1036.5–1038.5
Si IV	1066.0–1067.0
O IV	1067.0–1069.0
C IV	1107.0–1108.2
Si III	1113.0–1114.0
Fe V	1113.5–1115.3
Fe VII	1116.5–1118.0
Si IV	1122.0–1129.0
Fe VI	1165.0–1165.9
Fe VII	1165.9–1167.0
C IV	1168.5–1170.0
Ni V	1178.0–1180.0

calculations resulted in 1,440 synthetic spectra. These were split into four smaller grids to make them easier for the XSPEC program to handle. Therefore, four model grids were created, one each for log g = 6.5, 7.0, 7.5 and 8.0. For each object, the model grid used was the one with log g closest to the measured log g of the star.

The FUSE spectra were split into sections, each only containing useful information, i.e. strong absorption lines. These regions, and the dominant species they contain, are listed in Table 9.1. Unfortunately, the abundances of nickel are based on a single Ni V line only, which is weak at temperatures above 100,000 K, whereas all the other elements have at least 2 spectral regions, many containing more than one strong line. If lines due to other elements were present in a region, then those features were excluded from the analysis to prevent them from influencing the fit. $T_{\rm eff}$ and log $\frac{\rm He}{\rm H}$ were constrained to lie within the 1σ error boundaries that were found in Chapters 3 and 7, but were allowed to vary within those ranges. The best fitting element abundance was then found by performing a simultaneous fit to all the lines of a particular element. 3σ errors are found using the $\Delta\chi^2$ distribution with one degree-of-freedom, which allows comparison with the results of Barstow et al. (2003c).

9.3 Results

Tables 9.2-9.7 list the abundance measurements. Those objects whose T_{eff} exceeds 120,000 K are included in order to compare the line strengths of different ionisation stages of elements in the real data to those predicted by the models. Where a heavy element abundance or the -3σ error are less than the lowest grid point, the value is entered as 0.00. In this case, the + error represents the 3σ upper limit. Abundances that were greater than the highest grid point are indicated by a @ symbol.

9.4 Discussion

9.4.1 Objects whose optical and FUSE T_{eff} and log g disagree

For many of the DAOs, T_{eff} obtained from fitting the Balmer lines is different to the Lyman line temperature. These can be divided into those where an empirical relationship can be found between the two temperatures, and those whose FUSE temperature is in excess of 120 000 K. These are listed in Table 9.8. The ionisation balance of the elements, and therefore the abundance inferred from a given line strength, will be affected by the temperature of the white dwarf, hence it is important to determine which is the correct temperature.

FUSE T_{eff} <120,000 K

The relative line strengths of different ionisation stages of each element are more consistent with the temperatures obtained using the FUSE wavelength range rather than from the optical data. To illustrate this, fits to the nitrogen lines in the spectrum of LB 2 are shown in Figure 9.1. N IV is reproduced well by the model when using both the optical and FUSE parameters. However the observed N III line is too weak to be detected at this signal-to-noise, whereas it is present in both the models, although its strength is similar to the noise level in the models with the T_{eff}, log g and log $\frac{\text{He}}{\text{H}}$ determined from FUSE data. As the FUSE derived T_{eff} is higher, the nitrogen is more strongly ionised, hence there is less absorption due to that species.

Table 9.2. Measurements of carbon abundance, with all values expressed as a number fraction with respect to hydrogen.

Object	Source of WD parameters	C/H	-3σ	+3σ
S 216	Optical	1.09×10^{-5}**	2.30×10^{-6}	4.44×10^{-6}
A 7	Optical	1.38×10^{-5}	5.31×10^{-6}	1.54×10^{-5}
	FUSE	4.17×10^{-5}	1.09×10^{-5}	3.84×10^{-5}
H 0505+0112	Optical	1.11×10^{-4}	3.63×10^{-5}	@
	FUSE	@		
PuWe 1	Optical	1.44×10^{-5}**	9.75×10^{-6}	2.22×10^{-5}
	FUSE	4.00×10^{-5}**	1.74×10^{-5}	5.08×10^{-5}
RE 0720-318	Optical	1.10×10^{-6}	5.63×10^{-7}	7.28×10^{-7}
	FUSE	2.97×10^{-6}	1.45×10^{-6}	1.90×10^{-6}
Ton 320	Optical	7.21×10^{-6}	3.01×10^{-6}	4.73×10^{-6}
	FUSE	2.61×10^{-5}	1.39×10^{-5}	2.63×10^{-5}
PG 0834+500	Optical	2.91×10^{-6}**	1.44×10^{-6}	3.51×10^{-6}
	FUSE	6.93×10^{-5}	4.35×10^{-5}	@
A 31	Optical	2.11×10^{-5}	1.41×10^{-5}	2.10×10^{-5}
	FUSE	4.09×10^{-5}	1.52×10^{-5}	5.50×10^{-5}
EGB 6	FUSE	4.00×10^{-5}**	5.98×10^{-6}	9.63×10^{-6}
NGC 3587	FUSE	@		
HS 1136+6646	Optical	1.83×10^{-6}**	4.18×10^{-7}	4.88×10^{-7}
	FUSE	3.19×10^{-5}**	1.24×10^{-5}	1.29×10^{-5}
Feige 55	Optical	2.84×10^{-6}**	1.99×10^{-7}	1.97×10^{-7}
	FUSE	5.01×10^{-6}**	3.11×10^{-7}	5.42×10^{-7}
PG 1210+533	FUSE	4.15×10^{-6}	1.86×10^{-6}	2.85×10^{-6}
LB 2	Optical	2.26×10^{-5}	1.22×10^{-5}	1.17×10^{-5}
	FUSE	2.28×10^{-5}	1.27×10^{-5}	3.05×10^{-5}
HZ 34	Optical	1.27×10^{-6}	5.63×10^{-7}	3.56×10^{-6}
	FUSE	4.01×10^{-6}	1.43×10^{-6}	9.51×10^{-6}
A 39	Optical	1.66×10^{-6}	1.16×10^{-6}	2.18×10^{-6}
	FUSE	1.66×10^{-6}	9.52×10^{-7}	2.14×10^{-5}
NGC 6720	FUSE	@		
NGC 6853	Napiwotzki (1999)	@		
RE 2013+400	Optical	1.61×10^{-6}	1.49×10^{-6}	3.09×10^{-6}
	FUSE	1.61×10^{-6}	1.52×10^{-6}	4.01×10^{-6}
WD 2115+118	FUSE	@		
DeHt 5	FUSE	7.60×10^{-7}	7.20×10^{-7}	9.66×10^{-6}
NGC 7293	FUSE	4.00×10^{-5}**	5.02×10^{-6}	4.11×10^{-6}
GD 561	Optical	1.16×10^{-5}**	4.09×10^{-6}	1.96×10^{-5}
	FUSE	9.19×10^{-5}**	5.64×10^{-5}	@

* C absorption lines obscured by H_2.

** χ^2_{red}>2.

@ Value exceeds $10^{2.5}$ times that in G 191-B2B.

Table 9.3. Measurements of nitrogen abundance, with all values expressed as a number fraction with respect to hydrogen.

Object	Source of WD parameters	N/H	-3σ	+3σ
S 216	Optical	3.37×10^{-7}	2.54×10^{-7}	6.90×10^{-7}
A 7	Optical	7.96×10^{-8}	5.96×10^{-8}	1.22×10^{-7}
	FUSE	6.43×10^{-6}	5.96×10^{-6}	2.33×10^{-5}
H 0505+0112	Optical	7.36×10^{-8}**	4.60×10^{-8}	7.98×10^{-8}
	FUSE	@		
PuWe 1	Optical	@		
	FUSE	@		
RE 0720-318	Optical	1.29×10^{-7}	7.14×10^{-8}	7.78×10^{-8}
	FUSE	1.21×10^{-7}	4.67×10^{-8}	6.89×10^{-8}
Ton 320	Optical	1.36×10^{-6}	1.13×10^{-6}	2.13×10^{-6}
	FUSE	4.99×10^{-5}	6.60×10^{-7}	@
PG 0834+500	Optical	6.89×10^{-6}	2.84×10^{-6}	5.71×10^{-6}
	FUSE	@		
A 31	Optical	1.24×10^{-7}	0.00	1.49×10^{-6}
	FUSE	5.45×10^{-7}	0.00	5.02×10^{-6}
EGB 6	FUSE	@		
NGC 3587	FUSE	2.81×10^{-6}	0.00	4.59×10^{-5}
HS 1136+6646	Optical	6.67×10^{-7}**	1.62×10^{-7}	6.46×10^{-7}
	FUSE	@		
Feige 55	Optical	2.11×10^{-6}**	1.03×10^{-7}	2.05×10^{-7}
	FUSE	@		
PG 1210+533	FUSE	1.50×10^{-6}	6.41×10^{-7}	1.46×10^{-6}
LB 2	Optical	2.51×10^{-6}**	8.64×10^{-7}	1.40×10^{-6}
	FUSE	@		
HZ 34	Optical	2.74×10^{-6}	2.59×10^{-6}	1.27×10^{-5}
	FUSE	3.21×10^{-5}	3.08×10^{-5}	@
A 39	Optical	5.60×10^{-6}	5.06×10^{-6}	@
	FUSE	4.08×10^{-5}	3.87×10^{-5}	@
NGC 6720	FUSE	@		
NGC 6853	Napiwotzki (1999)	@		
RE 2013+400	Optical	8.36×10^{-7}	2.03×10^{-7}	2.62×10^{-7}
	FUSE	3.01×10^{-6}	1.11×10^{-6}	6.36×10^{-6}
WD 2115+118	FUSE	@		
DeHt 5	FUSE	1.08×10^{-5}	0.00	@
NGC 7293	FUSE	@		
GD 561	Optical	@		
	FUSE	@		

* N absorption lines obscured by H_2.

** $\chi^2_{red}>2$.

@ Value exceeds $10^{2.5}$ times that in G 191-B2B.

Table 9.4. Measurements of oxygen abundance, with all values expressed as a number fraction with respect to hydrogen.

Object	Source of WD parameters	O/H	-3σ	+3σ
S 216	Optical	@		
A 7	Optical	#		
	FUSE	#		
H 0505+0112	Optical	#		
	FUSE	#		
PuWe 1	Optical	9.58×10^{-7}**	6.54×10^{-7}	6.10×10^{-7}
	FUSE	2.30×10^{-6}**	2.06×10^{-6}	1.19×10^{-6}
RE 0720-318	Optical	2.95×10^{-6}	1.38×10^{-6}	1.12×10^{-6}
	FUSE	3.04×10^{-7}	8.77×10^{-8}	3.18×10^{-7}
Ton 320	Optical	@		
	FUSE	3.05×10^{-6}**	1.09×10^{-6}	7.86×10^{-8}
PG 0834+500	Optical	@		
	FUSE	5.67×10^{-7}**	2.77×10^{-7}	4.28×10^{-7}
A 31	Optical	3.11×10^{-5}**	7.98×10^{-6}	2.76×10^{-5}
	FUSE	3.04×10^{-5}**	9.02×10^{-6}	6.49×10^{-6}
EGB 6	FUSE	#		
NGC 3587	FUSE	#		
HS 1136+6646	Optical	4.76×10^{-5}**	9.19×10^{-6}	1.13×10^{-5}
	FUSE	9.60×10^{-7}**	7.64×10^{-8}	1.62×10^{-7}
Feige 55	Optical	1.03×10^{-5}**	8.20×10^{-6}	1.26×10^{-5}
	FUSE	3.80×10^{-7}**	3.37×10^{-8}	3.70×10^{-8}
PG 1210+533	FUSE	2.99×10^{-6}	2.00×10^{-6}	2.40×10^{-6}
LB 2	Optical	@		
	FUSE	3.98×10^{-7}**	1.11×10^{-7}	2.97×10^{-7}
HZ 34	Optical	3.03×10^{-5}**	6.06×10^{-6}	3.62×10^{-6}
	FUSE	3.04×10^{-7}**	1.19×10^{-7}	2.09×10^{-8}
A 39	Optical	#		
	FUSE	#		
NGC 6720	FUSE	#		
NGC 6853	Napiwotzki (1999)	#		
RE 2013+400	Optical	2.36×10^{-5}**	6.27×10^{-6}	1.03×10^{-5}
	FUSE	9.60×10^{-6}**	3.47×10^{-7}	5.39×10^{-6}
WD 2115+118	FUSE	9.58×10^{-7}	6.97×10^{-7}	1.30×10^{-6}
DeHt 5	FUSE	7.00×10^{-6}	1.92×10^{-6}	1.30×10^{-5}
NGC 7293	FUSE	#		
GD 561	Optical	2.64×10^{-4}**	1.28×10^{-4}	@
	FUSE	#		

* O absorption lines obscured by H_2.

** $\chi^2_{red}>2$.

No reasonable match to lines possible.

@ Value exceeds $10^{2.5}$ times that in G 191-B2B.

Table 9.5. Measurements of silicon abundance, with all values expressed as a number fraction with respect to hydrogen.

Object	Source of WD parameters	Si/H	-3σ	+3σ
S 216	Optical	7.38×10^{-7}**	8.07×10^{-8}	9.06×10^{-8}
A 7	Optical	7.54×10^{-6}**	3.97×10^{-6}	3.57×10^{-6}
	FUSE	2.27×10^{-5}**	1.08×10^{-5}	1.04×10^{-5}
H 0505+0112	Optical	1.67×10^{-6}**	4.98×10^{-7}	6.95×10^{-7}
	FUSE	7.71×10^{-5}**	2.94×10^{-5}	1.77×10^{-5}
PuWe 1	Optical	9.51×10^{-6}**	6.55×10^{-6}	1.01×10^{-5}
	FUSE	2.99×10^{-5}**	2.09×10^{-5}	1.11×10^{-5}
RE 0720-318	Optical	6.28×10^{-7}	1.26×10^{-7}	2.47×10^{-7}
	FUSE	6.06×10^{-7}	1.45×10^{-7}	1.17×10^{-7}
Ton 320	Optical	4.33×10^{-7}**	3.16×10^{-7}	4.33×10^{-7}
	FUSE	3.73×10^{-6}**	2.02×10^{-6}	5.44×10^{-6}
PG 0834+500	Optical	2.81×10^{-6}**	9.12×10^{-7}	7.58×10^{-7}
	FUSE	3.00×10^{-5}**	4.20×10^{-6}	9.61×10^{-6}
A 31	Optical	3.53×10^{-6}**	1.51×10^{-6}	2.71×10^{-6}
	FUSE	9.42×10^{-6}**	2.42×10^{-6}	4.33×10^{-6}
EGB 6	FUSE	1.68×10^{-5}	7.45×10^{-6}	1.23×10^{-5}
NGC 3587	FUSE	1.43×10^{-5}**	8.08×10^{-6}	9.70×10^{-6}
HS 1136+6646	Optical	4.40×10^{-8}**	0.00	2.96×10^{-8}
	FUSE	1.32×10^{-6}**	7.48×10^{-7}	1.50×10^{-6}
Feige 55	Optical	5.52×10^{-7}**	7.32×10^{-8}	8.20×10^{-8}
	FUSE	5.15×10^{-6}**	1.02×10^{-6}	1.01×10^{-6}
PG 1210+533	FUSE	1.90×10^{-7}	4.58×10^{-8}	5.16×10^{-8}
LB 2	Optical	1.81×10^{-6}	5.87×10^{-7}	7.30×10^{-7}
	FUSE	9.84×10^{-6}	3.53×10^{-6}	6.69×10^{-6}
HZ 34	Optical	4.73×10^{-6}	2.41×10^{-6}	3.76×10^{-6}
	FUSE	5.76×10^{-6}	2.74×10^{-6}	2.09×10^{-5}
A 39	Optical	2.33×10^{-6}	1.24×10^{-6}	1.81×10^{-6}
	FUSE	3.00×10^{-6}	1.27×10^{-6}	5.11×10^{-6}
NGC 6720	FUSE	3.63×10^{-5}**	7.31×10^{-6}	1.71×10^{-5}
NGC 6853	Napiwotzki (1999)	@		
RE 2013+400	Optical	3.68×10^{-7}	8.45×10^{-8}	9.63×10^{-8}
	FUSE	4.71×10^{-7}	1.06×10^{-7}	1.31×10^{-7}
WD 2115+118	FUSE	@		
DeHt 5	FUSE	8.22×10^{-7}	4.10×10^{-7}	1.18×10^{-6}
NGC 7293	FUSE	3.00×10^{-5}**	3.19×10^{-6}	3.93×10^{-6}
GD 561	Optical	5.24×10^{-6}**	2.36×10^{-6}	2.35×10^{-6}
	FUSE	9.51×10^{-6}**	1.34×10^{-6}	4.11×10^{-6}

* Si absorption lines obscured by H_2.

** $\chi^2_{red}>2$.

@ Value exceeds $10^{2.5}$ times that in G 191-B2B.

Table 9.6. Measurements of iron abundance, with all values expressed as a number fraction with respect to hydrogen.

Object	Source of WD parameters	Fe/H	-3σ	+3σ
S 216	Optical	1.16×10^{-5}**	2.38×10^{-6}	3.40×10^{-6}
A 7	Optical	1.24×10^{-5}**	7.44×10^{-6}	1.17×10^{-5}
	FUSE	8.22×10^{-5}	3.82×10^{-5}	7.25×10^{-5}
H 0505+0112	Optical	8.77×10^{-5}**	2.93×10^{-5}	1.31×10^{-4}
	FUSE	9.68×10^{-5}**	6.19×10^{-5}	4.06×10^{-5}
PuWe 1	Optical	2.96×10^{-6}	0.00	1.12×10^{-5}
	FUSE	3.40×10^{-6}	0.00	1.64×10^{-5}
RE 0720-318	Optical	1.32×10^{-6}	0.00	6.62×10^{-6}
	FUSE	2.44×10^{-6}	0.00	1.33×10^{-5}
Ton 320	Optical	1.70×10^{-5}**	1.16×10^{-5}	2.37×10^{-5}
	FUSE	8.73×10^{-5}**	4.64×10^{-5}	1.63×10^{-4}
PG 0834+500	Optical	1.82×10^{-5}**	9.26×10^{-6}	3.18×10^{-5}
	FUSE	4.75×10^{-4}**	3.42×10^{-4}	4.17×10^{-4}
A 31	Optical	9.42×10^{-5}**	5.52×10^{-5}	8.36×10^{-5}
	FUSE	3.16×10^{-4}**	1.52×10^{-4}	2.20×10^{-4}
EGB 6	FUSE	3.16×10^{-5}	2.39×10^{-5}	7.72×10^{-5}
NGC 3587	FUSE	3.36×10^{-5}	2.12×10^{-5}	4.35×10^{-5}
HS 1136+6646	Optical	5.38×10^{-6}**	0.00	1.15×10^{-5}
	FUSE	0.00**	0.00	2.31×10^{-6}
Feige 55	Optical	1.40×10^{-5}**	4.39×10^{-6}	6.16×10^{-6}
	FUSE	1.41×10^{-5}**	3.58×10^{-6}	4.80×10^{-6}
PG 1210+533	FUSE	4.70×10^{-6}	0.00	6.01×10^{-5}
LB 2	Optical	1.73×10^{-5}**	1.10×10^{-5}	1.92×10^{-5}
	FUSE	2.09×10^{-5}	1.06×10^{-5}	2.42×10^{-5}
HZ 34	Optical	2.42×10^{-5}	1.68×10^{-5}	5.82×10^{-5}
	FUSE	7.64×10^{-5}	5.91×10^{-5}	5.10×10^{-4}
A 39	Optical	4.89×10^{-6}	0.00	2.14×10^{-5}
	FUSE	3.74×10^{-6}	0.00	1.53×10^{-5}
NGC 6720	FUSE	6.52×10^{-6}	4.13×10^{-6}	1.01×10^{-5}
NGC 6853	Napiwotzki (1999)	3.16×10^{-5}	2.05×10^{-5}	1.71×10^{-5}
RE 2013+400	Optical	0.00	0.00	2.83×10^{-5}
	FUSE	0.00	0.00	2.16×10^{-5}
WD 2115+118	FUSE	0.00**	0.00	3.76×10^{-5}
DeHt 5	FUSE	3.34×10^{-5}	2.58×10^{-5}	6.20×10^{-5}
NGC 7293	FUSE	3.12×10^{-4}**	7.49×10^{-5}	1.90×10^{-4}
GD 561	Optical	1.55×10^{-5}	9.67×10^{-6}	1.76×10^{-5}
	FUSE	1.45×10^{-5}	8.28×10^{-6}	1.43×10^{-6}

* Fe absorption lines obscured by H_2.

** $\chi^2_{red}>2$.

@ Value exceeds $10^{2.5}$ times that in G 191-B2B.

Table 9.7. Measurements of nickel abundance, with all values expressed as a number fraction with respect to hydrogen.

Object	Source of WD parameters	Ni/H	-3σ	+3σ
S 216	Optical	5.00×10^{-6}	2.69×10^{-6}	4.57×10^{-6}
A 7	Optical	0.00	0.00	1.63×10^{-6}
	FUSE	0.00	0.00	8.94×10^{-6}
H 0505+0112	Optical	1.53×10^{-6}	0.00	5.30×10^{-6}
	FUSE	0.00	0.00	@
PuWe 1	Optical	1.23×10^{-6}	0.00	3.14×10^{-5}
	FUSE	5.65×10^{-6}	0.00	@
RE 0720-318	Optical	3.45×10^{-7}	0.00	4.61×10^{-6}
	FUSE	7.21×10^{-7}	0.00	1.02×10^{-5}
Ton 320	Optical	5.43×10^{-7}	0.00	6.51×10^{-6}
	FUSE	1.82×10^{-6}	0.00	2.97×10^{-5}
PG 0834+500	Optical	8.41×10^{-6}	0.00	4.25×10^{-5}
	FUSE	2.21×10^{-5}	0.00	@
A 31	Optical	2.22×10^{-7}	0.00	3.95×10^{-6}
	FUSE	7.36×10^{-7}	0.00	2.34×10^{-5}
EGB 6	FUSE	2.24×10^{-5}	0.00	@
NGC 3587	FUSE	3.14×10^{-5}	0.00	@
HS 1136+6646	Optical	0.00**	0.00	5.89×10^{-7}
	FUSE	0.00**	0.00	2.48×10^{-5}
Feige 55	Optical	5.55×10^{-6}	3.73×10^{-6}	8.54×10^{-6}
	FUSE	3.71×10^{-6}	2.21×10^{-6}	6.22×10^{-6}
PG 1210+533	FUSE	3.29×10^{-6}**	0.00	1.92×10^{-5}
LB 2	Optical	0.00	0.00	3.12×10^{-6}
	FUSE	0.00	0.00	7.37×10^{-6}
HZ 34	Optical	5.30×10^{-8}	0.00	6.63×10^{-6}
	FUSE	5.12×10^{-8}	0.00	1.92×10^{-5}
A 39	Optical	4.37×10^{-6}	0.00	2.54×10^{-5}
	FUSE	9.93×10^{-6}	0.00	8.87×10^{-5}
NGC 6720	FUSE	3.57×10^{-5}	0.00	@
NGC 6853	Napiwotzki (1999)	@		
RE 2013+400	Optical	0.00	0.00	2.93×10^{-5}
	FUSE	0.00	0.00	3.11×10^{-5}
WD 2115+118	FUSE	@		
DeHt 5	FUSE	1.21×10^{-5}	1.19×10^{-5}	7.27×10^{-5}
NGC 7293	FUSE	@		
GD 561	Optical	1.84×10^{-6}	0.00	1.12×10^{-5}
	FUSE	1.78×10^{-6}	0.00	2.81×10^{-5}

* Ni absorption lines obscured by H_2.

** $\chi^2_{red}>2$.

@ Value exceeds $10^{2.5}$ times that in G 191-B2B.

Table 9.8. A list of objects whose optical and FUSE temperatures agree and those that disagree, separated into those where an empirical relationship between the two can be found, and those with FUSE temperatures greater than 120 000 K.

Agree	Disagree	
	FUSE T_{eff}	
	<120,000 K	>120,000 K
RE 0720-318	A 7	HS 0505+0112
PG 1210+533	PuWe 1	PG 0834+500
RE 2013+400	Ton 320	HS 1136+6646
DeHt 5	A 31	
	Feige 55	
	LB 2	
	HZ 34	
	A 39	
	GD 561	

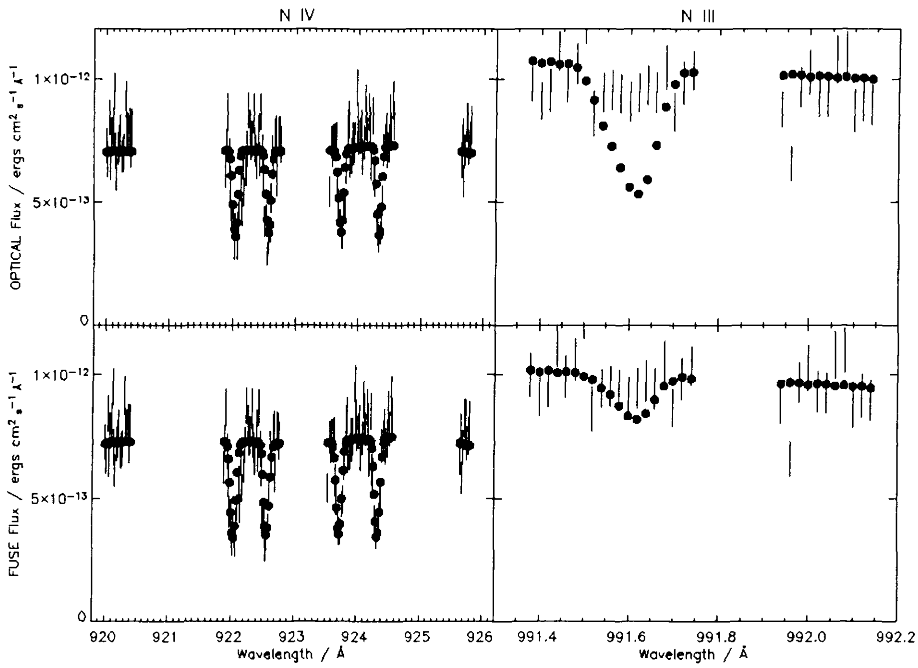

FIGURE 9.1. Best fitting models (black circles) to the nitrogen lines in the FUSE data for LB 2 (error bars), with T_{eff}, log g and log $\frac{\mathrm{He}}{\mathrm{H}}$ as determined from optical (upper plots) and FUSE (lower plots) data.

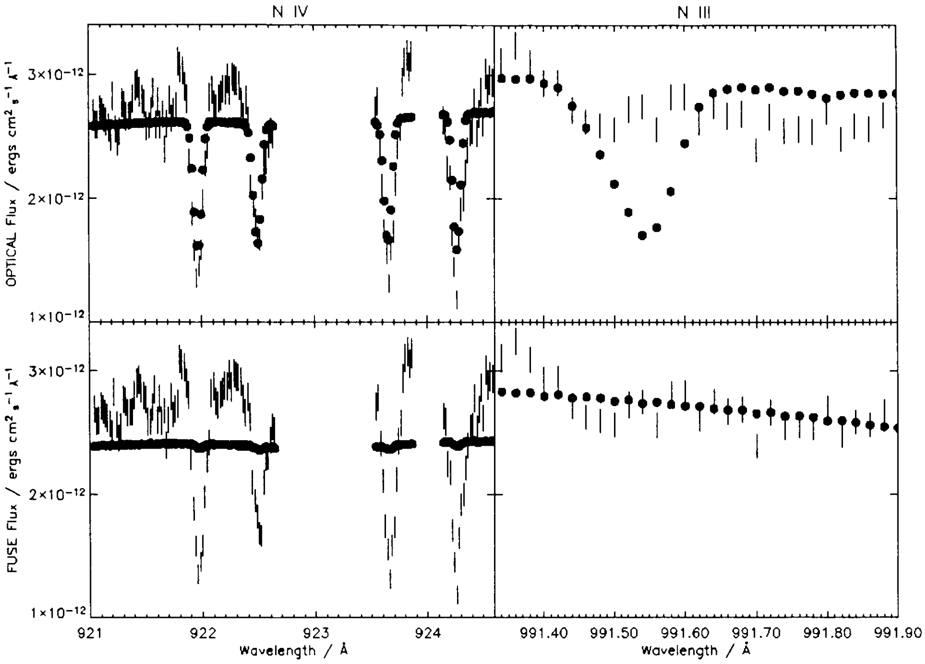

FIGURE 9.2. Best fitting model (black circles) to the nitrogen lines in the FUSE data for HS 1136+6646 (error bars), with $T_{\rm eff}$, log g and log $\frac{\rm He}{\rm H}$ as determined from optical (upper plots) and FUSE (lower plots) data.

FUSE $T_{\rm eff}$ >120,000 K

For objects where the FUSE temperature exceeded the bounds of the model grid, extremely high heavy element abundances are required to reproduce any lines, because of the high ionisation. Figure 9.2 demonstrates this; in this case the predicted strength of the N III in the model that uses the temperature found from optical data is much larger than is allowed by the signal-to-noise of the data. However, the lines in the model disappear almost completely when using the FUSE temperature. Therefore, for these objects, neither the optical or the FUSE temperatures are consistent with the ionisation balance of elements in the FUSE spectrum.

An unknown in the comparisons of predicted line strengths in models with different effective temperatures to real data is the effect of stratification of heavy elements in the white dwarf atmosphere. Although the models used in this chapter assume chemical homogeneity, current research is focusing on using the balance between radiative equilibrium and gravitational settling to predict the abundance distribution of elements within the white dwarf atmosphere (Schuh et al., 2002). For example, assuming homogeneity, lines due to O VI are not predicted to be seen in the FUSE observations if the target star is cooler than $\sim$50,000 K (Barstow et al., 2001b). However if equilibrium between radiative levitation and gravitational settling is assumed in H+O models, strong O VI are seen at temperatures cooler than this (Chayer et al., 2003). Therefore, the change in the temperature structure of the white dwarf atmosphere that stratification would bring about might explain the fact that lines such as N III are not detectable in the data, but appear in the models. Also, a problem with the homogeneous models is that if an absorption line is strong, very large overall abundances of an element are required to reproduce the line strength, whereas in a stratified atmosphere, as the element is concentrated in a layer, a lower overall abundance is required. The equilibrium models are not appropriate for DAOs, however, since if mass loss or accretion is occurring, as is suspected, the diffusion velocity of elements within the atmosphere will not be zero. Therefore, in the future, the investigation of the heavy element abundances in DAOs using physically realistic models would be an important improvement to this work.

9.4.2 Abundance patterns in the different groups of DAOs

As found in the previous chapters, DAOs can be separated into a number of different groups. The heavy element abundance patterns are plotted in Figure 9.3 and the following discusses the results for each group separately. Where the abundances are compared to those of the DAs, I refer to the results of Barstow et al. (2003c). It should be noted, however, that Barstow et al. used $T_{\rm eff}$ and log g from fits to the Balmer lines, although since the Balmer/Lyman temperature problem is not as strong in DAs, as they are in general cooler than DAOs, this will have less of an effect on the measured abundances than is seen in this chapter for the DAOs.

EGB 6, NGC 6720, HS 2115+1148 and NGC 7293

For each of these objects there are no optical observations and the measured $T_{\rm eff}$ from the fits to FUSE data is in excess of 120,000 K. As described in §9.4.1, the predicted line strengths in models this hot are too weak to reproduce the observed lines, hence the measured heavy element abundances are unreliable.

PG 1210+533

PG 1210+533 cannot easily be associated with any group of objects as it does not belong with the low mass DAOs, yet does not appear to have a companion. Homogeneous

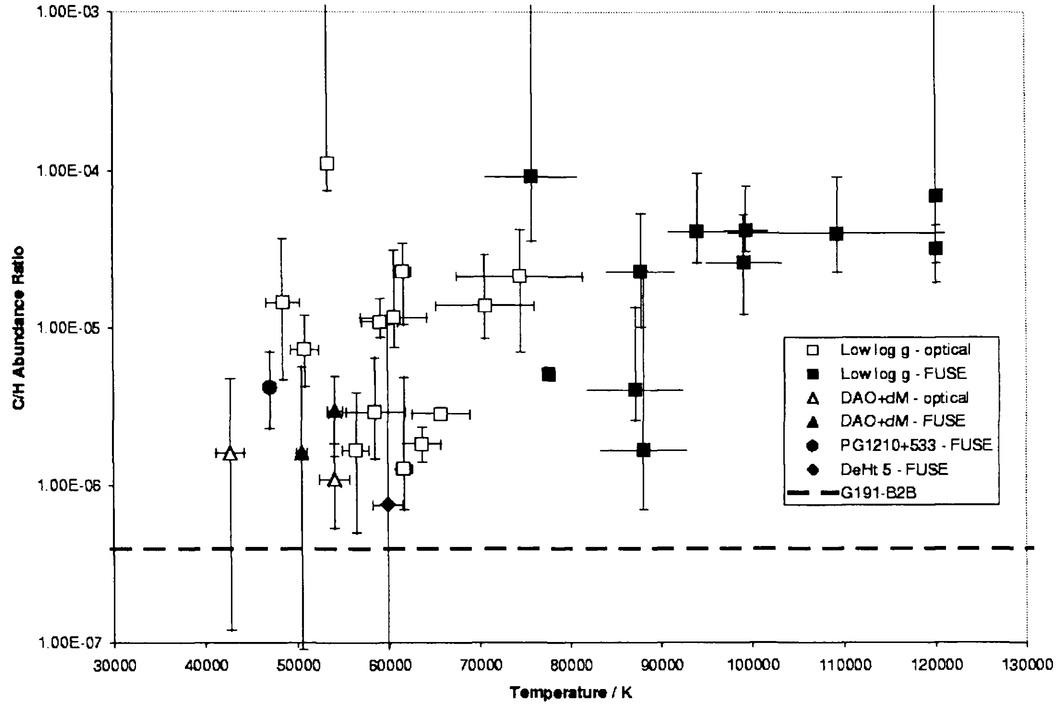

Carbon

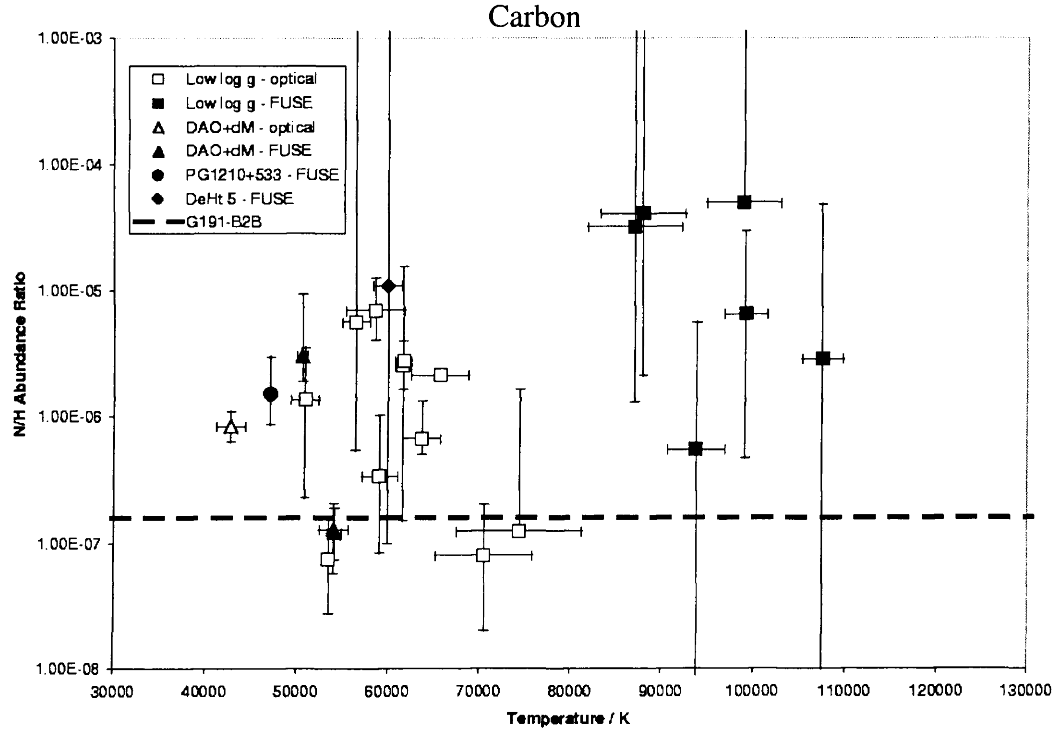

Nitrogen

FIGURE 9.3. Plots of the heavy element abundances. The dashed line indicates the G 191-B2B abundance, from Barstow et al. (2000).

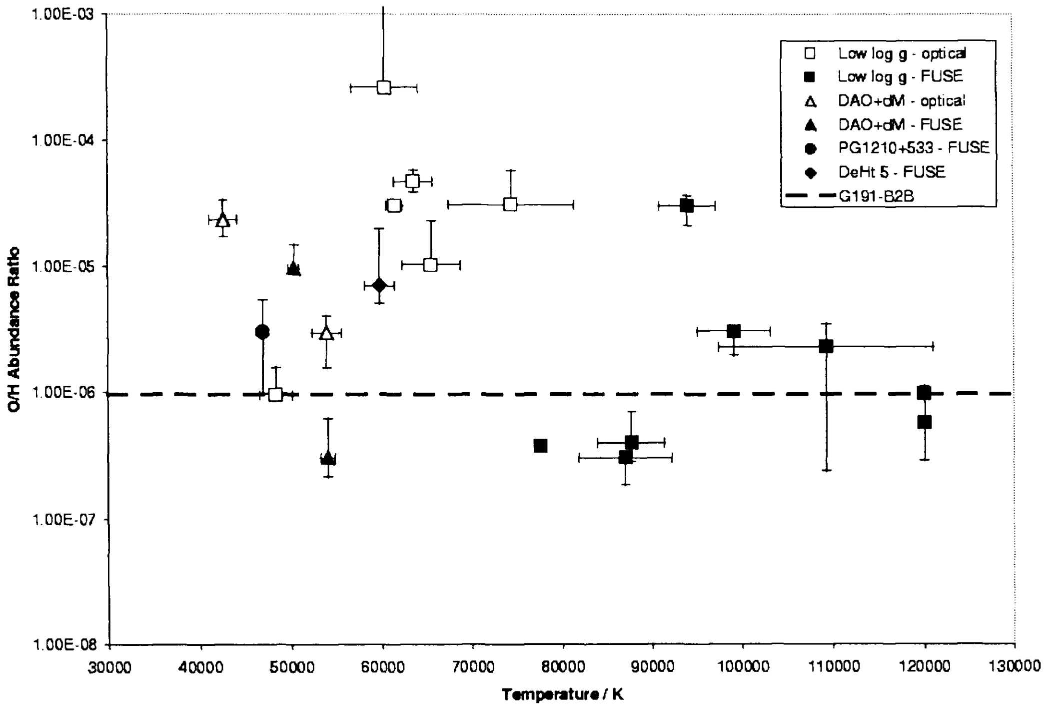

Oxygen

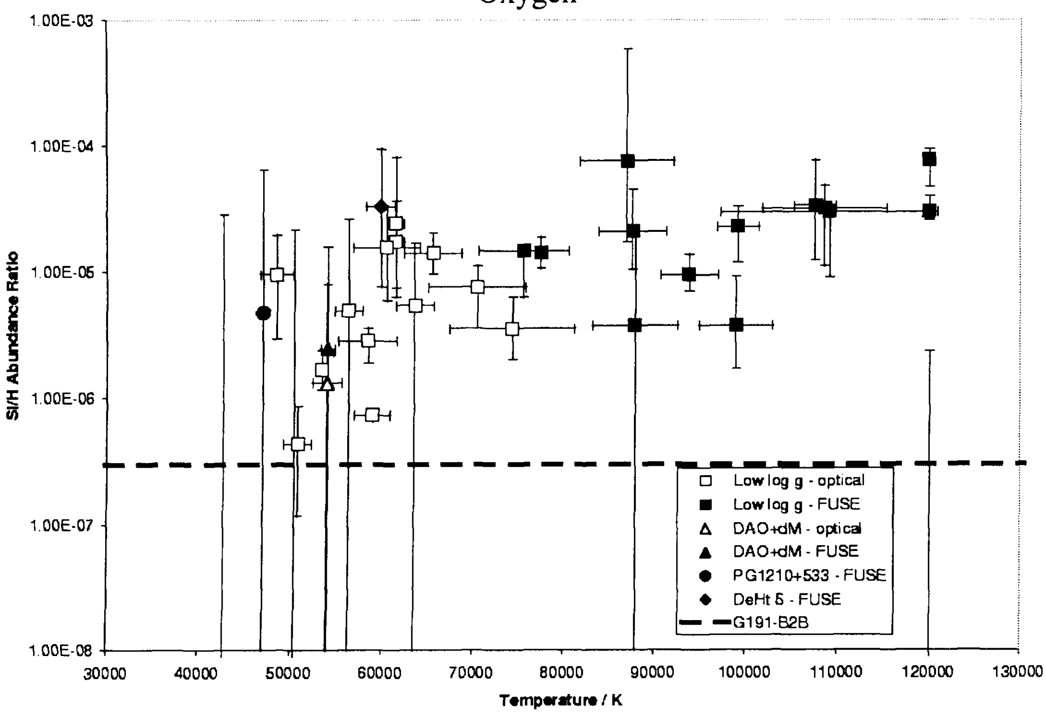

Silicon

FIGURE 9.3. continued...

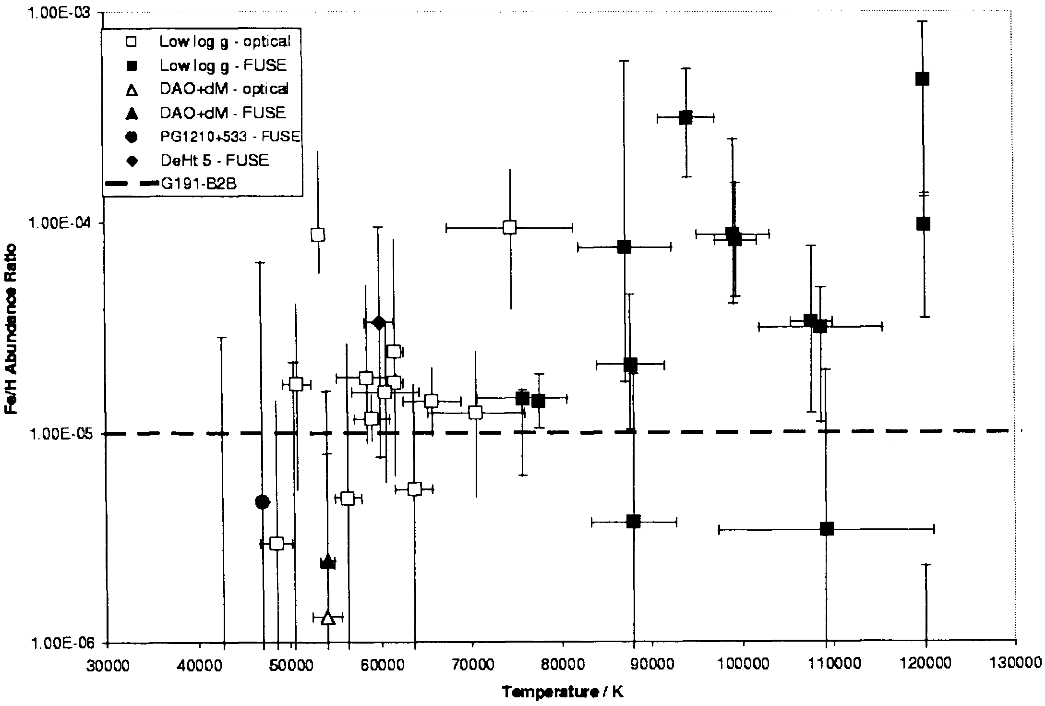

Iron

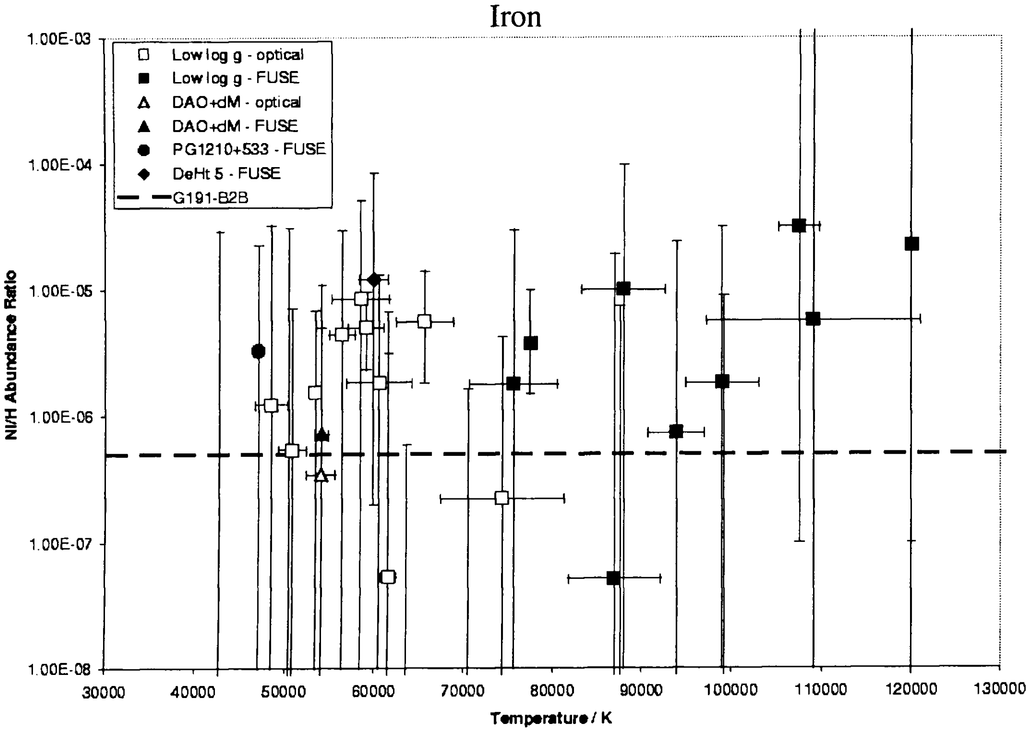

Nickel

FIGURE 9.3. continued...

models provide a reasonable fit to all the elements, and the measured abundances are similar to those seen in the DAs.

DeHt 5

This object has a low helium abundance and was only identified as a DAO from its HST STIS spectrum. Its heavy element abundances seem slightly higher than those seen in the DAs. This object is difficult to classify; it appears to be isolated and has a low mass, yet its helium abundance does not match the other DAOs with similar characteristics. Objects experiencing mass loss will have elevated heavy element abundances, therefore if DeHt 5 has just passed the wind limit, and the elements are sinking back into the atmosphere, this is qualitatively what might be expected.

RE 0720-318 and RE 2013+400

Both RE 0720-318 and RE 2013+400 have similar mass to the DAs, and have dM companions. It is likely that at least one of these (RE 0720-318, Dobbie et al., 1999) is accreting from the wind of its companion. The optical and FUSE T_{eff} and log g agree well for these objects, although the measured helium abundance is lower from the FUSE data as compared to the optical value for both. Carbon is overabundant in both, compared to the DAs. The nitrogen abundance of RE 0720-318 is similar to that seen in the DAs, but is overabundant in RE 2013+400. The oxygen abundances for RE 0720-318, measured using the optical and FUSE parameters, are different by a factor of 10. This seems related to the different helium abundances measured from the two wavelength regimes, as the strength of the predicted oxygen lines in the models changes if log $\frac{\text{He}}{\text{H}}$ is altered but the other parameters are kept constant. This also appears to be the case for RE 2013+400, although a good fit to the oxygen lines could not be obtained. For the DAs, the observed silicon abundance falls for objects cooler than $\sim$55 000 K. Both the RE 0720-318 and RE 2013+400 silicon abundances appear to fit in well with this fall away. The iron abundances also match those observed in the DAs very well; RE 0720-318, which is slightly hotter than 50,000 K has an abundance of $\sim 10^{-6}$, whereas iron is not detected in RE 2013+400, which is cooler than 50 000 K. The same is observed for nickel.

The results for suggest that RE 0720-318 and RE 2013+400 are very similar to the DAs, although the lighter elements, particularly C, appear be relatively overabundant. If these objects are accreting lighter elements, then this could explain their overabundance in the white dwarf atmosphere, and also the observed helium lines. It appears less compatible with the explanation that common envelope evolution has stripped hydrogen from the progenitor, as naively you would then expect increased abundances of all the heavy elements.

The low log g DAOs

This group have low log g and low mass, and consist of the remainder of the DAOs. The results of Chapter 6 suggest that they are isolated white dwarfs, apart from PG 0834+500 and Feige 55. Some of the results appear unusual compared to the others; the carbon abundance of LB 2 and HS 0505+0112 is high if T_{eff} and log g determined from optical data are used, but do not seem strange if the FUSE parameters are adopted. Some of the objects had nitrogen abundances that exceeded the bounds of the model grid; the abundances for PuWe 1 and GD 561 were greater than $10^{2.5}$ times the G 191-B2B nitrogen abundance when both the optical and FUSE parameters were used, and the same occurred for the measurements using the FUSE parameters for Feige 55 and LB 2. Fits to the oxygen lines were poor; O VI was much stronger in the real data than in the models. This suggests that oxygen is stratified in the white dwarf atmospheres - see Chayer et al. (2003). Like oxygen, the fits to silicon lines were generally poor. The abundance of iron was poorly constrained by the lines that are present in the FUSE data, but nickel appears to be underabundant, and was only detected in a few cases. This may be due to the small number of nickel lines that could be used to measure abundance – the Ni V line that was used was at the upper end of the FUSE wavelength range and the data was consequently noisy.

Overall the abundances do not appear to be consistent with those predicted by radiative levitation (Chayer et al., 1995b), for example iron is underabundant compared to the models. However, mass loss, which is currently the most likely explanation for the observed helium lines in DAOs, will modify the heavy element stratification. The heavy element abundances should be enhanced (Unglaub & Bues, 2000), and some correlation with luminosity might be expected, since mass loss rate is a strong function of L in radiatively driven winds. Figure 9.4 shows the dependance of carbon and nitrogen abundance on luminosity. In general, there is no clear correlation between luminosity and heavy element abundance, but scatter is expected, since the abundances will depend on the evolutionary history of the object (Unglaub & Bues, 1998, 2000). Both A 39 and HZ 34 have lower carbon abundances than would be expected for their luminosities, whether using the optical or FUSE parameters. Overall, the measured abundances are generally

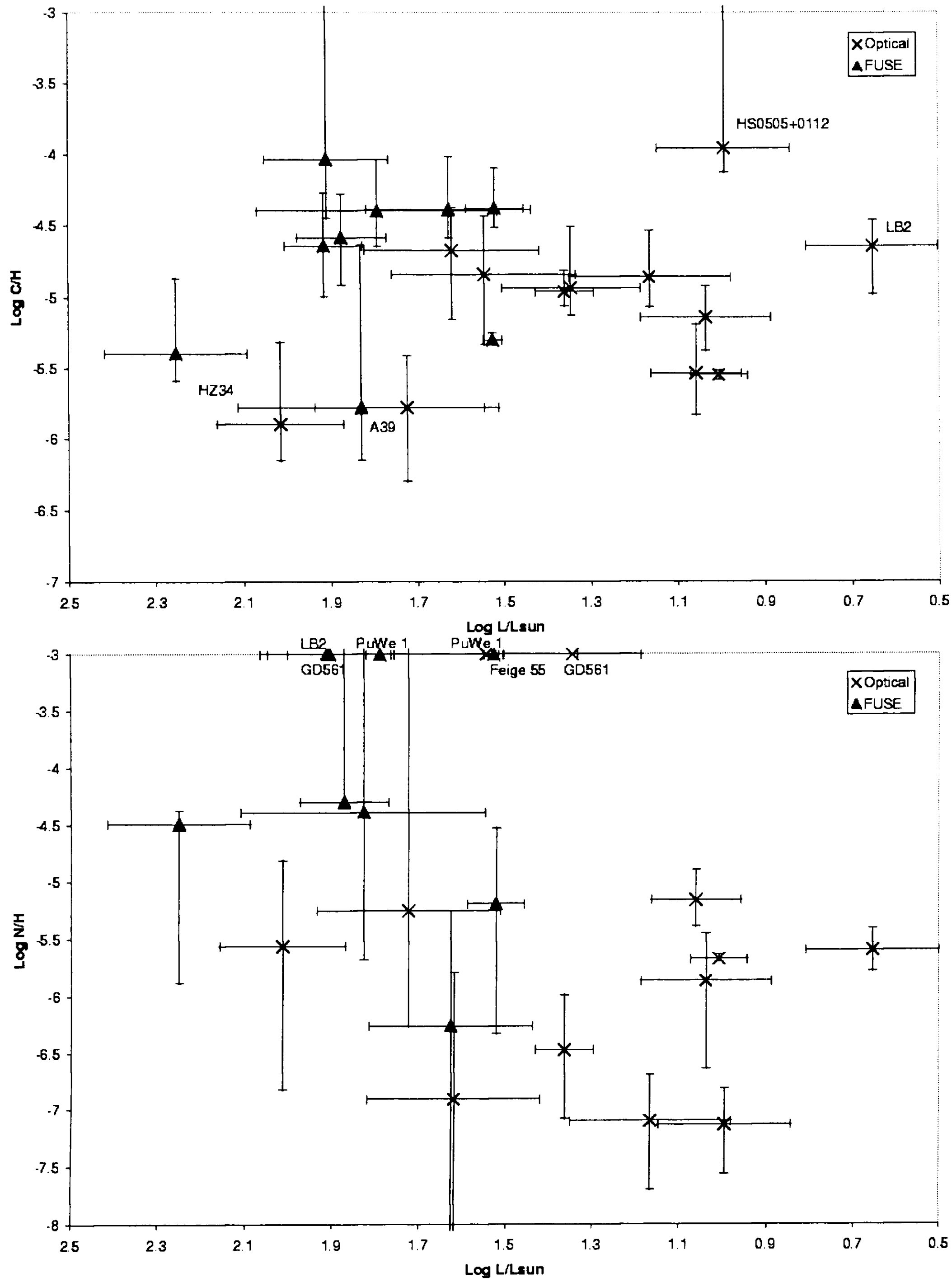

FIGURE 9.4. The dependance of the measured carbon (top) and nitrogen (bottom) abundances on luminosity.

lower than predicted by Unglaub & Bues for a $0.529\,M_{\odot}$ white dwarf, although only C, N and O were included in their models, and so the effect of heavier elements than these is unknown.

Heavy element abundance can also be compared to the effective temperature and gravity of the white dwarfs. The abundances do not appear to be correlated with $T_{\rm eff}$ (Figure 9.5). However, the carbon abundances increase with log g, which is unexpected since the effect of gravitational settling will be more marked in the higher gravity stars, and should provide greater resistance to the effects of radiative levitation or mass loss. By contrast, the nitrogen abundance does not appear to be related to log g. It is possible that this is a subtle affect caused by the different heavy element stratifications changing the temperature structure of the white dwarf. However, the same effect was not observed in the DAs.

9.5 Conclusions

For those white dwarfs whose optical and FUSE temperatures can be described by an empirical relation, the models which use the parameters obtained by fits to the Lyman lines seem consistent with the relative strengths of absorption lines in the FUSE spectrum. For those objects whose Lyman line $T_{\rm eff}$ is $>$120,000 K, neither the models which use the optical or FUSE parameters give a good match to the data. However, the strength of the O VI lines in the spectra of most objects indicates that heavy elements are stratified in the atmospheres of the DAOs.

The measured heavy element abundances of PG 1210+533 and DeHt 5 are similar to those seen in DAs. The white dwarfs in DAO + dM binaries have abundances that are similar to those seen in the DAs, but with enhanced abundances of lighter elements. This seems more consistent with accretion being the mechanism that is producing the high abundance of helium, rather than it being related to the common envelope stage. There is no clear correlation between heavy element abundance and luminosity for the low log g DAOs, or between $T_{\rm eff}$ and abundance. However, carbon abundance was observed to increase with log g, although the same was not observed for nitrogen.

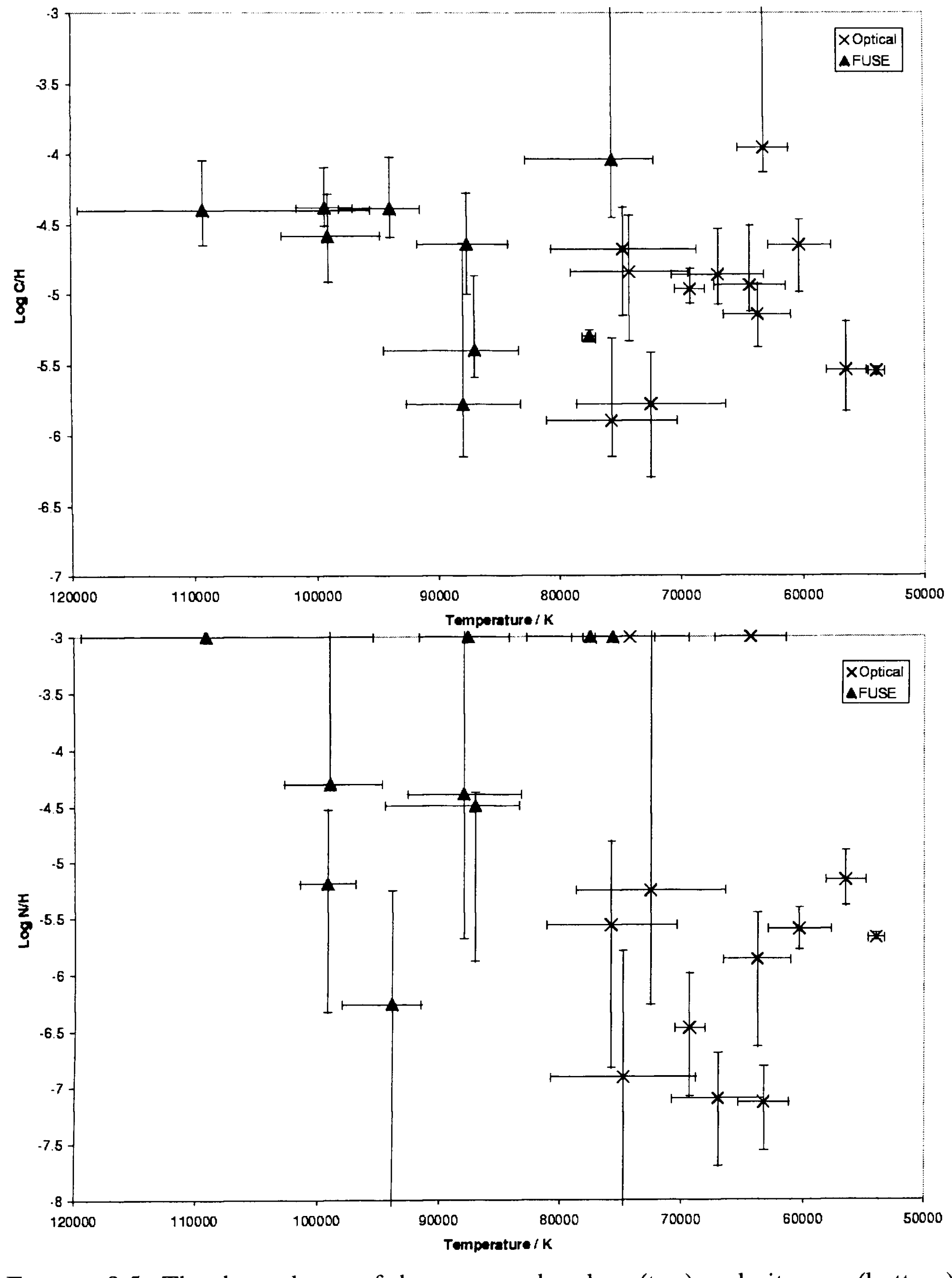

FIGURE 9.5. The dependance of the measured carbon (top) and nitrogen (bottom) abundances on $T_{\rm eff}$.

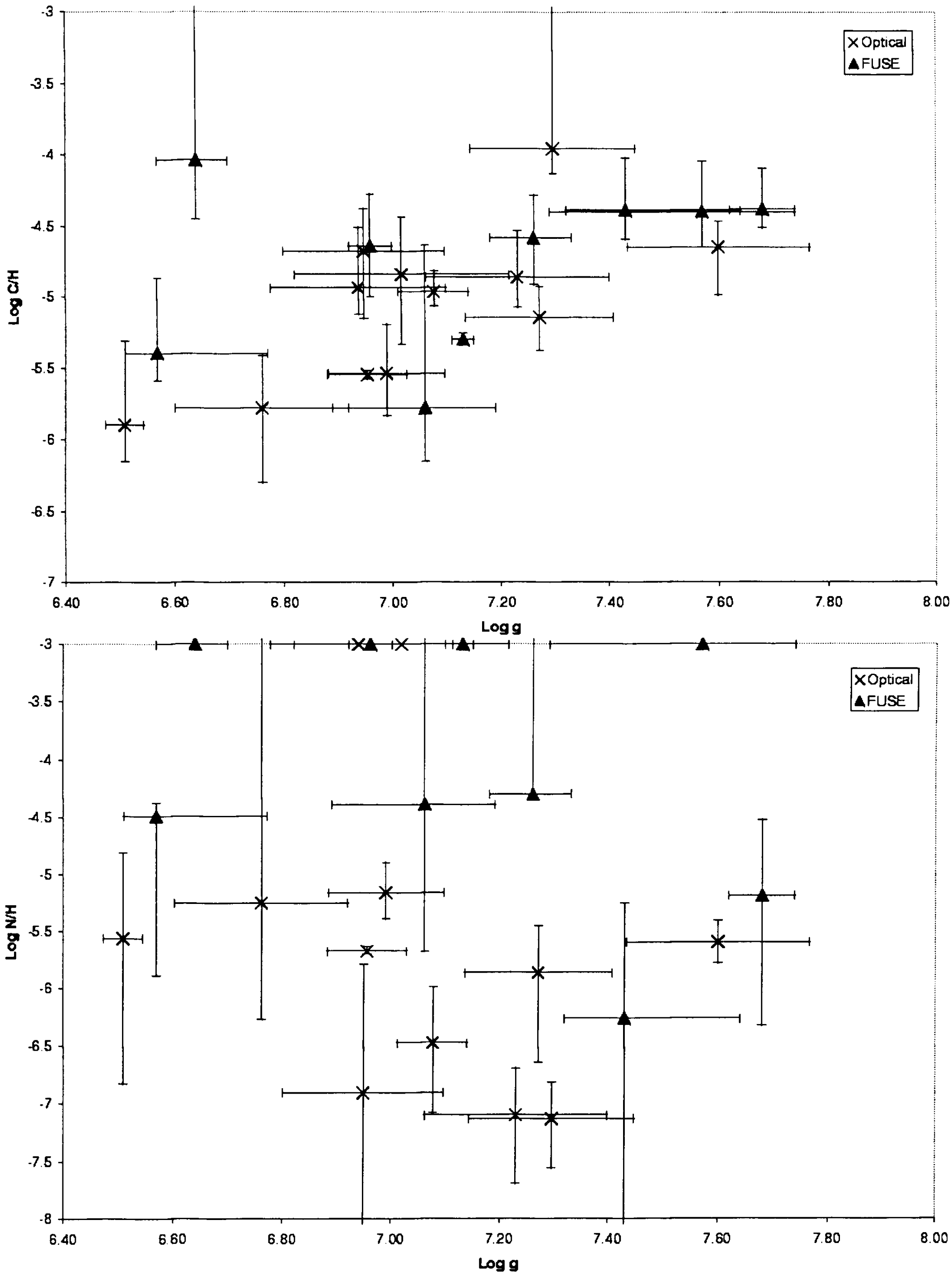

FIGURE 9.6. The dependance of the measured carbon (top) and nitrogen (bottom) abundances on log g.

Chapter 10

Summary

The evolution and physical properties of a sample of DAOs has been investigated using optical and far-UV data. In §10.1-10.7 I briefly summarise the main points from each chapter of this thesis, using bullet points for clarity. Then in §10.8 I bring all the results together in my final conclusions, and in §10.9 I provide ideas for expanding on this work in the future.

10.1 Optical data

- Optical spectra for 22 DAOs were obtained, with a number of the objects having multiple observations.

- Homogeneous and stratified H+He models were fitted to each spectrum, and the F test was used to determine which reproduced the real data better. Only one object (PG 1305-017) was found where the stratified model was preferred with greater than 90% confidence. Homogeneous models better reproduced the spectra of the remainder of the objects, although this was marginal in a number of cases. Only 10 objects could be said to have homogeneous H+He in their line forming regions with better than 90% confidence, although these included in their number PG 1210+533, the spectrum of which was found by Bergeron et al. (1994) to be poorly reproduced by both homogeneous and layered composition models.

- Although statistically the fits to the data were good, the Balmer line problem was noticed when a number of the spectra were fitted. The problem occurred in different degrees, with no statistical difference found between fits to individual Balmer lines in some spectra, to the extreme where no agreement could be found between any lines. There does not appear to be a satifactory solution to this problem at present, and it will require improved models, for example including Stark broadened C, N and O, for it to be resolved.

- The log g distribution of the DAOs is bimodal, with approximately two thirds having surface gravities less than 7.5, while virtually all DAs have higher gravity than this. The masses of these low log g objects are consistent with some having evolved within close binary systems, some as post-EHB objects and some as post-AGB stars. Therefore the details of the stars evolution does not appear to determine if they are DAOs.

- Mass loss is a possible explanation for the helium lines that are observed in the low log g objects. In a radiatively driven wind, mass loss rate is a strong function of luminosity, and these objects are relatively luminous compared to other white dwarfs. One object (DeHt 5) did not fit into this trend as its helium abundance is lower than that of others with similar luminosity – this may be because it has passed the wind limit predicted by Unglaub & Bues (2000). In contrast, others have higher helium abundances than similarly luminous objects. This is expected to some extent, however, since composition will depend on the evolutionary history of the object as well as mass loss rate.

- The remainder of the DAOs have log g that is similar to those seen in DAs. These objects appear to be unusual (PG 1210+533, which has a varying helium abundance), possible transitional objects between the He- and H-rich cooling sequences (PG 1305-017), or DAO+dM binaries. For the latter, accretion from the wind of their companion, or the loss of mass in the CE phase could explain the presence of helium lines in their optical spectra.

10.2 FUSE data

- FUSE data for 23 DAOs were obtained. These were reprocessed using version 2.0.5 or later of the CalFUSE pipeline, and a single, high signal-to-noise spectrum created from the eight spectral segments and multiple exposures that make up a FUSE observation.

10.3 Molecular hydrogen

- Molecular hydrogen absorption was observed in the spectra of 13 of the objects.
- The profiles of the H_2 absorption lines due to different rotational states were fitted. It was found that for 3 objects a satisfactory to a single H_2 model could not be obtained. In reality, the H_2 in the line of sight is likely to be made up of different components with different temperatures and velocities, hence the models are simplistic compared to what is being observed.
- From the measurements, a parameterisation of the H_2 absorption was found, allowing the white dwarf spectra to be separated from the ISM H_2 component.

10.4 Radial velocity varitions

- A search was conducted that looked for shifts in the photospheric heavy element absorption lines between FUSE exposures, which would indicate binarity. The spectrum of 1 object was too contaminated by H_2 absorption to allow radial velocities to be determined.
- Using a Monte Carlo routine, it was found that significant radial velocity shifts were seen in the data for 9 objects. However, the positive results for 4 are likely to be erroneous, although one of these is a binary, as it has a known infrared excess.
- Under the assumption that all the DAOs are in close binary systems, radial velocity shifts should have be detected in the observations of $\sim$20 objects, hence it seems that most are isolated white dwarfs.
- The mode of the DAO mass distribution is between 0.45 and 0.5 $M_{\odot}$. For most of these no radial velocity variations were seen, suggesting they have evolved as single stars via the EHB.

10.5 Lyman line analysis

- Homogeneous models were used to fit the Lyman lines and He II lines in the FUSE spectra of 21 objects.

- For 7 of these objects, the T_{eff} that would be required to obtain a good fit to the Lyman lines was in excess of 120,000 K. The same problem has not been seen in the DAs (Barstow et al., 2003b).

- The log g distribution found from the FUSE data was flat. However, the T_{eff} distribution, determined from FUSE data, extended to higher temperatures than found from the optical spectra, and in this case it was the T_{eff} distribution that seemed bimodal.

- As with the optical results, the luminosities of the majority of DAOs were found to be higher than those of the DAs, the exceptions being the DAO+dM binaries. This is again consistent with mass loss and accretion with the wind of a companion being the mechanism that is preventing the gravitational settling of helium.

- No correlation between log g and log $\frac{\text{He}}{\text{H}}$ was evident, but there was some suggestion of a relationship between T_{eff} and log $\frac{\text{He}}{\text{H}}$.

10.6 Comparison between the results from optical and FUSE data

- The results from the Balmer and Lyman fits showed that the DAOs extended the findings of Barstow et al. (2003b) to higher temperatures i.e. that T_{eff} found from the Lyman lines for objects hotter than $\sim$55,000 K was greater than that obtained from the Balmer lines.

- The temperature discrepancies could not be resolved by invoking the Balmer line problem.

- Although there was considerable scatter in the results, the log g measurements from the two wavelength regions seem to agree.

- Helium abundances also agreed well, which is perhaps surprising given the discrepancies in the temperatures. The exception are the two DAO+dM white dwarfs, where the abundance measured from the FUSE data was lower than that obtained from the optical data. This may be due to changing abundance with depth in the white dwarf atmosphere, or, if the objects are accreting it could be caused by surface inhomogeneities of helium abundance.

10.7 Heavy element abundances

- Using homogeneous models to fit photospheric absorption lines in FUSE data, the abundances of C, N, O, Si, Fe and Ni were measured for each object.
- The relative strengths of lines were more consistent with models with $T_{\rm eff}$ as found from the fit to Lyman lines, rather than the Balmer lines.
- For those objects whose Lyman line determined $T_{\rm eff}$ exceeded 120,000 K neither models that used the optical or FUSE parameters produced a good match to the line strengths.
- The above two points rely on homogeneous models being a good approximation to the abundance distributions in the white dwarf atmosphere. In reality, this is not likely to be the case, however.
- The DAO+dM binaries were found to have slightly higher abundances of the lighter elements than the DAs, whereas the heavier elements were present at approximately the same abundances. This is as might be expected if the objects were accreting the lighter elements from their companions.
- The high $T_{\rm eff}$, low log g had elevated heavy element abundances compared to the DAs. This qualitatively consistent with what is expected if mass loss were occurring.

10.8 Conclusions

DAO white dwarfs fall into two groups. The objects that make up the first group are characterised by low log g and high $T_{\rm eff}$ compared to the DAs, and hence have comparitively high luminosities. These objects made up approximately two thirds of the sample. Since mass loss rate in radiatively driven winds is a strong function of luminosity, and because these objects are relatively luminous, mass loss is currently the most likely explanation for the way in which the gravitional settling of helium in their atmospheres is prevented. However, no strong correlation between luminosity and helium abundance has been found; in fact, $T_{\rm eff}$ seems the better indicator of helium abundance. This group of white dwarfs appears to be of DAO spectral type because of their low gravities and high temperatures, rather than their evolutionary path. To have these characteristics, they will tend to have low mass compared to the majority of white dwarfs. Therefore, some are formed in close binary systems, where mass is lost in the common-envelope phase, resulting in low mass He-core white dwarfs. However, the majority appear to be isolated white dwarfs, and most would not have been massive enough to ascend the AGB after core helium burning and will have evolved via the EHB. According to the masses found for these objects, some are also likely to be post-AGB objects. There is one object that does not seem to fit in with the rest: the central star of the planetary nebula DeHt 5. This object is one of the cooler examples of this group of DAOs and has log g of 7.08 or 6.75, depending if the Balmer or Lyman line measurements are believed respectively. In the former case, DeHt 5 is very close to the wind limit that was predicted by Unglaub & Bues (2000). Hence, it is possible that this may be an example of an object whose wind has switched off – this might also explain the slightly elevated heavy element abundances compared to the DAs.

The second group have $T_{\rm eff}$, log g and mass that are apparently normal when compared to the DAs. In the sample of stars analysed in this thesis, there were 6 objects that belonged in this group, 4 of which were DAO+dM binaries. The results for these are consistent with material being accreted from their companions, and hence these objects must be part of a close binary system to be DAOs. In addition there were two unusual objects: PG 1305-017 is probably an object transferring between the He- and H-rich cooling sequences. This type of object appears to be rare since it is the only one out of 22 objects where stratified models significantly reproduced the He II line at 4686 Å better than chemically homogeneous models. The helium abundance of PG 1210+533 is relatively high and is variable, but no indication of the mechanism that is acting against the gravitational settling of helium has been found in the data analysed in this thesis.

Therefore, in summary, three ways in which DAOs fit into the general evolution of white dwarfs can be identified. These are:

1. Low log g, high $T_{\rm eff}$ objects are DAOs because of mass loss; when this ceases they will become low mass DAs. These may be He-core post-CE white dwarfs, or low mass isolated stars that have evolved via the EHB or AGB.

2. White dwarfs may be DAOs if they are accreting material from the wind of a companion. These are normal mass white dwarfs that are in close binary systems.

3. Finally, an object can have DAO spectral type if it is transferring between the He- and H-rich cooling sequences. The only example of this type is a post-AGB white dwarf.

The DAOs were found to exhibit the same Balmer/Lyman temperature differences that have been observed in the DAs. This only afflicted the low log g, high $T_{\rm eff}$ DAOs, but this is as expected since the other group of objects are at or below the minimum temperature where the problem is seen. The relative strengths of the heavy element absorption lines in the FUSE data suggests that it is the Lyman line derived parameters that are the more reliable, although this conclusion is uncertain since the chemical homogeneity that is assumed within the models is unlikely to hold true in the atmospheres of real white dwarfs. An extreme form of the temperature problem was found in the data for 7 of the stars, where models hotter than 120,000 K were required to reproduce the Lyman lines. Models that reproduced the Balmer lines of these objects well were irreconcilable with the shallow Lyman lines. Neither models that used the parameters obtained from Balmer or Lyman line fits were able to match the line strengths of the heavy element lines successfully. The result of these problems was that log g was the better indicator of to which group a DAO belongs when optical data were being analysed as the difference in temperatures between the two groups was relatively small, whereas $T_{\rm eff}$ was better if using FUSE data. To date, no explanation for these problems is evident.

10.9 Future work

This thesis has examined the properties of a large sample of DAO white dwarfs, but there is much scope for follow up work. I list some examples of future work here:

- Incorporate Stark broadened C, N and O into the atmospheric models to attempt to resolve the Balmer line problem.
- Investigate the molecular hydrogen absorption that is seen in FUSE spectra in more detail. In particular, try to determine why some objects required two H_2 components to obtain a good fit, and compare the techniques of curve of growth fitting and line profile fitting to determine if the results from both agree.
- Many white dwarfs have been observed by FUSE, and the data is available for most in the public archive. The techniques that has been used to search for binarity in this thesis and to determine mass from Lyman line fits could be extended to these to determine the proportion of different mass white dwarfs that are in binary systems.
- Exploit other wavelength regimes, e.g. infrared, STIS data which spans between 1200 and 1700 Å, to further investigate each white dwarf individually, in particular the unusual object PG 1210+533.

- The assumption of chemically homogeneous atmospheres is not physically realistic. If models could be developed that incorporated gravitational settling, radiative levitation, mass loss and accretion, then it may be possible to resolve the issues with the high heavy element abundances in some of the DAOs and the discrepancies between the results of different wavelength regimes.

Bibliography

Abbott, D. (1982), *ApJ.* **259**, 282–301.

Abell, G. O. (1966), 'Properties of Some Old Planetary Nebulae', *ApJ.* **144**, 259.

Barstow, M. (2003a), 'Measuring the fundamental parameters of hot hydrogen-rich white dwarfs', *Chin. J. Astron. Astrophys.* **3**(4), 287–310.

Barstow, M. A. (1989), ROSAT - an all-sky X-ray and EUV survey of white dwarfs, *in* 'IAU Colloq. 114: White Dwarfs', pp. 156–159.

Barstow, M. A. (1993), 'Photospheric composition and structure in white dwarfs', *Advances in Space Research* **13**, 15–.

Barstow, M. A. & Hubeny, I. (1998), 'An alternative explanation of the EUV spectrum of the white dwarf G191-B2B invoking a stratified H+He envelope including heavier elements', *MNRAS* **299**, 379–388.

Barstow, M., Bannister, N., Holberg, J., Hubeny, I., Bruhweiler, F. & Napiwotzski, R. (2001a), 'Far-ultraviolet spectroscopy of the hot DA white dwarf WD2218+706 (DeHt5) with STIS', *MNRAS* **325**, 1149–1156.

Barstow, M., Burleigh, M., Bannister, N., Holberg, J., Hubeny, I., Bruhweiler, F. & Napiwotzki, R. (2000), Heavy elements in DA white dwarfs, *in* J. Provencal, H. Shipman, J. MacDonald & S. Goodchild, eds, '12^{th} European Conference on White Dwarfs', ASP conference series, pp. 128–134.

Barstow, M., Burleigh, M., Fleming, T., holberg, J., Koester, D., Marsh, M., Rosen, S., Rutten, R., Sakai, S., Tweedy, R. & Wegner, G. (1995), 'The orbital period of the pre-cataclysmic binary RE 2013+400 and a study of the atmosphere of the DAO white dwarf primary', *MNRAS* **272**, 531–543.

Barstow, M., Good, S., Burleigh, M., Hubeny, I., Holberg, J. & Levan, A. (2003b), 'A comparison of DA white dwarf temperatures and gravities from FUSE Lyman line and ground-based Balmer line observations', *MNRAS* .

Barstow, M., Good, S., Holberg, J., Burleigh, M., Bannister, N., Hubeny, I. & Napiwotzki, R. (2001b), 'FUSE observations of PG1342+444: new insights into the nature of the hottest DA white dwarfs', *MNRAS* .

Barstow, M., Good, S., Holberg, J., Hubeny, I., Bannister, N., Bruhweiler, F., Burleigh, M. & Napiwotzki, R. (2003c), 'Heavy-element abundance patterns in hot DA white dwarfs', *MNRAS* **341**, 870–890.

Barstow, M., Hodgkin, S., Pye, J. & King, A. (1993), *in* M. Barstow, ed., 'White dwarfs: advances in observation and theory', Dordrecht, Kluwer.

Barstow, M. & Holberg, J. (2003), *Extreme Ultraviolet Astronomy*, Cambridge Astrophysics Series, Cambridge University Press.

Barstow, M., Holberg, J., Hubeny, I., Good, S., Levan, A. & Meru, F. (2001c), 'A comparison of DA white dwarf temperatures and gravities from lyman and balmer studies', *MNRAS* **328**, 211–222.

Barstow, M., Hubeny, I. & Holberg, J. (1998), 'The effect of photospheric heavy elements on the hot DA white dwarf temperature scale', *MNRAS* **299**, 520–534.

Bergeron, P., Saffer, R. & Liebert, J. (1992), 'A spectroscopic determination of the mass distribution of DA white dwarfs', *ApJ.* **394**, 228–247.

Bergeron, P., Wesemael, F., Beauchamp, A., Wood, M., Lamontagne, R., Fontaine, G. & Liebert, J. (1994), 'A spectroscopic analysis of DAO and hot DA white dwarfs: the implications of the presence of helium and the nature of DAO stars', *ApJ.* **432**, 305–325.

Bergeron, P., Wesemael, F., Lamontagne, R. & Chayer, P. (1993), 'Metal line-blanketing and the peculiar h-beta line profile in the dao star feige 55', *ApJ. Letters* **407**, L85–L88.

Blöcker, T. (1995), 'Stellar evolution of low- and intermediate-mass stars. II. post-AGB evolution', *A&A* **299**, 755–769.

Burleigh, M. (1997), Hot white dwarfs in detached binaries from the ROSAT WFC all sky survey, PhD thesis, University of Leicester.

Carroll, B. W. & Ostlie, D. A. (1996), *An Introduction to Modern Stellar Astrophysics*, Addison-Wesley Publishing Company Inc.

Chandrasekhar, S. (1939), *An introduction to the study of stellar structure*, Chicago, Ill., The University of Chicago press [1939].

Chayer, P., Oliveira, C., Dupuis, J., Moos, H. W. & Welsh, B. (2003), Detection of Photospheric O VI in the FUSE Spectra of Low Metallicity White Dwarfs, *in* 'NATO ASIB Proc. 105: White Dwarfs', p. 127.

Chayer, P., Vennes, S., Pradhan, A., Thejll, P., Beauchamp, A., Fontaine, G. & Wesemael, F. (1995b), 'Improved calculations of the equilibrium abundances of heavy elements supported by radiative levitation in the atmospheres of hot DA white dwarfs', *ApJ.* **454**, 429–441.

Cheselka, M., Holberg, J., Watkins, R., Collins, J. & Tweedy, R. (1993), 'UBV photometry of hot white dwarf stars', *AJ* **106**(6).

Ciardullo, R., Bond, H., Sipior, M., Fullton, L., Zhang, C.-Y. & Schaeffer, K. (1999), 'A Hubble Space Telescope survey for resolved companions of planetary nebula nuclei', *AJ* **118**, 488–508.

de Kool, M. (1992), 'Statistics of cataclysmic variable formation', *A&A* **261**, 188–202.

de Kool, M. & Ritter, H. (1993), 'On the formation rate and space density of close white dwarf main sequence star binaries', *A&A* **267**, 397–409.

de Loore, C. & Doom, C. (1992), *Structure and evolution of single and binary stars*, Kluwer Academic Publishers.

Dobbie, P., Barstow, M., Burleigh, M. & Hubeny, I. (1999), 'Opacities along the line of sight to and in the atmosphere of the white dwarf in the close detached DAO+dM binary RE J0720-318', *A&A* **346**, 163–174.

Dopita, M. & Liebert, J. (1989), 'The nebula around EGB 6/PG 0950+139: evidence for ablation of a Jovian planet?', *ApJ.* **347**, 910–914.

Dorman, B., Rood, R. T. & O'Connell, R. W. (1993), 'Ultraviolet Radiation from Evolved Stellar Populations. I. Models', *ApJ.* **419**, 596.

Dreizler, T., Heber, U., Napiwotzki, R. & Hagen, H. (1995), 'Ultra-high excitation features in hot white dwarfs: one DAo and three DO stars discovered by the Hamburg-Schmidt survey', *A&A* **303**, L53–L56.

Driebe, T., Schönberner, D., Blöcker, T. & Herwig, F. (1998), 'The evolution of helium white dwarfs. I. the companion of the millisecond pulsar PSR J1012+5307', *A&A* **339**, 123–133.

Duley, W. & Williams, D. (1984), *Interstellar chemistry*, Academic Press.

Finley, D. S., Koester, D. & Basri, G. (1997), 'The Temperature Scale and Mass Distribution of Hot DA White Dwarfs', *ApJ.* **488**, 375.

Fleming, T. & Liebert, J. (1986), 'The luminosity function of DA white dwarfs', *ApJ* **308**, 176–189.

Fontaine, G. & Wesemael, F. (1987), *in* A. Philip, D. Hayes & J. Liebert, eds, 'The second conference on faint blue stars', IAU Coll. No. 95, p. 319.

Fulbright, M. & Liebert, J. (1993), 'JHK photometry of WD 0950+139', *ApJ* **410**, 275–280.

Fulbright, M., Liebert, J., Bergeron, P. & Green, R. (1993), 'Spectroscopic observations of the detached binary PG1413+015', *ApJ* **406**, 240–246.

Green, R., Schmidt, M. & Liebert, J. (1986), 'The Palomar-Green catalog of ultraviolet-excess stellar objects', *ApJ* **61**, 305–352.

Greenstein, J. (1974), 'A new list of 52 degenerate stars VII', *ApJ* **189**, L131–L133.

Greenstein, J. L. (1984), 'Spectrophotometry of the white dwarfs', *ApJ.* **276**, 602–620.

Hamada, T. & Salpeter, E. E. (1961), 'Models for Zero-Temperature Stars.', *ApJ.* **134**, 683.

Heber, U., Dreizler, S. & Hagen, H.-J. (1996), 'On the hot ends of the white dwarf spectral sequences: hot white dwarfs containing helium from the Hamburg-Schmidt survey', *A&A* **311**, L17–L20.

Hillwig, T. C., Honeycutt, R. K. & Robertson, J. W. (2000), 'Post-Common-Envelope Binary Stars and the Precataclysmic Binary PG 1114+187', *AJ* **120**, 1113–1119.

Holberg, J. (1987), *in* A. D. Philips, D. Hayes & J. Liebert, eds, 'The second conference on faint blue stars', number 95 *in* 'IAU Colloq.', p. 285.

Holberg, J. B., Sandel, B. R., Forrester, W. T., Broadfoot, A. L., Barry, D. C. & Shipman, H. L. (1980), 'Extreme-UV and far-UV observations of the white dwarf HZ 43 from Voyager 2', *ApJ.* **242**, L119–L123.

Holberg, J., Saffer, R., Tweedy, R. & Barstow, M. (1995), 'The binary double-degenerate nature of the bright DAO white dwarf Feige 55', *ApJ.* **452**, L133–L136.

Holberg, J., Sing, D., Barstow, M. & Good, S. (2001), HS 1136+6646: a new short period DAO + dMe system, *in* 'Abstracts of Contributed Talks and Posters presented at the Annual Scientific Meeting of the Astronomische Gesellschaft', Vol. 18 of *Astronomische Gesellschaft Abstract Series*.

Holberg, J., Wesemael, F. & Basile, J. (1986), *ApJ.* **306**, 629–641.

Hubeny, I. & Lanz, T. (1995), 'Non-LTE line-blanketed model atmospheres of hot stars. I. hybrid complete linearization/accelerated lambda iteration method', *ApJ.* **439**, 875–904.

Iben, I.-J. (1965), 'Stellar evolution I. The approach to the main sequence', *ApJ.* **141**, 993.

Iben, I.-J. & Livio, M. (1993), 'Common envelopes in binary star evolution', *PASP* **105**, 1373–1406.

Iben-Jr, I. (1991), 'Single and binary star evolution', *ApJS* **76**, 55–114.

Jordan, S. & Koester, D. (1986), 'Model atmospheres and synthetic spectra for white dwarfs with chemically stratified atmospheres', *A&AS* **65**, 367–377.

Kidder, K. (1991), PhD thesis, University of Arizona.

Koester, D., Liebert, J. & Hege, E. K. (1979), 'The effective temperatures and helium abundances of DO white dwarfs', *A&A* **71**, 163–168.

Kruk, J., Chayer, P. & Dupuis, J. (2003), FUSE observations of the DAO white dwarf Feige 55, *in* D. de Martino, R. Silvotti, J.-E. Solheim & R. KKalytis, eds, 'White Dwarfs', NATO science series, Kluwer Academic Publishers, pp. 131–134.

Kwitter, K., Jacoby, G. & Lydon, T. (1988), 'Identification of faint central stars in extended, low-surface-brightness planetary nebulae', *AJ* **96**(3), 997–1182.

Lampton, M., Margon, B. & Bowyer, S. (1976), *ApJ.* **208**, 177–190.

Lemke, M. (1997), 'Extended VCS Stark broadening tables for hydrogen – Lyman to Brackett series', *A&AS* **122**, 285–292.

Liebert, J., Green, R., Bond, H., Holberg, J., Wesemael, F., Fleming, T. & Kidder, K. (1989), 'A compact planetary nebula around the hot white dwarf EGB 6/PG 0950+139', *ApJ.* **346**, 251–264.

Marsh, M. (1995), PhD thesis, University of Leicester.

Marsh, T. R., Dhillon, V. S. & Duck, S. R. (1995), 'Low-Mass White Dwarfs Need Friends - Five New Double-Degenerate Close Binary Stars', *MNRAS* **275**, 828.

McCandliss, S. (2003), 'Molecular hydrogen optical depth templates for fuse data analysis', *PASP* .

McCandliss, S., Sembach, K., Burgh, E., Sahnow, D. & FUSE Team (2000), 'Hot Molecular Hydrogen in M27 Observed by FUSE', *Bulletin of the American Astronomical Society* **197**, 611.

McCook, G. P. & Sion, E. M. (1999), 'A Catalog of Spectroscopically Identified White Dwarfs', *ApJS.* **121**, 1–130.

Mendez, R. (1991), 'Photospheric abundances in central stars of planetary nebulae, and evolutionary implications'.

Mendez, R., Kudritzki, R. & Simon, K. (1985), 'SIT vidicon and IDS spectra of central stars of planetary nebulae', *A&A* **142**, 289–296.

Moos, H. W., Cash, W. C., Cowie, L. L., Davidsen, A. F., Dupree, A. K., Feldman, P. D., Friedman, S. D., Green, J. C., Green, R. F., Gry, C., Hutchings, J. B., Jenkins, E. B., Linsky, J. L., Malina, R. F., Michalitsianos, A. G., Savage, B. D., Shull, J. M., Siegmund, O. H. W., Snow, T. P., Sonneborn, G., Vidal-Madjar, A., Willis, A. J., Woodgate, B. E., York, D. G., Ake, T. B., Andersson, B.-G., Andrews, J. P., Barkhouser, R. H., Bianchi, L., Blair, W. P., Brownsberger, K. R., Cha, A. N., Chayer, P., Conard, S. J., Fullerton, A. W., Gaines, G. A., Grange, R., Gummin, M. A., Hebrard, G., Kriss, G. A., Kruk, J. W., Mark, D., McCarthy, D. K., Morbey, C. L., Murowinski, R., Murphy, E. M., Oegerle, W. R., Ohl, R. G., Oliveira, C., Osterman, S. N., Sahnow, D. J., Saisse, M., Sembach, K. R., Weaver, H. A., Welsh, B. Y., Wilkinson, E. & Zheng, W. (2000), 'Overview of the Far Ultraviolet Spectroscopic Explorer Mission', *ApJ.* **538**, L1–L6.

Morton, D. (1991), 'Atomic data for resonance absorption lines. I. Wavelengths longward of the Lyman limit', *ApJ.* **77**, 119–202.

Napiwotzki, R. (1992), Analysis of central stars of old planetary nebulae: problems with the Balmer lines, *in* 'LNP Vol. 401: The Atmospheres of Early-Type Stars', p. 310.

Napiwotzki, R. (1999), 'Spectroscopic investigation of old planetaries IV. Model atmosphere analysis', *A&A* **350**, 101–119.

Napiwotzki, R., Green, P. J. & Saffer, R. (1999), 'A comparitive study of the mass distribution of extreme-ultraviolet-selected white dwarfs', *ApJ* **517**, 399–415.

Napiwotzki, R. & Schönberner, D. (1993), White dwarf central stars of old planetary nebulae, *in* M. Barstow, ed., 'White Dwarfs: Advances in observation and theory', NATO ASI Series, Kluwer Academic Publishers, pp. 99–104.

Napiwotzki, R. & Schönberner, D. (1995), 'Spectroscopic investigation of old planetaries III. Spectral types, magnitudes, and distances', *A&A* **301**, 545–558.

O'Dell, C. & Handron, K. (1996), 'Cometary knots in the Helix Nebula', *AJ* **111**(4), 1630.

Oke, J. B., Weidemann, V. & Koester, D. (1984), 'Temperatures and surface gravities of DB white dwarfs', *ApJ.* **281**, 276–285.

Pauldrach, A., Puls, J., Kudritzki, R. P., Mendez, R. H. & Heap, S. R. (1988), 'Radiation-driven winds of hot stars. V - Wind models for central stars of planetary nebulae', *A&A* **207**, 123–131.

Saffer, R., Livio, M. & Yungelson, L. (1998), 'Close binary white dwarf systems: numerous new detections and their interpretation', *ApJ* **502**, 394–407.

Sahnow, D., Moos, H. et al. (2000), 'On-orbit performance of the Far Ultraviolet Spectroscopic Explorer satellite', *ApJ* **538**, L7–L11.

Schuh, S., Dreizler, S. & Wolff, B. (2002), 'Equilibrium abundance in hot DA white dwarfs as derived from self-consistent diffusion models I: Analysis of spectroscopic EUVE data', *A&A* .

Seaton, M. (1979), 'Interstellar extinction in the UV', *MNRAS* **187**, 73P–76P.

Shafer, R., Haberl, F., Arnaud, K. & Tennant, A. (1991).

Shull, J. & Beckwith, S. (1982), 'Interstellar molecular hydrogen', *Ann. Rev. Astron. Astrophys.* **20**, 163–190.

Sing, D., Holberg, J., Burleigh, M., Good, S., Barstow, M., Oswalt, T., Howell, S. & Brinkworth, C. (2003), 'Spectroscopic and photmetric analysis of HS 1136+6646: a young DAO+K7V post-common-envelope pre-cataclysmic-variable binary', *ApJ.* **0**, 0.

Sion, E., Greenstein, J., Landstreet, J., Liebert, J., Shipman, H. & Wegner, G. (1983), 'A proposed new white dwarf spectral classification system', *ApJ.* **269**, 253–257.

Speck, A., Meixner, M., Jacoby, G. & Knezek, P. (2003), 'Molecular Hydrogen in the Ring Nebula: Clumpy Photodissociation Regions', *PASP* **115**, 170–177.

Tweedy, R., Holberg, J., Barstow, M., Bergeron, P., Grauer, A., Liebert, J. & Fleming, T. (1993), 'RE1016-053: a pre-cataclysmic binary, and the first extreme ultraviolet and x-ray detections of a DAO white dwarf', *AJ* **105**(5).

Unglaub, K. & Bues, I. (1998), 'The effect of diffusion and mass loss on the helium abundance in hot white dwarfs and subdwarfs', *A&A* pp. 75–84.

Unglaub, K. & Bues, I. (2000), 'The chemical evolution of hot white dwarfs in the presense of diffusion and mass loss', *A&A* pp. 1042–1058.

Vennes, S., Pelletier, C., Fontaine, G. & Wesemael, F. (1988), 'The presence of helium in hot DA white dwarfs: the role of radiative leviation and the case for stratified atmospheres', *ApJ.* pp. 876–897.

Vennes, S. & Thorstensen, J. (1996), 'An ephemeris for the pre-cataclysmic binary EUVE J0720-317', *ApJ.* **112**(1), 284–288.

Werner, K. (1996), *A&A* **457**, L39.

Wesemael, F., Green, R. & Liebert, J. (1985), *ApJS* **58**, 379.

Wesemael, F., Greenstein, J. L., Liebert, J., Lamontagne, R., Fontaine, G., Bergeron, P. & Glaspey, J. W. (1993), 'An atlas of optical spectra of white-dwarf stars', *PASP* **105**, 761–778.

Wood, M. (1992), 'Constraints on the age and evolution of the galaxy from the white dwarf luminosity function', *ApJ.* **386**, 539–561.

Zeilik, M., Gregory, S. A. & v. P. Smith, E. (1973), *Introductory Astronomy and Astrophysics*, Saunders College Publishing.